Conceptual design of a concentrating solar power plant for a combined electricity and water supply of the city El Gouna

Johannes Wellmann

Technische Universität Berlin
Fakultät III: Prozesswissenschaften
Institut für Energietechnik
Fachgebiet Energieverfahrenstechnik und Umwandlungstechniken regenerativer Energien

Dissertation

Conceptual design of a concentrating solar power plant for a combined electricity and water supply of the city El Gouna

vorgelegt von

Dipl.-Ing.
Johannes Wellmann
geb. in Bonn

von der Fakultät III - Prozesswissenschaften
der Technischen Universität Berlin
zur Erlangung des akademischen Grades

Doktor der Ingenieurwissenschaften
- Dr.-Ing. -

genehmigte Dissertation

Promotionsausschuss

Vorsitzende:	Prof. Dr.-Ing. Tetyana Morozyuk
Gutachter:	Prof. Dr. Frank Behrendt
Gutachter:	Prof. Dr.-Ing. Christoph Nytsch-Geusen

Tag der wissenschaftlichen Aussprache: 01. September 2015

Berlin 2015

Contents

List of Figures

List of Tables

Acronyms

Afc	Aftercooler, heat exchanger of feed water preheating
BPE	Boiling point elevation
CAPEX	Capital expenditures
CC	Capacity credit
CEPCI	Chemical engineering construction price index
CF	Capacity factor
CSIRO	Commonwealth scientific and industrial research organization, Australia
CSP	Concentrated solar power
DAAD	German academic exchange service, Deutscher Akademischer Austausch Dienst
Dii	Desertec Industrial Initiative
DLR	German Aerospace Center, Deutsches Zentrum fuer Luft und Raumfahrt
DSG	Direct steam generation
ECO	Economizer, heat exchanger of the steam generator
ED	Electro dialysis, desalination technology
EPC	Engineering, construction and procurement costs
EVA	Evaporator, heat exchanger of the steam generator
FLH	Full load hours
FWP	Feed water preheater
GOR	Gained output ratio
HEX	Heat exchanger
HP	High pressure, turbine
HTF	Heat transfer fluid
IEA	International Energy Agency
IRENA	International Renewable Energy Agency
LCOE	Levelized cost of electricity
LFC	Linear fresnel collector, line focusing CSP collector
LP	Low pressure, turbine

LTD Low temperature distillation
LWC Levelized water cost
MD Membrane distillation, desalination technology
MED Multi effect distillation, thermal desalination technology
MENA Middle East and North Africa
MP Medium pressure, turbine
MSF Multi stage flash distillation, thermal desalination technology
NREL National Renewable Energy Laboratory
OPEX Operational expenditures
ppm Parts per million
PR Performance ratio, water to power
PTC Parabolic trough collector, line focusing CSP collector
PV Photovoltaic, solar panel or module
RO Reverse osmosis, membrane desalination technology
SAM System Advisor Model
SEGS Solar electricity generation system
SH Superheater, heat exchanger of the steam generator
SM Solar multiple
ST Solar tower, point focusing CSP collector
TDS Total dissolved solids, seawater salinity
TES Thermal energy storage
WMO World Meteorological Organization
ZLD Zero liquid discharge

Symbols

Symbol	Unit	Name
A	m^2	Area
α_m	$\mathrm{W/m^2K}$	Averaged heat transfer coefficient
B	$\mathrm{W/m^2}$	Beam horizontal irradiation
c_b	$\%$	Betz factor or power coefficient, wind power
C_t	US \$	Capital cost
I_{mpp}	A	Current, PV module, maximum power point
D	$\mathrm{MWh_{el}}$	Demand, electricity
ρ_{air}	$\mathrm{kg/m^3}$	Density
D	$\mathrm{W/m^2}$	Diffuse horizontal irradiation
DN	$\mathrm{W/m^2}$	Diffuse normal irradiation
DNI	$\mathrm{W/m^2}$	Direct normal irradiation
η	$-$	Efficiency
ϵ	$-$	Emissivity
h	$\mathrm{kJ/kg}$	Enthalpy
ϵ_k	$-$	Exergetic efficiency, component
ϵ_t	$-$	Exergetic efficiency, total
E	kW	Exergy, physical, chemical, kinetic, potential
y_D	$-$	Exergy, ratio of exergy destruction
v	$\mathrm{m/s}$	Flow velocity
F_t	US \$	Fuel cost
G	$\mathrm{W/m^2}$	Global horizontal irradiation
GTI	$\mathrm{W/m^2}$	Global tilted irradiation
k	$\mathrm{W/m^2K}$	Heat transfer coefficient
Q	$\mathrm{MW_{th}}$	Heat, thermal
τ_{PV}	$\mathrm{K/W/m^2}$	Heat-up coefficient, photovoltaic module
h	m	Height
i_r	$\%$	Interest rate

Symbol	Unit	Name
ν	$\mathrm{m^2/s}$	Kinematic viscosity
M	kg	Mass
$\dot{m}_d$	$\mathrm{m^3/d}$	Mass flow, desalinated water
$\dot{m}$	$\mathrm{t/h}$	Mass flow, water and steam
n	$-$	Number of heliostats, desalination stages or PV modules
$O\&M$	US $	Operation and maintenance costs
P_{el}	$\mathrm{MW_{el}}$	Power, electric
p	bar	Pressure
rh	$\%$	Relative humidity
z_0	m	Roughness factor, ground condition, wind power
b	$\mathrm{g/kg\ TDS}$	Salt concentration in total dissolved solids
I	$\mathrm{kWh/m^2}$	Solar irradiation
I_a	$\mathrm{kWh/m^2a}$	Solar irradiation, annual, mostly direct normal irradiation
c_p	$\mathrm{J/gK}$	Specific heat capacity
x	$-$	Steam content
σ	$\mathrm{W/m^2K^4}$	Stefan Boltzmann constant
γ	$^\circ$	Sun elevation angle
T	$^\circ\mathrm{C}$	Temperature
α_{PV}	$\%/\mathrm{K}$	Temperature coefficient, photovoltaic module
δ	m	Thermal boundary layer
λ	$\mathrm{W/mK}$	Thermal conductivity
R_d	$\mathrm{m^2K/W}$	Thermal resistance in thermal desalination systems
t	h	Time
U_{mpp}	V	Voltage, PV module, maximum power point
d_w	$^\circ$	Wind direction
v_w	$\mathrm{m/s}$	Wind speed
W	$\mathrm{MW_{el}}$	Work, mechanical
ζ	$^\circ$	Zenith angle

Acknowledgment

I would like to express my special appreciation and thanks to my supervisor Prof. Dr. Frank Behrendt, who supported me greatly during my activities at TU Berlin and Campus El Gouna since six years. I would like to thank him for constant encouraging me in my research and for allowing me to grow as a scientist. Furthermore, I would also like to thank my committee members, Prof. Dr. Tetyana Morozyuk and Prof. Dr.-Ing. Christoph Nytsch-Geusen for serving as my committee members and especially because of the great cooperation in the "Energy Engineering" master program at Campus El Gouna during the last years.

Special thanks also belongs to the following persons:

- Markus Lehmann for the development of the low-temperature desalination, his great inventiveness, straightforward approaches and the fruitful discussions about small details. He and his family hosted me greatly during several visits in Switzerland and we always had a tremendous good time.
- Dr. rer. nat. Franz Trieb for his great research during the last ten years, his work at the German-Center for Aerospace (DLR), his pioneering studies, his lectures at Campus El Gouna and his great character. Several ideas of the case study base on inspiring discussions while having pleasant evening dinners in El Gouna during his lectures.
- All students, who contributed with the final theses to this research. There is especially mentioned Karl Neuhäuser, Norman Schweimanns, Frederic Krakau, Jonas Balyos, Eric Schmerse and all students of the Campus El Gouna. I would also like to thank my colleagues of the Energy Engineering department, especially Timo Blumberg who has been substituting my position accepting a high additional workload,
- All my friends and my family for the encouraging support, especially Pia-Katharina Nieder, Dr. Nina Kuckländer, Marie-Therese Scharl, Norman Schweimanns and Eva Wellmann for the proofreading as well as their questions and comments to the manuscript, and
- especially my parents and my sister, for allowing me to realize my own potential, for financing of my studies as well as the continuous support throughout my life and my career development.

Abstract

The cogeneration of power and water in large concentrating solar power (CSP) plants with thermal storage can have significant energetic and economic benefits to supply regions with high direct irradiation and good seawater access. Due to increasing water scarcity, the Middle-East North-Africa (MENA) region has a high demand of desalinated water and a strongly increasing energy demand which cannot be completely covered using fossil fuels.

In the first six chapters of the thesis, a combined approach of power generation by a solar tower plant and a thermal seawater desalination unit is examined in detail. In order to perform the analysis, the most commercialized and demonstrated technologies are derived from literature and modeled for an integrated simulation. The applied thermal desalination technology bases on a new process using an improved internal heat transfer which has been extensively tested. The obtained data have been used to derive a simulation to integrate the desalination unit as power plant condenser. The results of the energy analysis are presented by different parameter variations of boundary conditions in order to examine the most important design factors. The exergy analysis points out thermodynamic inefficiencies in certain components of the CSP plant, the heat exchangers of the desalination unit and the power plant condenser. The economic analysis focuses on capital and operational expenditures as well as the derivation of optimal cogeneration ratios based on different product prices. All simulations are carried out using real meteorological measurement data by a weather station in El Gouna, Egypt. The obtained meteorological data are compared to literature and satellite data obtained by yearly observations.

In the last chapter, the simulated cogeneration system is then used to build a real demand scenario of El Gouna. The scenario is developed in order to optimize the share of renewable energy supply. This requires the integration of a photovoltaic and a wind power plant to complement the renewable power generation. The analysis shows that the integrated energy supply system covers up to 71 % of the annual energy at around 17 $¢/\mathrm{kWh}$ and up to 31 % of the yearly water demand. In addition, a new process for a short-term storage of surplus power is proposed and analyzed. The surplus power is converted into heat and stored in the thermal storage system of the CSP plant which results in an extended operation time and increased capacity factor.

Zusammenfassung

Die Kraft-Wärme Kopplung eines großen Solarkraftwerks (CSP) mit thermischer Meerwasserentsalzung kann für die gemeinsame Erzeugung von Strom und Wasser für die Versorgung von Regionen mit hoher solarer Direktstrahlung und Meerwasserzugang erhebliche energetische und ökonomische Vorteile bieten. Vor dem Hintergrund einer Wasserknappheit und eines stark steigenden Energiebedarfs in der Middle-East North-Africa (MENA) Region muss Trinkwasser meistens aufwendig entsalzt werden, wobei die nötige Energie in Zukunft kaum noch aus fossilen Quellen gedeckt werden kann.

In der vorliegenden Arbeit wird die gemeinsame Erzeugung von Strom und Wasser mittels eines Solarturmkraftwerks mit thermischen Speicher und einer neuartigen thermischen Meerwasserentsalzung detailliert analysiert. Dazu wurde in einer Literaturrecherche die effizientesten Verfahren ausgewählt und in einer Simulation integriert. Die thermische Meerwasserentsalzung nutzt einen verbesserten Prozess zur Steigerung der internen Wärmeübertragung und wurde als Kondensator des Kraftwerks in die Simulation integriert. Die Modellierung der Entsalzungsanlage wurde basierend auf den Messdaten an einer Demonstrationsanlage erarbeitet. In einer Energie- und Exergieanalyse wurden die wichtigsten Einflussgrößen auf das System mittels Parametervariation untersucht und diskutiert. Die Exergieanalyse verdeutlicht thermodynamische Ineffizienzen, die im Solarfeld, den Wärmetauschern der Meerwasserentsalzung und im Kraftwerkskondensator am größten sind. Die ökonomische Analyse beschreibt die Investitionskosten und leitet daraus ein optimales Kraft-Wärme Kopplungsverhältnis für die Strom- und Wasserproduktion in Abhängigkeit der Strompreise ab. Alle Simulationen basieren auf realen Messdaten einer meteorologischen Station in El Gouna, Ägypten, die mit Literatur- und Satellitendaten verifiziert wurden.

In dem letzten Kapitel wird das modellierte System in ein reales Verbrauchszenario der Stadt El Gouna gesetzt und hinsichtlich der Deckung von Strom- und Wasserbedarf analysiert. Dazu werden zusätzliche Modelle für die Stromerzeugung aus PV und Windkraftanlagen erarbeitet. Das integrierte Energiesystem deckt bis zu 71 % des jährlichen Energiebedarfs für ca. 17 $¢/\mathrm{kWh}$ und bis zu 31 % des Wasserbedarfs . Außerdem wird ein Verfahren vorgeschlagen und analysiert, mit dem Überschussstrom kurzzeitig in dem thermischen Speicher des CSP Kraftwerks gespeichert wird, um die Laufzeit des Kraftwerks zu verlängern.

Chapter 1

Introduction

Today, our society has to face several challenges of the 21st century at different levels. The negative effects of the climate change become more evident and the increasing population in some parts of the world is accompanied by an escalating energy demand. The global energy demand is expected to rise by two-thirds of todays demand to the year 2035 which is described in the World Energy Outlook 2013 by IEA [1, 45]. Up to now, this demand is mainly satisfied by fossil fuels with increasing cost development and unpredictable future. The renewable energy generation can solve at least the dependencies of fossil primary energy carriers. However, it requires high financial and research effort to develop the respective technologies and assess appropriate locations. The main future energy demand will concentrate on the emerging countries which can be expected to increase up to 90% until 2035. In addition to China, India and Asia, the region Middle-East and North-Africa (MENA region) is developing to a large energy consumer itself. Nowadays, the energy demand is satisfied mainly by fossil natural gas reserves but it can be expected to grow to more than the energy demand of the whole OECD countries (see WEO2013 [45]). This will have severe consequences for the price development and the future climate change.

Additionally, the MENA region is also known as one of the most water-scarce regions in the world. In light of the growing population the consequences are the exploitation of groundwater resources which results in deteriorated water quality and poor agricultural productivity [46, 47]. However, there is a strong interdependency between energy generation and water use in the field of energy processing and cooling purpose. Generally, around 70% of the available fresh water is used for agricultural purposes, followed by the industry and municipal use (see UN FAO 2012 and [1, 47]). Figure 1.1 visualizes the physical water scarcity, using renewable water resources per capita and an estimated

demand for the population. Special attention should be given to the MENA region where severe water scarcity is already reality.

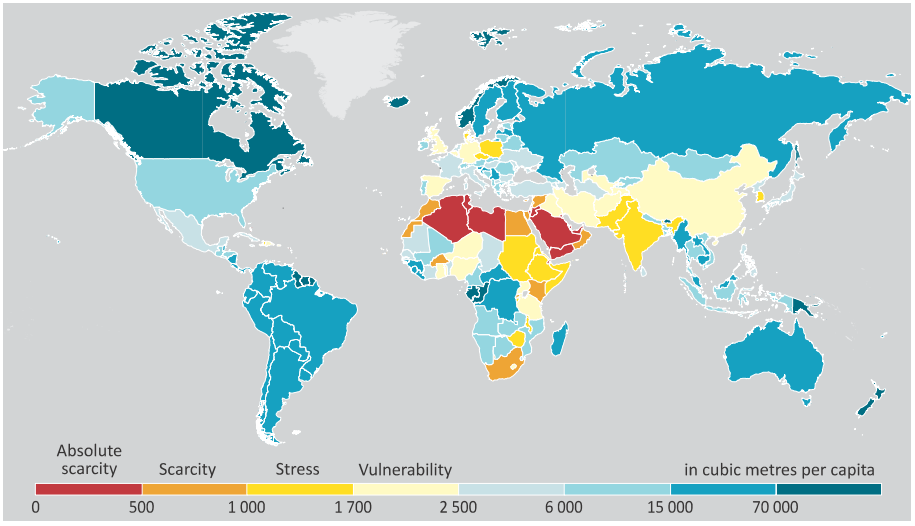

Figure 1.1: *Renewable water resources per capita, data from AQUASTAT and FAO [1]*

It can be stated that the widening gap between water supply and demand can seriously threaten the social and economic development of the MENA region. Besides the application of appropriate technologies for waste water treatment, improved irrigation as well as efficiency gains, the only solution could be the large deployment of seawater desalination plants in coastal areas. The challenges associated with this goal are multi-dimensional:

- *Energy consumption*: Desalination plants consume large amounts of energy, depending on the applied technology and other boundary conditions which is added to the power consumption of air conditioning systems.
- *Seawater access:* Desalination plants need an access to sea water which is opposed by high land costs and environmental impacts in coastal areas. Furthermore, the treatment of waste water (concentrated salt solution, brine) remains an unsolved problem and is mostly discharged with strong influence on maritime life.
- *Financial efforts:* High plant costs, real estate and maintenance create significant costs which result in considerable higher water costs than nowadays.
- *Qualified personnel:* The training and education of appropriate staff to plan, build and maintain desalination plants require strong efforts and investments.

Figure 1.2 illustrates the average irradiation of Africa and the parts of the Middle East region. The MENA region is located in the sun belt of the earth which is highly suitable for solar power plants. Therefore, the highest water-scarcity and the highest solar

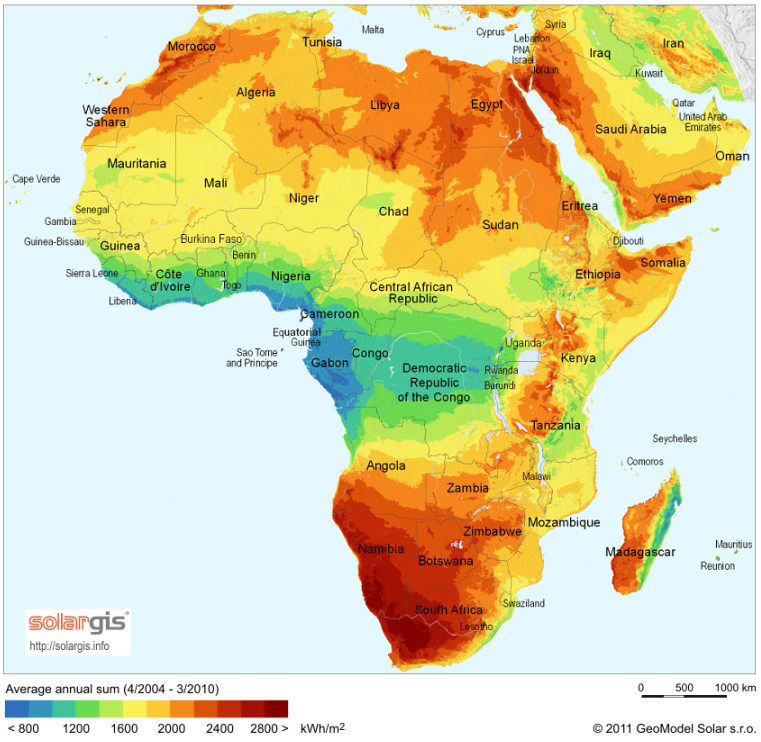

Figure 1.2: *Direct normal irradiation for Africa and Middle East [2]*

radiation are located in the same region. This would impose to research technological solutions for the energy supply gap in combination with the water supply gap. One solution could be the deployment of solar power plants coupled with desalination plants which are located in coastal areas. Within this field, especially low-grade heat driven systems have attracted special attention since they have several advantages compared to other desalination processes. There have been many studies performed proposing cogeneration systems for power generation and seawater desalination powered by renewable energies, such as the AQUA CSP Study of the German Aerospace Center (DLR) [29], the TRANS-CSP study [48] and the MENA Regional Water Outlook of Fichtner [49].

1.1 Motivation and scope

The scope of this thesis is the complete analysis of one possible technological concept to generate power and desalinate water at the same time. For this purpose, a innovative low temperature desalination is assessed and analyzed in detail. It is the logical continuation of an optimized process integration of concentrating solar power (CSP) plants and thermal desalination which has already been described in the AQUA CSP study [29]. In contrast to membrane-based seawater desalination by reverse osmosis plants (RO), those systems use thermal energy instead of electricity required for pumping. Under certain

boundary conditions and proper dimensioning, the combination of CSP and thermal desalination can become financially beneficial for the deployment of CSP plants. Currently, there are also several research and demonstration plants for so called "solar desalination", but those systems do solely focus on desalination systems powered by solar energy. So, solar desalination is not a subject of this thesis.

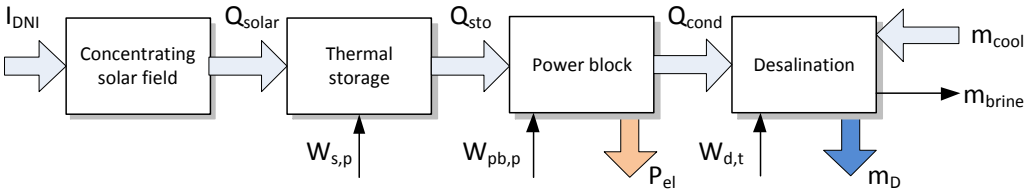

Figure 1.3: *System components and integration*

Figure 1.3 presents the general approach which focuses on an optimized thermal integration of all system components. The direct solar irradiation I_{DNI} is concentrated by a solar field and supplied to the thermal storage system. Using a sufficient dimensioning of the thermal storage, the power block can operate independently from solar irradiation. The complete condensation heat Q_{cond} is the input energy for the thermal desalination unit which requires an efficient conversion of the available waste heat. The process integration is examined by an innovative thermal desalination system (low temperature desalination, LTD) which has been developed by a Swiss company Watersolutions AG [12]. The desalination process has been demonstrated in El Gouna, Egypt, in cogeneration with diesel generators in 2009. The measurement data of the demonstration plant could be analyzed in order to derive a simulation to calculate the correlations between supplied heat and distilled water production under different boundary conditions. The evaluation can only be achieved by respective simulation programs to respect the thermodynamic behavior of the power plant as well as the desalination unit. As there are no present comparable plants operating so far, it does not allow a comparison of the simulated results with real operational data.

1.2 Structure

In order to understand the underlying technology concepts, the theoretical and fundamental mechanisms for the most important plant components are discussed in chapter 2. Here, the focus is on technological solutions and the maturity level with respect to the overall system design. This includes the brief assessment of current CSP and thermal

storage technologies. Furthermore, a strong focus is given to the internal heat transfer in thermal desalination plants to assess and to derive the technological innovation of the LTD process.

Chapter 3 provides the development of a model plant using standard components and describes the simulation approach for the components. The principal calculation methods for the plant components as well as for the cogeneration system are discussed in detail. Especially the simulation development of the thermal desalination unit is carefully described according to the data obtained by the demonstration plant. The implementation is performed using a special kernel scripting module which has been programmed separately. In addition to that, real measured weather data by a meteorological station are converted to enable an implementation in the simulation environment.

The complete energy analysis of the cogeneration system is performed in chapter 4. Special attention is given to the dependencies and limits of combined power and water generation. The variation of several selected boundary parameters analyze the sensitivity to the obtained products. Concerning the CSP plant, the operation in part-load is also assessed. All simulation results base on real measured environmental and irradiation data of an exemplary site in Egypt.

The methodology of the exergy is introduced in chapter 5. The model plant is detailed analyzed by the calculation of exergetic balances for each sub-process and all plant components. Special focus is given to the desalination unit and the respective exergy destruction within this unit. The influence of different solar irradiation levels on the exergy destruction is analyzed.

Chapter 6 provides an overview of the economic performance of the overall cogeneration plant. Special attention is paid to the overall investment costs by the application of methods proposed in other publications. The calculation of capital and operational expenditures allow for the derivation of levelized electricity and water costs. In order to operate the model plant under economical considerations, the analysis of optimal power and water cogeneration ratios provides results for the most important financial boundary conditions.

The integration of the modeled plant into a real power and water demand scenario is examined in a case study in chapter 7. This includes the calculation of the plant performance with real meteorological data as well as power and water demand of the selected site El Gouna in Egypt. The overall goal of a maximized supply with renewable energies is examined in combination with a small PV and wind power plant in combination with the modeled plant. In addition to that, a new methodology is introduced to store

surplus power to extend the operation of the CSP plant and a short financial calculation of the investment costs.

The last chapter 8 summarizes the key findings of this thesis and outlines the future potentials of this technology combination. As there are currently no projects to planning or realize such a plant, the requirement of further research is assessed.

Chapter 2

Technologies

The following chapter provides an overview about the used technologies and their combinations. Each technology is briefly explained and evaluated to meet the overall goal for the system design. Especially state the of art technologies and the level of commercialization is reviewed which is the basis for the selection of the components. A special focus is given to thermal desalination systems and the underlying heat transfer mechanisms in order to introduce a novel thermal desalination technology.

2.1 Concentrating solar power

Solar thermal collectors are widely used to generate heat for domestic and industrial purposes. Normal flat plate collectors are limited in their upper process temperature and heat transfer media to about 150 $^{\circ}\mathrm{C}$, which makes them unsuitable for electricity generation. Collectors which use an optical system to concentrate solar radiation are therefore required. Concentrating collectors can generate higher process temperature up to 800 $^{\circ}\mathrm{C}$ depending on the applied optical technology. In contrast to photovoltaic (PV) modules, concentrating solar power (CSP) plants generate electricity by steam expansion in a turbine [50, 51]. Basically, they are designed similar to fossil fuel power plants with a replaced boiler by a concentrating solar field.

During the 1970s and 1980s, the oil crisis pushed the research and development for CSP plants in the United States. In the time from 1985-1991, nine CSP plants have been build in the deserts of California and Nevada. The installed capacity of those "Solar Electricity Generation Systems" (SEGS) accumulate to 354 $\mathrm{MW_{el}}$ [36]. The build-up of the next CSP plants has been delayed for several years, due to cheap oil prices and high installation costs of such systems. The first European CSP plants have been commissioned and put

into operation in Spain in 2008. Since 2011, several CSP plants have been built with a total installed capacity of around 2.5 $\mathrm{GW_{el}}$ [52]. The Spanish legislation subsidized this type of renewable power generation and the direct solar radiation of about 1800 $\mathrm{kWh/m^2}$ has been enough to run CSP plants economically.

Table 2.1 gives an overview about possible CSP collector technologies [3, 53]. The optical concentration can be achieved using four different mirror constructions which can be divided into two groups: line focusing and point focusing collectors [35]. The line focusing collector tracks the sun along one single axis on a linear receiver. Point focusing collectors need tracking systems using two axes to focus the irradiation on the receiver. The receiver is a fixed device which remains independent of the collector assembly during sun tracking while the mobile receiver is connected to the focusing device with respective joints [3]. An important factor to distinguish between the CSP systems is the geometrical concentration factor C which is defined by the quotient between real receiver area and the collectors aperture area. High concentration factors increase the operation temperature and are summarized in tab. 2.1.

Receiver and focus type	Line focusing	Point focusing
Fixed receiver	Linear Fresnel, LFC $\mathrm{C_{LFC}} = 10 \ldots 160$	Solar Tower, ST $\mathrm{C_{ST}} = 100 \ldots 1000$
Mobile receiver	Parabolic trough, PTC $\mathrm{C_{PTC}} = 10 \ldots 100$	Parabolic Dish $\mathrm{C_{D}} = 1000 \ldots 3000$

Table 2.1: *Four possible CSP collector technologies, modified from [3]*

The parabolic dish collector is usually designed as stand-alone conversion machine with limited options to combine it to a large power plant. Due to the special character of solar parabolic dish systems, they are not applicable to the desired system and thus excluded from this technology review.

2.1.1 Line focusing

In order to concentrate the sunlight to a line, there are two optical solutions possible: the parabolic trough collector (PTC) and the linear fresnel collector (LFC). The majority of the currently build and operated CSP plants use a PTC which can be considered as fully commercialized. Several disadvantages and high construction costs of PTC systems fostered the development of the linear fresnel collector (LFC). Having a lowered optical efficiency by its construction, the LFC compensates that by several advantages.

Parablic trough collector

The PTC collector consists of two parallel mirror rows which are fixed to a metal structure on the ground. Figure 2.1 illustrates a common PTC collector with the pipework for the heat transfer fluids and fig.2.2 shows the schematics of the collector. The mirrors are specially curved in one dimension to focus the solar radiation above the structure to the receiver. The receiver is a special component containing an absorber tube fitted with a selective coating. The receiver is insulated by an evacuated glass tube to minimize the convective heat losses. Due to different heat expansion coefficients of glass and steel, the receiver is interconnected by flexible bellows to compensate the material expansion.

Figure 2.1: *PTC collector, Kuraymat, Egypt*

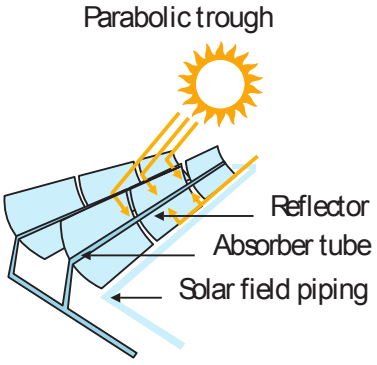

Figure 2.2: *PTC collector schematics, modified from [3]*

The collector tracks the sun according to the orientation over one axis [3, 53]. Due to the construction, the receiver needs to be moved together with the collector, which requires special movable joints [36, 54]. Due to the weight of the support structure, the maximal length of the collector is currently limited to 150 m [4]. Due to the large mirror surfaces, the PTC is also prone to wind loads. If the wind speed exceeds about 15 $\mathrm{m/s}$ the collector needs to be parked in a stowed position. More information about PTC systems can be found in [3, 35, 53–57].

Linear Fresnel collector

To overcome the disadvantages of the PTC collector, the linear fresnel collector (LFC) has been developed. It uses the optical concentration mechanism known as Fresnel lens[1]. The compact construction provides a short focal length with large aperture areas [3, 53]. The main advantages of the LTC are the application of long flat mirror rows and the usage of significantly less construction material [53]. The receiver is designed as fixed device

[1]The lens has been originally invented by the French physicist Augustin-Jean Fresnel as application for lighthouses in 1823

but the compensation of the material heat expansion requires flexible joints. Several realized systems are constructed as solar boilers for direct steam generation.

Figure 2.3: *Novatec LFC collector, Puerto Erado, Spain*

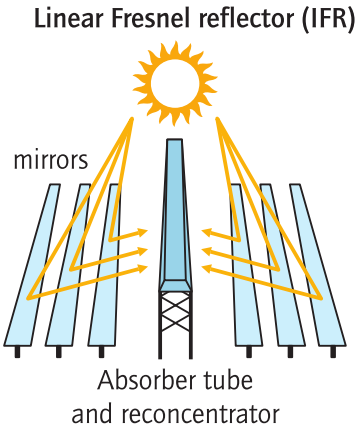

Figure 2.4: *LFC collector schematics, modified from [3]*

Compared to the PTC collector, the construction of the LFC collector is cheaper with slightly decreased thermal power output [3, 53] as a result of a lowered concentration factor C. Figure 2.3 shows one possible design of a Fresnel-collector from NOVATEC Solar in Puerto Erado, Spain. The schematics are visualized in fig. 2.4. Most systems use a secondary reflector located on top of the receiver pipe. This reduces the requirements for precise mirror adjustment and increases the collectors efficiency. Furthermore, the resistance against high wind speeds is increased compared to the PTC. Due to the mirror position close to the ground, the assembly resists wind speeds up to 30 $\mathrm{m/s}$. More information on the LFC can be found in [3, 35, 53, 56, 57].

2.1.2 Point focusing

The construction of point focusing solar collectors allow much higher concentration ratios and thus higher process temperatures. This raises generally the power conversion efficiency of the steam cycle. In addition, the receiver area is drastically decreased which lowers the radiation losses and has a positive influence on the process efficiency [36, 58]. All point focusing collectors have the two-axes sun tracking in common which require more sophisticated technical solutions. Two setups are possible: the solar tower (ST) and parabolic dish systems, the latter mostly combined with stirling engines [59]. The latter is not described any further because it is not relevant for this thesis.

Solar Tower

The solar irradiation is focused using so-called heliostats to the receiver located on the top of a tower (lattice steel or concrete construction possible). Each heliostat is sun-tracked using a two axis tracking system and reflects the solar image to the fixed receiver [60, 61]. All heliostats are operating as a single optical concentration device. The mirrors are composed of single facets which can be flat or slightly curved. Typical reflective areas of heliostats range between 70 - 150 m^2. The heliostats are mostly positioned in a circular array northwards of the solar tower. Depending on the size of the solar field, the distances of the heliostats to the tower can vary between 100 - 1000 m [35]. Large fields are influenced by effects of the atmospheric attenuation which lowers the irradiation reflected to the receiver. The effect increases on heliostats which are positioned in large distance to the receiver. Depending on the designed thermal output of the solar system, it can be necessary to install several thousand heliostats. The high operating temperatures have a positive influence on the overall process efficiency which can reach up to 40%. Figure 2.5 and 2.6 present the Gemasolar tower and the system schematics.

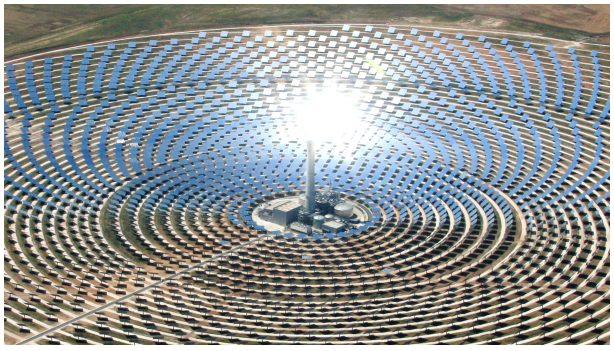

Figure 2.5: *Torresol Energy, Gemasolar tower, Seville, Spain [4]*

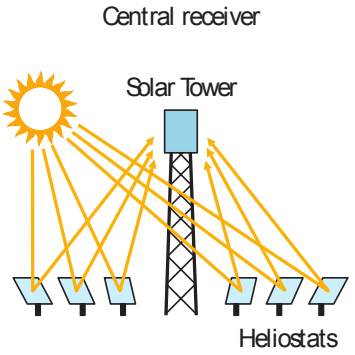

Figure 2.6: *ST collector schematics, modified from [3]*

In addition, the receiver on top of the tower is a key component of the ST system and its design is strongly dependent of the heat transfer fluid applied. The construction is technically challenging in order to withstand the large heat flux densities of 500 - 1000 $\mathrm{kW_{th}/m^2}$ caused by the concentrated irradiation. Currently, there have been demonstrated three possible receiver constructions:

1. *Water/Steam receiver*: demonstrated technology with high reliability, low technical risk, but moderate annual efficiency, superheated steam possible, thermal storage not fully developed, see also [60, 61].

2. *Molten Salt receiver*: suitable for combination with direct thermal storage, temperature limitation to 600 $^{\circ}\mathrm{C}$, process equipment not fully developed at commercial scale, see also [6, 58, 62–65].

3. *Volumetric air receiver:* temperatures above 600 $^{\circ}\mathrm{C}$ possible, no costs for heat transfer fluid, good performance under transient conditions with low thermal losses, suitable for hybrid and combined cycle systems, but low specific heat capacity of the air and complex receiver construction, see also [56].

Compared to normal boiler and steam generators, the higher thermal flux requires more sophisticated designs and materials. Table 2.2 presents the main differences of receiver constructions showing typical values of thermal flux rates and maximum receiver output temperatures.

Receiver construction	Averaged $\mathrm{kW/m^2}$	Peak $\mathrm{kW/m^2}$	Outlet temperature $^{\circ}\mathrm{C}$
Water/Steam	100-300	400-600	490-525
Molten salts (nitrates)	400-500	700-800	540-580
Volumetric air	500-600	800-1000	700-800

Table 2.2: *Receiver thermal flux rates and outlet temperatures, modified from [35]*

Compared to the other collector constructions, the biggest advantage of solar tower systems is the possible combination with a molten salt receiver for direct thermal storage. Molten salt is suitable for the collection, the transport as well as the storage of the thermal energy [58]. Due to the large usable ΔT, the needed storage volume can be decreased which leads to a higher energy density [58]. This type of CSP plant can also operate at night and deliver firm capacity to the grid. In addition, the annual electricity share (capacity factor) is increased depending on the dimensioning of the storage system. Ideally, the power block does not have any load changes because transient conditions are buffered by the storage system and allow for a high efficiency in power generation. As the advantages of the solar tower compared to line focusing systems are evident, the technology is selected as model plant for the integration of the desalination unit. The exact configuration and the design capacity is discussed in section 3.3.

2.1.3 Heat transfer media

The heat transfer media are of special importance for CSP plants. Due to the large solar field arrays with kilometers of pipework, the application of heat transfer fluids (HTF)

is technically useful. These fluids collect the solar thermal energy and are also used for thermal storage or steam generation, depending on the systems configuration. It is favorable for the process that the HTF have a high specific heat capacity. Generally, the following heat transfer fluids have been applied :

1. *Synthetic thermal oil*: applied in most commercial plants, but limited maximum temperature and expensive, decomposition at high temperatures possible, environmentally hazardous and flammable, see also [4, 35, 36, 54].

2. *Molten salt*: very suitable for thermal energy storage at high temperature levels, but due to high solidification temperature problematic to handle in large solar fields arrays during night time, see also [38, 63–65].

3. *Water and steam:* direct steam generation (DSG) has many advantages compared to synthetic oils, but requires a more sophisticated solar field layout, thermal storage is technologically complicated and still in a research and development stage, see also [60, 66].

4. *Air*: only applicable with point focusing systems with high process temperatures (volumetric air receiver), cogeneration with combined-cycle power plants possible, pressurized volumetric air receiver in research stage, no thermal storage possible until now, see also [56].

Until now, synthetic thermal oil is used in most commercial plants and is known as "Therminol VP-1". The advantage of this fluid is that the solidification temperature lays around 12 $^{\circ}\mathrm{C}$, which simplifies the handling of the solar field during the night. However, one drawback is the limitation of the operation temperature to 400 $^{\circ}\mathrm{C}$. Exceeding this temperature causes cracking reactions and the formation of hydrogen destroying the vacuum for thermal insulation in the receiver tubes.

Heat transfer fluid	$C_{12}H_{10}$ %	$C_{12}H_{10}O$ %	$Ca(NO_3)_2$ %	$NaNO_2$ %	KNO_3 %	$NaNO_3$ %
Therminol VP-1	73.5	26.5	-	-	-	-
Solar Salt	-	-	-	-	40	60
Hitech	-	-	-	40	53	7
Hitech XL	-	-	48	-	45	7

Table 2.3: *Composition of common heat transfer fluids [36–38]*

Table 2.3 summarizes the chemical composition of some heat transfer fluids. For thermal storage purposes, so called "solar salt" is being used which is composed of a mixture of 40% potassium nitrate and 60% sodium nitrate salt [37, 38].

Heat transfer fluid	T_{melt} °C	T_{max} °C	ΔT °C	$c_p, 300°C$ kJ/kgK	$\rho, 300°C$ kg/m^3	Costs US \$/kg
Therminol VP-1	12	400	388	2.319	815	2.20
Solar Salt	238	600	380	1.495	1899	0.49
Hitech	142	535	393	1.560	1640	0.93
Hitech XL	120	500	380	1.447	1992	1.19

Table 2.4: *Thermodynamic properties of different heat transfer fluids [37, 38]*

Table 2.4 gives some important thermodynamic properties and specific costs. It can be stated that the temperature range ΔT is more or less constant, so that raising the solidification temperature T_{melt} will also lower the maximal process temperature T_{max}. The specific heat capacity is denoted with c_p and the density with ρ at 300 °, respectively. In terms of costs, all salts are significantly cheaper compared to thermal oil.

2.2 Thermal Energy Storage

In contrast to other renewable energy technologies as PV and Wind power plants, concentrating solar power has the great advantage of the simple process integration of thermal energy storage systems (TES) and conventional fuels (hybridization) [28, 29]. The thermal energy storage decouples the power generation from the natural resources. The integration of storage systems also has economic advantages: the raised annual share of electricity generation lowers the levelized cost of electricity (LCOE) of around 10-20% [4, 5, 63, 67, 68]. More details are discussed in chapter 6.

The comparison of different energy storage systems is visualized in fig. 2.7 while the rated power does not distinguish between electrical and thermal energy. This allows the comparison of several electrical, chemical and mechanical systems by rated power output and discharge time, respectively. The thermal energy storage has been added manually [4]. Thermal energy storage using molten salt has numerous advantages compared to other energy storage solutions like mechanical and chemical systems [69], which are mainly lowered capital costs and high operating efficiencies. Furthermore, from fig. 2.7 and tab. 2.5 it can be concluded that those systems fit to the typical plant size of CSP plants allowing hours of additional operation.

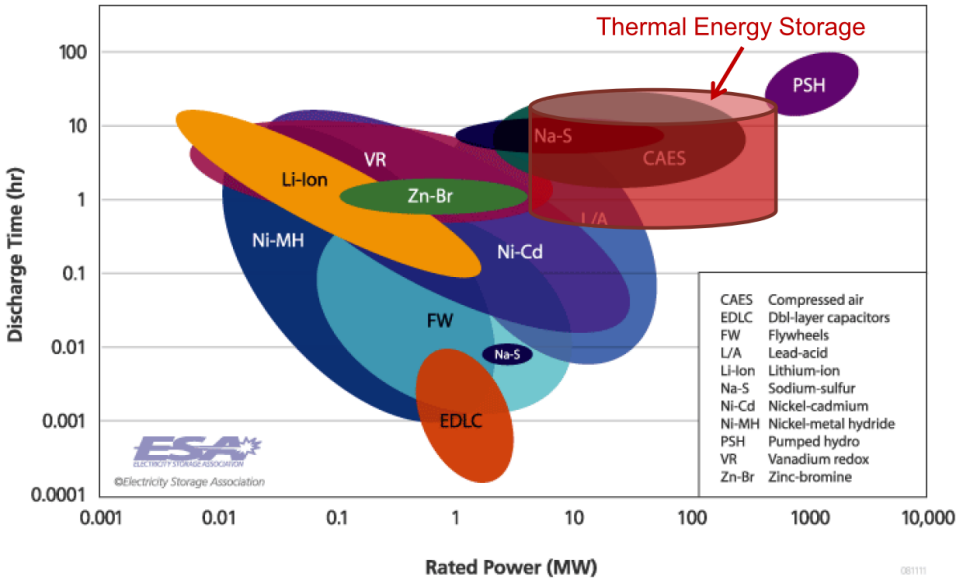

Figure 2.7: *Thermal energy storage in comparison to electrical and mechanical, status 2008, modified from [4, 5]*

Storage technology	Typical capacity $\mathrm{MWh_{th,\ el}}$	Efficiency %	Duration h	Capital costs US \$/$\mathrm{kWh_{el}}$	Lifetime a
Thermal energy storage	500-1000	98	24	72-210	30
NaS Flow battery	5-15	75	24	750-1500	15
Compressed air	600-1000	50	48	90-200	30
Hydro power	1000-10,000	75	48	75-150	30

Table 2.5: *Typical parameters of thermal, electrical and mechanical storage systems, modified from [4, 5]*

Table 2.5 compares the systems in terms of efficiency, capacity and capital cost. It can be stated that combining thermal energy storage with solar tower plants has the most cost advantages. By dimensioning a CSP plant with sufficient storage system, start up and shut down cycles can be also decreased. It results in efficiency gains of the power plant avoiding part-load during transient conditions [36, 38]. CSP systems using direct steam generation (DSG) need different storage solutions like sensible heat storage systems fabricated of concrete and examined in [70]. They are still subject to research and not yet commercially available.

The current state-of-the-art and commercially proven technology are the molten salt storage systems, which store sensible heat on a daytime basis [5, 38]. Several CSP plants are equipped with such storage systems, dimensioned for about 6-15 hours of full-load

operation. The storage media for sensible heat storage have certain requirements, which can be summarized as follows [68, 69]:

- *Physical*: large gravimetric storage capacity (high specific heat capacity, high latent heat of phase change or heat of reaction), large volumetric storage capacity (high density and gravimetric values), high heat transfer rate (high thermal conductivity), low volume change with temperature and mechanical stability.

- *Chemical*: long term chemical cycle stability, no toxicity nor fire hazard, compatibility with construction materials.

- *Economical*: operational experience, high availability and low costs.

In practice only a limited number of materials are considered for commercial application due to the specific requirements above associated to the individual storage mechanisms [69]. Depending on the collector type and the process design, different types of thermal storage systems can be distinguished. Using molten salt as a storage medium, the technical realization can be distinguished by direct or indirect storage systems, which are discussed as follows.

2.2.1 Indirect thermal storage

Indirect storage are mostly applied together with line focusing collectors such as PTC and LFC systems. Molten salt is a challenge as a heat transfer fluid for line focusing collectors which is mainly due to the high solidification temperature at around 240 $^{\circ}\mathrm{C}$ [37, 38]. Otherwise, during night the kilometers of pipework through the solar field need to be auxiliary heated to maintain the salt in the liquid phase. Indirect thermal storage systems have a different heat transfer fluid in the solar field (see chapter 2.1.3) compared to the storage media [38]. Figure 2.8 illustrates the process configuration.

In this case, heat transfer fluids like synthetic oils (e.g. Therminol VP-1) are mostly applied in the pipework of large solar field arrays but the process design is more sophisticated. The heat that has to be stored in the molten salt tanks needs to pass through an additional heat exchanger, which causes higher investment costs. Loading is realized during day time by pumping the molten salt from the cold to the hot tank.

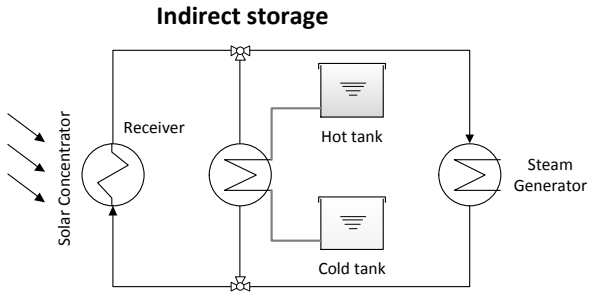

Figure 2.8: *Indirect thermal storage*

2.2.2 Direct thermal storage

Direct thermal storage systems are characterized by using the same type of heat transfer fluid in the solar receiver and the storage. Due to the use of only one heat transfer fluid, direct thermal energy storage has significant cost advantages compared to indirect storage systems. It can be applied in combination with point focusing systems like the solar tower, where the pipe network is much shorter compared to line focusing systems. Figure 2.9 visualizes this configuration.

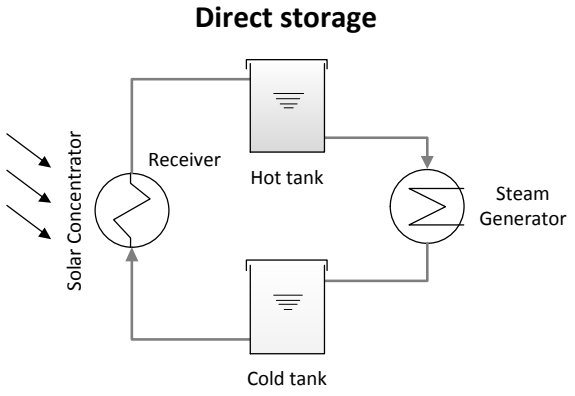

Figure 2.9: *Direct thermal storage*

The technology has been realized at the plants PS-2 and GEMA Solar, Spain [58, 65]. The loading occurs during daytime operation while charging the hot tank to the designed temperature level. Unloading occurs during night time by pumping the molten salt through the steam generator to the cold tank.

Process integration

The possible working temperatures are limited by the thermodynamic properties of molten salt. The solidification (freezing) can be seen as crucial and requires the maintenance of sufficiently high temperatures. It is realized by special auxiliary heating overnight to avoid freezing below temperatures of 250 °C. The freezing point differs depending on the special blends (see also tab. 2.3 and 2.4), but is given with 220 °C in literature [65]. Figure 2.10 illustrates a two tank molten salt storage system with pumps, heat exchangers and process equipment.

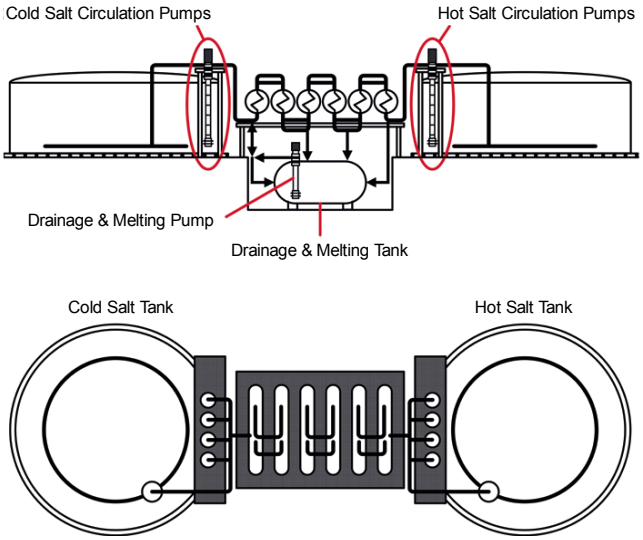

Figure 2.10: *Process design of a two tank molten salt storage system [6]*

Current research focuses on the examination of special low-melting salt mixtures and the influencing parameters [38, 62, 65], but those new mixtures have not been applied in a commercial scale yet. The maximum temperatures for stable conditions are given with 565 °C [38], which are mainly influenced by the mass loss with gas evolution due to three mechanisms: nitrite formation and oxygen release, alkali metal oxides formation and vaporization of the nitrate salts. Furthermore, the thermal decomposition of solar salt depends mostly on the respective heating rate and on the partial oxygen pressure [38]. More information can be also found in [62, 65].

2.3 Power block

The power block of concentrating solar power plants usually work like conventional fossil fuel power plants with e.g. coal, lignite and nuclear boilers. The energy conversion from thermal to electrical power takes place here. Due to the integration of a thermal

storage system, the power block has less requirements in terms of starts per day, ramp rates, regulating ranges and overall flexibility [26]. The integration of thermal storage consequently reduces part-load conditions and improves the overall plant performance which as also economic advantages. Using an additional reheat turbine increases the thermal efficiency and also wet steam erosion in the low-pressure sections of the turbine [7].

The steam generation is realized by using the molten salt from the hot tank of the thermal storage system. Due to the temperature limitations below 600 $^{\circ}\mathrm{C}$ the steam condition stays sub-critical. The steam generation is usually implemented in the process by three process steps: preheating, evaporation and super-heating. The preheating and evaporation require the majority of the heat supplied. The technical design of the steam generator working with molten salt has some special constraints. Most important is the proper dimensioning of the evaporator because the steam generator have to be able to work with the high pressures and temperatures. The material has to withstand severe thermal stress during load changes and heat transfer instabilities [64].

The steam turbine is used to expand the generated steam and to generate electric power. High temperatures and pressure of the steam are favorable for a high thermodynamic efficiency and increased power output. Generally, steam turbines in concentrating solar power applications need to be designed differently from fossil fueled power plants. The reasons are mainly due to the complex cycle conditions, frequent load changes and variable steam conditions. In order to keep the investment costs as low as possible, industrial standard steam turbines from Siemens are mostly adapted for existing CSP projects [7]. When there is no thermal storage integrated, the daily start-up and shut down cycles cause a lot of material stress and the turbine needs to be designed accordingly.

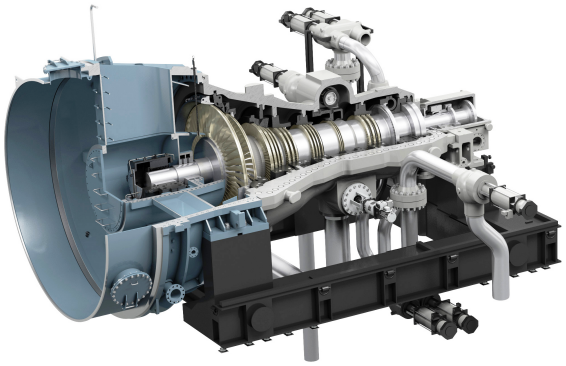

Figure 2.11: *Siemens steam turbine SST-600 [7]*

Figure 2.11 shows a standard industrial reheat steam turbine from SIEMENS [7] which could be applied in the model plant. The power output can be designed up to 100 $\mathrm{MW_{el}}$ according to the system requirements. The selected turbine is specially adapted for solar tower applications and prepared for reheat design. The intake pressures can reach up to 140 bar and the temperatures up to 540 $^{\circ}\mathrm{C}$ [7]. In order to meet the plant requirements the building block design is flexible enough to allow an uncomplicated integration in the process. The integration of a thermal desalination unit requires variable thermal condenser loads. Up to now, the operation in cogeneration with variable condensing pressures is no standard application in CSP plants. Special requirements need to be considered during the design phase and require close consultation with the manufacturer. More information are available in [7, 64, 65].

2.4 Thermal desalination

The desalination of seawater can be done by numerous processes with specific boundary conditions and energy requirements. The effectivity of desalination highly depends on the physical separation process and the water salinity. All processes have one requirement in common: water and salt do not split spontaneously, it requires quite large amounts of energy to supply the separation process. However, all desalination systems can be classified according to the following criteria [71]:

1. *Separation process:* The separation of salt and water can be achieved using membranes (diffusion) or evaporation (distillation), typical examples are membrane processes like reverse osmosis (RO) or electro dialysis (ED), for thermal processes multi-stage flush (MSF) and multi-effect distillation (MED), cross over technologies like membrane distillation (MD) use both mechanisms.

2. *Extraction method:* water or salt extraction, where as water extraction can be done with a phase change (evaporation) or without a phase change (membrane), salt extraction through electrical processes like electro dialysis (ED) and ionic exchange.

3. *Energy requirements:* electrical, thermal or mechanical energy, RO requires mainly mechanical energy for pumping provided by motors, thermal distillation process need thermal energy for the evaporation and auxiliary electricity for pumping.

During the last decades, the global market of desalination systems has roughly split up in two equal portions on thermal processes (MSF, MED) and membrane processes like reverse osmosis (RO) [71, 72]. This thesis focuses entirely on thermal desalination systems

which are based all on the principle of distillation, thus evaporation and condensation. For the combined generation of power and water, the assumption is made that the heat integration of thermal desalination systems could be more efficient compared to generate electricity and desalinate water using RO (see also [73]). More information about thermal desalination processes can be found in [10, 11, 72].

Nevertheless, in thermal desalination markets, the multi-stage flush (MSF) processes are still predominant while multi-effect distillation (MED) have a minor market share. MED plants turn out to have a higher thermal efficiency and lowered investment costs. Compared to MSF, the MED process consumes about 20% less of the pumping power and needs about 50% less heat transfer area [74]. The increased efficiency results in decreased number of stages. Another newly demonstrated system called low-temperature distillation (LTD) promises to further lower energy and electricity consumption [12, 15, 75], which are examined in detail in the following sections.

The salinity of seawater is measured in the amounts of dissolved solids, which has a significant influence on the thermodynamical properties like freezing and evaporation temperature. Furthermore, the salinity affects the density of seawater. The changed fluid properties need to be respected for the design of seawater desalination plants. Generally, the salinity of seawater can be roughly expressed by the mass of dissolved matter per kg seawater or in parts per million ppm [39]. It can also be measured more simple by electrolytic conductivity in $\mu\mathrm{S/m}$. Both methods are directly linked to the amount of total dissolved solids (TDS), which is a common simplification to measure the salinity of seawater. The normal salinity of seawater ranges about 35 $\mathrm{g/kg\ TDS}$ and depends on the balance between evaporation and precipitation as well as mixing between surface and deeper water [39]. The major ions in the seawater are given in tab. 2.6.

Name	Symbol	% of TDS
Chloride	$\mathrm{Cl^-}$	55.29
Sodium	$\mathrm{Na^+}$	30.74
Magnesium	$\mathrm{Mg^{2+}}$	3.69
Sulphate	$\mathrm{SO_4^{2-}}$	7.75
Calcium	$\mathrm{Ca^{2+}}$	1.18
Potassium	$\mathrm{K^+}$	1.14

Table 2.6: *Typical chemical composition of seawater, 35 $g/kg\ TDS$, [39]*

2.4.1 Principal mechanism

The thermal separation of water and salt is basically achieved by the phase change from liquid to vapor. Due to the different boiling temperatures of water and salt, the evolving seawater steam can be assumed free from dissolved and suspended solids. Naturally, the remaining seawater increases its salt concentration and is discharged as "brine". The brine constitutes an environmental hazard in all desalination plants which is not fully solved until now. New developments aim for a complete separation of water and solids and are summarized as "zero-liquid-discharge" (ZLD), but the technical realization can be considered as challenging.

Principally, the evaporation can be realized by heat addition (MED, mostly steam) or by flashing (MSF, initiated by lowered pressure) [9, 11, 71, 72]. After the steam generation, the heat removal initiates the condensation. This requires intensive cooling to gain the distilled water.

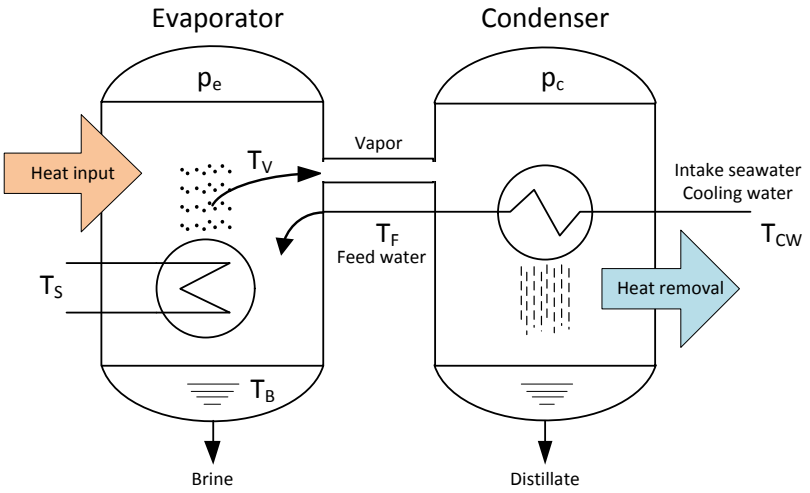

Figure 2.12: *Single effect evaporation and condensing, modified from [8]*

Figure 2.12 illustrates the single effect evaporation in general. The main components are the reactor vessels for evaporation and condensation with the pressures p_e and p_c as well as the respective heat exchangers. The reactors are interconnected by a vapor channel passing through the generated vapor at the temperature T_V. Typically, there is a demister installed to prevent brine droplets entering the condenser. The condenser operates in counter-current mode and transfers the latent heat of the condensed vapor to the incoming seawater with the temperature T_{CW}. The incoming seawater also acts as preheating for the feed water and has a positive influence on the efficiency. The main

media flows and its temperatures are the feed of seawater, the heating steam T_S, as well as brine T_B and distillate streams.

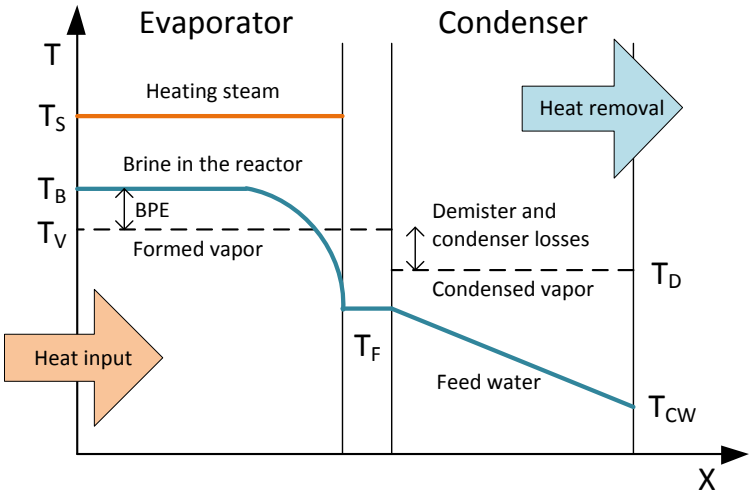

Figure 2.13: *Single effect temperature profiles, modified from [8–10]*

Figure 2.13 shows the basic temperature levels qualitatively for evaporator and condenser with its pressures p_e and p_c, respectively. The heat source is supplied by a heat exchanger to the seawater in the reactor and is denoted with the temperature T_S. The incoming feed saltwater acts as cooling water for the condenser with the temperature T_{CW}. The cooling water is heated up while absorbing the heat of the steam condensation and increases its temperature to T_F. The saltwater starts boiling at the temperature T_B by heat addition with the temperature T_S.

Inside the evaporator, the evolving vapor has the temperature T_V which is lower than the temperature T_B of the remaining saltwater. The temperature difference is called "boiling point elevation" (BPE) which is a function of the respective salt concentration (the effects are analyzed in section 4.4.4 and 5.6.4). The temperature of the condensed vapor or the distillate T_D is also decreased by losses in the demister and the vapor channel, but does not necessarily influence the process itself.

2.4.2 Process integration

Lowering the pressure p_e in the evaporator decreases the necessary temperature level of the process without affecting the required energy for the phase change. This enables the

reduction of the top brine temperatures (TBT) to values below 100 °C which is favorably for the process design to increase the heat efficiency. Furthermore, the performance of one single stage or effect is limited by the evaporation enthalpy of water[2]. Therefore, large scale thermal desalination plants use up to 20 stages in a series using a heat recovery between the stages. The utilization of the latent heat subsequently over more stages increases the efficiency and lowers the specific thermal energy consumption per distillate.

Multi-effect distillation

The multi-effect distillation (MED) is one possible option to integrate the single effect evaporation in a larger plant array to increase its capacity and efficiency. In addition to desalination, this principle has been first used for food and petrochemical industries. Due to the low thermal efficiency of multi-stage flush systems, the MSF is not further described here. More information to MSF plants can be found in [8–11, 76–80].

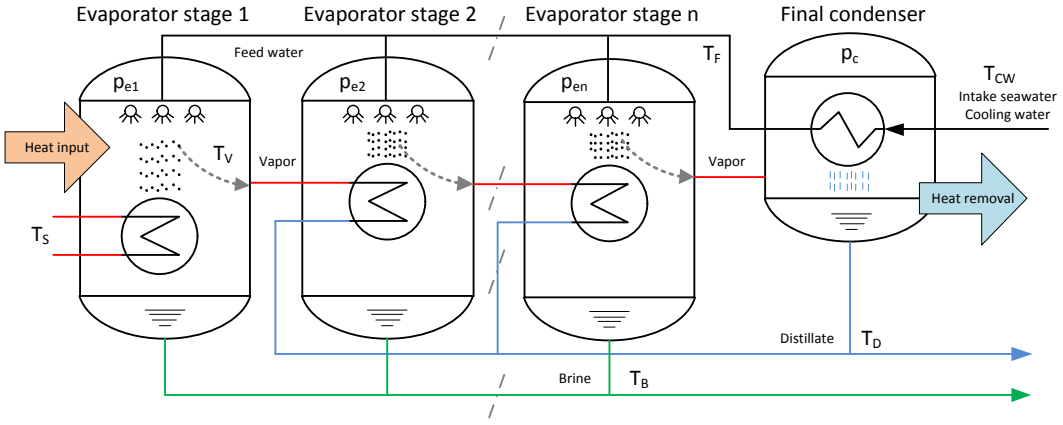

Figure 2.14: *Multi-effect desalination, simplified process, modified from [8, 11]*

Figure 2.14 shows one possible configuration of the multi-effect distillation for n stages (or effects) while pumps and valves are not visualized. More configurations have been realized concerning the feed water flow (forward- or backward feed) and preheating design. In order to increase the overall temperature and pressure spread for higher distillate production, combinations with thermal or mechanical vapor compression (TVC, MVC) are common. More details of these systems can be found in literature [8,11,76,81].

Furthermore, fig. 2.14 also shows that the heating steam is supplied only to the first stage. All subsequent stages are heated by the vapor formed in the previous stage. In

[2] 2426 $\mathrm{kJ/kg}$ at ambient pressure [41]

each stage, the steam from the previous stage is condensed while the brine evaporates at lowered pressures.

In order to run this process efficiently, the heat exchange between the vapor and the feed water has a special importance for the overall performance. The available area for the heat transfer determines the efficiency of the complete plant. If this connection is obstructed by the respective process conditions, the water production is significantly affected. For example, the part-load behavior with changed process conditions can initiate such problems. Part-load operation can be seen critically with respect to the intended integration as power plant condenser. In addition to that, it can be expected that with increasing operation time the effects of scaling and fouling also influence the water production negatively.

Low-temperature desalination

The low-temperature desalination (LTD) process proposed and demonstrated by Watersolutions AG [12, 15, 75, 82, 83], Switzerland, tries to overcome the previously mentioned challenges by using an innovative process design. The most prominent difference can be seen in the drastically improved heat transfer by droplet condensation inside the reactors which has been extensively researched [82, 84–86]. Furthermore, the relocation of the heat supply to a standardized plate heat exchanger outside of the reactors simplifies the process design significantly and reduces the sizes of the pressure vessels. This design also has cost advantages.

The LTD is similar to conventional systems like MSF regarding the process flow, but it uses the temperature and pressure dynamics of a MED. The process has first been build up and tested in El Gouna, Egypt, in a combined heat and power configuration with diesel generators in 2009. The innovation can be seen in the application of a special spray system to generate millions of droplets by special perforated metal sheets to act as heat exchanger. The spray system increases the surface of the water inside the respective reactor which causes an efficient and drastically improved specific heat transfer by dropwise condensation (see also tab. 2.7) [12, 15, 75, 83]. In addition to that, all scaling and fouling problems cannot arise during operation.

The basic system layout for one exemplary stage is visualized in figure 2.15 though pumps and valves are not visualized. Several stages in series allow more heat recovery and therefore increase the water production. Each stage consists of two connected reactors with an evaporation (1) and condensation (2) side. They are connected by a demister or droplet separator (3) to avoid the transportation of saline aerosols into the distillate. The

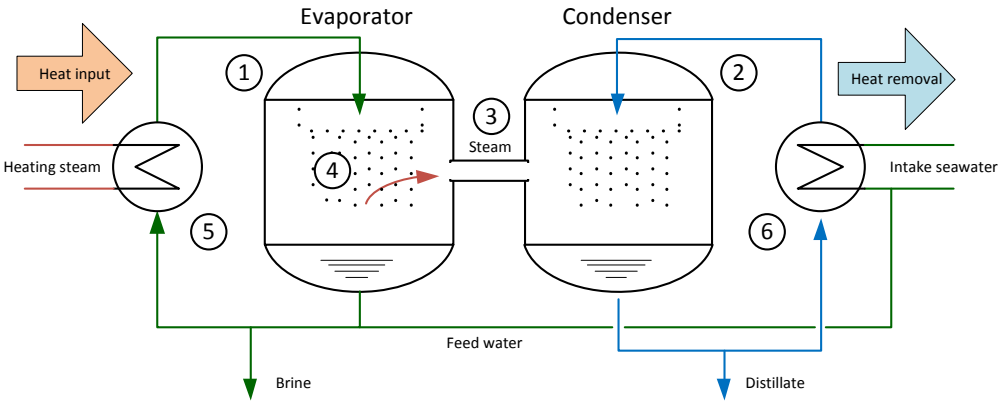

Figure 2.15: *Process scheme of the LTD system [12]*

system can contain several reactor vessels (evaporation and condensation for each stage) which are fed by two large mass flows on each side of the system. Both major mass flows (circulation) can be understood as transportation and heat exchange media through the respective standard plate heat exchanger (5, seawater and 6, distillate). Furthermore, the large mass flows ensure the operation of the spraying system (4) inside the reactors generating steam or condensing distillate. The design of the perforated metal sheets has been specially developed for the reactors taking several years with the goal to optimize the droplet formation and the steam condensation behavior [82, 84–87].

The low-temperature desalination has significant advantages for the operation in cogeneration. In order to understand those, it requires some deeper investigation of the heat exchange designs and mechanisms involved in this process.

2.4.3 Heat exchanger design

Tube-bundle heat exchanger

In MED and MSF desalination units, the heat transfer from condensing vapor to evaporating brine is usually realized through tube-bundle heat-exchangers. They can be arranged vertically or horizontally [88]. The horizontal tube evaporator is commonly used for desalination plants like MED or MSF [8–11].

Figure 2.16 illustrates the design and flow direction of tube-bundle heat exchanger construction. The steam is condensed inside of the heat exchanger tubes while the intake feed water is distributed by spraying nozzles over the tubes, which fall down by gravity.

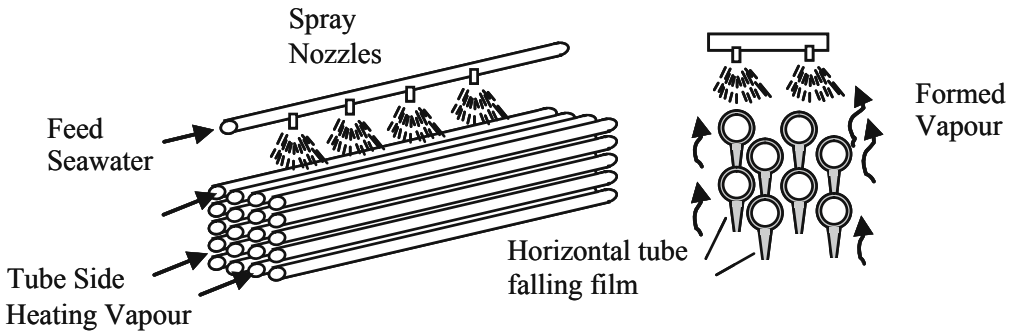

Figure 2.16: *Principle of a horizontal tube evaporator [8]*

Corresponding to El-Dessouky [8], the horizontal falling film evaporator is the most distributed process in thermal desalination units. The following influence factors are most crucial for the heat exchange:

- Danger of scale formation, bio-fouling, material depositions, and mechanical tube damage (see also section 2.5.1).
- Influence of non-condensable gases like CO_2, N_2 and O_2 hindering the heat exchange (see also section 2.5.1).
- Sufficient tube wetting and water distribution to avoid dry patches, which foster scale formation and material depositions.
- Material requirements to allow for a sufficient heat transfer and prevent corrosion.

It turns out that the efficiency of thermal desalination systems solely depends on the heat transfer mechanism, because the production of distillate is directly proportional to the heat supplied to the evaporation/condensation processes. The critical part here is the condensation process which mostly occurs on a cooled surface inside the horizontal tube bundle heat exchanger. This allows a direct contact with the vapor. The local temperature needs to be less than the local saturation temperature of the vapor, so the single molecules get into contact with the tube surface and condense to liquid (see also [13, 14]).

Figure 2.17 exemplary visualizes the flow regime inside a heat exchanger tube. It can be concluded, that the flow regime is drastically changing during the condensation process from an annular to a stratified pattern. Naturally, this substantially influences the heat transfer coefficients and the two-phase pressure gradient [14]. The condensate acts as insulation and inhibits the heat transportation by increasing the transmission resistance of

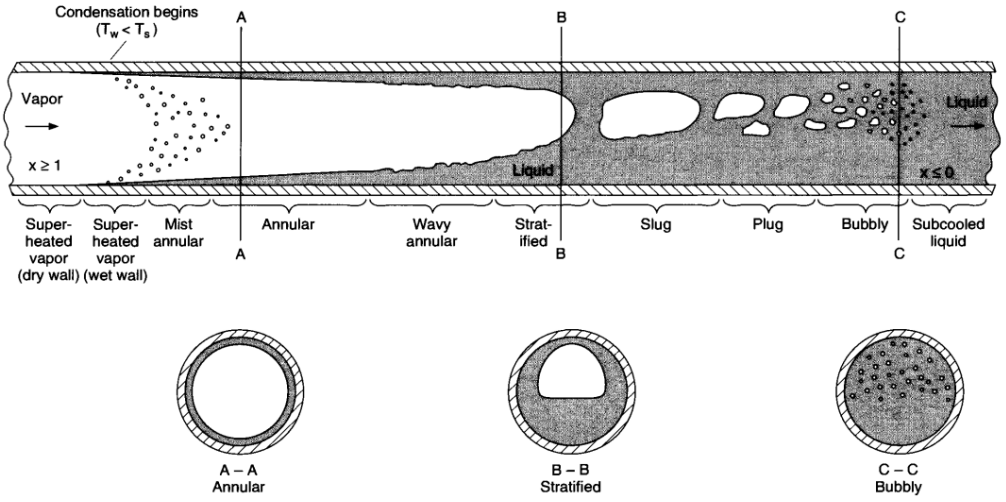

Figure 2.17: *Flow regime during condensation inside one horizontal tube [13, 14]*

the heat exchanger. As the density ρ of water and steam differs by factor 1000, the flow velocity v is also influenced by the condensation process. During part-load conditions, a completely different flow regime can be expected which leads to a considerably negative influence on the whole condensation process.

Droplet condensation

Referring to section 2.4.2 and the introduced LTD system, one option to overcome the limitations and operational challenges from tube-bundle heat exchangers could be the condensation on single droplets. The condensation on droplets can achieve a significantly higher heat transfer coefficient compared to tube-bundle heat exchangers [42]. The reason is a substantially increased specific heat exchange surface which is free from heat transfer resistances through tube walls and additional process related resistances (such as water films, non-condensable gases and scaling). The active heat exchange surface is proportionally increased with the reduction of the droplet size [42, 43].

Figure 2.18 shows the the formed droplets within the condensing reactor of the LTD. It can be seen that the droplet size is smaller than 1 mm. The efficiency of the internal heat transfer is optimized by increasing the heat exchange area to the droplet surface. In consequence of that, all transmission resistances are minimized. The danger of scaling and corrosion is not present. Furthermore, the experiments on the demonstration plant have shown an excellent part-load behavior proportional to the heat supplied [15]. The ability of part-load operation qualifies this system for the integration as power plant condenser.

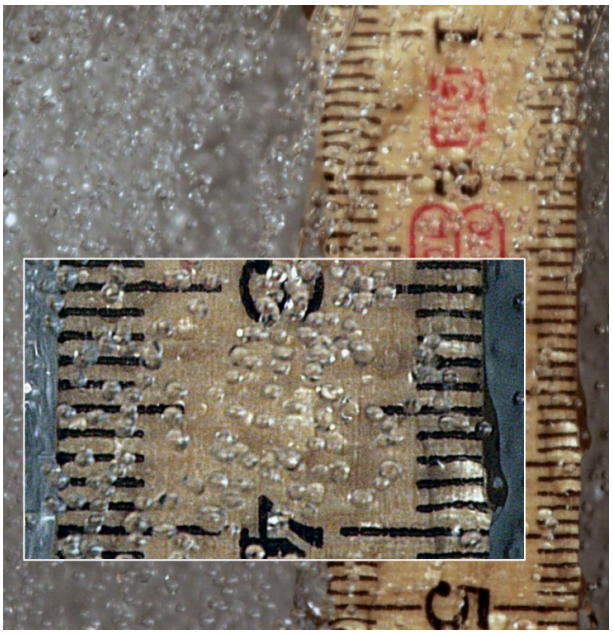

Figure 2.18: *Size of water droplets in the condensing reactor [12, 15]*

The spraying system is operated by relatively large mass flows for seawater and distillate (see also fig. 2.15) to generate the heat exchange surfaces. The operation requires electrical power to pump depending on the available temperature difference in the heat exchangers. Experiments performed on the demonstration plant have shown that a minimum heat gradient between evaporator and condenser could be approximated to 0.5 K for one single stage [15, 83].

2.5 Heat transfer mechanisms

Due to the importance of the heat transfer for the overall system and thermal desalination systems in specific, some general correlations are given in the following section. The description is briefly summarized from [13]. The heat transfer describes the process of the transportation of heat energy from a defined system with respective boundaries. The flow direction always follows from the hot to the cold system, while the transported energy changes the condition of the thermodynamic state. The heat transportation is influenced by three basic mechanisms, which are mostly all involved:

- *Conduction:* heat transport through direct contact of solids without exchange of material,
- *Convection:* heat transport through contact of streaming fluids,

- *Radiation:* heat transport through exchange of electromagnetic radiation at surfaces with different temperatures.

The mechanisms for heat exchange strongly depends on the properties of the involved media and materials. While radiation is important for the solar field, the convection and conduction are important for the power block and the thermal desalination. According to the first law of thermodynamics, the heat energy flow $\dot{Q}$ of a system can be described with two temperatures T_1 and T_2, the heat transfer coefficient k and the heat exchange area A:

$$\dot{Q} = k \cdot A \cdot \Delta T_m \tag{2.1}$$

The mean temperature difference ΔT_m is defined between the temperatures T_1 and T_2 as follows:

$$\Delta T_m = \frac{T_2 - T_1}{\ln(\frac{T_2}{T_1})} \tag{2.2}$$

One important factor is the heat transfer coefficient k in equation 2.1 which is subject in the following sections. The heat transfer coefficient in $\mathrm{W/m^2K}$ is influenced by all three heat transfer mechanisms. They include fluid properties like specific heat transfer coefficient α, dynamic viscosity η, flow velocity v, as well as geometrical and material conditions. Therefore, the operating conditions have a strong influence on the heat transfer coefficient k and can hinder the heat exchange in the desalination systems. The thermal conductivity of the heat exchanger wall itself is described with thermal conduction λ and the material thickness d.

In order to understand the convective heat transfer, the thermal boundary layer δ_T has a special importance and strongly depends on the fluid regime and its properties. This is visualized in fig. 2.19 for the heat exchange through a solid wall for two temperatures T_1 and T_2:

The flow boundary layer δ mainly depends on the flow velocity which is expressed through the Reynolds number Re (dimensionless). This ratio depends on fluid properties like the density ρ, the flow velocity v, the dynamic viscosity η and on the diameter of the tube. In terms of the kinematic viscosity ν, it can be also expressed as η/ρ. So it is defined as:

$$Re := \frac{\rho \cdot v \cdot d}{\eta} = \frac{v \cdot d}{\nu} \tag{2.3}$$

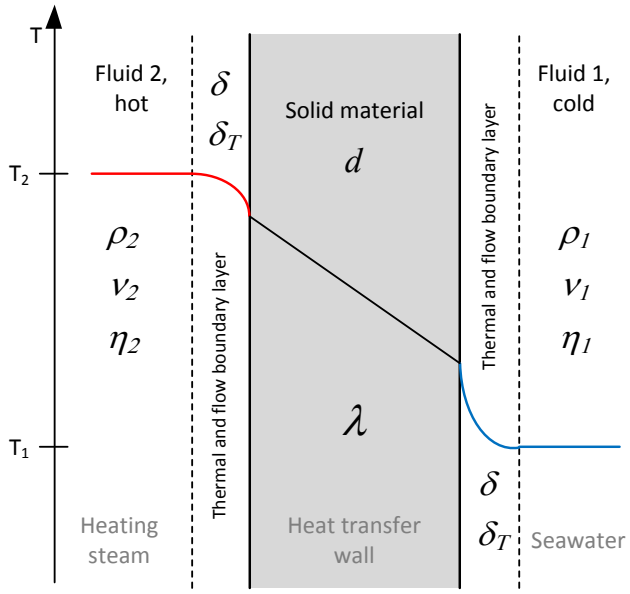

Figure 2.19: *Heat exchange of two fluids with a heat exchanger wall*

The Re number gives information about the flow condition which can be described as laminar and turbulent. When reaching the critical value Re_{crit}, the laminar flow changes to turbulent ($Re > Re_{crit}$). For a gaseous fluid in a tube with given inner diameter d and average flow velocity v_m, the literature describes $Re_{crit} = 2300$. The transition occurs gradually above this value, so there is no sudden change in the flow regime.

Within the thermal boundary layer δ_T shown in fig. 2.19, the convective heat transfer is predominant, compared to the other mechanisms. Even without any flow velocity v, some turbulences in the fluid are likely to form driven by the temperature difference between T_1 and T_2. The thermal and flow boundary layer can differ. The ratio between both boundary layers can be expressed using the Prandtl number Pr. It defines the ratio between the kinematic viscosity ν, the thermal diffusivity a or the specific heat capacity c_p and the thermal conduction λ. An approximation for the thermal boundary layer can be estimated using the following equation:

$$\begin{aligned} Pr &:= \frac{\nu}{a} = \frac{\eta \cdot c_p}{\lambda} \\ \frac{1}{\sqrt[3]{Pr}} &:= \frac{\delta_T}{\delta} \end{aligned} \tag{2.4}$$

For the heat exchanger design, it is more important to calculate with an average heat transfer coefficient α_m with a fixed geometry and an average wall temperature. In this

case, α_m is proportional with the Nusselt number Nu which is a function of Re and Pr. The Nusselt number describes the convective heat transfer on a solid surface. It can be understood as the ratio between the real convective heat transfer and an imagined heat conduction. It is defined in equation 2.5 as follows:

$$\begin{aligned} Nu &:= \frac{\alpha \cdot d}{\lambda} \\ \alpha_m &= \frac{\lambda}{d} \cdot Nu(Re, Pr) \end{aligned} \tag{2.5}$$

2.5.1 Thermal resistance

The thermal resistance R_s can be understood as the reciprocate value of the heat exchange coefficient k. The influence on the tube-bundle heat exchanger has a special importance for thermal desalination systems. For the purpose of heat exchanger dimensioning under given operating conditions with a fixed heat exchange area A, it will be summarized with the factor $k \cdot A$. This respects all mechanisms of heat transport which are defined by the averaged specific heat coefficient α_m, the material thickness d and the thermal conductivity λ. Through addition of the coefficients, the thermal resistance R_s can be calculated according to equation 2.6:

$$\begin{aligned} R_s &= \frac{1}{k_s} \\ &= \frac{1}{\alpha_m} + \frac{d}{\lambda} \end{aligned} \tag{2.6}$$

With regard to thermal desalination systems and tube-bundle heat exchangers, the influence of several heat resistances determines the operation and the possible heat transfer on a single tube [9, 15, 16]. The total heat transfer R_d in thermal desalination systems can be described extending equation 2.6 [16]:

$$\begin{aligned} R_d &= \frac{1}{k_d} \\ &= R_i + R_w + R_o + R_{foul} + R_{ncg} \\ &= \frac{d_{t,o}}{d_{t,i} \cdot \alpha_i} + \frac{d_{t,o}}{2\lambda_t} \ln(\frac{d_{t,o}}{d_{t,i}}) + \frac{1}{\alpha_o} + R_{foul} + R_{ncg} \end{aligned} \tag{2.7}$$

The total thermal resistance R_d given in equation 2.7 is summarized by the addition of the single thermal resistances [9, 16] which are defined as follows: R_i and R_o represent the inner and outer resistance of the tube, while R_w describes the thermal conductivity of the tube wall which depends on material properties. These variables depend mainly on the heat exchanger design. Other important design factors are the tube diameter d_t, as well as thermal conductivity λ determined by material properties[3]. The thermal resistance R_d is also influenced by the flow regime which can be annular, transition and stratified (compare also to fig. 2.17 in section 2.4.3).

Considering the heat exchange by droplets, the equation 2.7 can be simplified. Due to the absence of a distinctive tube wall, the values for R_i, R_o and R_w do not apply and can be assumed as nonexistent. Therefore, the heat exchange only depends on an averaged α_m between vapor and the sprayed distillate.

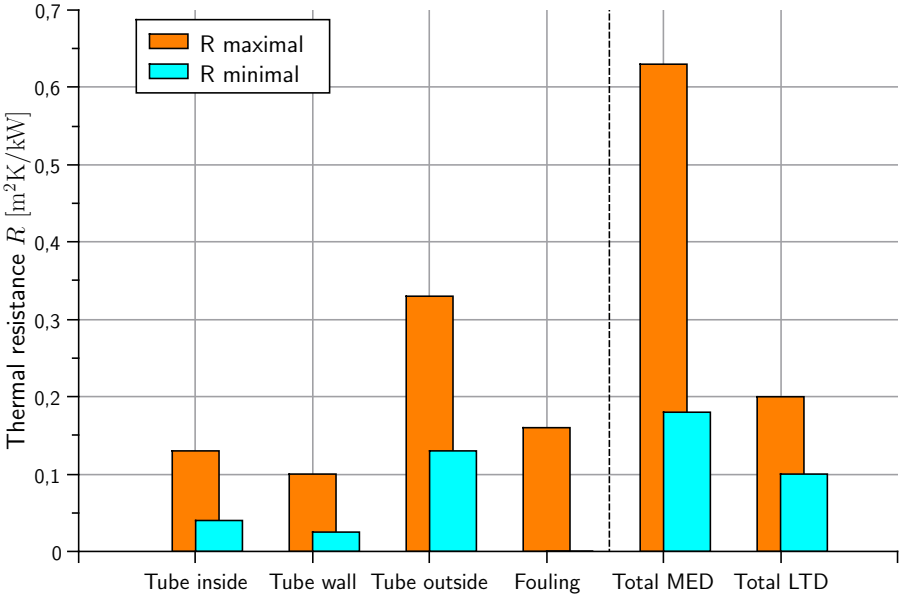

Figure 2.20: *Comparison of the cumulative heat exchange resistance, data taken from [15, 16]*

In order to give some quantitative values for R_d, fig. 2.20 compares the magnitude of the heat resistances on tube-bundle heat exchangers and droplets. The values for R_d range between 0.2 - 0.65 $\mathrm{m^2K/kW}$ for tube-bundles in MED plants and between 0.1 - 0.2 $\mathrm{m^2K/kW}$ for drop-wise condensation in the LTD process which are significantly lower (more information is given in [8, 15, 16]).

The description of the thermal resistance caused by fouling R_{foul} as well as the influence of non-condensible gases R_{ncg} is more difficult and requires special attention. The main mechanisms are explained briefly.

[3] Mostly stainless steel or titanium to prevent corrosion.

Scaling and fouling

Scaling and fouling describes the deposition of solid materials on the heat exchanger surface which mainly affects the outer tube thermal resistance R_o. Those solid materials can consist of inorganic or organic compounds, which is called scaling or bio-fouling, respectively. The latter can especially affect membrane systems operating at lower temperatures. Usually, the danger of scaling in MED and MSF units is encountered with the oversize of heat transfer areas [9–11].

Due to variable temperatures and salt concentrations over the tube length, certain minerals can fall below the solubility limit and cause scaling layers on the tube surface [11, 16, 89]. Scaling is mainly caused by inorganic compounds like calcium carbonates $\mathrm{CaCO_3}$, magnesium carbonates $\mathrm{Mg(OH)_2}$ and calcium sulfates $\mathrm{CaSO_4}$ which are components of the sea water composition [11, 16, 39], see also tab. 2.6. Those compounds also influence the ph-value of the seawater [9]. The scale formation is supported if the tube wetting of the heat exchanger tubes is incomplete. However, the prediction of the scale formation is almost not possible and depends on specific operating conditions and intake seawater. A completely clean heat exchange surface has no scaling resistance though it can be expected that R_{foul} increases with operating time (compare to fig. 2.20). Most scaling depositions can be partly removed by washing cycles with acidic detergents and special developed online ball-cleaning procedures [9, 11].

Scaling and fouling at the drop-wise condensation, it can be stated that this phenomena does not apply. The reason for that are missing heat exchanger walls to form deposits from scaling reactions [15]. The permanent prevention from clogging can be avoided by adding very small quantities of anti-scaling agents.

Non-condensable gases

Non-condensable gases have a significant effect to the heat exchange within the evaporator stage. They mainly consist of $\mathrm{CO_2}$, $\mathrm{N_2}$ and $\mathrm{O_2}$. Due to the thermodynamics of gases, they are very mobile and always tend to move to the coldest surface. In consequence of that, the gases form a film accumulating inside the tube which increase the thermal resistance R_i and hinder the condensation process. Besides the addition of another heat resistance, the vapor condensation temperature is reduced due to partial pressure differences [16].

Typically, the occurrence of non-condensable gases have two reasons. First, leakages of the evaporator reactor can cause air to enter the system. Due to the operation

below ambient pressure, it is easily possible and influenced by the manufacturing quality. Second, the evaporation temperatures cause a degassing of seawater. High temperatures foster the emergence of CO_2. The reactions are described in detail in [89].

Nevertheless, it can be stated that 1% non-condensable gases can decrease the heat transfer coefficient by up to 10% [16, 90]. The impact level also depends on present flow regimes. At elevated Re numbers, the turbulent flow can diminish the effects to the heat transfer coefficient [8].

Non-condensable gases also have an influence on the condensation on droplets and reduce the heat transfer. However, the experiments in the demonstration plant have shown that the removal can be easily realized by a proper venting design of the vacuum system [15]. The influence is significantly lower compared to condensation in tube-bundle heat exchangers.

2.5.2 Heat transfer coefficients

Table 2.7 gives some exemplary values for heat transfer coefficients k dependent on some common applications from [40, 41]. With respect to thermal desalination units, water flowing in tubes and film-wise condensation represents the most frequent case. The condensation described in the previous sections 2.4.3 and 2.5.1 limits the possible maximal heat transfer coefficient inside the reactors. The literature gives approximated total heat transfer coefficients for one effect in MSF desalination units with 2500 $\mathrm{W/m^2K}$ and for effects in MED units around 5300 $\mathrm{W/m^2K}$ [9, 11].

Application	Heat transfer coefficient k $\mathrm{W/m^2K}$
Gases, free convection	5 - 37
Gases, flowing between tubes	10 - 350
Gases, on surface	50 - 200
Water, free convection	100 - 1200
Water, flowing in tubes	500 - 1200
Condensation, water vapor film type	4000 - 17,000
Condensation, water vapor drop-size	30,000 - 140,000

Table 2.7: *Approximated values for heat transfer coefficient [40–43]*

However, tab. 2.7 also shows the superiority of drop wise condensation with heat transfer coefficients of more than 100 $\mathrm{kW/m^2K}$ [42]. This performance has been achieved in experiments using droplets of 0.6 mm and a velocity of 15 $\mathrm{m/s}$ at a heat flux density of

230 $\mathrm{kW/m^2}$ [43]. The results have shown that the heat exchange coefficient is reduced with lowered velocity and the presence of non-condensable gases [43]. At the same time, the volume of the reactor is specifically smaller compared to normal surface contact condensers [42]. It can be seen as a cost advantage.

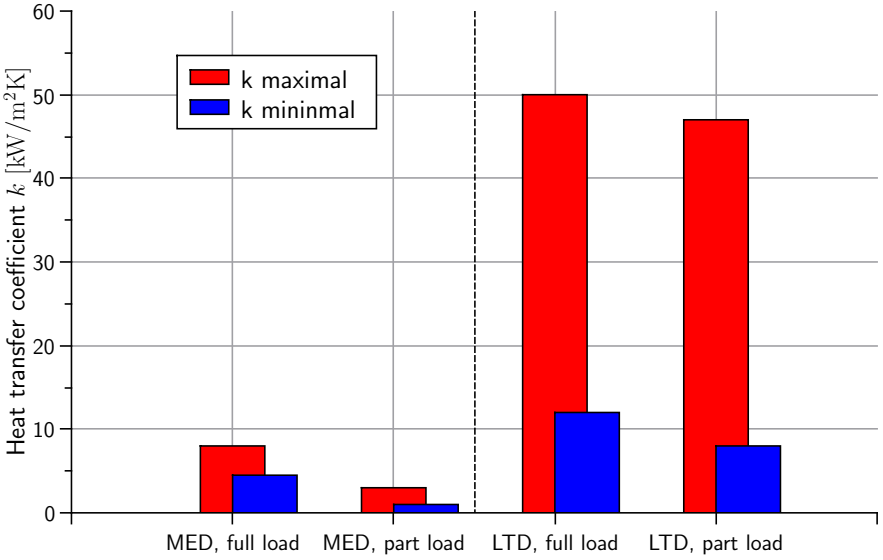

Figure 2.21: *Comparison of heat transfer coefficients, data taken from [15, 16]*

Figure 2.21 compares the heat exchange coefficient k during different operational conditions using tube-bundle heat exchangers within a MED unit and drop-wise condensation in the LTD unit. It can be seen that both systems react differently on part-load conditions. The mechanisms of rinsing water over tube-bundles are very sensitive to changed process parameters resulting in a lowered heat transfer. Concerning the LTD, the formation of the droplets is only sparsely influenced by changed load conditions. All data has been measured in the demonstration plant and has shown possible heat transfer rates up to 50 $\mathrm{kW/m^2K}$ in the reactors [12, 15].

In summary, it can be stated that the heat transfer in thermal desalination units can be significantly improved by using drop-wise condensation instead of condensation inside tube bundles. Drop-wise condensation design has positive effects on the water production as well as on the process integration possibility. The following chapters present a complete model to investigate the main influencing parameters for a process integration of the low-temperature desalination in a concentrating solar power plant.

Chapter 3

Modeling

This chapter describes the model design and the the calculations performed for selected system components. After the discussion on the plant components, the selected system is designed as cogeneration plant for power and water production. The novelty can be seen in the integration of the low-temperature desalination introduced in chapter 2, section 2.4 and 2.4.2. In order to assess this combined system, there are selected mature technologies of concentrating solar power plants and thermal storage systems. The selection bases on the results of chapter 2.1 and 2.2 which conclude the most benefits of direct molten salt thermal storage in combination with a solar tower system. The size of the system is selected basing on realized projects [4] and available data sets. The development of the simulation of the low-temperature desalination unit bases on [23]. The principal system design parameters are summarized in table 3.1.

Component	Technology	Capacity, thermal $\mathrm{MW_{th}}$	Power, electrical $\mathrm{MW_{el}}$	Water $\mathrm{m^3/d}$
Solar field	Solar tower with heliostat field	100	–	–
Thermal storage	Two-tank molten salt, in $\mathrm{MWh_{th}}$	720	-0.63	–
Power block	Steam turbine, reheat cycle	35.6	14.6	–
Desalination	Low-temperature desalination	22.6	-0.3	2300
Cooling	Seawater, direct	18	-0.2	–

Table 3.1: *Design parameters of the simulated system*

3.1 Simulation environment

The complete system is modeled using the software EBSILON® Professional V10.0 [20] especially using the solar library. Ebsilon has been developed to perform detailed

simulation for the design and engineering of power plants. The integration of a library for fluid properties allows the calculation of saltwater mixtures and heat transfer fluids. In addition to that, it contains extensive data sets of realized power plants which have been used for the validation. The program uses an one-dimensional numerical routine according to Newton-Raphson which allows only steady-state simulations [91]. The technical model of the concentrating solar power plant is derived from known projects using the solar library "EbsSolar" incorporating several designs from CSP manufacturers and other simulation environments (see also section 3.3.1) [18, 19].

Furthermore, EBSILON® Professional allows the use of own environmental data. Due to the extensive measurement of the ambient conditions at the selected site, it is possible to use own meteorological data of the selected site in El Gouna, Red Sea, Egypt, for performance calculations [31]. The power block simulation focus on the influence of flexible condensation pressures as well as optimized part-load behavior. Due to the thermal storage system, the power block can operate independently from the solar irradiation.

The technical model of the desalination unit (low-temperature desalination) has been developed in close cooperation with the project engineers of the demonstration plant using the kernel-scripting module of the Ebsilon environment (see also section 3.4). The validation of the simulation results have been carefully checked with the measurement results of the demonstration plant in El Gouna [12, 15, 75, 82]. Various simulations of several configurations have led to the model plant, which iss described in the following sections. The complete simulation design is visualized in appendix B.

3.2 Environmental data

In order to improve the simulation and to obtain more realistic results, own measurements of environmental data are used for the calculations. These data have been measured by a meteorological station which has been put in operation in February 2013. The station in figure 3.1 has been build in cooperation with the FU Berlin, Institute for Meteorology in the framework of a DAAD funded project[1].

To ensure that the obtained data correspond to criteria of the world meteorological organization (WMO) [92], the station has been designed by a certified expert company [93]. The whole system has been mounted to a modified electric tower which has been

[1] Climate Workshop in El Gouna from February, 2 until March, 3, 2013, Prof. Dr. U. Cubasch, Transformationspartnerschaften in Kooperation mit Hochschulen in den Transformationsländern Ägypten und Tunesien

Figure 3.1: *El Gouna meteorological station*

kindly provided by El Gouna Electrics. The meteorological station is positioned 3 km outside of El Gouna on latitude 27°24'46" N and longitude 33°38'18" E. The data are recorded since February, 26, 2013.

Table 3.2 gives an overview of the measured variables and the sensor technology. The system records every minute one data set averaged over 60 seconds. The sensors for wind speed and direction is mounted in 10 m above the ground, while the temperature and irradiation measurement is mounted in 2 m height. The installation of a special shadow ring allows for the measurement of the diffuse horizontal irradiation (DHI).

Name	Sensor	Symbol	Unit
Wind direction	Ultrasonic anemometer	d_w	$^\circ$
Wind speed	Ultrasonic anemometer	v_w	$\mathrm{m/s}$
Temperature	Pt100 resistance sensor	T_{amb}	$^\circ\mathrm{C}$
Rel. humidity	Capacitive sensor	rH_{amb}	$\%$
Global horizontal irradiation	Pyranometer	G	$\mathrm{W/m^2}$
Diffuse horizontal irradiation	Pyranometer	D	$\mathrm{W/m^2}$
Long wave irradiation	Pyrgeometer	I	$\mathrm{W/m^2}$
Air pressure	Piezo-ceramic sensor	p_{amb}	mbar

Table 3.2: *El Gouna meteorological station, sensors and measuring variables*

For the simulation of solar power plants, the measurement of the solar irradiation is the most important for the performance assessment. Instead of using averaged values from satellite observations [94] or software like Meteonorm [95, 96], own measurements can be used to simulate the expected power output from the concentrating solar power plant. Due to the indirect measurement of the direct normal irradiation DNI, this variable needs to be calculated by the irradiation energy balance using the measurements from the pyranometer sensors [97]. The calculation methods are outlined in the following sections.

3.2.1 Irradiation energy balance

The energy balance of a horizontal area by a given radiation can be expressed with the total energy Q, the global horizontal radiation (GHI) G, the reflected global radiation R as a fraction of G, the downwards directed thermal radiation I of the atmosphere (also called counter-radiation which is the thermal radiation of the atmospheric gases) as well as the thermal radiation of the earth surface E itself. More information can be found in [17].

$$Q = (G - R) + (I - E) \tag{3.1}$$

Each radiation flux density is given in the unit $\mathrm{W/m^2}$. The term $(G - R)$ represents the solar or short-wave radiant flux densities while $(I - E)$ represents the terrestrial or long-wave radiant flux densities. During a day, there is a strong diurnal variation of the solar irradiation in contrast to the terrestrial irradiation, which varies only a little. This can be explained by the almost constant temperature of the atmosphere and earth surface [17].

3.2.2 Calculation of the direct normal irradiation, DNI

For the energy conversion in solar thermal power plants, the short-wave irradiation $(G - R)$ is relevant. Furthermore, only the direct normal irradiation DNI can be concentrated by the solar field of a CSP plant. Due to the fixed positions of the pyranometer sensors, the measured irradiation is received on a horizontal surface with variable incident angles. The correlation between the diffuse horizontal irradiation D and beam (resp. direct) horizontal irradiation B can be expressed by the sum of the global irradiation G.

$$G = B + D \tag{3.2}$$

The balance given equation 3.2 accounts for the irradiation on a fixed horizontal area. The measured values of the G and D allow the calculation of beam horizontal irradiation B using equation 3.2. The beam horizontal irradiation B can be understood as the projection from the direct normal irradiation DNI on the reflective surface. In order to calculate the resulting DNI values, it is necessary to use the zenith angle ζ or the sun elevation angle $\gamma = 90° - \zeta$ for the respective hour of the year [17]. Those angles can be calculated by various possibilities according to the time of the year and the exact latitude and longitude of the respective position. Figure 3.2 visualizes the method for DNI calculation.

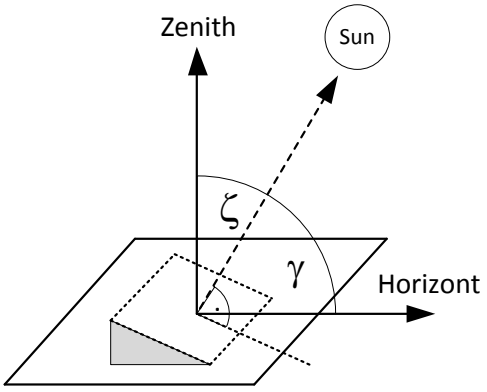

Figure 3.2: *Sun angles for the calculation of DNI, simplified from [17]*

In order to calculate exact sun angles for the position of the meteorological station, the calculation method of DIN5035 [98] is applied. The Ebsilon component "sun" can be configured with the exact latitude and longitude of the meteostation to render the angles accordingly. The DNI can now be calculated using trigonometric relations and equation 3.2 as follows [17]:

$$\begin{aligned} B &= DNI \cdot \cos\zeta = DNI \cdot \sin\gamma \\ DNI &= \frac{B}{\sin\gamma} = \frac{G - D}{\sin\gamma} \end{aligned} \tag{3.3}$$

An analysis and calculation results for the measured meteorological data in the year 2013 can be found in chapter 4, section 4.1 as well as in appendix A. All other measured values like temperature T_{amb} and wind data d_w, v_w can be directly used and do not require further calculations.

3.3 Solar power plant

The solar tower and heliostat field is designed to be suitable for base-load power generation by using an direct storage of the solar heat while allowing high operation temperatures for optimized thermodynamic efficiency. The yearly operation hours should exceed 6000 hours per year. The design capacity of the receiver is chosen with 100 $\mathrm{MW_{th}}$ solar heat at peak radiation during noon time. The heat is collected by a tubular-type receiver using molten salt as heat transfer and storage medium. This system size can be seen as smallest size for an economically operation with moderate technological risk. The following sections describe the model of the plant components.

3.3.1 Solar field and tower

The solar field of the power plant consists of several single two-axis steered heliostats. They function as a large optical device to focus the direct radiation to the central receiver on the top of the tower. In the focal point, the receiver transfers the generated heat to the molten salt fluid. The challenge in designing and optimizing such a system is the calculation of the radiation intensity resulting from the overlapping beams of each heliostat. The exact position of each heliostat has a high degree of freedom and requires a special modeling by ray-tracing software according to site specifications. The software HFLCAL is used to generate a 180° heliostat field layout [18,19], which has been included in the solar library of Ebsilon [20]. One possible solution for the 100 $\mathrm{MW_{th}}$ solar tower can be the heliostat field layout visualized in figure 3.3. The needed land area calculates to 1266 x 1126 m, which sums up to an total area of 1.426 $\mathrm{km^2}$.

The field is designed following the assumption that each ray from the heliostat is rotationally symmetric and normal distributed. The software HFLCAL integrates the radiation distribution of the aperture area on the central receiver which allows a much faster calculation [18, 19]. This assumption can be justified assuming that the standard deviation of the optical mirror quality has the same magnitude compared to the solar disk.

The data set [20] for this field layout is expressed in an efficiency matrix which has been created using HFLCAL [18, 19]. This matrix defines the heliostat field size (total reflective area, A_{ref}), the receiver geometry (size and tilt) as well as the relative receiver height to the field. In a second step, the matrix is used for calculating the field efficiency η_{fld} respecting cosine losses as well as effects from shading and blocking.

In this simulation, the heliostat field component calculates the total incident power Q_{inc} using measured DNI values [31] given by the sun positions for azimuth angle and

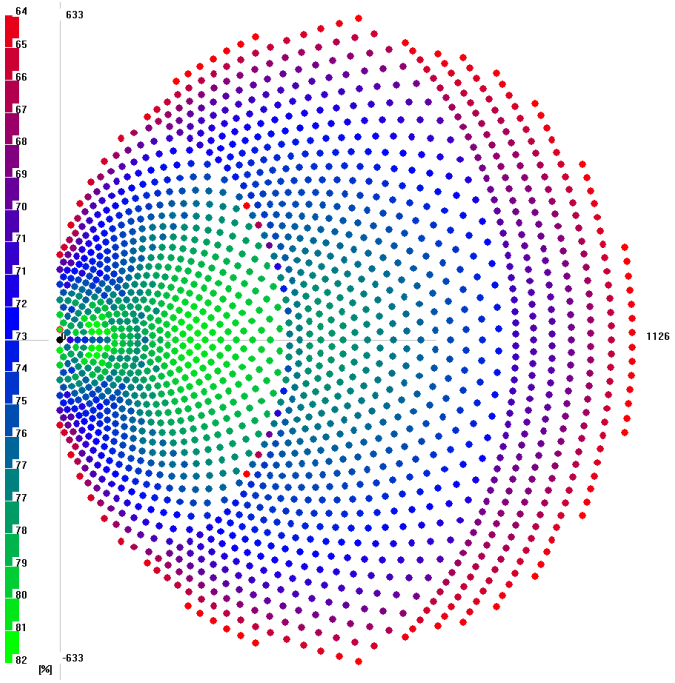

Figure 3.3: *Heliostat field layout with cosine losses [18–20]*

solar height. The transfer function is defined by a two-dimensional efficiency matrix. It is only valid for the given plant configuration. The attached solar tower receiver component transfers the reflected solar radiation into the fluid (here: molten salt) while calculating heat and pressure losses at a constant receiver temperature. However, the heat absorption directly depends on the geometry of the heliostat field.

Generally, a larger field has a lowered efficiency due to atmospheric attenuation. This applies especially to the heliostats with the greatest distance to the receiver on top of the tower, which can be also seen in figure 3.3.

Heat and mass balance for the solar field and the receiver

The solar incident power Q_{inc} transmitted to the receiver by the heliostat field can be described as the product of usable solar heat Q_{sol} and η_{fld}:

$$Q_{inc} = Q_{sol} \cdot \eta_{fld} = \frac{A_{ref}}{DNI} \cdot \eta_{fld} \tag{3.4}$$

The total solar heat Q_{sol} is also defined as the reflective area A_{ref} of the field divided by the direct radiation. Considering the optical losses, only a fraction can be converted in the receiver. Those losses are expressed by η_{fld} which assumes a fully tracked and clean reflective mirror condition. The exact value of η_{fld} is calculated by interpolation in the

prior mentioned field efficiency matrix according to the respective sun azimuth angle and height [20].

The receiver converts the incident power Q_{inc} to the effective heat Q_{eff} absorbed by the molten salt heat transfer fluid. In other words, the receiver is simulated as a heat exchanger for the concentrated solar heat by given outlet temperature of the molten salt fluid (set-value). The heat flux at nominal load condition can be considerably up to 900 $\mathrm{kW/m^2}$ which has been discussed in 2.1.2 and table 2.2. As a result, the receiver mass flow $\dot{m}_R$ is calculated according to the effective heat flux Q_{eff} absorbed by the fluid. The enthalpies of the molten salt before and after the heat supply are noted with h_1 and h_2, respectively.

$$\begin{aligned} Q_{eff} &= Q_{inc} - Q_{loss} = \dot{m}_R \cdot (h_2 - h_1) \\ \dot{m}_R &= \frac{Q_{inc} - Q_{loss}}{(h_2 - h_1)} \end{aligned} \tag{3.5}$$

Special attention has to be given to the term Q_{loss} which can have quite significant influence on concentrating systems. Generally, it can be expected that Q_{loss} increases with the operation temperatures. Q_{loss} summarizes all optical $Q_{L,opt}$, convective $Q_{L,con}$ and radiation $Q_{L,rad}$ losses. While the optical losses do not depend on the receiver temperature, the latter increases with larger ΔT to the ambient temperature. By assuming a constant receiver temperature, convective losses $Q_{L,con}$ and radiation losses $Q_{L,rad}$ can be calculated according to equation 3.6:

$$\begin{aligned} Q_{L,opt} &= (1 - \eta_{opt}) \cdot Q_{inc} \\ Q_{L,con} &= S_{con}\alpha_{con} \cdot A_{rec} \cdot (T_{rec} - T_{amb}) \\ Q_{L,rad} &= \epsilon_{rec} \cdot \sigma \cdot A_{rec} \cdot ({T_{rec}}^4 - {T_{amb}}^4) \end{aligned} \tag{3.6}$$

Concerning the thermal losses by radiation, the emissivity is described by ϵ_{rec} which is smaller than 1 (ϵ =1, black body radiation) and solely depends on the receiver outer material. The σ describes the Stefan-Boltzmann constant[2] while the temperatures need to be calculated in Kelvin. The term S_{con} respects forced convention by the wind and is corrected by a heat loss factor for convection α_{con}. The following table 3.3 summarizes all boundary conditions for the heliostat field and the solar tower.

[2]Stefan-Boltzmann constant $\sigma = 5.670 \cdot 10^{-8}\ \mathrm{W/m^2K^2}$

Name	Parameter	Value	Unit
Heliostat field	Fieldset	Hel180_25N_100MWth	-
Total reflective area	A_{ref}	173,800	m^2
Total number of heliostats	n_{hel}	1783	-
Heliostat reflective surface	A_{mir}	100	m^2
Mirror reflectivity	R_{ref}	0.8841	-
Tower, receiver aperture area	A_{rec}	223.56	m^2
Tower, design thermal power	Q_{inc}	106,400	$\mathrm{kW_{th}}$
Tower, receiver height	h_{to}	126.9	m
Tower, receiver diameter, width and height	d_{to}	16.87	m
Optical efficiency	η_{opt}	0.93	-
Emissivity, receiver	ϵ_{rec}	0.83	-
Heat loss, convective coefficient	α_{con}	7	$\mathrm{W/m^2K}$
Temperature, receiver	T_{rec}	580	$^{\circ}\mathrm{C}$
Nominal pressure drop	$\Delta p_{1,2}$	10	bar

Table 3.3: *Design parameters for heliostat field and solar tower*

3.3.2 Thermal energy storage

The basic design of a thermal energy storage has been given in chapter 2.2. The simulation models this system using the fluid properties of the selected molten salt mixture. The working fluid consists of a mixture from 60% nitrate salt $\mathrm{NaNO_3}$ and 40% alkali metal nitrite salt $\mathrm{KNO_3}$, which is commonly used as solar salt [38]. The direct storage system is modeled as two isolated tanks filled with hot and cold salt, respectively. Due to the high stability of solar salt, this can be realized at ambient pressure level [38]. The solar thermal energy generated in the receiver is directly stored in the hot tank at 580 $^{\circ}\mathrm{C}$. The high temperature allows for a higher process efficiency compared to CSP plants using parabolic trough collectors (PTC), which are limited to 400 $^{\circ}\mathrm{C}$.

However, the salt is pumped from the hot tank to the steam generation system to supply around 35 $\mathrm{MW_{th}}$ to the power block. After cooling down to 300 $^{\circ}\mathrm{C}$, the salt is stored in the cold tank. During day operation, the salt inside the cold tank is pumped through the receiver absorbing up to 100 $\mathrm{MW_{th}}$ depending on the solar radiation.

Figure 3.4 visualizes the Ebsilon model of the heliostat field, the solar tower and the attached thermal storage system. There are two pumps required to supply the receiver

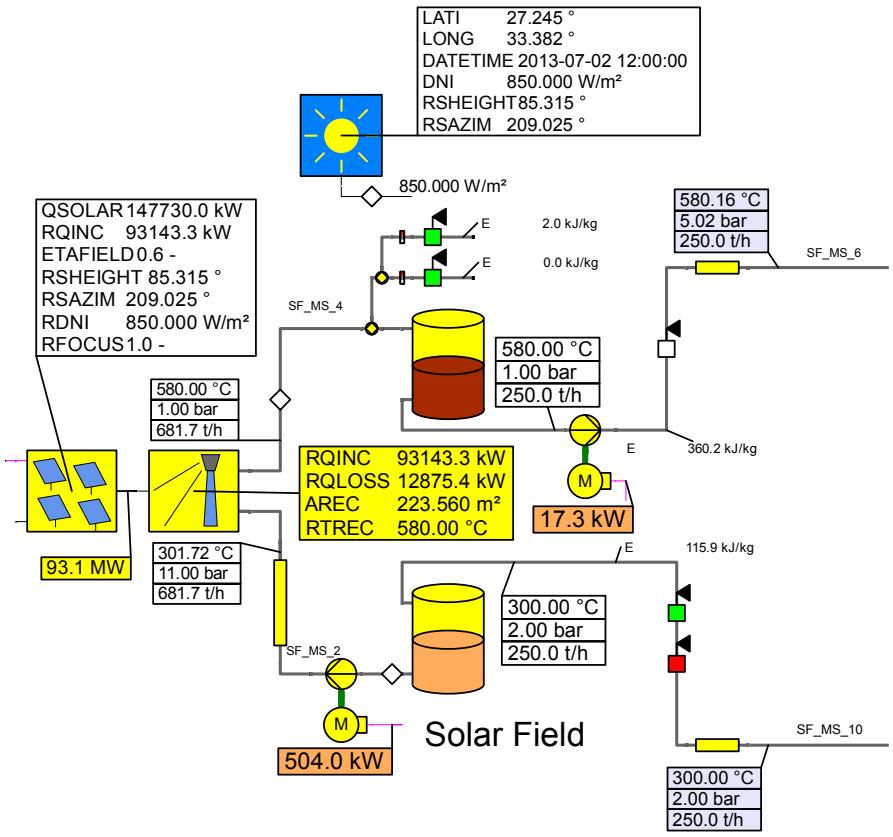

Figure 3.4: *Ebsilon Model of solar tower and thermal storage*

and the steam generator with the molten salt. Due to the tower height (see also table 3.3), the power consumption of the pumps differ significantly.

Heat and mass balance for the thermal energy storage

The amount of energy absorbed or released by increasing or decreasing the temperature of a material without a phase change is called sensible heat. The mechanism is suitable for one-phase heat transfer fluids. For a given temperature difference ΔT_{sto} and assuming a constant specific heat c_p, the stored heat $\dot{Q}_{sto}$ is given by the following equation:

$$\begin{aligned} \dot{Q}_{sto} &= \dot{m}_{sto} \cdot c_p \cdot (T_{sto,h} - T_{sto,c}) = \dot{m}_{sto} \cdot c_p \cdot \Delta T_{sto} \\ \dot{Q}_{sto} &= \dot{Q}_{pb} \cdot t_{sto} \end{aligned} \tag{3.7}$$

The total mass and specific heat coefficient used in the thermal storage system is defined with M_{sto} and c_p. To ensure a design capacity for full load operation to supply thermal energy $\dot{Q}_{pb}$ the power block, the storage system needs to be dimensioned for a maximal duration t_{sto}. The total mass of molten salt M_{sto} required for this operation can be calculated by:

$$M_{sto} = \frac{\dot{Q}_{pb} \cdot t_{sto}}{c_p \cdot (T_{sto,h} - T_{sto,c})} \tag{3.8}$$

The maximal storage time is determined by certain mass limits of upper and lower storage level. Due to the state depended density ρ_{ms} of the molten salt, the resulting maximal volumes need to be respected for the tank design. They are strongly influenced by the temperature. Therefore, the density ρ_{ms} needs to be calculated according to the actual storage temperature at the beginning of the time interval [20].

In order to perform a time series analysis, the mass balance of each tank needs to be defined. This requires the definition of a time interval t_i which is set to one hour. During this interval, the loading $\dot{m}_+$ and unloading $\dot{m}_-$ mass flows are constant. Now, the new mass $M_{sto,n}$ of the hot and cold tank after each time interval can be calculated using the actual storage level $M_{sto,a}$ in equation 3.9:

$$M_{sto,n} = M_{sto,a} + (\dot{m}_+ \cdot t_i) - (\dot{m}_- \cdot t_i) \tag{3.9}$$

Knowing the temperatures and the enthalpies of the loading and unloading mass flows, the final energetic enthalpy of the storage $H_{sto,n}$ can be calculated:

$$\begin{aligned} \Delta H_{sto} &= \frac{M_{sto,a} \cdot h_{sto,a} + \dot{m}_+ \cdot h_+ \cdot t_i}{M_{sto,a} + \dot{m}_+ \cdot t_i} \\ H_{sto,n} &= \Delta H_{sto} \cdot m_{sto,n} - \dot{Q}_{sto,+} \end{aligned} \tag{3.10}$$

The term $\dot{Q}_{sto,l}$ represents the heat losses to the environment which generally increase with the temperature. Therefore, the average storage temperature needs to be calculated using T_{sto} and $T_{sto,n}$, while the ambient temperature T_{amb} is subtracted per time interval. The calculation is summarized in equation 3.11.

$$\dot{Q}_{sto,l} = \dot{Q}_{sto,sl} \cdot \left(\left(\frac{T_{sto} + T_{sto,n}}{2} \right) - T_{amb} \right) \cdot t_i \tag{3.11}$$

The specific heat loss $\dot{Q}_{sto,sl}$ is given in $\mathrm{kW/kgK}$ as start parameter for the simulation and mainly depends on the tank isolation. The following table 3.4 summarizes all design parame ters for the molten salt thermal storage system.

Name	Parameter	Value	Unit
Maximum level by mass	M_{max}	5000	t
Minimum level by mass	M_{min}	100	t
Pressure in storage	p_{sto}	1	bar
Temperature in storage, hot tank	$T_{sto,h}$	580	°C
Temperature in storage, cold tank	$T_{sto,c}$	300	°C
Specific heat loss, both tanks	$Q_{sto,sl}$	0.8	kW/kg K

Table 3.4: *Design parameters for thermal storage system*

3.3.3 Power block

The power block consists of several components like the feed water pumps, the steam generator, turbines and condenser. It is designed as reheat cycle after the high-pressure turbine stage. Before the feed water enters the steam generator, it is heated up by several pre-heaters and degassed by the deaerator. This process design positively influences the overall efficiency of the steam cycle by raising the overall temperature difference.

The steam generator is heated by the molten salt from the hot tank. The feed water enters the main pre-heater or economizer (PRE) at design pressure in order to raise the temperature to the evaporation point. The largest portion of energy is used for the evaporation (EVA). The saturated steam is superheated in the last heat exchanger (SH) to the final temperature. All thermal energy is supplied by the molten-salt mixture from direct storage. Figure 3.5 visualizes the complete power block model with exemplary values. Blue lines indicate liquid water, red lines steam, grey lines molten salt and green lines a water/salt mixture.

Turbines

The turbines can be distinguished by different pressure sections, which can be divided into high, medium and low pressure stages. The modeled system uses five turbine stages, which consists of one high, two medium and two low pressure sections. After the high pressure section, the steam is reheated in the second super-heater before entering the medium pressure stages. This design optimizes the overall efficiency. The turbine stages are modeled according to the "Stodola law" where the incoming turbine pressure $p_{t,i}$ is calculated from the actual steam mass flow [99]. This is formulated in equation 3.12 by the law of the cone using the mass flows $\dot{m}_{t,i}$ for in- and out-coming pressures $p_{t,o}$ as well

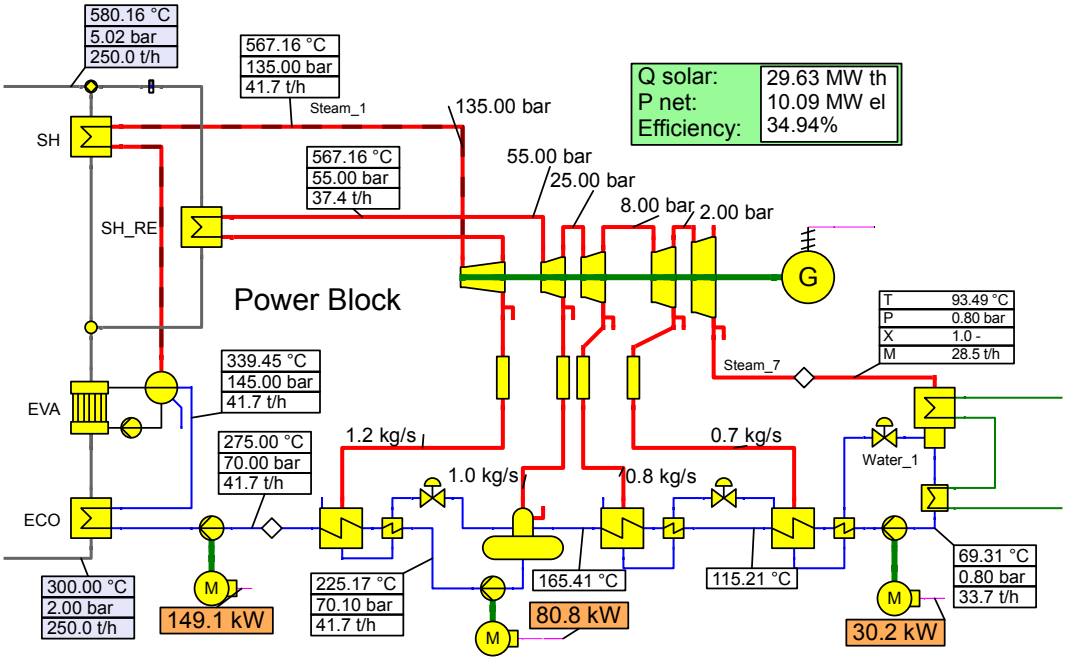

Figure 3.5: *Ebsilon Model of the power block*

as the nominal parameters marked with index n. The incomming steam temperatures are noted with $T_{t,i}$.

$$\frac{\dot{m}_{t,i}}{\dot{m}_n} = \frac{p_{t,i}}{p_{t,o}} \cdot \sqrt{\frac{1-(\frac{p_{t,o}}{p_{t,i}})^2}{1-(\frac{p_{t,o,n}}{p_{t,i,n}})^2}} \cdot \sqrt{\frac{T_{t,i,n}}{T_{t,i}}} \tag{3.12}$$

The equation 3.12 needs to be solved to $p_{t,i}$ in order to calculate the inlet pressure of the respective turbine stage:

$$p_{t,i} = \sqrt{p_{t,o}^2 + \left(\frac{\dot{m}_{t,i}}{\dot{m}_n}\right)^2 \cdot (p_{t,i,n}^2 - p_{t,o,n}^2) \cdot \frac{T_{t,i}}{T_{t,i,n}}} \tag{3.13}$$

Equation 3.13 allows the calculation of the inlet pressure $p_{t,i}$ especially in part-load operation using the turbine outlet pressure $p_{t,o}$ and the respective temperature T_i with respect to the design case. The power block is designed in order to operate with a nominal pressure of 135 bar at a temperature of 567 $^\circ\mathrm{C}$ with different mass flows. The pre-heating is realized by steam extraction of each turbine stage while the last stage directly leads to the final condenser which also acts as interface to the desalination unit. All turbine stages are connected with a single shaft to the electric generator.

In a next step, the pressure levels of each turbine stage needs to be defined. This is done according to table 3.5 with a given isentropic and mechanical efficiency ratio of $\eta_{is,t} = 0.86$ and $\eta_{m,t} = 1$, respectively.

Name	Inlet pressure $p_{t,i}$ in bar	Outlet pressure $p_{t,o}$ in bar
High pressure, HP1	135	58
Medium pressure, MP2	55	25
Medium pressure, MP3	25	8
Low pressure, LP4	8	2
Low pressure, LP5	2	0.1 - 0.8

Table 3.5: *Turbine stages with pressure levels*

The modeled system is designed for flexible condensation pressures in order to allow variable load conditions of the thermal desalination unit. Therefore, there is no fixed outlet pressure in the last turbine stage (see also table 3.5). This strongly influences the electrical efficiency η_{el} to that extent, that the generated electricity output varies up to 2 $\mathrm{MW_{el}}$ and the thermal condenser load around 4 $\mathrm{MW_{th}}$. The complete latent energy from the steam condensation is used for the thermal desalination unit. The behavior of the system with respect to power and water production will be discussed in chapter 4, section 4.4.

3.4 Thermal desalination unit

The simulation of the desalination unit [12, 15, 21, 82] can be seen as one of the core aspects of this thesis. The low-temperature desalination has been sufficiently discussed in chapter 2, section 2.4.2. After more than one year operational experience, it has been possible to derive enough data to develop a simulation [12, 21]. The implementation of this design in Ebsilon is performed by adapting the scripting kernel module. The modeling and the underlying equations are subject of this section. This simulation environment is suitable to respect the thermodynamic behavior of salt water mixtures[3] as well as the required electric power for pumping through different pressure vessels [21]. Furthermore, the development of this simulation in Ebsilon allows the integration in solar power plants and the analysis of the cogeneration behavior.

[3] This allows for the modeling of the boiling point elevation (BPE) in dependence of the salt content of the intake seawater

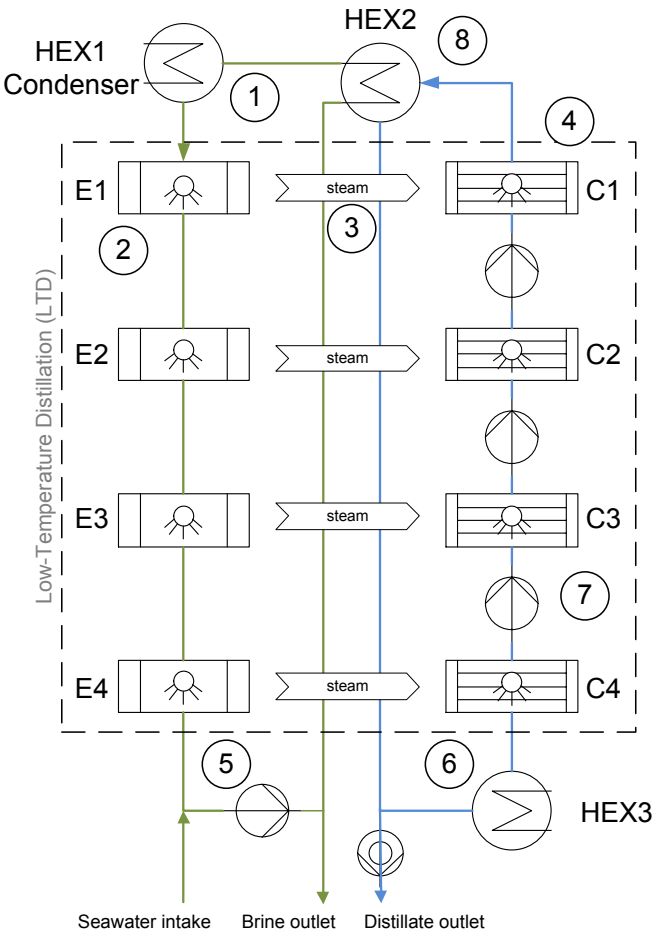

Figure 3.6: *Process flow of Low-Temperature-Desalination (LTD) [21, 22]*

The principal media flows are illustrated in figure 3.6 with four exemplary stages. The reactors on the left side show the evaporators with salt water while the right side show the condensation reactors with distilled water. In general, the temperature regime is decreasing for each evaporator stage and increasing for each condenser stage. The pressure regime follows the opposite direction.

The salt water is heated up in HEX1 by the latent heat of the steam turbine condenser from the solar power plant (1). The hot salt water is then released into the first evaporation reactor vessel E1 in a decreased pressure environment. It is released on top of perforated sheet metal trays to generate a large amount of small droplets to increase the surface of the water (2). Because of decreased pressure regime below the boiling point in E1, the salt water partially changes its phase to vapor while the not-evaporated salt water decreases its temperature according to evaporation enthalpy. The non-evaporated part of the salt water enters the next stage with lowered pressure $p_{E1} > p_{E2}$ and increased its salt content. The evaporation principle leads to a perpetual steam flow which

is assumed to be free of ions. The steam passes through the demister / droplet separator (3) to the condensation reactor vessel C1 (4). This mechanism applies for all following stages at decreasing temperature and pressure ranges.

The complete condensation of the saturated steam is realized by the same spray system on fresh water with lowered temperature at almost isobaric conditions. However, the design of the perforated sheets to generate the droplets is different. Because of the condensation, the temperature of the distillate increases by the amount of the steam enthalpy. The salt water circulation is driven by a pump (5) to ensure sufficient volume flow for running the spray system. Furthermore, there are auxiliary pumps for brine discharge and distillate outlet.

In order to realize the condensation, the distillate needs to have a lower temperature compared to the generated steam. The cooling of the distillate occurs in HEX3 (6) using direct seawater. This process continues under different temperature and pressure conditions in the following stages E2-E4 and C2-C4, respectively. In the condensation reactor, the pressure increases in the flow direction from C4 to C1. This requires additional pumping between each stage to deliver the distillate to the next condensation level (7). Using the enthalpies for the temperature and pressure calculation resulting from evaporation and condensation, the temperature of the distillate leaving C1 is much hotter compared to the concentrated salt water leaving E4 (same mass flows assumed). To recover this heat and use it for heating up the seawater, HEX2 is required (8). All heat exchangers can be designed as plate heat exchanger and need to be dimensioned appropriately to allow for a sufficient ΔT_m and an optimized heat transfer coefficient. The applied material needs to be also seawater resistant in order to prevent corrosion.

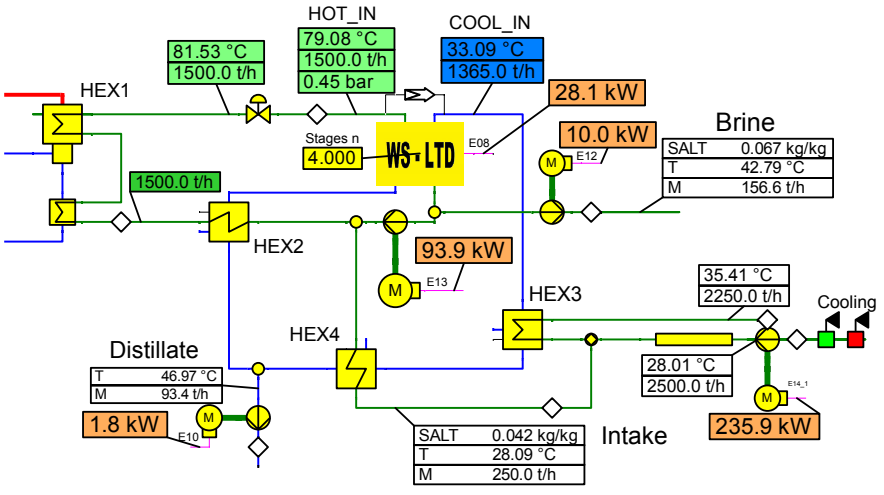

Figure 3.7: *Ebsilon implementation of the low-temperature desalination (LTD)*

Figure 3.7 shows the Ebsilon implementation of the LTD system. The heat exchanger HEX1 is modeled as power plant condenser while for HEX2-4 standard components are used. The model has parameters for defining the number of stages n, the temperature difference between the reactor vessels ΔT_{ves}, the isentropic efficiency η_s as well as the electric efficiency η_{el} of the pumps in the desalination unit. Furthermore, the experiments carried out on the demonstration plant have shown that a slightly lowered condenser mass flow is favorable for the condensation process. The reason is the different design of the perforated sheets inside the reactor vessels. In order to respect this in the simulation, the condenser mass flow is set to 91 % of the mass flow in the evaporators.

3.4.1 Temperature correlations

For the description of the temperature correlation in the desalination system, the total temperature gradient of the system needs to be defined with ΔT_{sys}. The hot intake stream in HEX1 is defined as $T_{h,i}$ and the cooling medium in HEX3 as cold intake $T_{c,i}$ [75] [21], respectively:

$$\Delta T_{sys} = T_{h,i} - T_{c,i} \tag{3.14}$$

In order to allow for a maximal distillate condensation, a temperature gradient of 10 K should be respected for each stage, which is denoted as ΔT_{stg}. The temperature difference in the single evaporation or condensation reactor vessels are ΔT_{ves}, respectively. The evaporation and condensation in each stage can be written as ΔT_{stg} depending on i stages:

$$\Delta T_{stg} = \frac{\Delta T_{sys} - \Delta T_{ves}}{i+1} \tag{3.15}$$

The experiments on the demonstration plant have shown a possible temperature difference ΔT_{ves} in the single reactor vessels ranging from 0,5 to 3 K, which depends on the respective flow regime and droplet formation. The distillate output $\dot{m}_d$ of each stage can be calculated using the following equation 3.16:

$$\dot{m}_d = \frac{\left(\sum_{i=1}^{n} \dot{m}_i \cdot c_p \cdot \Delta T_{stg,i}\right) \cdot t}{h_v} \tag{3.16}$$

3.4.2 Evaporator model

It is necessary to model the evaporation and the condensation process separately for each stage. Therefore, it is necessary to reduce each stage i with one predecessor and one successor stage. The reduction of each stage with one evaporator and one condenser can be seen in Figure 3.8, which illustrates the previous $i-1$ and the subsequent stage $i+1$. Because of the incoming saltwater flow after the heat supply in HEX1, the first stage needs to be modeled differently [21, 23].

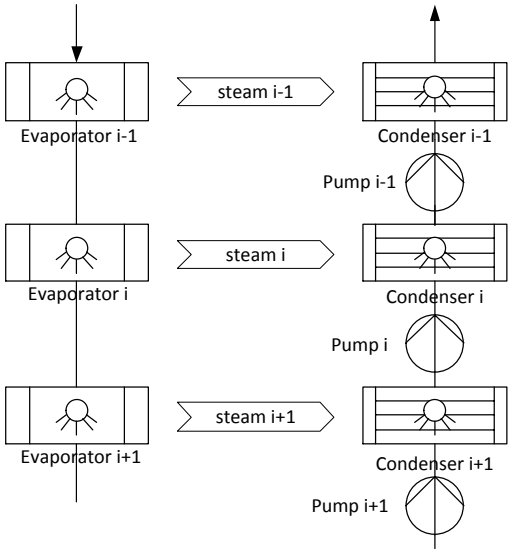

Figure 3.8: *Reduction of the model to the stage i [21, 23]*

In order to design the model with reasonable effort, some simplifications are made. The simulation neglects all heat and friction losses. This assumption is justifiable due to the negligible temperature difference to the environment. Furthermore, the spraying process is assumed as isenthalpic state change which means as a steady flow with a constant enthalpy. This allows for the formulation of the following enthalpy balance, where as $h_{ev,i-1}$ is the specific enthalpy before the spraying and $h_{sp,i}$ after the spraying [23].

$$\frac{dU}{d\tau} = h_{ev,i-1} - h_{sp,i} = 0 \tag{3.17}$$

The steam generation takes place during the spraying process in the evaporator stage. The pressure of the saltwater is lowered to the pressure of the stage i until the vapor pressure $p_{ev,i}$ is reached. This pressure $p_{ev,i}$ can be calculated from the system temperatures $T_{ev,i}$ in the last section using formula 3.15. The steam content is described with

$x_{ev,i}$. The gained steam amount can be calculated by the respective differences of the stages, while h' is defined as specific enthalpy of the boiling liquid and h'' as saturated steam, respectively:

$$x_{ev,i} = \frac{h'(T_{ev,i-1}) - h'(T_{ev,i})}{h''(T_{ev,i}) - h'(T_{ev,i})} \tag{3.18}$$

The salt content of the steam is assumed to be zero and is not respected. The measurements on the demonstration plant have shown residual salt content lower than 30 $\mathrm{ppm\ TDS}$ [12]. However, the distillate mass flow $\dot{m}_{d,i}$ of stage i can be now calculated except from the distillate generated in the first stage.

$$\begin{aligned} \dot{m}_{d,i} &= \frac{h'(T_{ev,i-1}) - h'(T_{ev,i})}{h''(T_{ev,i}) - h'(T_{ev,i})} \cdot \dot{m}_{ev,i-1} \\ &= x_{ev,i} \cdot \dot{m}_{ev,i-1} \end{aligned} \tag{3.19}$$

The specific enthalpy of the distillate $h_{d,i}$ corresponds to the state of saturated steam $h''(T_{ev,i})$ due to the isenthalpic assumption in each stage. Consequently, the specific enthalpy of the salt water flowing in the subsequent reactor $i+1$ is assumed to have the enthalpy of boiling liquid $h'(T_{ev,i})$. Using the distillate mass flow $\dot{m}_{d,i}$, it is now possible to calculate the mass flow $\dot{m}_{ev,i+1}$ entering the subsequent stage $i+1$.

$$\dot{m}_{ev,i+1} = \dot{m}_{ev,i} - \dot{m}_{d,i} \tag{3.20}$$

The process also implies that after each stage the salt concentration $b_{s,i}$ needs to increase according to the steam amount generated by $\dot{m}_{ev,i}$. The salt concentration in the next stage is denoted as $b_{s,i+1}$. This correlation is given by the salt balance in equation 3.21:

$$b_{s,i+1} = b_{s,i} \cdot \frac{\dot{m}_{ev,i}}{\dot{m}_{ev,i+1}} \tag{3.21}$$

The correlations in equations 3.17 - 3.21 allow for the calculation of any desired amount of stages within this simulation at given salt water mass flows.

3.4.3 Condenser model

The condensation process is modeled by using all fluid properties, mass flows and enthalpies calculated in the evaporation process. The most significant difference compared to the evaporator can be seen in modeling the pumps as well as the required electrical work for pumping the distillate into the subsequent condenser. This is necessary, because the following condensation reactor has an increased pressure environment. The flow direction is reverse compared to the evaporation which requires the pumping of the distillate from condenser i to $i-1$ (see figure 3.8). From the macroscopic perspective, the interaction of evaporator and condenser can also be compared to a large counter-flow heat exchanger.

The simulation of the required pumping power is implemented by using enthalpy differences resulting from the pressure differences. Each condenser stage increases its pressure level from i to $i-1$ under the assumption of an ideally isentropic pumping of the distillate, excluding the first condenser stage. The pressure level corresponds to the evaporator stage $i-1$ calculated in the evaporator part by $p_{ev,i-1}$. This allows the calculation of the ideal specific enthalpy of the pump $h_{p,is,i}$ in dependence of the specific entropy $s_{co,i}$ and the pressure $p_{ev,i-1}$ respectively. To calculate the real specific enthalpy $h_{p,r,i}$, the prior defined isentropic efficiency ratio η_s is used [21, 23].

$$h_{p,r,i} = \frac{1}{\eta_s} \cdot (h_{p,is,i} - h_{co,i+1}) + h_{co,i+1} \tag{3.22}$$

The required pumping work $W_{d,i}$ from one condenser stage $i+1$ to i can be derived using the mass flow $\dot{m}_{co,i+1}$ and the mechanical efficiency ratio η_m of the pump. Summing up all pumps between the condenser stages gives the total pumping power $\dot{W}_{d,t}$ required.

$$\begin{aligned} \dot{W}_{d,i} &= \frac{1}{\eta_m} \cdot (h_{p,r,i} - h_{co,i+1}) \cdot \dot{m}_{co,i+1} \\ \dot{W}_{d,t} &= \sum_{i=1}^{n-1} \dot{W}_{d,i} \end{aligned} \tag{3.23}$$

After pumping the distillate $\dot{m}_{co,i+1}$ to the next condenser stage, the steam generated in the evaporator is condensed to $\dot{m}_{co,i}$. This causes an increased mass flow and temperature of the distillate $\dot{m}_{co,i}$ by each condenser stage. Using the mass and entropy balances allow for the exact calculation of the added distillate quantity under the new fluid properties of

the distillate stated in equation 3.24. However, the procedure is similar to the evaporator part described in section 3.4.2.

$$\begin{aligned} \dot{m}_{co,i} &= \dot{m}_{co,i+1} + \dot{m}_{d,i} \\ h_{co,i} &= \frac{(h_{p,r,i} \cdot \dot{m}_{co,i+1}) + (h_{d,i} \cdot \dot{m}_{d,i})}{\dot{m}_{co,i}} \end{aligned} \tag{3.24}$$

So the thermodynamic state of the fluid at the exit of the reactor i is sufficiently defined. For the determination of the total pumping work $W_{d,t}$, the specific entropy $s_{c,i}$ needs to be calculated depending on $h_{co,i}$ and $p_{co,i}$. It is assumed that the pressure level $p_{co,i}$ is above the boiling point in order to avoid any phase change in the condensers (boiling distillate). This has a strong negative influence on the spraying process. It needs to be ensured that the distillate mass flow can easily take up all condensation energy from the generated steam. If the temperatures are set too high, the simulation results with an error. During the operation of the real demonstration plant, the condensation pumps have shown a tendency for cavitation due to the same reasons.

Chapter 4

Energy analysis

The energy analysis presents several calculation results from the modeled system as well as the parameter variation of selected components with respect to power and water cogeneration. As the solar irradiation can be considered as the only fuel of the system, specific meteorological data collected from different sources and own measurements from the selected location are analyzed. Furthermore, the solar field, the thermal storage, the power block and the thermal desalination unit is analyzed in detail. Special focus is given to the cogeneration of power and water.

4.1 Meteorological analysis

Referring to chapter 3.2, the following section evaluates the different data obtained by available sources. The primary focus lays on the comparison of that data and own measurements that have been obtained by the meteorological station in the year 2013. The analysis compares the global horizontal irradiation (GHI), the direct normal irradiation (DNI) and the ambient temperature T_{amb}. Another analysis can be found in [100]. In the following, the three different sources are briefly outlined:

- **Meteonorm:** The software can be considered as the standard meteorological database for solar engineering applications used by several companies and research institutions. The results are stochastically generated using measurements over several years. The software also allows for the calculation of the solar radiation on arbitrarily orientated surfaces. The data set used is from the year 2005 and consists of hourly values. More information can be found on the Meteonorm Handbooks [95] and [96].

- **Solar MED Atlas:** The website compiles GHI and DNI data from observation satellites for the southern and eastern Mediterranean region. The data used reaches back more than 20 years and can provide long-term coverage with validation of available ground-based measurements in the region. The data is mainly provided by SOLEMI and Helioclim-3 to visualize GHI and DNI values. For the spatial resolution, the website compiles monthly values for 1 km which is considered as sufficiently accurate. More information can be found on the website of the SolarMEDAtlas project [94].

- **Meteorological station:** The meteorological station is sufficiently described in chapter 3.2. The data used for the calculations have been measured from March 2013 until February 2014 [31, 100]. The time period is chosen due to the quality and the completeness of the data. The data consist of minutely values which are averaged to one value per hour.

The data from the above stated sources are compared on a monthly basis. The aggregation of the own measurements to hourly values is done by averaging the recorded data per minute. The method gives one hourly value for e.g. 8:00 am, which contains the averaged readings from 8:00 am until 8:59 am. The sun elevation angles γ used for the DNI calculation are simulated on the corresponding half hour, e.g. 8:30 am. This conversion ensures the proper DNI calculation avoiding incorrect data shifts, especially in morning and evening hours. Very small sun elevation angles below $\gamma < 1^\circ$ are set to zero. The procedure is necessary to avoid unrealistically high DNI values at low incident angles (see also $\sin\gamma$ in equation 3.3, section 3.2).

With regard to the quality of the own measurements by the meteorological station, the completeness can be considered as very high. Nevertheless, there is a period of 10 days with missing data in September/October which has been due to a failure of the data logger system[1]. The measurement of the DHI is performed using a shadow ring, which requires a regular adjustment according to the maximal sun elevation angle. Due to the irregular attendance of qualified staff at the meteorological station, this has not been possible over the complete year. However, the inaccurate measurements can be easily identified by comparing to the measured GHI values and are replaced by representative days with proper adjusted shadow ring of the same months. To respect possible deviations, the estimated uncertainty range for the corrected DHI values is assumed with 10%.

[1] Malfunction of the data logger ring storage from Sep, 26, 18:06 until Oct, 6, 15:30. Afterwards, the data have been recorded on an extra SD card

4.1.1 Global horizontal irradiation (GHI)

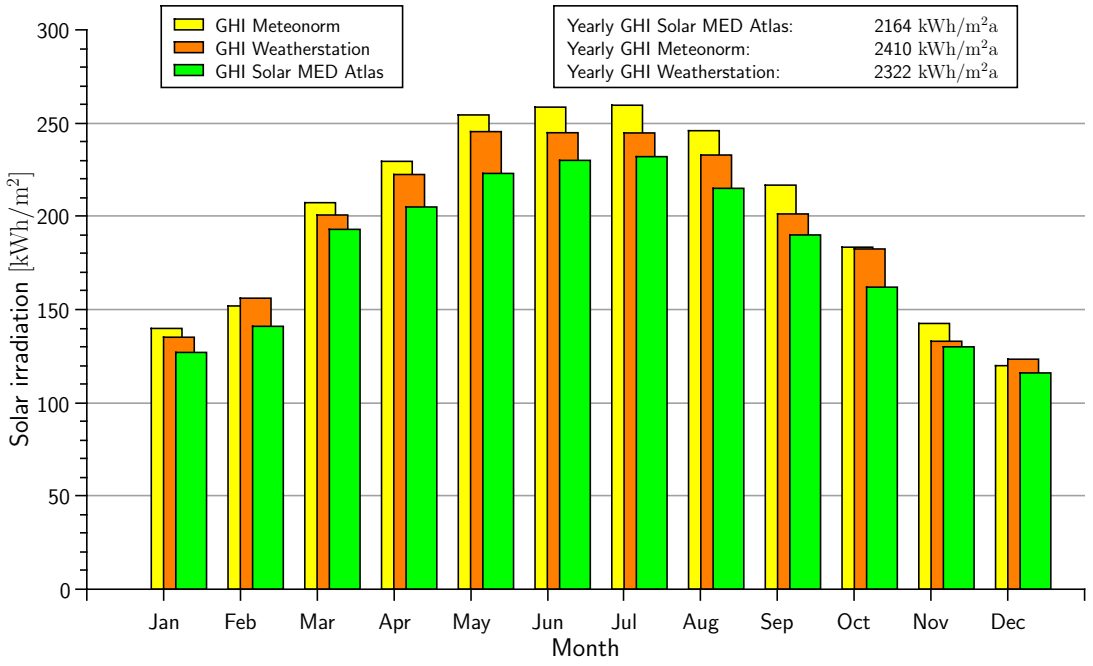

Figure 4.1: *Global horizontal irradiation (GHI)*

Figure 4.1 shows the comparison of the monthly data of the global horizontal irradiation in $\mathrm{kWh/m^2}$. It can be stated that monthly values range generally between 120 $\mathrm{kWh/m^2}$ in winter season and up to 250 $\mathrm{kWh/m^2}$ in summer times. In average, the deviation between the GHI values is about 20% while the values from Meteonorm software [95] gives generally the highest values. The satellite measurements evaluated by Solar MED Atlas [94] tend to underestimate the global irradiation which can be also concluded from the total yearly irradiation of only 2164 $\mathrm{kWh/m^2a}$. The meteorological station shows values in between the software and the satellite measurements except for February 2014 and October 2013. This can be explained by yearly variations and uncertainties in the measurement. A more precise evaluation of the satellite data and the own measurements can be found in appendix A, figures A.5, A.6, A.7, A.8, A.9 and A.10.

4.1.2 Direct normal irradiation (DNI)

The interpretation of the results for the direct normal irradiation is more difficult compared to the interpretation of the GHI results. The reason for that can be seen in the high variations of the data sources up to 35%. All data are summarized in figure 4.2. Generally, the obtained values range around 200 $\mathrm{kWh/m^2}$ in winter season and up to 300 $\mathrm{kWh/m^2}$ in summer times. Furthermore, it can be stated that the diurnal deviation

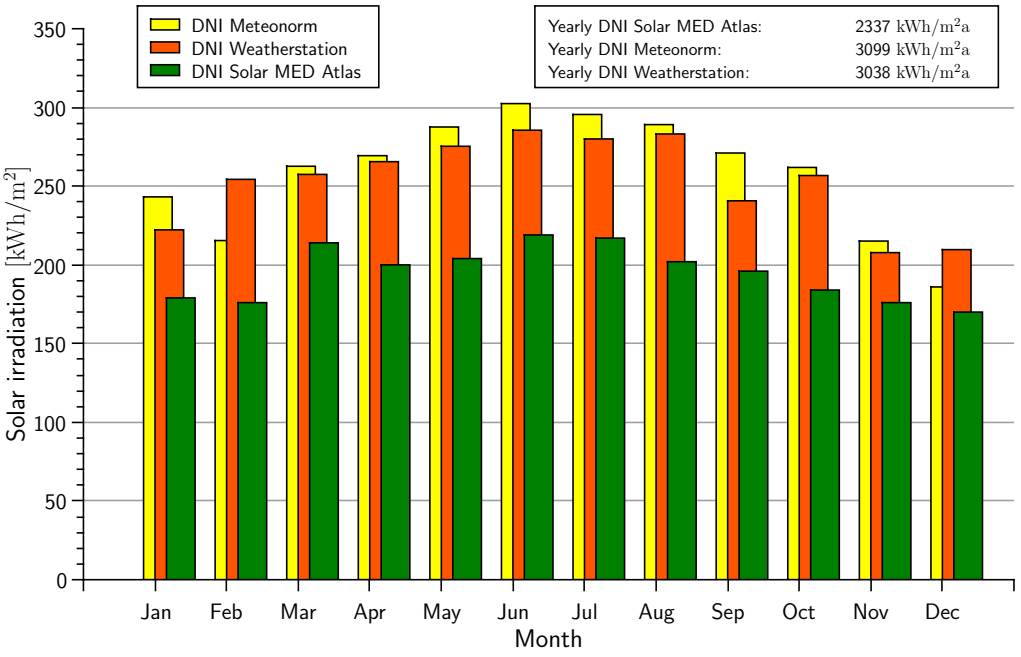

Figure 4.2: *Direct normal irradiation (DNI)*

over the complete year is not strongly pronounced compared to GHI values in figure 4.1. It is assumed that during winter times the shorter daylight and the cloudy sky have the strongest influence. Regional weather phenomena like sand storms have also an influence on this measurement and dampen the irradiation through atmospheric attenuation. The satellite measurements show significantly lower values compared to Meteonorm and own measurements. This can be also concluded from the yearly summarized values ranging from 2337 $\mathrm{kWh/m^2a}$ up to almost 3100 $\mathrm{kWh/m^2a}$. It can be concluded that the satellite measurements show significantly lower values which cannot be verified by the ground measurement. Comparing Meteonorm and the own measurement results, a very good match can be concluded. This applies for all months except for February 2014 and December 2013. With respect to the uncertainty of the own measurements, the yearly DNI values can be estimated reaching up to 3000 $\mathrm{kWh/m^2a}$ in total for this location. More information and visualizations can be found in appendix A, figures A.11, A.12, A.13, A.14, A.15 and A.16.

4.1.3 Temperature

The results of the averaged ambient temperature is visualized in figure 4.3. It shows a clear trend over the year by all data sources. In contrast to the above analyzed data, the own measurements show slightly higher values compared to the other sources. This can be also seen in the averaged yearly values of more than 25 $^{\circ}\mathrm{C}$. Minimum and maximum

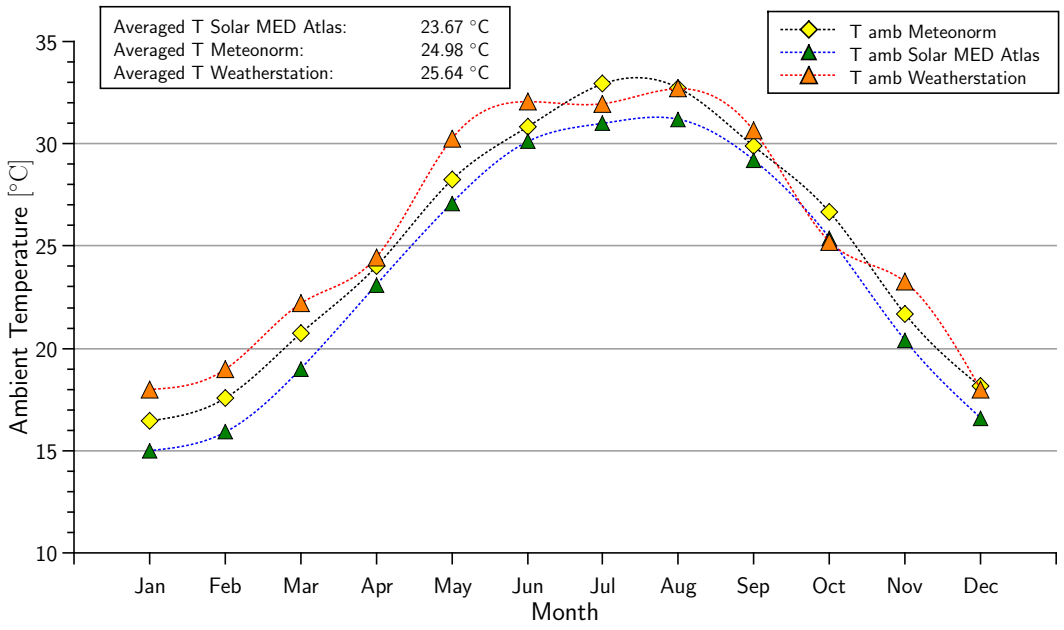

Figure 4.3: *Ambient Temperature* T_{amb}

monthly temperatures average around 15 °C and 33 °C, respectively. During the months January till June, the own measurements lay always above the values of Meteonorm and the satellite data. This deviation could be interpreted as effect of possible correction factors for atmospheric attenuation of the satellite measurements. Furthermore, the data models of Meteonorm can be affected by uncertainties. Generally, ground-based measurements are subject to annual variations. The analysis of the future measurements of the meteorological station would allow for a more reliable statement.

4.2 Solar power plant

The concentrating solar power plant is simulated using the solar libraries of Ebsilon [20] as stated in chapter 3 and section 3.3. The system has a designed thermal heat input Q_{PB} of approximately 35 $\mathrm{MW_{th}}$ supplied by molten salt of the hot storage tank. Due to the spacious dimension of the storage system, the diurnal variations of the irradiation are fully compensated and basically allow for an operation of the system which is independent form the solar radiation. The live steam parameter T_s reaches up to 567 °C and p_s 135 bar. The steam mass flow $\dot{m}_s$ is set to 50 $\mathrm{t/h}$ resulting in an electrical power generation P_{el} of 12.4 - 14.6 $\mathrm{MW_{el}}$ through expansion in the five stage steam turbine system. The electrical power generation mainly depends on the condensation pressure p_{co} in HEX1 which is variable from 0.1 - 0.8 bar. As a result, the condensation temperatures T_c in the power plant condenser (HEX1) range from 41.5 - 93.5 °C.

The condensing temperature and pressure are determined by the mass flow and by the possible heat transfer to the desalination unit. Higher pressures result in increased heat transfer but lower the electric power generation. In any cases, the complete condensation of the steam needs to be ensured under all operating conditions.

To improve the heat extraction for the desalination unit, an additional sub-cooler is modeled, which cools the CSP feed water. In a real system, this heat exchanger would be designed as one condenser allowing for the needed sub-cooling of the condensate. This results in a total heat transfer Q_{co} to the desalination unit between 20.2 - 22.6 $\mathrm{MW_{th}}$. In the following, the condenser is treated as one component.

Due to the flexibility of the available heat for the desalination unit, the examination of two limiting cases is required in order to analyze the cogeneration of power and water. The different operating points have a great effect to the CSP condenser (HEX1) which results in variations of the power generation and the electrical efficiency. These limiting cases also determine the operational system boundaries:

- **Case 1, maximal water production**: This operating point aims to maximize the condensation heat and temperature in the CSP condenser (HEX1) to supply as much thermal energy as possible to the desalination system. The other parameters are adjusted in order to maximize the water production.
- **Case 2, maximal power generation**: In this case, the desalination system is used as a cooling device for the CSP plant. It requires that the system parameters allow for the lowest possible condensation temperatures. In consequence of that, the power generation in the CSP plant is maximized.

The parameters for each case are summarized in table 4.1. In between these two operating cases, several operating points are possible which are subject to the following analysis.

The power plant condenser (HEX1) can be understood as an interface between power generation and the desalination unit. The desalination system is supplied by the condensation heat of the steam in the power block Q_{co}. All operating points vary in terms of power and heat generation. These points are plotted in figure 4.4 including the boundary cases. It needs to be mentioned that the heat exchanger requirements of HEX1 for the case 2 are drastically increased. This results from the small temperature differences, which require very low ΔT_m at high heat transfer rates and large heat exchange areas. Before the analysis of the cogeneration of power and water, the desalination unit needs to be modeled.

Parameter	Symbol	Case 1: max. water	Case 2: max. power	Unit
Solar thermal heat supplied	Q_{PB}	35.6	35.6	$\mathrm{MW_{th}}$
Live steam: temperature	T_s	567	567	°C
Live steam: pressure	p_s	135	135	bar
Live steam: massflow	m_s	50.1	50.1	t/h
Condenser: temperature	T_{co}	93.5	41.5	°C
Condenser: pressure	p_{co}	0.8	0.1	bar
Condenser: available heat	Q_{co}	22.6	20.2	$\mathrm{MW_{th}}$
Generated electricity	P_{el}	12.4	14.6	$\mathrm{MW_{el}}$
Power block efficiency	η_{el}	34.9	41.7	%

Table 4.1: *Operating cases for CSP plant*

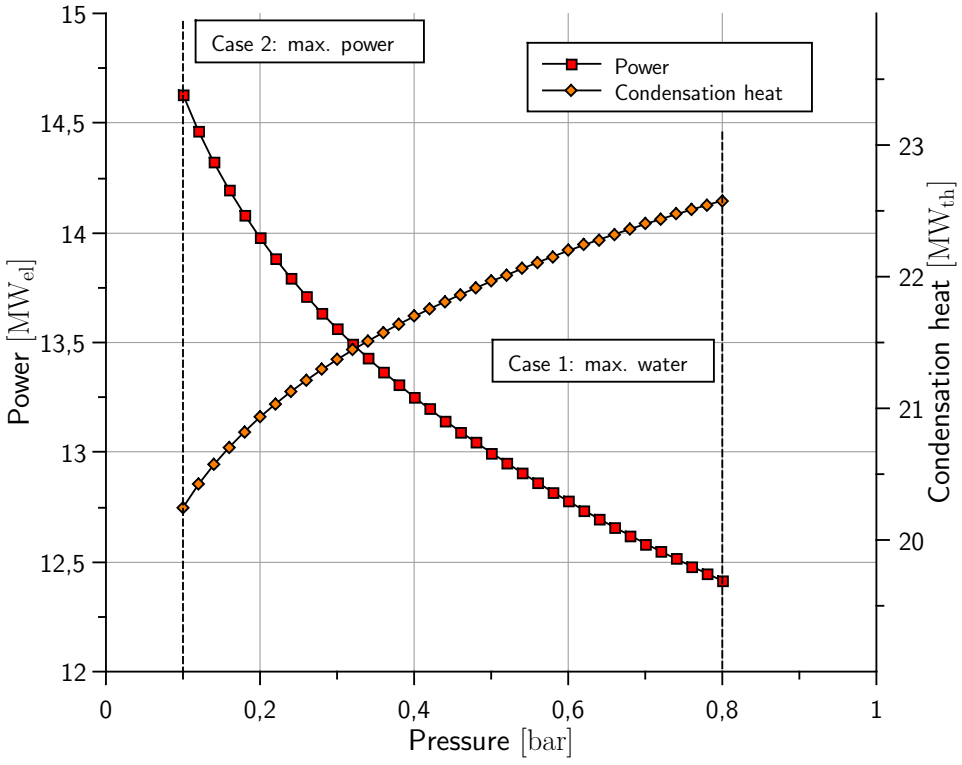

Figure 4.4: *CSP power output and resulting condensation heat*

4.3 Desalination unit

The low-temperature desalination unit shows a special behavior which has been examined on the demonstration plant. The results of the simulation point out some additional requirements when operating this plant in cogeneration with a steam cycle. The most important initial parameters are summarized in table 4.2 for both cases and are dis-

cussed in the following chapters by parameter variation. It should be mentioned that the temperature difference ΔT_m in HEX1, 2 and 4 is smaller compared to HEX3. The reason is that HEX3 acts as a cooling cycle using directly seawater. For the simulated cases, the cooling mass flow is set to 2500 $\mathrm{m^3/h}$ to ensure sufficient heat removal in the desalination system. In this analysis, the whole seawater intake and cooling in HEX3 has not been optimized.

Parameter	Symbol	Case 1: max. water	Case 2: max. power	Unit
Heat input HEX1	Q_{co}	22.6	20.2	$\mathrm{MW_{th}}$
Temperature, hot in	$T_{h,i}$	79.1	45.5	°C
Temperature, cool in	$T_{c,i}$	30.1	30.1	°C
Temperature difference, system	ΔT_{sys}	49	15.4	K
Temperature difference, reactor	ΔT_{ves}	0.5	0.5	K
Evaporator mass flow	$\dot{m}_{ev,i}$	1500	3500	$\mathrm{m^3/h}$
Condenser mass flow	$\dot{m}_{co,i}$	1365	3185	$\mathrm{m^3/h}$
Stages	n_d	4	4	-
Efficiency ratio, isentropic	$\eta_{d,is}$	0.85	0.85	-
Efficiency ratio, electric	$\eta_{d,el}$	0.9	0.9	-
Salt content	b	43	43	$\mathrm{g/l}$ TDS
Intake and cooling temperature	T_{cool}	25	25	°C
Intake and cooling mass flow	$\dot{m}_{cool}$	2500	2500	$\mathrm{m^3/h}$

Table 4.2: *Operating cases for desalination unit*

The efficiency ratios of the pumps and the motors are taken from the literature. The salt content corresponds to the measured sea water salinity of the selected location in the Red Sea, Egypt, and is set to 43 $\mathrm{g/kg\ TDS}$ [33]. All simulations have been carried out for a desalination unit with four stages.

The heat input depends directly on the condensation pressure of the steam turbine and is therfore subject to variations (compare also to figure 4.4). The temperatures hot-in $T_{h,i}$ and cool-in $T_{c,i}$ describe the usable system gradient ΔT_{sys} within the desalination unit. For the right dimensioning of the system, the manufacturer recommends to design a temperature difference ΔT_{stg} of 10 K for each stage [12]. The temperature difference ΔT_{ves} in the reactor vessels depends on the operation condition of the plant and can increase up to 3 K.

The temperature difference ΔT_{ves} influences especially the circulating mass flows in the evaporator and condensing reactors. First, the spray system needs sufficient volume

flow through the perforated sheets to ensure the formation of droplets acting as heat exchangers. Secondly, experiments on the demonstration plant have shown that it is favorably to set the condenser mass flow lower compared to the evaporator mass flow in order to support the condensation process. One possible explanation is the strong decreasing specific volume of the steam during the condensation process (see also section 3.4).

4.3.1 Case 1: maximized water production

The simulation results of the four stage unit are visualized in figure 4.5. This figure shows all temperatures, pressures and steam mass flows by each stage. After comparison of the manufacturer data [12, 75] and measured data from the demonstration plant [15], it can be stated that the simulation gives satisfactory accordance with the experimental data of this desalination process.

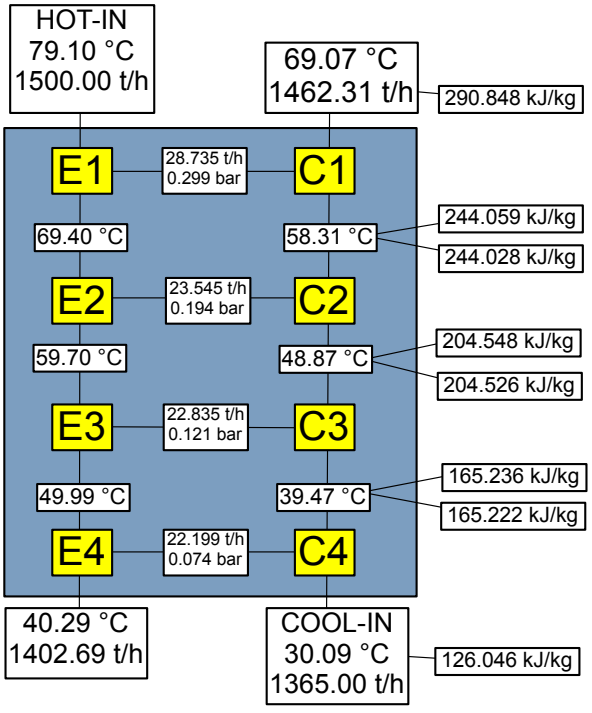

Figure 4.5: *Case 1: LTD simulation results for 4 stages, maximized water production*

Referring to figure 4.5, it can be observed that the salt water temperature in the evaporator part is successively decreasing from E1 to E4 of around 10 K per stage. This results in a steam generation of approximately 25 $\mathrm{t/h}$ for each stage while the steam generation in the E1 is significantly raised compared to E4. The averaged pressure is almost equal in both reactors. The steam tends to move directly to the colder side (condenser) caus-

ing the phase change on the sprayed distillate. This is also accompanied by a strongly decreased volume (water/steam) which ensures maintaining the pressure environment.

4.3.2 Case 2: maximized power generation

For maximized power generation, the process parameters for the desalination unit are completely different. The complete results are visualized in figure 4.6. The operating conditions of this case are only feasible due to the heat exchange through droplets, allowing for very high heat transfer rates and thus an increased performance. The total system temperature difference calculates to 15 K, which gives every stage only approx. 3 K of usable ΔT_{stg}. This also results in a strongly lowered steam generation per stage of approx. 16 $\mathrm{t/h}$. In contrast to case 1 and figure 4.5 it is remarkable, that the steam generation is almost equally distributed over all stages.

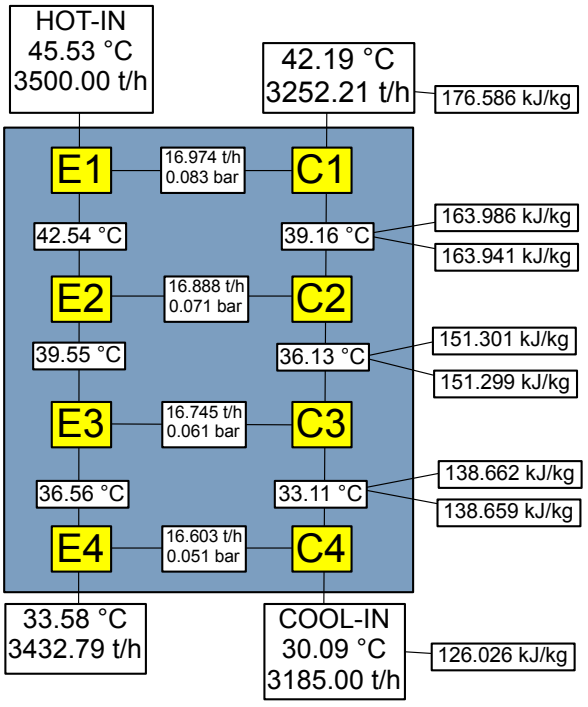

Figure 4.6: *Case 2: LTD simulation results for 4 stages, maximized power*

Furthermore, it can be stated that the mass flows in the evaporator and condenser are more than double compared to case 1. The increased mass flows also have an influence on the steam generation within the stages. The steam cycle requires large mass flows to allow for complete condensation in HEX1. In consequence of that, the specific power consumption is strongly increased, which is analyzed in the next sections. Regarding the ΔT_m in HEX1, it can be considered as very small for real applications. It drops below

5 K with condensing pressures lower than 0.2 bar in HEX1. Due to large heat transfer areas required, the design of a heat exchanger can be seen as critical.

4.4 Results of the cogeneration system

The performance of the cogeneration plant can be now analyzed regarding the following parameters: electrical power generation in the CSP plant, distillate production, heat input and specific power consumption for a four stage system [21,22]. It can be expected that the main influences are the condensing steam pressure in HEX1 of the CSP plant, the circulation mass flow of the desalination unit and the seawater salinity. In order to evaluate the efficiency of this cogeneration plant, a new parameter is introduced to assess the power and water performance ratio (PR). Equation 4.1 shows the respective calculation:

$$PR = \frac{\dot{m}_{co}}{\dot{m}_d} = \frac{1}{GOR} \tag{4.1}$$

The PR can be understood as the reciprocal value of the gained output ratio (GOR) in equation 4.1. Nevertheless, the GOR is not used for the system evaluation because it does not gives accurate information about the unit efficiency and supplemental losses [9]. Generally, the PR like defined sets the CSP steam providing the desalination heat input into relation with the produced distillate. For the evaporation of 1 kg water are needed 2326 $\mathrm{kJ/kg}$ steam enthalpy [9]. The PR directly depends on the number of stages, so the ratio can be increased by adding more stages. For the discussed cases, all calculations are carried out for $n_d = 4$ stages. The results show that the low number of stages has a positive influence on the cogeneration system and gives more flexibility in power and water generation.

Figure 4.7 visualizes this correlation between electrical efficiency in the power block and the performance ratio of the desalination unit. The PR reaches up to 3 with sufficient heat supply. At condensation pressures below 0.2 bar, the performance ration drops to values close to 2.

Table 4.3 summarizes all results obtained from the simulations. For case 1, a power generation P_{el} of 12.4 $\mathrm{MW_{el}}$ and a water production $\dot{m}_d$ of 2335.2 $\mathrm{m^3/d}$ are simulated. The specific heat and power consumption gives a possibility to compare this system to conventional MED and MSF thermal desalination plants. But the availability of data for such small scaled systems is generally low. The specific heat consumption is quite

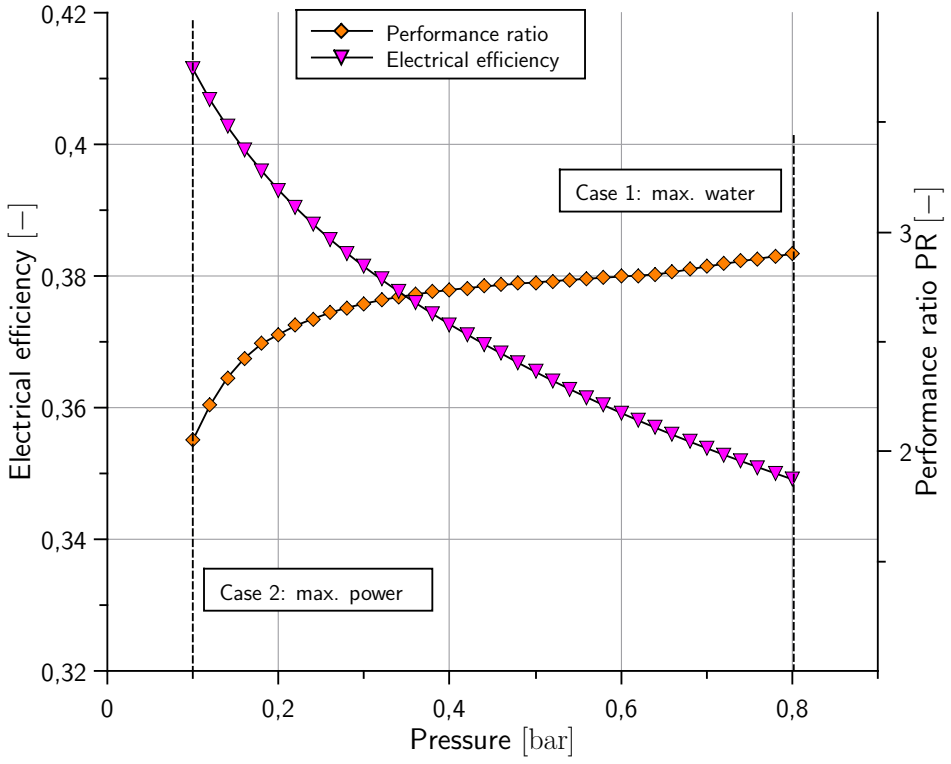

Figure 4.7: *Electrical efficiency and performance ratio*

large compared to literature values. The reason for the high value is the small number of stages which limits the water production.

Concerning the brine, the simulation results show an increased temperature and salinity for case 1. The raised values can be explained by the higher system temperatures and consequently the higher water production. The technical salinity limit of the applied technology is set by salt precipitation of the brine, which might cause clogging of the spray systems. The clogging has to be prevented because the fluids in the desalination unit should be maintained in liquid state to allow for passing through the metal sheets and the circulation pumps. To avoid this problem, more intake seawater can lower the salinity in the evaporators.

For case 2, a power generation P_{el} of 14.6 $\mathrm{MW_{el}}$ and a water production $\dot{m}_d$ of 1612.8 $\mathrm{m^3/d}$ are simulated, respectively. When the power output and the efficiency of the CSP plant raises, the water production falls below 2000 $\mathrm{m^3/d}$ and the electricity consumption of the desalination unit increases. All temperature levels are generally lower. The requirements for HEX1 or the CSP condenser are increased due to the low ΔT_m and larger heat exchange areas. It can be concluded that this design requires more investment costs. The following sensitivity analysis examines certain specific parameters to understand the system behavior and its limits.

Parameter	Symbol	Case 1: max. water	Case 2: max. power	Unit
CSP Heat input HEX1	Q_c	22.6	20.2	$\mathrm{MW_{th}}$
CSP Power generation	P_{el}	12.4	14.6	$\mathrm{MW_{el}}$
CSP Steam temperature	T_{co}	93.5	41.5	°C
CSP Condenser pressure	p_{co}	0.8	0.1	bar
CSP Efficiency, electric	η_{el}	34.9	41.7	%
Distillate mass flow, per hour	$\dot{m}_d$	97.3	67.2	$\mathrm{m^3/h}$
Distillate mass flow, per day	$\dot{m}_d$	2335.2	1612.8	$\mathrm{m^3/d}$
Total pumping power, desalination	$\dot{W}_{p,t}$	72.4	138.3	$\mathrm{kW_{el}}$
Specific power consumption	$W_{p,s}$	0.74	2.1	$\mathrm{kWh_{el}/m^3}$
Specific heat input	$Q_{p,s}$	230	301	$\mathrm{kWh_{th}/m^3}$
Performance ratio (PR)	PR	2.84	2.05	-
Brine, temperature	T_b	40.4	33.6	°C
Brine, mass flow	$\dot{m}_b$	152.7	182.8	$\mathrm{m^3/h}$
Brine, salinity	b_b	70.4	58.8	g/kg TDS

Table 4.3: *Results for cogeneration of power and water*

4.4.1 Condensation pressure

As discussed in section 4.2 and figure 4.4, the CSP condensation pressure p_{co} is the only influence on the available heat in HEX1. An increased heat supply should result in an increased water production. Considering that the heat is supplied by the CSP steam condenser, the complete condensation needs to be ensured under all operating conditions. Setting the evaporator mass flow $\dot{m}_{ev}$ to sufficient high values can ensure the complete steam condensation, but is not favorable for the distillate output.

Figure 4.8 shows the effect of optimized mass flows to the distillate production for $n = 4$ stages. In order to increase the distillate output, the circulating seawater mass flow in the evaporator should be optimized. As the available temperature differences vary for each condensation pressure, the mass flow needs to be increased with decreasing heat availability (resp. lower condensation pressure) [21]. If the evaporator mass flow $\dot{m}_{ev}$ is set to the lowest possible value limited by the complete steam condensation, more heat can be supplied to the desalination system. This results in a maximized water production.

Figure 4.8 also shows the optimized curve. All further calculations base on optimized mass flows to always allow for maximizing the distillate production. As previously mentioned, this requires a special design of the heat exchanger to allow for lowered con-

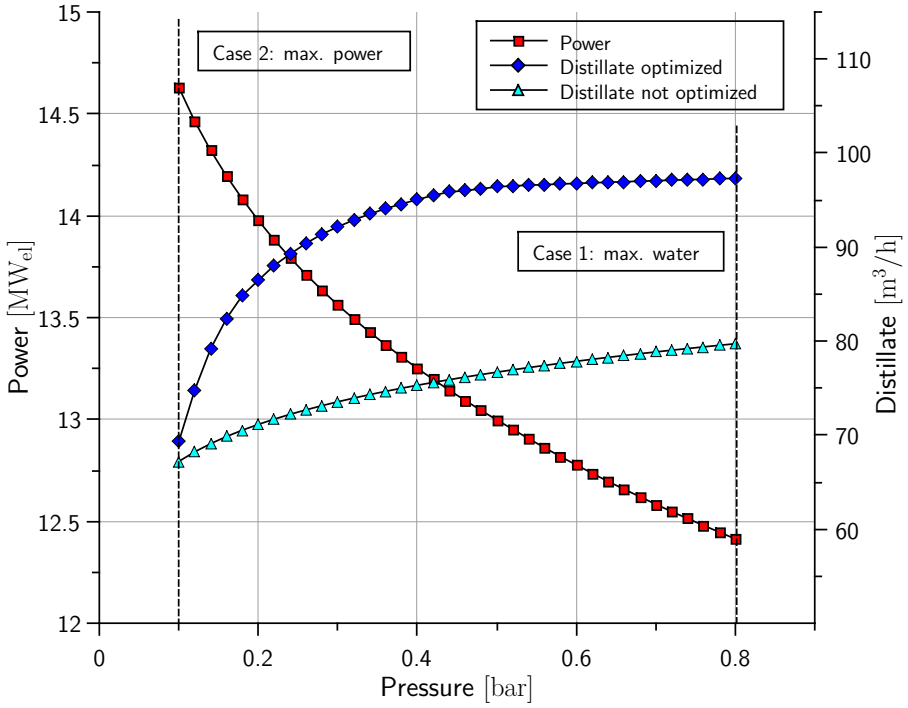

Figure 4.8: *Cogeneration of power and water*

densation pressures of 0.3 bar. The heat exchanger areas needs to be substantially increased.

4.4.2 Specific electricity consumption

The specific electricity consumption $\dot{W}_{p,s}$ is mainly influenced by the pumping power for the circulation mass flows in the evaporator and condenser. Using the optimized mass flow discussed in section 4.4.1 maximizes the distillate production $\dot{m}_d$ and significantly lowers the electricity consumption.

Figure 4.9 illustrates this effect of minimized circulation mass flows by ensuring a complete heat removal in HEX1 for the steam condensation in the CSP system. The CSP condensing pressure p_{co} in HEX1 is varied from 0.1 to 0.8 bar with adapted mass flows to the respective temperature levels.

Furthermore, figure 4.9 shows a significant increase in the distillate production due to decreased circulation mass flows and higher condensation pressures. This effect could also be proven by experiments using the demonstration plant. One possible explanation could be the higher retention time due to the decreased mass flow which causes an increased steam generation in the evaporators. In addition to that, decreased mass flows

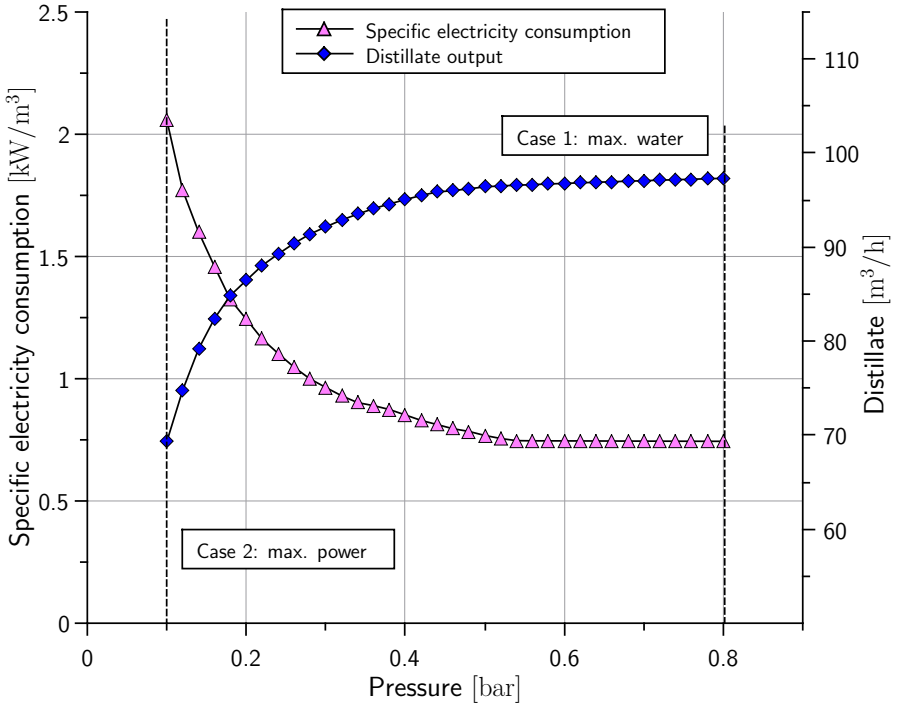

Figure 4.9: *Specific electricity consumption and distillate output*

result in higher top brine temperatures and higher distillate production with decreasing specific energy consumption (compare also to table 4.3).

The specific power consumption and the distillate production are almost constant at pressures above 0.5 bar. On the other hand, the opposite conclusion implies that for lowered condensation pressures a higher mass flow is necessary which increases the electricity consumption. It can be concluded that the optimization of the mass flows has a major impact on the specific energy consumption and distillate production [21, 23].

4.4.3 Number of desalination stages

More stages in the desalination unit increases the distillate production due to the reuse of heat in the stages. Here, the number of desalination stages is varied from 2 to 14. Both design cases calculate with $n = 4$ stages to keep flexibility in condensation pressures and power generation. The necessary mass flows through the evaporators ensure the complete steam condensation. As the required mass flows increase with the number of desalination stages, the temperature gradients ΔT_{stg} in each stage get smaller. In order to allow for the examination of the influence, the mass flows have been keep constant at values allowing for complete condensation. The condensation pressure p_{co} is fixed to 0.6 bar to ensure a sufficient heat supply.

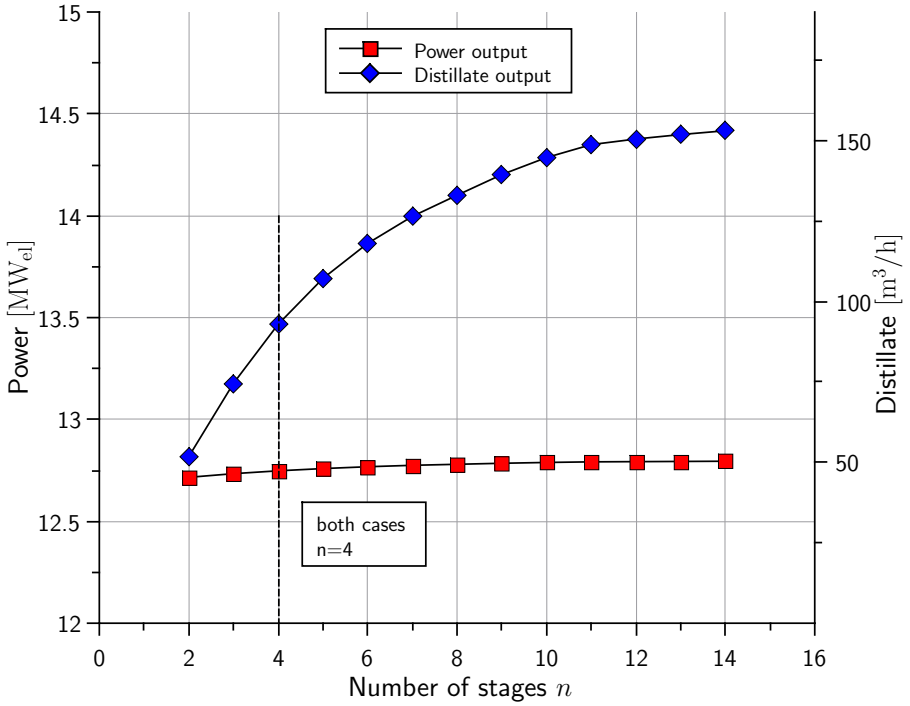

Figure 4.10: *Number of stages and CSP power generation*

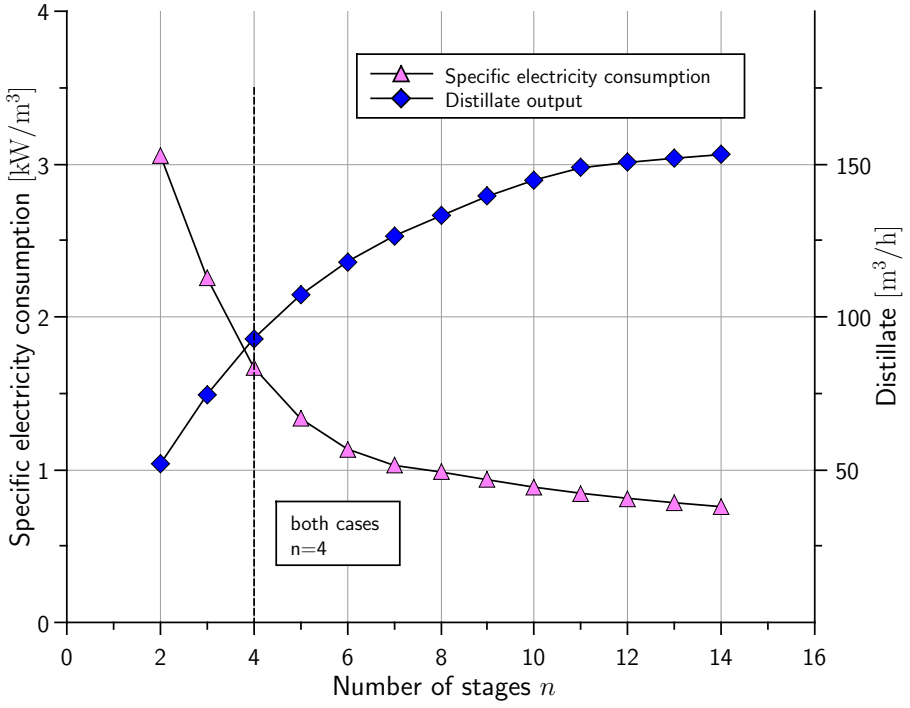

Figure 4.11: *Number of stages and specific electricity consumption*

In figure 4.10, the influence of the number of stages and the power generation P_{el} in the CSP plant are examined. It can be stated that the power generation is almost not influenced with increasing stages. Over the complete examined range, the power

output varies only in the range of 40 $\mathrm{kW_{el}}$. The reason for that can be seen in the right adjustment of the mass flow, which allows for steady conditions in the power plant condenser (HEX1).

Figure 4.11 also visualizes the increasing distillate production with the number of stages, but in comparison to the specific electricity consumption of the desalination unit. It is not necessary to double the circulation mass flows for each additional stage which is a result of the process design. This mechanism causes the strongly decreasing tendency of the curve for the specific electricity consumption. However, the lowered distillate production for 2 stages provides for high specific consumption due to the requirement of minimal mass flows for steam condensation. In consequence of the discussed figures 4.10 and 4.11, it is concluded that the optimal compromise between specific energy consumption, investment costs and distillate production is reached within 10 stages.

4.4.4 Seawater salinity

Figure 4.12 shows the influence of the intake seawater salinity b_b with effects to distillate production and specific electricity consumption. The results are simulated for salinity values from 30 to 50 $\mathrm{g/kg\ TDS}$ for $n_d = 4$ which corresponds 30,000 to 50,000 $\mathrm{ppm\ TDS}$. The complete desalination unit is not sensitive to high concentration of salt in the high feed water. This generally applies to all thermal desalination units compared to membrane systems like RO.

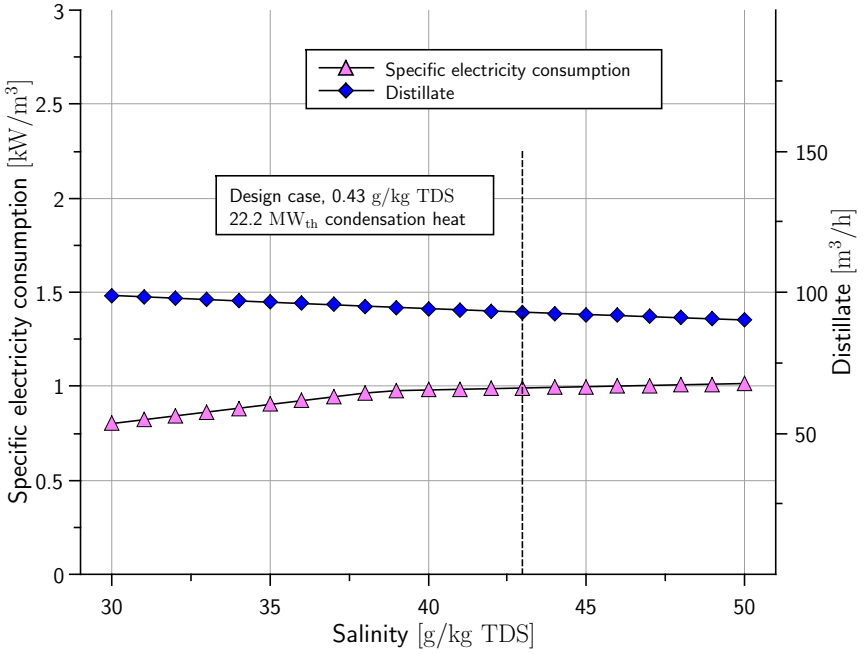

Figure 4.12: *Salinity and specific electricity consumption*

However, figure 4.12 also shows that the specific power consumption is only increasing in a small range while the distillate production decreases with increasing feed water salt content. The reason can be found in the changed fluid properties of salt/water mixtures which is called boiling point elevation (see also chapter 2, section 2.4.1 and figure 2.13). This effect is well understood and has been expected. The consequence is a small shift to higher evaporation temperatures on high concentrated solutions at constant pressures. It consequently decreases the distillate production.

4.4.5 Limitations of the system

As conclusion from the results described in the previous sections, the question arises to investigate the system limits in power and water production with this cogeneration system. The easiest way to obtain more distillate is the increase of the number of stages and to design for the lowest possible condensation pressures. This condition maximizes the power generation but limits the available heat for the desalination unit. Figure 4.13 visualizes the cogeneration for $n = 2$ to $n = 12$ stages.

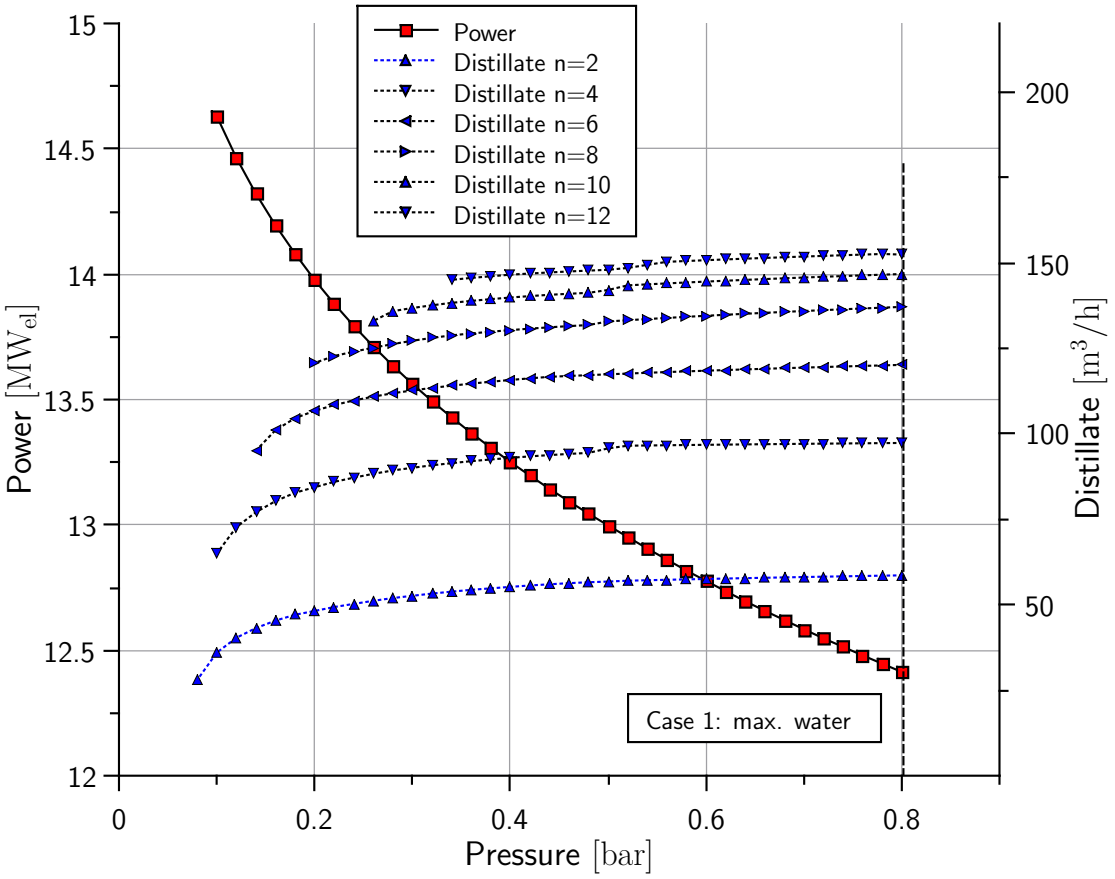

Figure 4.13: *Cogeneration of power and water with different stages*

It can be recognized that the minimal possible condensation pressures are increasing with more desalination stages. One explanation could be that more desalination stages with constant thermal heat input decrease the possible steam generation in each stage. As a result, the distillate production is not doubled for each additional stage. In addition to that, the available ΔT in each evaporator is also decreased which lowers the total system temperature gradient ΔT_{sys} of the desalination unit. As higher the number of stages, as more ΔT_{sys} is favorable in order to maximize the distillate production. The heat exchanger requirements on the condenser (HEX1) also increase in terms of needed area and small ΔT_m in order to allow for an increased condenser mass flow. Generally spoken, the operational flexibility of this specific system configuration with high number of stages is constrained by the effectiveness of the heat exchangers and available temperature gradient.

4.5 Discussion

The simulation results show the broad variability of the cogeneration system in terms of electricity generation and water production. Especially the discussed case 2 in section 4.3.2, maximized power generation, cannot be realized with a conventional MED unit due to very small temperature differences between the reactor stages. Despite the electricity consumption is strongly increased in case 2, it is a feasible operation point in order to maximize the power generation. The salt concentration has only a small influence on the thermodynamic behavior of the system and the effects on the distillate production are fairly low. The strongest influence on the distillate production has the number of desalination stages which also limits the operational flexibility of the power plant due to the temperature gradients within the desalination stages.

Due to the novelty of the plant design, the low-temperature desalination has still much room for process optimizations and a lowered electricity consumption. The simulation described in sections 3.4 and analyzed in 4.3 bases on the measuring results obtained by the demonstration plant [12, 15, 75]. During the experiments it has turned out, that there are many possibilities to optimize the whole system with respect to lower the electricity consumption and increased distillate production. The optimizations do not concern the principal design itself which has been explained in the previous sections. Some modifications should be mentioned here briefly in order to give an outlook to the future potential of this technology [83]:

- *Electricity consumption:* The positioning of the single reactor vessels could be improved in order to lower the required pumping power. One reactor vessel contains the evaporating and the condensing reactors. Putting two vessels above each other could use the geodetic height to allow for natural pressure to direct the water into the next stage. The new alignment has a positive influence on the needed pumping power.

- *Lowered temperature:* For the operation in cogeneration it is favorable to supply the power plant condenser HEX1 with the lowest possible temperature. The lowest temperature of the evaporator mass flow results after the salt water has passed through all stages (see also figures 4.5 and 4.6). The analyzed design recovers the heat of the concentrated evaporator solution in HEX2 by the distillate mass flow. In order to maximize the cooling for the power plant condenser (HEX1) and thus realize lower condensation pressures as well as higher electricity generation, the process design could be changed. One approach would be the separation of the mass flows after passing through all evaporators, while one half is bypassed directly to HEX1 while the other half follows the process scheme according to figure 3.6.

The implementation in the developed simulation can be considered as subject to further research. The results need to be verified by realized plants in order to assess the desalination performance depending on thermal and electrical energy inputs.

Chapter 5

Exergy analysis

The exergy analysis of the evaluated system shows the potential of enhancing the efficiency of the CSP plant in combination with the low-temperature desalination. For a deeper evaluation of the cogeneration system, the exergetic analysis is applied in order to estimate the thermodynamic inefficiencies within the system. In the following chapters, several design parameters are examined regarding their influence to the overall efficiency of the model plant. As discussed in the previous chapter the condensing pressure in the CSP plant, the seawater salt content, the number of stages and the cooling temperature of the desalination unit have the biggest effects on the power and water production. Furthermore, highest amount of exergy destruction is considered to arise in the solar collector. After the exergetic balancing of each component, the exergetic resources and the exergetic efficiency is calculated for all plant components. The results show the potentials for further optimization of the cogeneration system. The complete analysis has been developed based on [101].

5.1 Methodology and assumptions

In addition to the energy analysis provided in chapter 4, the exergetic analysis bases on the first and second law of thermodynamics [24, 102]. The exergy is the part of the energy which can be used theoretically if the system is brought into equilibrium with the ambient conditions [103]. The exergetic analysis is especially useful to analyze processes at different ambient conditions which can be found in arid or desert regions. Therefore it is important to exactly define the ambient conditions and the system boundaries.

The total exergy of a system is composed of the following four different components which are the physical exergy E^{PH}, chemical exergy E^{CH}, kinetic exergy E^{KN} and potential exergy E^{PT} [24]. The total exergy of a system calculates like follows:

$$E_{sys} = E^{PH} + E^{CH} + E^{KN} + E^{PT} \tag{5.1}$$

5.1.1 Methodology

All thermodynamic analysis base on the conservation laws of mass and energy which cannot be created or destroyed. The influences of irreversibilities destroy exergy on a component level and become zero only for reversible processes. This difference to a real processes is expressed by the exergy destruction term E_D. Exergy losses on system level are material or energy streams exiting the system boundaries and are expressed with E_L. Exergy losses are only relevant on system level [24, 101, 102].

The correlation is expressed in an exergy balance for open systems [24, 101–103] defining the rate of exergy change:

$$\frac{E_{cv}}{d\tau} = \sum_j (1 - \frac{T_0}{T_j})\dot{Q}_j + (\dot{W}_{cv} + p_0 \frac{dV_{cv}}{d\tau}) + \sum_i \dot{E}_i - \sum_e \dot{E}_e - \dot{E}_D \tag{5.2}$$

However, focusing on an open system, material and energy streams can be transferred by work or heat across the system boundary. This involves several inlet and outlet streams of the control volume which are visualized in figure 5.1.

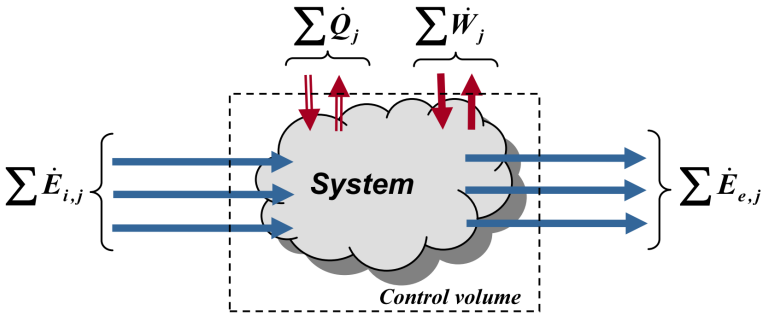

Figure 5.1: *Schematics for an exergy balance of an open system [24]*

The indices i and j describe the total exergy transfer rates for inlet and outlet streams. Assuming steady state conditions, the terms $\frac{E_{cv}}{d\tau}$ and $\frac{dV_{cv}}{d\tau}$ turn to zero. This simplifies the equation 5.2 significantly. Considering the component level, the exergy balance for each component as well as for the overall system is written in the terms of exergy of fuel E_F and exergy of product E_P instead of ingoing and outgoing streams [24, 103]. The exact definition of the exergy of the fuel and the product are essential to evaluate the performance of a system. However, all exergetic resources and incoming streams supplied to the component are considered as exergy of the fuel. The exergy of product

expresses the desired resulting streams which are achieved by the component. This can be also applied to the system level. So the balancing includes all exergy increasing stream between inlet and outlet. Regarding the total system, the exergy losses E_L need to be calculated.

For an energy conversion system and a single process component, the exergy balances can be expressed like follows [24, 102, 103]. The balance can be applied to the overall system with the index tot or to a single component using the index k, as follows:

- For the overall energy conversion system:

$$E_{F,tot} = E_{P,tot} + E_{D,tot} + E_{L,tot} \tag{5.3}$$

- For the k-th component of the energy conversion system:

$$E_{F,k} = E_{P,k} + E_{D,k} \tag{5.4}$$

5.1.2 Assumptions

In order to perform the exergetic analyis, some assumptions are made to simplify the calculations. The potential and kinetic exergies are neglected because there is only a negligible influence expected. However, for the exergetic analysis, the physical and chemical exergies can be considered as key variables.

In general, the sum of physical and chemical exergies are considered for the evaluation of the power generation and desalination process. In this thesis, the effects of the chemical exergy is neglected because it is assumed that it has only a minor effect on the obtained simulation results. This is justified by the following reasons [101]:

- Absence of any combustion processes in the power plant and the solar field.
- The desalination process separates the saltwater without chemical reactions and therefore without release of heat.
- In the examined range of salt concentrations, the chemical exergy from mixing and separation of saltwater is very low.
- The temperature and concentration of cooling water and the brine is not further used for any energy conversion process.

5.1.3 Exergetic efficiency

The exergetic efficiency ϵ is used for the evaluation of the exergetic performance. The efficiency is a dimensionless criteria that can be used to compare single components which are operating under the same process conditions or to compare the efficiency on a system level. It can be applied to a single component or to the overall system. The exergetic efficiency ϵ can also be described as the ratio between product and fuel and is defined as follows [24, 102, 103]:

- For the overall system:

$$\epsilon_{tot} = \frac{\dot{E}_{P,tot}}{\dot{E}_{F,tot}} = 1 - \frac{\dot{E}_{D,tot} + \dot{E}_{L,tot}}{\dot{E}_{F,tot}} \tag{5.5}$$

- For the k-th component of the energy conversion system:

$$\epsilon_k = \frac{\dot{E}_{P,k}}{\dot{E}_{F,k}} = 1 - \frac{\dot{E}_{D,k}}{\dot{E}_{F,k}} \tag{5.6}$$

The process evaluation is completed by considering two other exergetic variables: ratios of the exergy destruction on component k and on system level tot. The calculations are shown in equation 5.7:

$$\begin{aligned} y_{D,k} &= \frac{\dot{E}_{D,k}}{\dot{E}_{F,tot}} \\ y*_{D,k} &= \frac{\dot{E}_{D,k}}{\dot{E}_{D,tot}} \end{aligned} \tag{5.7}$$

The analysis is separated in three parts considering the solar field, the power block and the desalination unit. The values for each component obtained by the simulation are used to calculate exergy destruction, exergetic efficiencies and exergy losses [102, 103]. The exergy losses are streams exiting the system boundaries to the environment and they are not converted into other energy forms. The calculation the ratios of exergy destruction require the definition of the used exergy of the fuel $\dot{E}_{F,tot}$ which is performed for the solar collector and the desalination unit in the following sections.

5.2 Exergy of the solar collector

The solar collector can be considered as central component of the modeled system because the irradiation of the sun represents the fuel of the whole system. As a consequence,

a detailed description of the sun convertible irradiation is needed. In contrast to fossil fuel powered systems, the radiation of the sun and the resulting direct normal irradiation (DNI) can be understood as exergy carrier. Assuming the surface temperature of the sun T_{st} and the ambient temperature T_{amb}, the exergy of the sun irradiation $\dot{E}_s$ can be described as follows [104–106]:

$$\dot{E}_s = A_{col} \cdot I_{DNI} \cdot 1 + \frac{1}{3} \cdot \left(\frac{T_{amb}}{T_{st}}\right)^4 - \frac{4}{3} \cdot \left(\frac{T_{amb}}{T_{st}}\right) = A_{col} \cdot I_{DNI} \cdot \eta_p \tag{5.8}$$

For the calculation of $\dot{E}_s$ the following input variables need to be taken into account: the gross collector area A_{col} in m^2 and the direct normal irradiation I_{DNI} in $\mathrm{W/m^2}$. In addition, the temperature of the sun surface T_{st} is given with 5762 K [105, 106]. Equation 5.8 is derived from the first and second law of thermodynamics with influences from the entropy of the black body radiation by integration. The literature gives several methods for the calculation [25, 104]. The reason for this are different approaches to calculate firstly differences in the description of the black body radiation of the sun and secondly to which extend the diffuse radiation needs to be considered. To describe the influence of the back body radiation on the exergy of the sun radiation, the method used in [25, 106] is applied. However, in a next step equation 5.8 is solved to the exergy of the primary radiation η_p [25, 106]:

$$\eta_p = \frac{\dot{E}_s}{A_{col} \cdot I_{DNI}} = 1 + \frac{1}{3} \cdot \left(\frac{T_{amb}}{T_{st}}\right)^4 - \frac{4}{3} \cdot \left(\frac{T_{amb}}{T_{st}}\right) \tag{5.9}$$

The results of the equation 5.9 are plotted in figure 5.2 and show the change of the radiation exergy by the temperature of the primary radiation [25]. The sun irradiation temperature T_{st} is assumed with $T_{st,1} = 5780\ \mathrm{K}$ and $T_{st,2} = 5300\ \mathrm{K}$. In this context, the exergy content of both T_{st} has only of minor relevance for the determination of the exergy of the sun. The portion η_p can be assumed in both cases around 93% [25, 106] which is also used for the following calculations.

The most influence on the exergy of the solar collector have the heat losses Q_{loss} discussed in section 3.3.1. The losses are mainly depending on the level of the receiver temperature T_{rec}, the ambient temperature T_{amb} and the wind speed (forced convection on receiver, see also chapter 3, equations 3.5 and 3.6). The collector model of Ebsilon Professional considers several losses which account to the exergy destruction of the solar collector. The exergy destruction of solar collectors are generally quite high which is increasing with the temperature difference between the ambient and the receiver temperature. However, the only energy source is the direct normal irradiation (DNI) concentrated by the heliostat field and considering several correction terms:

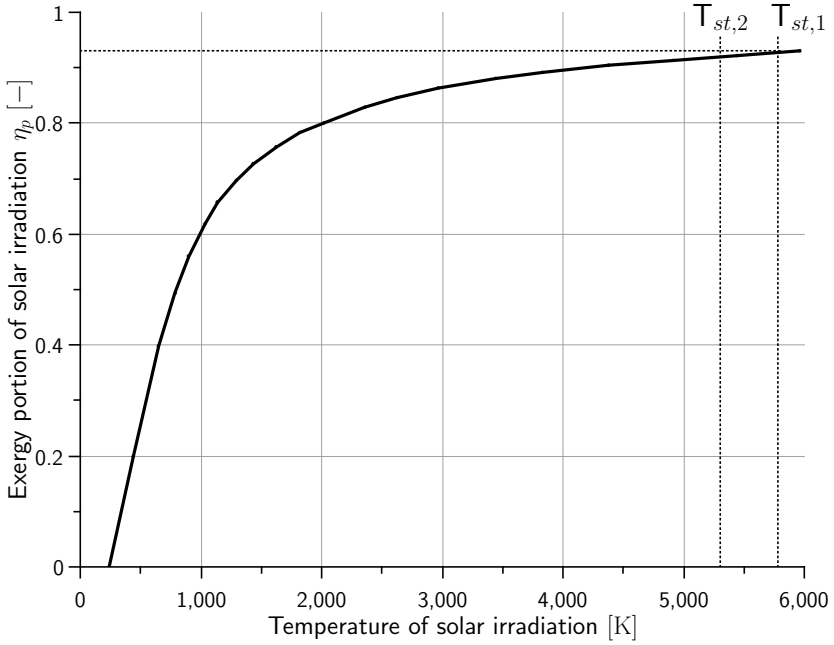

Figure 5.2: *Exergy content of the solar irradiation, adapted from [25]*

- Net aperture area of the collector.
- The optical efficiency, expressed by efficiency matrix.
- Incident angle and mirror shadowing.
- Real reflective area of the mirrors and
- Focus state of the collector.

The receiver model also considers the losses of pressure drops by friction and heat exchange. Due to the molten salt in the receiver, it is not required to calculate E_D with respect to any phase change. There is only sensible heat transferred (see section 3.3.1).

5.3 Exergy of the desalination unit

The entire condensation heat of the steam cycle is transferred to the desalination unit in the power plant condenser (HEX1) to the saltwater stream which has been discussed in sections 2.4.2, 3.4 and 4.3. More information about the modeling of the plant can be found in chapter 3, section 3.4.1 and in [21, 22]. The nomenclature for the stream numbering is visualized in figure 5.3.

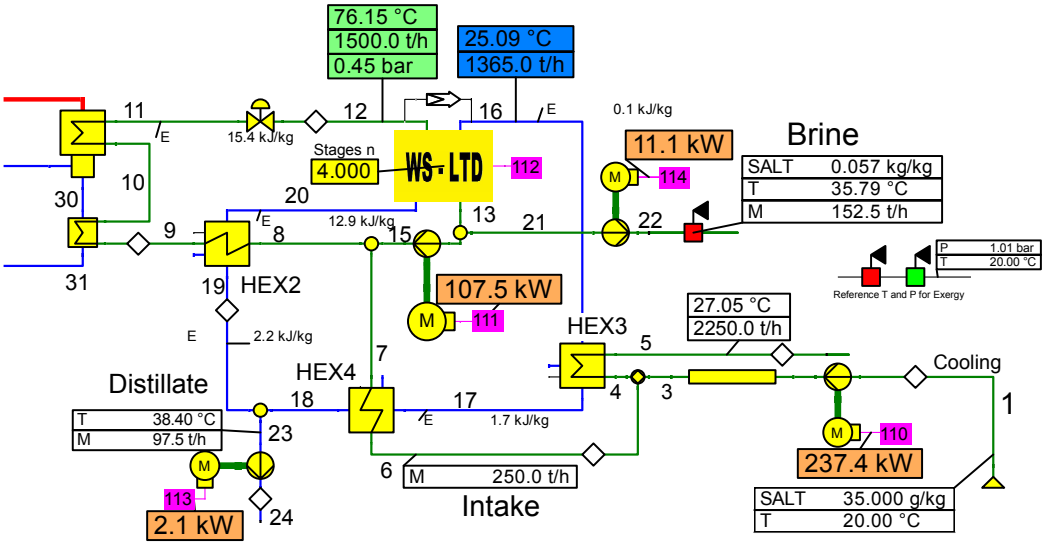

Figure 5.3: *Ebsilon Model of the desalination with stream numbering*

It is favorable to generate as much steam as possible in each evaporation reactor E1-E4 which can be then condensed in the reactors C4-C1. The condensed steam can be understood as the amount of desalinated water. In order to create an exergetic balance, the exergy of fuel and product need to be defined. It is important to mention that the exergy method only considers the thermodynamic properties, not the additional value of desalinated water. So it can be assumed that the exergy of the product is the added to the exergy of the steam in all condensing reactors. In consequence of that, the exergy of the fuel is the generated steam in each evaporation reactor. Concerning the condensing reactors, the pumping work $\dot{W}_{p,t}$ (stream 112 in figure 5.3) needs to be taken into account. The above mentioned relationships allow the derivation of the following balances for the exergy of the fuel and the product:

$$\begin{aligned} \dot{E}_F &= \dot{E}_{12} - \dot{E}_{13} + \dot{W}_{112} \\ \dot{E}_P &= \dot{E}_{20} - \dot{E}_{16} \end{aligned} \tag{5.10}$$

The definition of the exergetic efficiency ϵ_d of the desalination unit leads to the following equation:

$$\begin{aligned} \epsilon_d &= \frac{\dot{E}_P}{\dot{E}_F} \\ &= \frac{\dot{E}_{20} - \dot{E}_{16}}{\dot{E}_{12} - \dot{E}_{13} + \dot{W}_{112}} \end{aligned} \tag{5.11}$$

The exergy destruction $\dot{E}_D$ provides information about process inefficiencies and has been defined as difference between the exergy of the fuel and the product. It is calculated as follows:

$$\begin{aligned} \dot{E}_D &= \dot{E}_F - \dot{E}_P \\ &= (\dot{E}_{12} - \dot{E}_{13} + \dot{W}_{112}) - (\dot{E}_{20} - \dot{E}_{16}) \end{aligned} \tag{5.12}$$

The exergy balances for the circulation, distillate and brine pumps are derived from [24,103]. In order to evaluate the whole thermal desalination unit, several heat exchanges for cooling and preheating need to be considered. As an example, the calculation of the exergetic efficiency ϵ_{HEX2} is shown on the heat recovery HEX2 defining the exergy of the fuel and the product according to the following equation 5.13:

$$\begin{aligned} \epsilon_{HEX2} &= \frac{\dot{E}_P}{\dot{E}_F} \\ &= \frac{\dot{E}_9 - \dot{E}_8}{\dot{E}_{20} - \dot{E}_{19}} \end{aligned} \tag{5.13}$$

The corresponding exergy destruction $\dot{E}_{D,HEX2}$ can be calculated using the following equation:

$$\begin{aligned} \dot{E}_{D,HEX2} &= \dot{E}_F - \dot{E}_P \\ &= (\dot{E}_{20} - \dot{E}_{19}) - (\dot{E}_9 - \dot{E}_8) \end{aligned} \tag{5.14}$$

The balancing of all other heat exchangers and pumps is performed according to the given example and to the literature [24, 103]. The analysis in [101] has shown that the minimal temperature differences fall below 2 K. In order to optimize the heat exchangers, a pinch-point analysis could be performed.

5.4 System and process boundaries

One important step in the definition of the exergy values is the measurement of the energy streams within the system. To calculate the energy streams it is necessary to define the system and process boundaries. Figure 5.4 shows the system and process boundaries for the solar field, the power block and the desalination. Each process has different in- and output streams which need to be considered in the calculation. It should be mentioned again that the exergetic methodology considers only the additional benefit of the condensation heat, not the economic and social value of the desalinated water.

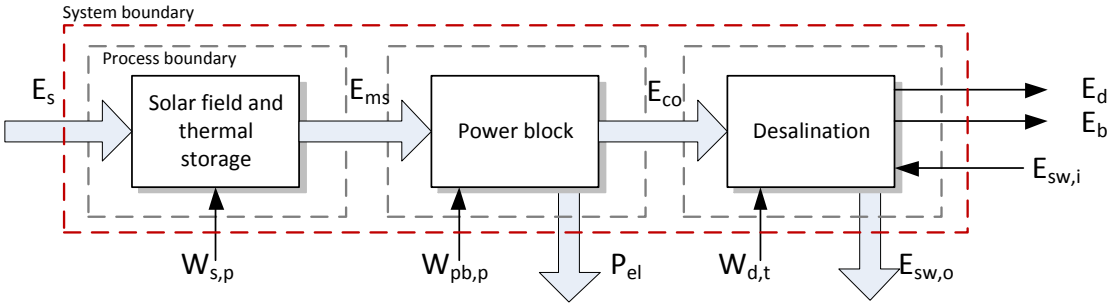

Figure 5.4: *System and process boundaries*

As visualized in figure 5.4, the exergy of the sun E_s is the sole fuel for the system and is calculated according to section 5.2. In addition, the solar tower and the thermal storage system need the supply of electric power $W_{s,p}$ which is mainly used by the molten salt pumps. The steam generator is supplied by the exergy of the molten salt E_{ms} delivering heat to the steam cycle. This heat is considered as exergy of the fuel for the power block. The net power output $P_{el,net}$ is obtained by the subtraction of the electric power for the feed water pumps $W_{pb,p}$.

After the steam expansion in the turbines, the complete latent heat of the condensation is denoted as the exergy of the condensation E_{co}. It represents the exergy of the fuel for the desalination system. The pumps in the desalination unit require electric power expressed by $W_{d,t}$. The exergy of the cooling medium is given with E_{sw}. Like shown in figure 5.3, this stream also supplies the feed water for the desalination unit in the magnitude of $\dot{m}_{d,fw} = 250\ \mathrm{m^3/h}$. The excess seawater is used for cooling the process. The exiting streams are the distillate E_d and E_b as well as the cooling water $E_{sw,o}$. Those streams are added to the exergy losses E_L which have been discussed in the last section 5.6.5.

To perform the exergy analysis within Ebsilon Professional environment [20], the fluid properties of the solar salt mixture need to be adjusted (60% sodium nitrate salt $\mathrm{NaNO_3}$ and 40% potassium nitrate salt $\mathrm{KNO_3}$, see also chapter 3.3.2). The default properties are only defined down to 240 $^\circ\mathrm{C}$ due to the solidification point of the eutectic mixture of the solar salt. In order to calculate system wide correct exergy values, a customized thermo-liquid with exactly the same fluid properties has been defined. In this simulation, the minimum temperature is set to the reference temperature T_{ref}.

5.5 Design conditions

The power output of the solar field varies during the day depending on the actual DNI. The design conditions of the heliostat field and the receiver are given on March, 21st, 12:00 at an irradiation of $I_{DNI} = 850\ \mathrm{W/m^2}$. The comparison with the meteorological measurements show a value of $I_{DNI} = 937,6\ \mathrm{W/m^2}$ for the respective hour [31]. In order to understand the real situation, the diurnal irradiation variation is hourly analyzed for the design day using real measurement values. Another cloudy day with consequently lower irradiation levels is chosen for the exergetic analysis.

Parameter	Symbol	Value	Unit
Heliostate field	$n_h = 1738$	173,800	$\mathrm{m^2}$
Design point DNI	I_{DNI}	850	$\mathrm{W/m^2}$
Solar irradiance on receiver	Q_{inc}	147,730	$\mathrm{kW_{th}}$
Mass flow, molten salt	$\dot{m}_{tes}$	300	$\mathrm{t/h}$
Mass flow, steam generator	$\dot{m}_{sg}$	50.1	$\mathrm{t/h}$
Live steam, temperature	T_{sg}	567	$\mathrm{°C}$
Live steam, pressure	p_{sg}	135	bar
Condenser, steam temperature	T_{co}	80.3	$\mathrm{°C}$
Condenser, pressure	p_{co}	0.48	bar
Electrical efficiency, motors	η_m	96.7	%
Isentropic efficiency, turbines	$\eta_{is,t}$	85	%
Isentropic efficiency, pumps	$\eta_{is,p}$	90	%
Desalination unit, evaporator mass flow	$\dot{m}_{ev}$	1500	$\mathrm{m^3/h}$
Desalination unit, condenser mass flow	$\dot{m}_{con}$	1365	$\mathrm{m^3/h}$
Desalination unit, stages	n	4	-
Salt content, intake seawater	b_i	35	$\mathrm{g/kg\ TDS}$
Reference temperature, cooling	T_{ref}	20	$\mathrm{°C}$
Reference pressure	p_{ref}	1013	mbar

Table 5.1: *Design conditions for exergy analysis*

All system parameters for the solar field, the power block and the desalination unit in the design point are summarized in table 5.1. Especially the desalination unit has defined operational conditions which are mainly the condensing pressure as well as the evaporator and condenser mass flows (see also section 4.4).

A further step in the process of exergy analysis is the definition of reference points. The coldest stream is represented by the incoming seawater serving as cooling medium for the desalination unit. The cold stream is defined with an exergy content of zero. The reference temperature and pressure are also given in table 5.1.

5.6 Results and discussion

All simulations assume steady state conditions for the specific operation point. In the following sections the results for each process are briefly analyzed and discussed. All values have been calculated using the methods described in the previous section 5.2 and 5.3.

5.6.1 Solar field

The exergy destruction and the exergetic efficiency are hourly analyzed for two exemplary days. In order to calculate the exergy balance for each component, the molten salt streams in the solar field of the Ebsilon model need to be numbered consistently. The part of the system starts with 80 at the outlet of the hot storage tank, 82-90 for the steam generator and 92-95 for the solar tower. All streams are visualized in figure 5.5.

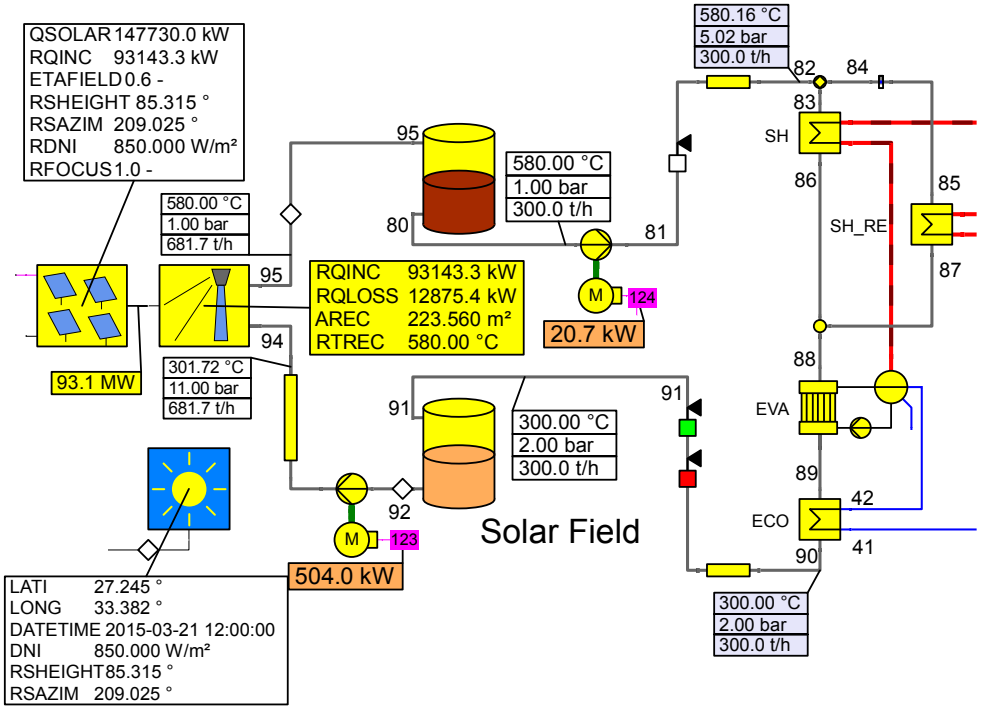

Figure 5.5: *Ebsilon model of the solar field with stream numbering*

The properties of the two selected days differ in terms of day length, weather condition, available irradiation and wind speed. All values are obtained by the measurements of the meteorological station in 2013 [31]. Table 5.2 summarizes the environmental conditions.

Day 1 represents the design day of the solar field given in section 3.3.1 [20]. Table 5.2 shows that the real measured DNI exceeds the design value of 850 $\mathrm{W/m^2}$ at 12:00 noon.

Parameter	Symbol	Day 1: March, 21, 2013	Day 2: May, 10, 2013	Unit
Maximal DNI	I_{DNI}	938	781	$\mathrm{W/m^2}$
Average DNI	$I_{DNI,av}$	740	659	$\mathrm{W/m^2}$
Maximal amb. temperature	T_{max}	28	34	$^{\circ}\mathrm{C}$
Minimal amb. temperature	T_{min}	16	23	$^{\circ}\mathrm{C}$
Average amb. temperature	T_{avg}	22	28	$^{\circ}\mathrm{C}$
Averaged wind speed	v_w	3.8	5.1	$\mathrm{m/s}$
Averaged wind direction	v_d	200	196	$^{\circ}$
Sky conditions	–	clear	cloudy	–

Table 5.2: *Environmental conditions of two exemplary days*

Day 2 has been chosen because of a significantly lower DNI compared to day 1. The higher ambient temperature in day 2 results in decreased heat losses in the solar field which has only a little impact on the calculation results.

Component	$\dot{E}_F$ kW	$\dot{E}_P$ kW	$\dot{E}_D$ kW	ϵ_k %	$y*_{D,k}$ %	$y_{D,k}$ %
Solar field	137389	47178	90211	34.3	98.0	65.1
Pump, hot	21	13	8	63.4	0.1	0.0
Pump, cold	563	266	297	52.7	0.3	0.2
Steam SH	7549	6984	566	92.5	0.6	0.4
Steam SH-RE	2297	1934	363	84.2	0.4	0.2
Steam EVA	7928	7334	594	92.5	0.6	0.4
Steam ECO	2823	2749	74	97.4	0.1	0.1

Table 5.3: *Exergy analysis for solar field of day 1 at design conditions*

Table 5.3 summarizes the exergy calculation for day 1 (design day) on March, 21st, at a solar irradiation of $DNI = 850\ \mathrm{W/m^2}$, including the thermal storage tanks, steam generator and pumps. The sun irradiation on the receiver represents the exergy of the fuel E_s. The rates of exergy destruction $y*_{D,k}$ and $y_{D,k}$ show the efficiency of each component in the whole process as indicator for the thermodynamic efficiency. As expected, the highest exergy destruction occurs in the heliostat field with the solar tower. Due to the high exergy destruction, the efficiency of this component is smaller than the efficiency of the others (see table 5.3). This leads to an efficiency ϵ_{st} of the component of around 34%.

The analysis in table 5.3 also shows a raised exergy destruction in the pump from the cold molten salt storage tank (pump cold). The reason can be found in a significantly

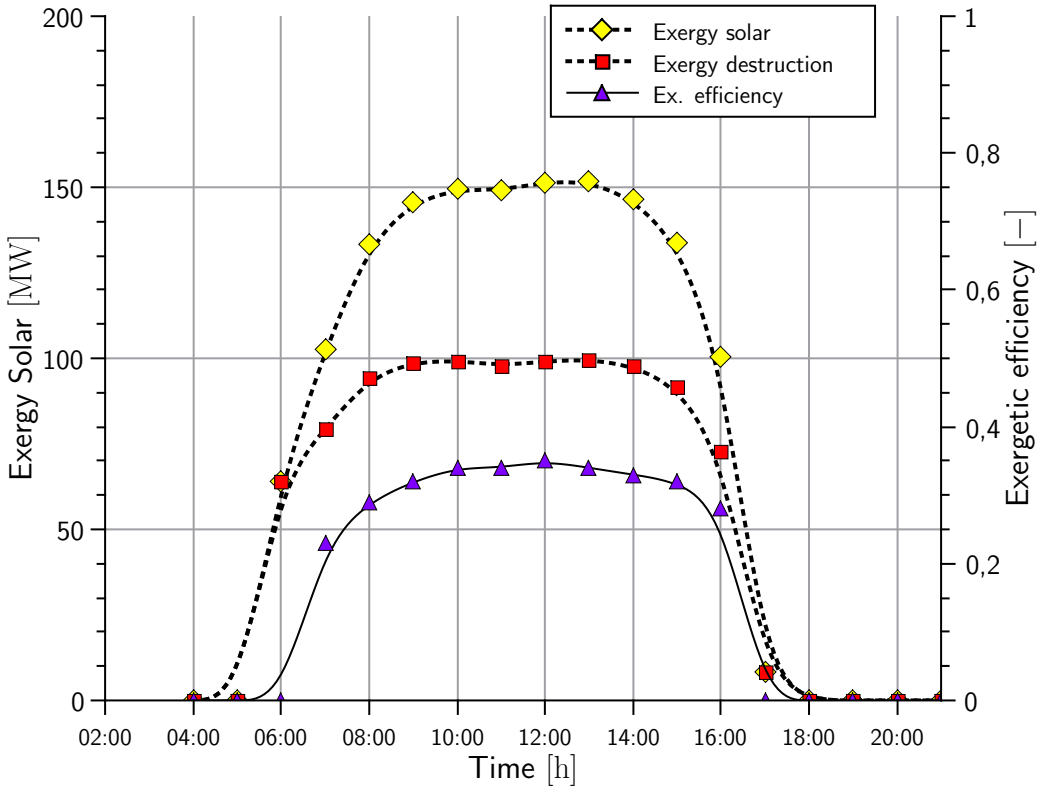

Figure 5.6: *Solar exergy and irradiation, day 1, clear sky, March, 21, 2013*

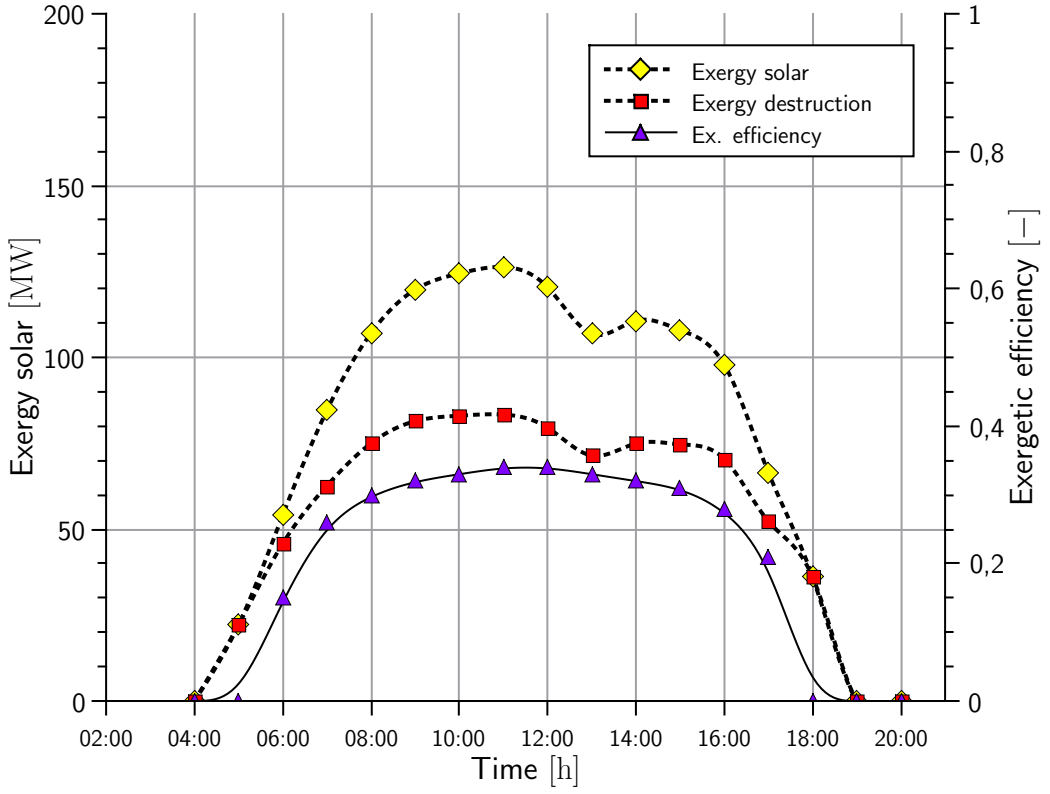

Figure 5.7: *Solar exergy and irradiation, day 2, cloudy sky, May, 10, 2013*

increased power consumption compared to the hot pump. The storage temperatures support this development. The tower height of 126 m (see also section 3.3.1) requires large pressures because of the geodetic head. Consequently, the pump (cold) consumes almost 25 times more electricity compared to the pump (hot). The outlet pressure of the cold storage pump exceeds more than 40 bar with noticeable temperature losses. The hot pump in comparison shows a higher component efficiency because it has to overcome no geodetic heads and the only source of exergy destruction is the pressure loss in the steam generator heat exchangers.

Figures 5.6 and 5.7 show the development of the exergy of the solar irradiation and the exergy destruction based on the measured solar irradiation on March, 21st, 2013 [31] for averaged hourly values. Figure 5.6 visualizes the calculation of this component. During the day, the usable solar exergy of irradiation reaches up to 150 $\mathrm{MW_{th}}$. The usable heat is specifically lower at low solar incident angles during sunrise and sunset. The resulting incident power on the receiver is interpolated using the efficiency matrix described in chapter 3.3.1. Concerning the exergetic efficiency, it can be seen that it is almost constantly above 20% even at low inclination angles during sunrise and sunset. The solar field requires a minimum DNI to start-up the heat generation.

Figure 5.7 shows the same analysis for the day 2 under cloudy weather conditions in May 2013 with measured DNI values of this day [31]. Compared to the design day and figure 5.6, it can be seen that the average direct normal irradiation $I_{DNI,av}$ lower (compare also to table 5.2). Nevertheless, figure 5.7 also shows that the efficiency reaches similar values compared to the design day. It can be concluded that the exergy destruction is proportional to the respective DNI values during the day.

5.6.2 Thermal storage

The exergetic analysis of the thermal storage system needs to be analyzed under transient conditions using time steps of one hour. The calculation is performed by balancing the exergy streams of both storage tanks of the design day 1. Inevitably, the definition of exergy of the fuel and product depends on the operation condition during day and night. The definition requires the consideration of both storage tanks with respect to loading and unloading mass flows on a hourly basis. In order to calculate the exergy difference of the hot and cold storage tank, the exergy differences per time are defined with $\Delta\dot{E}_H$ and $\Delta\dot{E}_C$, respectively.

$$\Delta\dot{E}_H = \dot{E}_{96} - \dot{E}_{80}$$
$$\Delta\dot{E}_C = \dot{E}_{91} - \dot{E}_{92} \tag{5.15}$$

The sum of $\Delta\dot{E}_H$ and $\Delta\dot{E}_C$ variables calculates to positive and negative exergy values for the whole system. If it is positive, the exergy difference of the hot storage $\Delta\dot{E}_H$ is defined as exergy of the fuel and turning negative as exergy of the product. During day operation, $\Delta\dot{E}_H$ turns positive while $\Delta\dot{E}_C$ stays negative. In this case, $\Delta\dot{E}_H$ is defined as an exergy increase (loading, raising hot storage level) and exergy decrease (unloading, raising cold storage level). The above described regime of loading and unloading exergy is reversed during night-time.

Operation time	Hot storage $\Delta\dot{E}_H$ in kW	Cold storage $\Delta\dot{E}_C$ in kW	Exergy storage $\sum$ in kW
Day operation	+39898	–13234	+26664
Night operation	–31054	+10300	–20753

Table 5.4: *Exergy analysis for thermal storage during day and night operation*

The simulated diurnal variations result in a set of exemplary exergy values of the storage system summarized in table 5.4 at noon time and during night operation. It can be observed that the exergy increase during day operation is much larger compared to the exergy decrease in the night which can be understood as charging the storage. The unloading mass flow is constant to supply an invariable heat amount to enable the power bock to stay in steady-state conditions.

5.6.3 Power block

For the power block the part-load behavior is of special interest and is analyzed in this section. During part-load operation, the unloading mass flow of the hot storage tank is lowered down to $\dot{m}_{tes} = 240$ t/h with the goal to increase the daily operation time of the plant. This corresponds to the operation of the power block at around 80% of the nominal design capacity. The operation mode might be necessary to lower the power output to meet the conditions with lowered irradiation and shorter day length (winter period). The part-load operation can increase the contribution to the firm capacity for those periods.

In order to discuss the exergy balancing, the stream numbers of the power block needs to be defined. The streams (water/steam) start with 30 at the condenser and 41 at the steam generator. The feed water preheating is described using numbers from 51-67. All streams are visualized in figure 5.8. The blue lines indicate liquid water while the red lines steam.

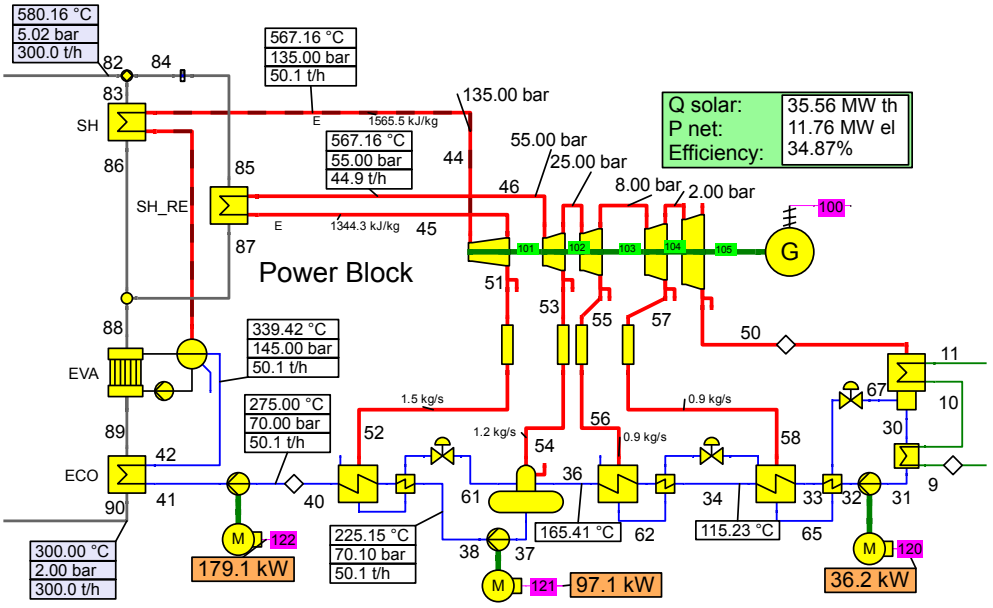

Figure 5.8: *Ebsilon model of the power block with stream numbering*

The exergy of the fuel E_F for the power block is represented by the thermal energy supplied by the molten salt from the hot storage tank and denoted as E_{ms}. Consequently, E_F is proportional to the unloading mass flow $\dot{m}_{tes}$ of the hot storage tank during part-load operation. The exergy of the molten salt E_{ms} represents the exergy of the fuel. The rates of exergy destruction $y_{D,k}$ show the efficiency of each component in the whole process as indicator for the thermodynamic efficiency. Table 5.5 shows the results of the exergy analysis for the power block in design conditions.

A closer examination of the results in table 5.5 reveals that the highest exergy destruction occurs in the condenser (HEX1) and the steam generator (ECO-SH). In order to lower the exergy destruction the heat exchanger areas can be increased which consequently decreases the mean logarithmic temperature ΔT_m of the heat exchanger. Especially the interaction with the desalination process requires spacious dimensioning in order to minimize heat exchanger losses. Comparing the efficiency of the other listed power block components to those of conventional power plants in [25], the results present that all turbine stages work within high efficiencies given in literature values. Especially deaerator has a relatively low efficiency compared to the other components. One possible

Component	$\dot{E}_F$ kW	$\dot{E}_P$ kW	$\dot{E}_D$ kW	ϵ_k %	$y*_{D,k}$ %	$y_{D,k}$ %
Turbine HP 1	3080	2888	192	93.8	4.1	0.8
Turbine MP 2	3113	2918	195	93.7	4.2	0.9
Turbine MP 3	3427	3161	266	92.2	5.7	1.2
Turbine LP 4	3059	2753	306	89.9	6.6	1.3
Turbine LP 5	2268	1998	270	88.1	5.8	1.2
Pump FWP 1	179	155	25	86.3	0.5	0.1
Pump FWP 2	97	83	14	85.2	0.3	0.1
Pump FWP 3	37	29	7	79.8	0.2	0.1
Steamgenerator ECO	2823	2749	74	97.4	1.6	0.3
Steamgenerator EVA	7928	7334	594	92.5	12.8	2.6
Steamgenerator SH	7549	6984	566	92.5	12.2	2.5
Steamgenerator SH-RE	2297	1934	363	84.2	7.8	1.6
Condenser HEX 1	3610	2424	1186	67.1	25.6	5.2
Condenser Afc.	117	74	43	63.3	0.9	0.2
Deareator	1262	1086	176	86.1	3.8	0.8
Preheater FWP 3a	79	55	24	69.9	0.5	0.1
Preheater FWP 3	463	406	58	87.5	1.5	0.2
Preheater FWP 2a	61	51	10	83.4	0.2	0.1
Preheater FWP 2	774	651	123	84.1	2.6	0.5
Preheater FWP 1a	160	150	10	93.5	0.2	0.1
Preheater FWP 1	1456	1330	125	91.4	2.7	0.5
Throttle Valve 1 *	–	–	4	–	0.1	0.0
Throttle Valve 2 *	–	–	0.5	–	0.1	0.0
Throttle Valve 3 *	–	–	0.2	–	0.1	0.0

*) considered as dissipative component

Table 5.5: *Exergy analysis for the power block*

explanation could be the mixing of two streams with large temperature and pressure gradients.

Efficiency

The process efficiency ϵ_{pb} can be calculated according to equation 5.16. The exergy fuel is supplied by the molten salt E_{ms} from the hot storage tank. It needs to be noted that equation 5.16 disregards the connected desalination system and is consequently not suitable for the selected case. The released exergy of the condensation E_{co} in the condenser is treated as loss. The generated net power $P_{el,net}$ integrates the required electricity for the feed water pumps $\dot{W}_{pb,p}$. For more information, see also figure 5.4 in section 5.4.

$$\epsilon_{pb} = \frac{P_{el,net}}{\dot{E}_{ms}} \tag{5.16}$$

The cogeneration systems adds the exergy of the condensation E_{co} as a useful stream to this ratio. This results in an increased efficiency $\epsilon_{pb,cg}$. Inevitably, the exergy of the condensation heat E_{co} is considered as exergy of the fuel for the desalination unit. The electric power required by the pumps in the desalination unit denoted as $\dot{W}_{d,t}$ needs to be subtracted in equation 5.17.

$$\epsilon_{pb,cg} = \frac{P_{el,net} + \dot{E}_{co} - \dot{W}_{d,t}}{\dot{E}_{ms}} \tag{5.17}$$

The exergetic efficiency ϵ_{pb} for the power block results in 64.5% which can be considered as very high. In the first place, this value does not consider the losses of the solar field and has been calculated using the hot molten salt as exergy of fuel. Secondly, another explanation can be found in the mechanism of the heat exchange during steam generation. In most fossil fuel power plant, the highest exergy destruction occurs due to high boiler losses (e.g. coal fired) which are a result from the heat transfer of hot combustion gases to the feed water. In this case, the thermal energy is supplied by liquid molten salt to liquid water resulting in a better heat transfer. Furthermore, the calculation on process level does not include the solar field losses (see also section 5.4 and figure 5.4).

The operation in cogeneration and considering the condensing heat in HEX1 for the desalination, the efficiency $\epsilon_{pb,cg}$ increases to 81.6% using the calculation in equation 5.17. It can be concluded that the cogeneration improves the total process efficiency by 17.1 percentage points. The pumps of the desalination unit account only for a small portion in comparison to the total power generation in the power block. The total share ranges approx. 1% of the total generated electric power.

It can be stated that the other exergetic efficiencies of the respective components are within literature values. However, further improvement should focus on the maximization of pressure and temperature of the live steam, but are limited by material constraints in the steam generator. Due to the relatively small size of this system, the economic feasibility can be seen critically. More information concerning the economics are discussed in chapter 6.

Part-load operation

The operation in part-load has an influence on the exergetic efficiencies and the power generation. At design point conditions, the hot molten salt enters the steam generator and supplies around 35 $\mathrm{MW_{th}}$ thermal energy to the power block (compare also to chapter 4, section 4.4). For the part-load calculation, the thermal energy supply is lowered down to 28.7 $\mathrm{MW_{th}}$ simulated by a decreased molten salt mass flow $\dot{m}_{tes,n}$ from 300 to 240 $\mathrm{t/h}$. The calculation mode in Ebsilon is changed to part-load which calculates with fixed $k \cdot A$ coefficients for the heat exchangers. The live steam pressures are decreased according to the available heat energy and change the efficiency of the steam expansion in the turbines which has been discussed in chapter 3, section 3.3.3.

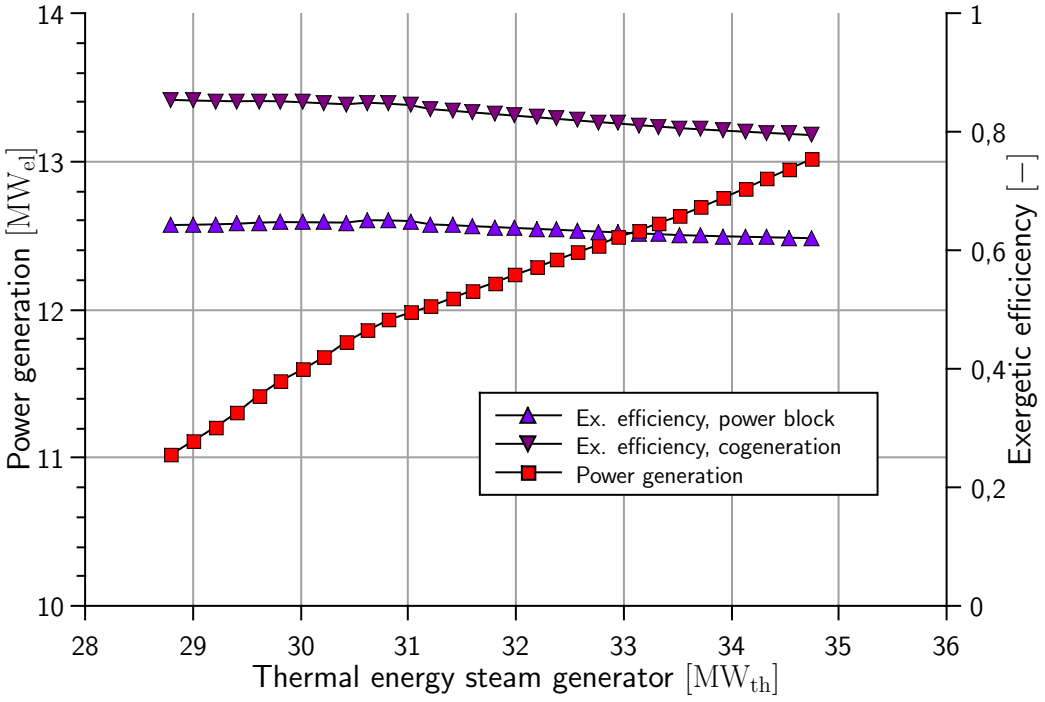

Figure 5.9: *Power generation and exergetic efficiencies ϵ_{pb} and $\epsilon_{pb,cg}$*

Figure 5.9 visualizes the power block behavior and compares the net power generation to the exergetic efficiency defined in equations 5.16 and 5.17. It can be concluded that the exergetic efficiency of the steam generator increases marginally in part-load and reaches the highest values around 31 $\mathrm{MW_{th}}$ heat supplied. The effect is accompanied by a stronger decrease of the power generation due to turbine part-load operation. Nevertheless, the examined range is very small. So it can be concluded, that the overall exergetic efficiency ranges above 60% for the power block and 80% for cogeneration, respectively. The main reason for small increase of the exergetic efficiencies could be the reduced exergy destruction in the steam generator heat exchangers due to decreasing

heat supply. It also lowers the temperature difference and allows for a compensation of the heat transfer at given $k \cdot A$.

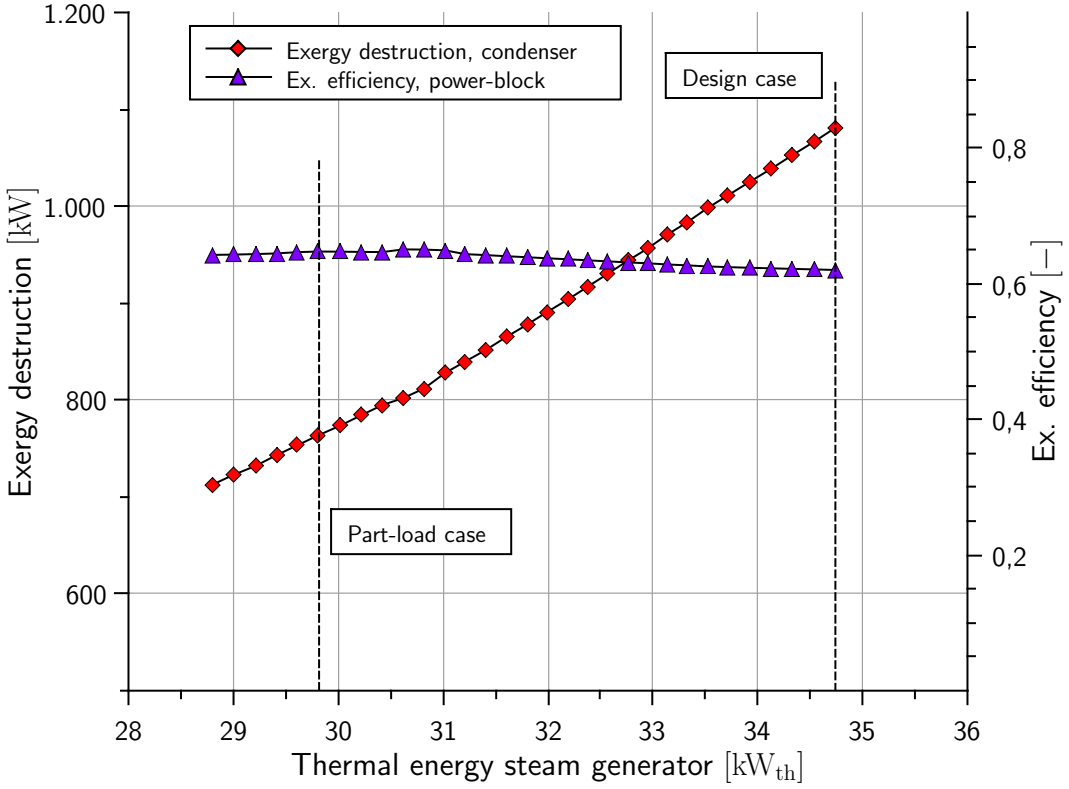

Figure 5.10: *Exergy destruction in the condenser (HEX1)*

The condenser has the largest exergy destruction as power block component, which can be seen in table 5.5. It requires to have a closer look on this heat exchanger, as it also acts as interface between the power block and the desalination unit. Figure 5.10 plots the exergy destruction and the exergetic efficiency. It can be concluded that the exergy destruction decreases in part-load operation while the component efficiency shows an almost constant efficiency. The behavior can be explained by fixed heat exchanger coefficients $k \cdot A$ which positively influence the efficiency. For design condition, it confirms the requirement for a careful dimensioning of the power plant condenser, especially for the operation in cogeneration.

5.6.4 Desalination

The exergy analysis for the desalination system can be found in Table 5.6. As a main result, the analysis shows significant differences in the exergy destruction and efficiency of the pumps. The differences are a consequence of variations in pressures and volume flows. The distillate and brine pumps convey only small mass flows while the pump

supplying the evaporation reactors has a significantly higher mass flow. The exergy destruction of the heat exchangers are a result of the different temperature gradients. Large temperature differences are always a reason for high irreversibilities.

Component	$\dot{E}_F$ kW	$\dot{E}_P$ kW	$\dot{E}_D$ kW	ϵ_k %	$y*_{D,k}$ %	$y_{D,k}$ %
Condenser HEX 1	3610	2424	1186	72.8	26.6	32.6
Condenser Aftercooler	117	74	43	70.1	0.9	1.1
Heatrecovery HEX 2	4336	3175	1161	73.2	32.6	40.0
Cooling HEX 3	604	208	396	34.5	11.1	13.6
Preheating HEX 4	205	83	123	40.2	3.4	4.2
Desalination stages	6025	5206	819	86.4	23.0	28.2
Pump. Evaporators	107	32	76	29.4	2.1	2.6
Pump. Distillate	2	2	0	99.9	0.0	0.0
Pump. Brine	11	4	7	35	0.2	0.3
Mixer *	–	–	19	–	0.5	0.7
Throttle valve *	–	–	14	–	0.4	0.5

*) considered as dissipative component

Table 5.6: *Exergy analysis for the desalination unit*

The highest exergy destruction occurs within the condenser (HEX1) and the heat recovery (HEX2). The reason can be seen in the relatively large heat quantities to transfer while the available temperature gradients are rather small. Compared to that, the heat and mass transfer in the four desalination stages can be considered as more efficient. The value includes the needed pumping power between the condensing reactors. It is assumed that the exergy destruction even decreases with increasing number of desalination stages. The heat exchanger HEX3 for cooling shows a low efficiency compared to the others. The reason might be the high cooling mass flow, which ensures a sufficient cooling of the desalination unit. It has not been further optimized for an efficient operation.

Heat exchanger

For the analysis of the power plant condenser or HEX1, the specific exergy demand of the desalination unit is introduced. It sets the transferred condensation heat into relation to the produced distillate and consequently has the unit $\mathrm{kWh/m^3}$. It is expected that raising condensation pressures result in an increased specific exergy demand of the desalination unit. The explanation can be the increased temperature level in HEX1 which is accompanied with a higher pressure level in the LP turbine. The heat extraction from

the power cycle requires more pumping power while the produced distillate just increases around 2 m^3/h in the examined area.

Due to the high exergy destruction, the condenser (HEX1) requires some attention. In figure 5.11, the specific exergy demand per m^3 water distilled is plotted together with condensing pressures. It shows that the demand is increasing with higher pressures as priory discussed. Furthermore, the exergetic efficiency of HEX1 shows a minimum around 0.3 bar. From the exergetic point of view, higher condensation pressure and temperatures are favorably for a high efficiency. However, this statement needs also to be discussed under economic considerations with respect to energy and water pricing.

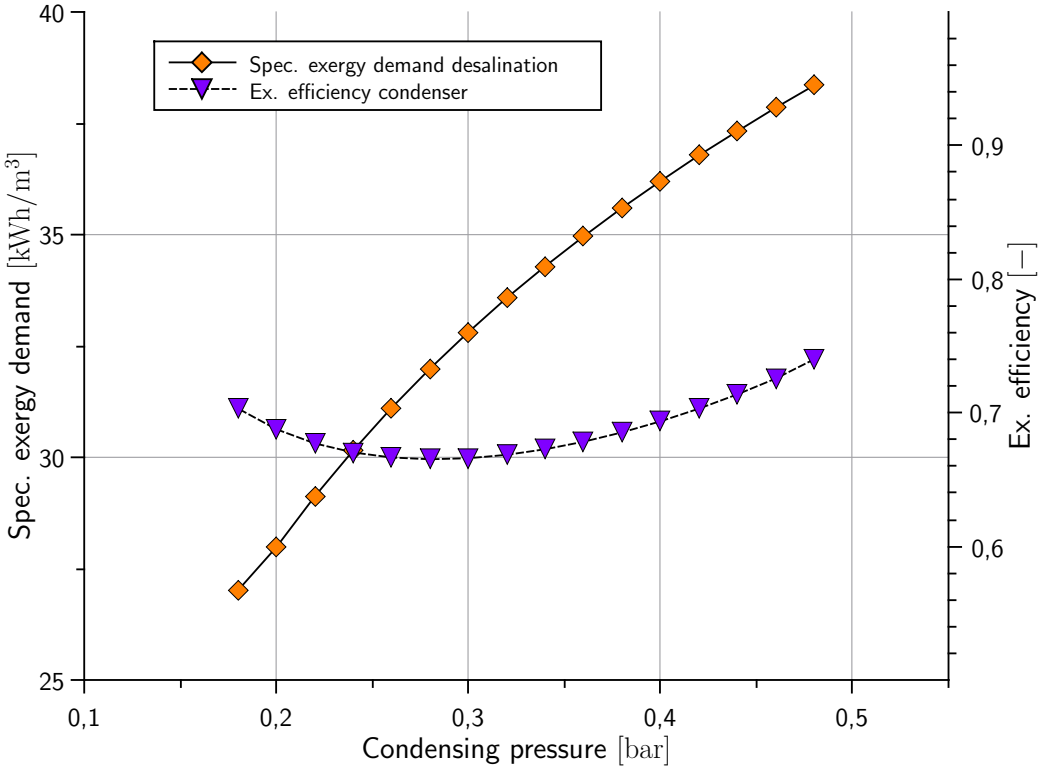

Figure 5.11: *Exergy results for the condenser (HEX1)*

Salt content

Generally, the salt content of the intake water has noticeable effects to the overall system and to some components in the desalination system and is presented in figure 5.12. The influence is caused by the changed physical properties of water with increasing salt content, which are respected by the simulation environment. The main effect is an increased boiling temperature of a salty solution with a rising concentration which is

called boiling point elevation (BPE). It is well known for the construction of thermal desalination systems (see also chapter 2, section 2.4.1).

In addition, figure 5.12 shows the development of exergy destruction in condenser, all heat exchangers and the desalination stages. The results obtained from the simulation show a decreasing exergy destruction in the desalination unit with increasing salt content. Comparing the results to the exergy destruction in HEX1 (condenser) and HEX2 (heat recovery), it can be observed a contrary development. One explanation could be the raised entropy generation in the heat exchangers. However, within the examined salt concentrations, the impact of the salt content is only minor to the distillate production (compare also to section 4.4.4 and figure 4.12).

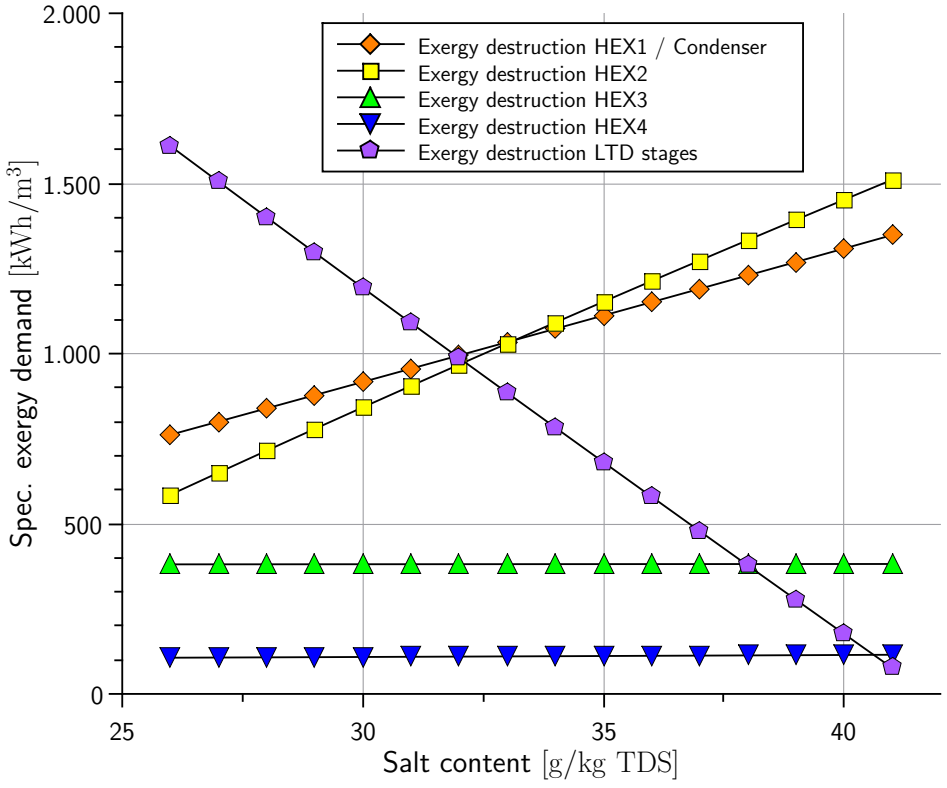

Figure 5.12: *Exergy destruction in heat exchangers with different salt concentrations*

Desalination stages

For the examination of the influence of the desalination stages to the specific exergy demand, all other operation conditions and process parameters of the desalination system are kept constant. Under these assumptions, the numbers of desalination stages can be examined. The same implications like described in section 4.4.3 apply here as well. One additional stage means adding one evaporating and condensing reactor with additional

steam generation. More stages generally increase the produced distillate by the reuse of the condensation heat within the desalination unit. The effect can be clearly seen in figure 5.13. The shape of the curves are very similar to the discussed influence of the number of stages in section 4.4.3, figures 4.10 and 4.11, respectively.

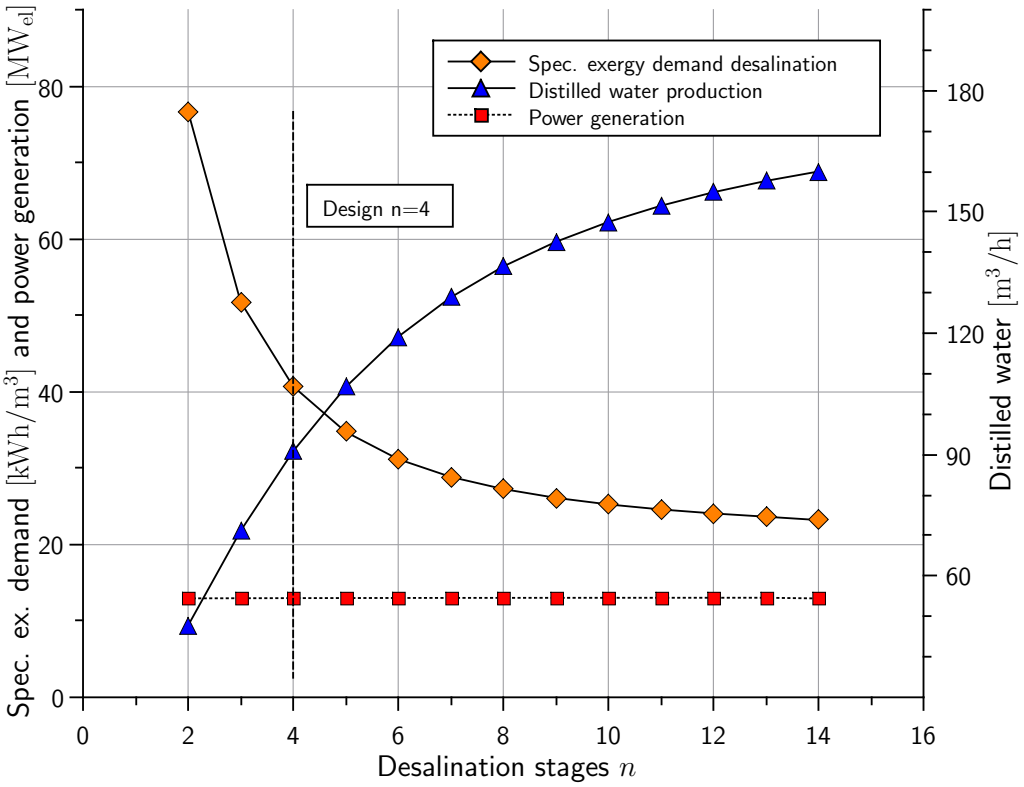

Figure 5.13: *Specific exergy demand and distilled water production per stage*

Regarding each stage individually, it can be stated that the available temperature difference is specifically lowered with increasing number of stages. This results in a decreased distillate output while the total distillate production is increased. Furthermore, it can be stated that an increasing number of stages lowers the exergy destruction and thus the specific exergy demand of the desalination system per m^3 distillate. From the engineering point of view, the reasons are the additionally generated distillate and the increased heat transfer area for each stage. So the overall irreversibilities in the system are also decreased. In addition, figure 5.13 also shows that the power generation is unaffected from the number of stages. This effect has also been discussed in section 4.4.3 and figure 4.10.

5.6.5 Exergy losses

The exergy losses are calculated for the overall system including all three processes (compare to figure 5.4). The total exergy losses are formed by the difference in exergy streams of outgoing and incoming seawater in HEX3, the stream of brine as well as the stream of distillate. Consequently, the exergy loss E_L are calculated as follows in equation 5.18:

$$\begin{aligned} \dot{E}_{L,tot} &= \dot{E}_{L,HEX3} + \dot{E}_{L,b} + \dot{E}_{L,d} \\ &= \dot{E}_5 + \dot{E}_{22} + \dot{E}_{24} \end{aligned} \tag{5.18}$$

The stream numbering of the desalination unit has been introduced in figure 5.3. The system exergy loss $\dot{E}_{L,tot}$ are calculated by adding the exergy of the exiting cooling water stream in HEX3, the brine exergy $\dot{E}_{L,b}$ (concentrated saltwater) and the distillate exergy $\dot{E}_{L,d}$ according to equation 5.18. The cooling water holds the biggest share while distillate and brine are only minor mass flows. Table 5.7 summarizes the exergy losses for the discussed system. The total exergy loss of the system sums up to 313.9 kW.

Component	Stream	$\dot{E}_L$ kW
HEX3 cooling	$\dot{E}_5$	213.5
Distillate	$\dot{E}_{24}$	57.1
Brine	$\dot{E}_{22}$	43.3

Table 5.7: *Exergy losses of the complete system*

Concluding, this chapter presented an exergetic analysis based on the three plant sections. The examination of different influences such as condensation pressure, number of stages and seawater salinity have provided a good picture of the entire system. Lowering the condensation pressure decreases the distillate production but raises the efficiency of the steam cycle, which has been analyzed in section 4.4.1. An increased number of stages enlarges the distillate production accompanied by an increased efficiency of the desalination system. High saline seawater has a comparatively small influence on the distillate production but caters for raised entropy generation in the desalination stages. The performed analysis could be used as base for an exergo-economic analysis but is not chosen for the economic analysis in the following chapter.

Chapter 6

Economics

The cogeneration of power and water has been extensively discussed in the previous chapters from a thermodynamic and exergetic point of view. These results are now used to evaluate this cogeneration plant and the respective technologies from an economic perspective, which requires the investigation of the key influence parameters. A literature review of the general economic assessment in the field of concentrating solar power plants shows the existence of several calculation methods. Due to the design of the model plant, it needs to be discussed under which circumstances the integration of the thermal desalination unit supports the economics of concentrating solar power plants. The analysis given in this chapter bases on [107].

6.1 Literature review

During the last years, there has been a consortium of international partners including the German Aerospace Center (DLR) which carried out various research on the combination of CSP and desalination. The most important publications focus on combined solar power and desalination plants (MED-CSD) [108,109], Concentrating Solar Power for the Mediterranean Region (MED-CSP) [109, 110], Concentrating Solar Power for Seawater Desalination (AQUA-CSP) [29] and Trans-Mediterranean Interconnection for Concentrating Solar Power (TRANS-CSP) [48]. All those comprehensive research publications focus on deployment of concentrating solar power plants in the Mediterranean or Middle East and North Africa (MENA) region. In addition to that, there are case studies and recommended projects available for many locations in the described regions [111–113]. Using some of this research, the World Bank commissioned a research study on the expected water gap in the MENA region, concluding the inevitable use of renewable energies for desalination [47]. Furthermore, the U.S. based National Renewable Energy

Laboratory (NREL) developed an extensive model and a tool chain to evaluate renewable energy power plants. This software is called "System Advisor Model" (SAM) [114]. There exist first approaches to extend this model and integrate desalination plants as well [115]. The Desertec Industrial Initiative (Dii) endorsed some of the DLR surveys on the feasibility of concentrated solar power and water cogeneration plants and promotes research in the field of renewable energy and desalination. The corresponding Dii Eumena Conference awarded the Best Paper Award to the development of a new approach for combined power and water generation in 2012 [22].

6.1.1 Cogeneration costs

The economic evaluation of power and water production especially from renewable energy is highly complex. Most renewable power plants have comparably high investment costs which result in high electricity generation costs. The integration of one additional product (water) requires an accurate analysis of the cost structure while considering different product costs. The overall assumption is the increase of the overall energetic efficiency which has been proven for the exergetic efficiency in chapter 5, section 5.6.3. As the generated heat is not only used for electricity generation, the solar collector and the power plant also supply low-grade heat for the thermal desalination at low temperatures. Due to the special design of the model plant, the thermal desalination is able to replace the cooling system of the steam cycle. While the desalination unit holds only a minor share of the power plant investment cost, it introduces a new product with an economic value. Depending on the boundary conditions, this new product has a strong influence on the efficiency and enhances the total economic value of the plant. From the thermodynamic point of view, the produced water can not assigned an exact energetic value.

Generally, several indicators can be applied to compare different energy sources and technologies. An overview can be found in the work of Mauléon [116] and Narbel et al. [117]. Each indicator serves well for different purposes, but they all have certain limitations.

6.1.2 Thermal storage and integration costs

The "Concentrating Solar Power Alliance" (CSPA) aims to quantify the additional benefits of CSP plants with thermal storage system [26] like the modeled plant in the previous chapters. Especially the combination of a steam cycle with a thermal storage system can provide additional services to the transmission grid. The support can be mainly

summarized in short-term energy balancing and protection of system contingencies. The following points stand for an added value of such plants [26]:

- *Ancillary services*: spinning power reserves and regulatory reactive-power, black start ability.
- *Reduced integration requirements*: influence of transmission grid ramps by varying power production from PV and wind power plants.
- *Power quality*: reactive power and dynamic voltage support, frequency control for the prevention of backouts.

The study [26] comes to the conclusion, that the strong development of renewable energies like PV and wind power plants causes significantly higher net system costs for regulators and utility operators. If the total share of fluctuating renewable energies exceeds 33%, the additional costs are compared to CSP plants with thermal storage [118]. As a result of the calculations of grid integration and market costs, such plants have an additional value of 1.9 to 3.5 $\mathrm{ct/kWh}$ at 10% market penetration [26] which lowers the LCOE.

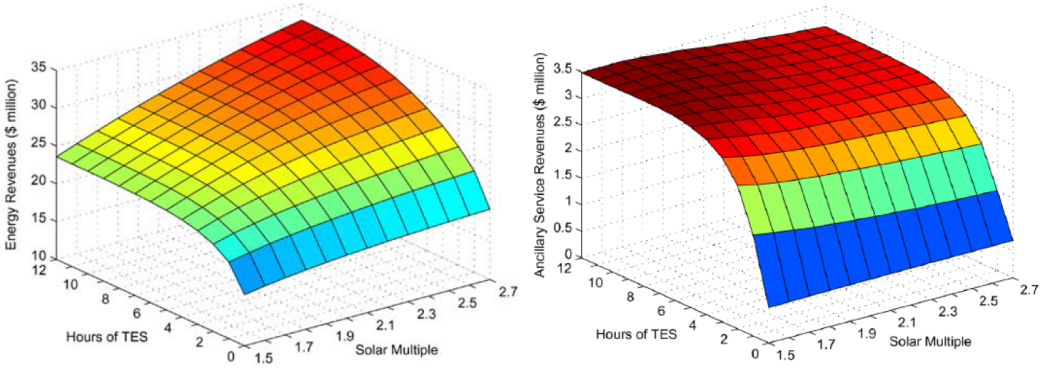

Figure 6.1: *Annual revenues from energy and ancillary services of a CSP plant with storage [26, 27]*

Figure 6.1 visualizes the energy revenues (left) and ancillary service revenues (right) from a CSP plant with thermal storage system per year. The additional revenues increase with the dimension of the storage system and the extended operation time per day. There has been reported annual revenues for spinning reserves as well. The variations in capacity ratings for the thermal storage can strong affect the market modeling. For the examined configuration in [26, 27], the additional benefit sums up to 10% of the energy revenues. Most literature studies do not consider large storage systems above 6 hours of full-load operation. However, CSP plants with thermal storage act as stabilizing element in grids with large share of renewable energies. It can be concluded that the stabilizing effect creates additional revenues can be substantial to the total energy system [26].

6.2 Methodology

The following sections describe the used methodology for the economic analysis, basic calculation methods, cost allocations and the known limitations.

6.2.1 Levelized cost of electricity

One common approach is the use of the levelized cost of electricity (LCOE) to compare different renewable energy technologies [116, 119]. The LCOE is defined as the total lifetime expenditures of the plant divided by the total power generation during this time frame. The total lifetime expenditures are composed of the capital costs C_t, the operation and maintenance costs $O\&M_t$ and the fuel costs F_t for each year. The total power generation is noted with P_t and discounted using the interest rate i_r for the complete plant lifetime t_c. Equation 6.1 summarizes the calculation of the LCOE:

$$LCOE = \frac{\sum_{t=1}^{t_c} \frac{C_t + O\&M_t + F_t}{(1+i_r)^t}}{\sum_{t=1}^{t_c} \frac{P_t}{(1+i_r)^t}} \tag{6.1}$$

Since the selected system consists of a CSP plant with an integrated high capacity thermal energy storage system, the LCOE is a valid option to evaluate the economic feasibility of the model plant. It also ensures the comparability of the results to other technical solutions. The calculations for the model plant are summarized in section 6.5.1.

6.2.2 Levelized cost of water

The levelized costs of water are comparable to the LCOE calculation. In the literature it is also referred as levelized water cost LWC [120]. The calculation consists of the total lifetime cost of the desalination plant divided by the total gross water production in equation 6.2. The parameters are identical compared to the given definitions in section 6.2.1 and equation 6.1 except from the total water production W_t. Many advantages and problems are identical to these in the calculation of the LCOE, while again the common use of this method enables it for a first comparison of technologies.

$$LWC = \frac{\sum_{t=1}^{t_c} \frac{C_t + O\&M_t + F_t}{(1+i_r)^t}}{\sum_{t=1}^{t_c} \frac{W_t}{(1+i_r)^t}} \tag{6.2}$$

The most interesting factor in the calculation of LWC is the fuel cost F_t. Its definition is crucial for the results and is also depending on the examined technology. Basically, it accounts for the energy demand assigned to the water production and can be considered as major cost factor for desalination. Different methods of calculation are described in the section 6.2.4.

6.2.3 Limitations of LCOE and LWC

The LCOE and the LWC are widely used to compare different renewable energy and water treatment technologies with each other. Mostly, the investment decisions depend on low levelized costs neglecting other relevant dimensions such as security of supply or social aspects. The definition may be sufficient for the assessment of fossil fuel powered plants where the fuel costs account to more than 70% of the total lifetime costs. However, the LCOE does not respect the risk of future price escalation and shortages of fuel supply. Applied to the evaluation of renewable energies, the LCOE is basically calculated using the investment costs instead of the fuel price and after the pay-off of the plant, the risk of fuel price escalations is not present any more. Despite this advantage, the LCOE has also several shortcomings.

In its basic form like described in section 6.2.1, the levelized costs do not consider any externalities like CO_2 emissions, grid distribution costs or other environmental impact factors. Since most power generation from renewable energies is subject to the availability of the natural resources like solar irradiation and wind, the power generation is fluctuating depending on the actual situation. Usually, this does not match with the actual power demand and requires the modeling of a competitive electricity price according to the demand curve.

The implementation of PV and wind technology is not sufficient to generate a base load and a secure supply of energy. In consequence of the installation of many fluctuating solar and wind power plants, they can generate significant additional costs on grid level if fixed prices are assumed. The costs are especially increasing at high penetration levels opening a huge gap between installed power and demand coverage. These "integration costs" of renewable energies are not respected by the levelized costs approach. It can sum up to 40% of the total system costs, if the integration is not planned and executed properly [26, 117].

Another approach could be the incorporation of externalities into the calculation of LCOE under the constraints of the added value of renewable energies in [121]. The U.S. Energy Information Administration proposed levelized avoided cost of electricity as a supplement

for LCOE. The approach calculates a net value of electricity, but is rather complicated and still does not incorporate important details [122]. Recently, the NREL introduced the concept of total value for renewable energy production to underline the positive effects of partly or fully overcoming intermittency. This concept adds a capacity value to the operational value taking demand oriented dispatch into account [118]. In conclusion of the stated facts, are substantial attempts to overcome the limitations of the LCOE.

6.2.4 Cost allocation

The cost allocation in cogeneration plants has a strong influence on the evaluation of technical solutions and the discussed plant designs. The literature gives several approaches for the respective cost allocation and are abundantly applicable for electricity and water generation. Principally, the costs can be allocated in four different ways:

- *Functional costing*: The method allocates the cost based on functional considerations. Capital and operational expenditures attributable to a single product are completely allocated to its account. Common capital and operational expenditures are allocated using a distinct ratio. This ratio can be defined for example as the share of capital expenditures or energy consumption of the respective plant component. More information can be found in [80, 123].

- *Exergy costing*: The costing method allocates cost based exergy destruction that can be attributed to the respective product or plant component. This method as well as methods using a similar approach are referred as exergoeconomics [102]. There are several literature sources to describe this approach [124–126].

- *Reference cycle costing*: The method bases on the comparison with a reference plant to allocate the fuel costs. The plant performance operated in cogeneration is compared with a single purpose plant for one product. This is called the reference cycle. For example, the cost of heat used to operate the desalination plant is calculated as the loss of electricity output in comparison to pure electricity generation. This approach is also known as the lost kilowatt method and was proposed in international publications [72, 120, 127–129].

- *Combinations*: Cost allocations which cannot be sorted into one of the mentioned groups could be calculated by a separate method. They are usually applied to very specific problems. One example can be found in [79].

In the following evaluation, the reference cycle costing method is applied in order to calculate the economics of the model plant. The main reason for this decision is to ensure the comparability to other research publications in this field. The calculation results can be found in section 6.5.1.

6.3 Data acquisition

The objective of this section is to rate the economic feasibility of the selected technological plant combination in different scenarios based on different markets. In order to carry out a realistic evaluation, the technical, meteorological and financial data need to be as accurate as possible. This section describes the approach to acquire sufficient data for the calculation.

6.3.1 Key indicators

In order to assess the economic performance of the model plant, it is important to define several technological key indicators. The following definitions briefly describe common concepts for the assessment of solar power plants. For the integration of the thermal desalination, some modifications are necessary and are described in the respective sections.

Annual DNI

The annual DNI describes the available sun irradiation at the selected location. The concentrated irradiation is converted into usable heat and is mostly transferred to working and/or storage media. Furthermore, the annual DNI has a high impact on the production and significantly influences other important indicators like the capacity factor or the solar multiple [130]. The output of the plant rises with a higher level of irradiation which also has a positive effect to the plant efficiency. For the actual calculation, own measurements are used to assess the plant performance (see also section 3.2 and 4.1).

Capacity factor (CF)

Most renewable energy plants are delivering fluctuating power and do not generate energy on demand (see also section 6.2.3). The capacity factor can be understood as ration

between rated capacity and actual generated electricity in a certain time period. Equation 6.3 compares the maximal possible power generation at rated capacity $P_{el,max}$ to the actual power generation of the plant $P_{el,gen}$ depending on available resources over a certain time period t [131].

$$CF = \frac{\sum_{t=1}^{t} P_{el,max}}{\sum_{t=1}^{t} P_{el,gen}} \tag{6.3}$$

The availability is not only determined by the available hours of wind or sunlight, but can be also extended by the utilization of energy storage systems. The name of the factor is derived from the rated total capacity of the respective plant (installed capacity). Figure 6.2 visualizes the operation extension of the CSP plant depending on the storage dimension, but covering the evening peak demand with 6 hours thermal storage.

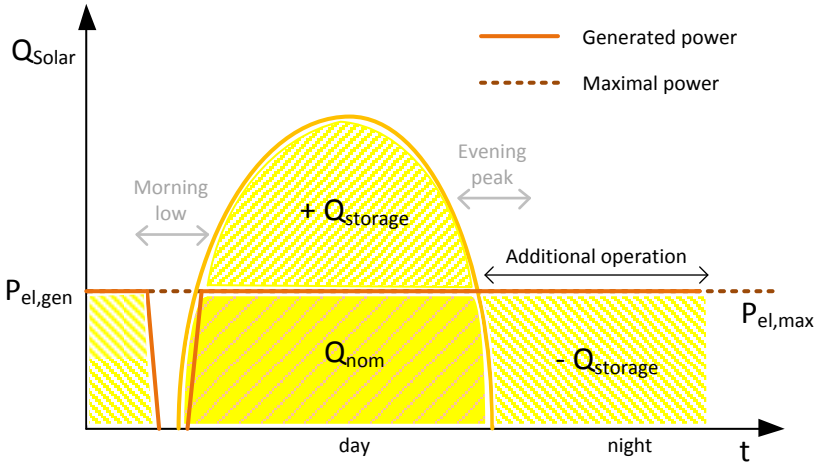

Figure 6.2: *Capacity factor and thermal storage, modified from [28]*

The influence of the CF is significant for the economical assessment of renewable energy driven plants. It has a very strong influence on the investment amortization and thus directly on the levelized cost of electricity. Furthermore, it is also an indicator for the evaluation of the total plant value, especially in grid connected cases to avoid expensive energy storage systems. Usually, renewable energy technologies like solar photovoltaic (without storage) and wind turbines achieve only small capacity factors depending on the location and the available resources (around 10 to 30%). Especially for wind power plant, the location is essential for a high CF. Fluctuating energy resources always need a corresponding dispatchable (mostly fossil-fueled) power plant to replace the generated

electricity in hours without sunlight or wind. CSP with thermal storage can reach much higher CF which are comparable to hydro power or fossil fuel power plants. Only those technologies can replace corresponding dispatchable power plants and deliver power on demand.

Capacity credit (CC)

The CF only describes the availability of power generation from an respective energy source by a time period. The plant availability at a certain point in time is not included and requires the introduction of the capacity credit (CC). As the power demand varies during the day, the peak demand does not necessary comply with the availability of power generation. Like already mentioned, the power generation from fluctuating renewable energies require almost the same capacity of dispatchable backup power. The CC is defined as the difference between total demand at peak time D_{peak} and the residual demand D_{res} served by fossil backup plants at peak time divided by the installed capacity $P_{el,max}$ of the respective renewable plant [132]. So the CC describes how much fossil backup capacity can be replaced by the renewable energy plant. It can be calculated according to equation 6.4.

$$CC = \frac{D_{peak} - D_{res}}{P_{el,max}} \tag{6.4}$$

Full load hours (FLH)

The availability of power generation can also be expressed in full load hours (FLH). The indicator sums up all hours where the plant is running at nominal capacity in a certain period of time. Assuming one complete year, the full load hours cannot exceed more than 8760 hours. Depending on the availability of information, the FLH can be calculated using the CF considering the same time period. A high share of FLH during the year increases the economic performance of the plant. The same implications are applicable like already mentioned for the CF.

Solar multiple (SM)

Like already discussed, the CF or FLH are of high importance for the value of a plant. So the maximization of CF or FLH implies that the power generation should occur as often as possible in the considered time frame. For solar or wind driven power plants,

the goal can be only achieved by coupling energy storage systems to the power plant. As CSP plants are basically normal steam driven power plants, they require a certain amount of thermal energy supplied Q_{nom} to the steam generator at design capacity. If the solar field is dimensioned in the design point, it will deliver this thermal energy only during daytime (solar field 1). Figure 6.3 shows the context of increasing solar field size and the extension of maximal thermal storage duration.

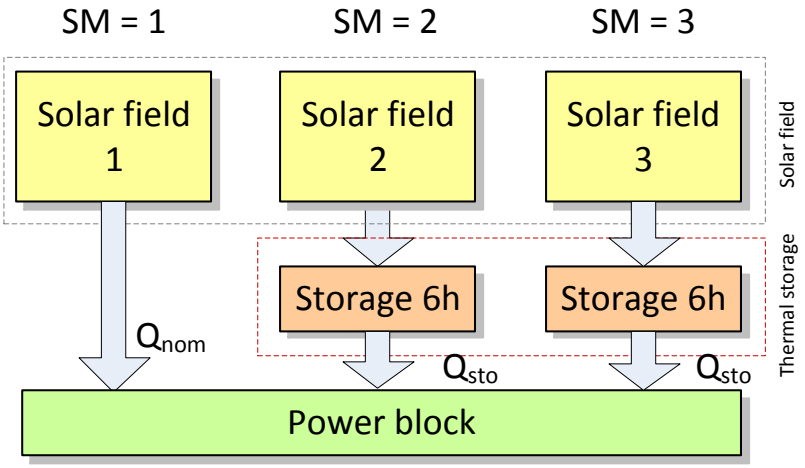

Figure 6.3: *Solar multiple and thermal storage, modified from [29]*

Adding another solar field with the same size (SM=2) allows the storage of this additional thermal energy. Depending on the dimensioning of the storage system, the solar thermal energy is stored during daytime for e.g. 6 hours. To be able to meet this demand over a certain period of time, the size of the solar field and the thermal capacity of the receiver needs to be multiplied. The factor used for this multiplication is defined as solar multiple (SM) which can be calculated according to equation 6.5. The calculation is performed using the total thermal energy demand for nominal power generation Q_{nom} and the thermal energy in the storage system Q_{sto} [131].

$$SM = \frac{Q_{nom} + Q_{sto}}{Q_{nom}} \tag{6.5}$$

6.3.2 Power plant parameters

The CSP plant described in the previous chapters is simulated and analyzed with the use of the software Ebsilon Professional [20]. The technical model of the CSP plant and especially the heliostate field is derived from known projects available from the Ebsilon

solar library and specially designed to meet the requirements of a cogeneration plant. The technical model of the desalination unit has been created in cooperation with the project engineers of an existing pilot plant using the kernel scripting module of Ebsilon. Various simulations of different configurations have led to the model plant. For this cogeneration plant, time series analysis of the extensive meteorological data of the given location have been executed to determine the optimal design parameters for the plant. All design parameters are summarized in table 6.1.

Category	Symbol	Parameter	Unit
Gross electricity	$P_{el,gen}$	13.2	$\mathrm{MW_{el}}$
Gross water	W_{gen}	2250	$\mathrm{m^3/d}$
Total reflective area	A_{ref}	178,530	$\mathrm{m^2}$
Total land use	A_{tot}	1,368,732	$\mathrm{m^2}$
Receiver, thermal capacity	Q_{rec}	100	$\mathrm{MW_{th}}$
Storage, thermal capacity	Q_{sto}	630	$\mathrm{MWh_{th}}$
Annual DNI	I_{DNI}	3087	$\mathrm{kWh/m^2}$
Solar multiple	SM	2.8	-
Capacity factor	CF	85.1	%
Full load hours	FLH	7448	h

Table 6.1: *Power plant operational parameters, adapted from 4.2*

In a further step, the operational parameters obtained from Ebsilon have been transferred to the System Advisor Model (SAM) of NREL [114]. The software and the corresponding data library have been developed to evaluate and compare various power generation technologies and most recently also first desalination designs. Furthermore, a special model for point focusing concentrated solar power technology utilizing thermal energy storage has been implemented. The model incorporates the knowledge of several realized projects and thus the results of a number of feasibility studies executed by different engineering consultants [114]. It is the most advanced publicly available tool for the economic evaluation of power generation.

The model plant with its solar tower and heliostat field design has been optimized using the SAM data library and merged to the simulation results from Ebsilon to ensure best performance at the lowest predicted expenditures. In order to obtain more realistic results from the simulation, a location data file with meteorological information has been implemented. The data from the own meteorological station are applied, see also chapter 4 in section 4.1 and [31].

6.3.3 Economic input data

The quality of the input data for the economic assessment of the modeled cogeneration plant have a strong influence to the calculation results. Therefore, a careful literature review has been conducted to collect as much information as possible. The economic assessment calculations also depend on the assumptions of the boundary conditions.

The plant design obtained and optimized in Ebsilon has been modeled and discussed in sections 3.3 and 4.4. It has been implemented in SAM and is used as reference for the collection of technology-specific economic data. The technologies for renewable energies, power generation and desalination are highly diverse which leads to specific economic characteristics. Due to the relatively small dimension of the model plant in comparison to plants in reviewed publications, the gathered data do not exactly fit to this research and need to be scaled accordingly (see deviations in table 6.1 and section 4.1).

The most applicable findings of the literature review are special costing schemes for solar tower technology and thermal desalination, which are briefly discussed in the following paragraphs:

- *Turchi et al.* [4, 63, 115]: The costing scheme has been developed for the U.S. National Renewable Energy Laboratory (NREL) and has been first published in 2013. It contains a vast amount of empirical information from realized plant projects as well as the results of many feasibility studies either commissioned or executed by NREL. It comes with a set of tools for adapting and scaling the cost model to new plant designs built in an integrated approach of SAM [114] and MS Excel.

- *Fichtner* [47,111,112,133]: The Fichtner GmbH & Co. KG is a renowned consulting agency for renewable energy projects. They have many cooperations especially with the German Aerospace Center (DLR), the World Bank and various governmental agencies. The cost scheme published in 2010 by Fichtner is not publicly available as a cost model. However, the presence of the evaluations, feasibility studies, technical reports and publications are roughly sufficient to apply their cost scheme to the examined model plant. The empirical information from Fichtner also relies on the data from realized projects and a big set of feasibility studies. The available financial information for reference plants has been adopted to the model plant by means of formulas published in works by Fichtner or simple linear regression. Therefore, the application of the financial information is not as accurate as done by the tool set, but it is a good source for comparison and verification of results obtained from the NREL cost model.

- *Desalination* [12, 15, 75, 82]: The financial information for the low-temperature desalination unit is not available in literature or technical reports. This is due to the reason that the technology has been recently developed and there has been build only one pilot plant. The financial data have been acquired by personal communication from Watersolutions AG (5033 Buchs, Switzerland). It can be assumed that the financial data are quite accurate and little subject to uncertainty.

To convert some information given in € to US $, the average exchange rate for the last five years has been applied. However, for the calculation is used a mean conversion factor of 1.326 US $/€. In a final step, all collected financial data have been adjusted for inflation and converted to real dollar using chemical engineering construction price index CEPCI of December 2014. This price index has the purpose to track the development of prices for land, components, engineering and construction observed in the United States. Although the index is bound to the U.S. market, it can be a first indicator for the world wide change in prices, whereas reliable information for the MENA region is hardly available. It can be assumed that local labor costs are significantly lower compared to the U.S. market, which needs to be examined separately.

6.4 Capital and operational expenditures

Due to the dimension of the model plant, the capital expenditures (CAPEX) for the model plant is estimated using the technical information described in table 6.1. One limitation of the used data is the validity in terms of actuality, so that some of the used financial values need to be checked carefully. Furthermore, possible exchange rate variations can not be respected. This results in estimations which are subject to a degree of uncertainty. The most recent publicly available cost model is developed and maintained by NREL [4, 63, 115, 118]. The organization conducted and commissioned many studies on the economics of renewable energies and implemented the results in their cost models [115]. The CAPEX are calculated in detail with a cost model specially developed for solar towers with molten salt storage. All results are compared to the CAPEX calculations by Fichtner for solar tower using molten salt thermal storage [47, 111, 112, 133]. Those data are roughly scaled using formulas proposed by Fichtner or linear functions composed out of respective projections. The calculations have been applied to a study of the World Bank for an site in South Africa in 2010 [47].

The site of El Gouna, Egypt, has been chosen as parameter for the cost model by Turchi et al. The local meteorological data has been obtained by the meteorological station

described in section 4.1. Compared to the examined site by Fichtner in Upington, South Africa, the weather conditions in El Gouna are quite similar. It ensures the comparability of the calculation results. Furthermore, the thermal energy storage of all plants need to be adjusted to 15 hours and to a solar multiple (SM) of 2.5. The consequence are slight deviations from the design given in table 6.1. All prices are converted to real US $ by using the chemical engineering plant construction index (CEPCI) in its most recent edition from December 2014.

6.4.1 Solar power plant

The special design of the model plant has been considered for the calculations. Although there are many different technological options to construct a solar tower plants with thermal energy storage, the CAPEX cost structure is very similar. It can be categorized by seven functional categories, which are examined as follows:

- *Site enhancement*: mainly ground preparation, leveling of soil.
- *Heliostate field*: poles and mirrors, two axis tracking system.
- *Receiver*: molten salt heat exchanger on top of the tower, including piping and insulation.
- *Tower*: concrete structure, piping insulation and pumps.
- *Thermal energy storage*: two liquid salt tanks including piping, molten salt heat transfer liquid corresponding to the thermal storage design.
- *Power plant*: turbine stages, power generator, feed water pumps and preheating lines.
- *Balance of plant*: molten salt steam generator with superheaters, piping, salt pumps, controls and support structures.

The indirect cost could be introduced as the eighth category to sum all expenditures not included in the other functional categories. These categories have been defined and assessed in various studies by NREL, DLR and CSIRO (Australia's national science agency) or their respective partners in different engineering consulting companies. The categories are used in the calculations by Turchi et al. and Fichtner with little deviations. The following sections briefly describe the respective category and the results for the dimension of the model plant.

Site enhancement

The category includes the cost of preparation of the site including clearing and leveling of the occupied area. The Turchi cost model includes also costs for flood water control, water supply infrastructure as well as roads and fences. The Fichtner model includes land cost in this category, which is allocated to indirect cost by Turchi et al. This variation is the main reason for the differences between the projections. The required land is given by a function of the total reflective area of the heliostats. Fichtner calculates the land use with the following equation 6.6. The total land area occupied by the plant is denoted as A_{tot} and the total reflective area of the heliostat field is given with A_{ref} [134].

$$A_{tot} = A_{ref} \cdot 1.3 + 180,000 \qquad [\mathrm{m}^2] \tag{6.6}$$

All results are summarized in table 6.2. The costs for the site enhancement are higher using the Fichtner calculation. This can be attributed to the included land cost. Whereas the scaled values show a lower cost factor by Fichtner. Due to the fact that the Fichtner values are calculated by linear regression, the calculation by Turchi can be considered as more accurate.

Parameter	Turchi 2013		Fichtner 2010		
	Design	Scaled	Design	Scaled	Unit
Gross power output	115	13.2	50	13.2	$\mathrm{MW_{el}}$
Site enhancement	19	24	24	15	$\$/\mathrm{m}^2$
Land used A_{tot}	12,232,530	1,516,260	1,007,240	412,089	m^2
Total	**31.1**	**4.7**	**24.1**	**6.4**	M$

Table 6.2: *Site enhancement costs*

Heliostat field

The category includes the cost of the heliostats as well as electric wiring and controls. The size of the heliostat field depends on several factors. First, the thermal design of the power block and its electrical power output have the strongest influence. Second, the solar multiple and the storage capacity have an impact on the heliostat field design. Furthermore, the meteorological ambient conditions defining the available solar energy need to be respected accordingly. The total reflective area A_{ref} can be calculated by the total thermal energy consumption of plant at nominal capacity Q_{nom} and the thermal energy in the storage system Q_{sto} divided by the efficiency of the field η_f, the receiver

η_{rec} and the available direct normal irradiation DNI_d at design point conditions. The calculation is summarized in equation 6.7:

$$A_{ref} = \frac{Q_{nom} + Q_{sto}}{\eta_f \cdot \eta_{rec} \cdot DNI_d} \qquad [\mathrm{m}^2] \tag{6.7}$$

The required investment costs for the solar field can be accounted for corresponding to table 6.3.

Parameter	Turchi 2013		Fichtner 2010		
	Design	Scaled	Design	Scaled	Unit
Gross power output	115	13.2	50	13.2	$\mathrm{MW_{el}}$
Heliostat field, specific costs	183	183	263	355	$\$/\mathrm{m}^2$
Total reflective area	1,601,000	192,948	636,339	178,530	m^2
Total	**293.1**	**35.3**	**167.2**	**63.3**	M$

Table 6.3: *Heliostat field costs*

The comparison of both sources shows significantly lower cost factors in the Turchi cost model. This deviation can be explained in two ways. One reason could be cost reductions in the heliostat manufacturing achieved in recent years. Another explanation can be the major difference in size and design of available heliostats which are quite similar to photovoltaic tracking systems. Since the heliostat field consists of a defined number of heliostats, the cost factor should be almost constant. The overall lower cost factor and its robustness to the economies of scale increase the credibility of the Turchi calculation method and it seems that the data from this cost model are more accurate. Using the obtained data from Turchi and the given design parameters of the model plant, one heliostat with 100 m^2 reflective area would cost approximately 18,300 US $, compare also to table 3.3 in section 3.3.1.

Receiver

The receiver category is composed of the cost requirements for the molten salt receiver, piping, pumps and controls. The dimensions of the receiver and subsequently its cost depend on the concentrated incident power Q_{inc} collected by the heliostat field at design conditions. Other parameters like the thermal energy demand of the storage Q_{sto} and the power block influence this cost category as well. The thermal design capacity of the receiver Q_{rec} can be calculated by adding the total thermal energy consumption of plant at nominal capacity Q_{nom} and thermal energy in the storage system Q_{sto} and the division of the receiver efficiency η_{rec}.

$$Q_{rec} = \frac{Q_{nom} + Q_{sto}}{\eta_{rec}} \qquad [\mathrm{MW_{th}}] \tag{6.8}$$

Applying equation 6.8 gives the required investment results for the receiver summarized in table 6.4.

Parameter	Turchi 2013		Fichtner 2010		
	Design	Scaled	Design	Scaled	Unit
Gross power output	115	13.2	50	13.2	$\mathrm{MW_{el}}$
Receiver, specific costs	113	227	274	538	$\$/\mathrm{kW_{th}}$
Receiver, thermal design	837	99	330.7	99	$\mathrm{MW_{th}}$
Total	**94.3**	**22.4**	**90.8**	**53.3**	M$

Table 6.4: *Receiver costs*

The Fichtner cost model gives a higher cost factor compared to the Turchi cost model for the reference and scaled model plant. It can be concluded that the impact of downsizing the receiver has almost the same influence for both sources. The scaled cost factors for the model plant almost double the specific costs of the reference plant using the Fichtner calculation method. The reason for that can be seen in high fixed costs for the receiver construction. Furthermore, the receiver requires special material qualities due to the intensive thermal flux per $\mathrm{m^2}$, which can reach up to 1,000 $\mathrm{kW/m^2}$. For more information see also chapter 2 and section 2.1.2.

Tower

The category includes the cost for the tower as well as piping and insulation. The tower height has the strongest cost influence and depends on the heliostat field dimension and layout. It requires careful consideration of all parameters influencing the heliostat field. Usually, the component costs are calculated as a function of the tower height. The Fichtner calculation method for solar towers without storage C_{to} estimates the component expenditures by a fixed amount of installation costs multiplied by an exponential function of the tower height h_t. The calculation is given in equation 6.9:

$$C_{to} = 552,000 \cdot e^{\frac{h_t}{100}} \qquad [\mathrm{US\ \$}] \tag{6.9}$$

The tower height h_t is given in m [134], see also section 3.3. Adding a fixed correction of 2,250,000 US$ converts the results from solar tower without storage to solar tower with storage system. Concerning this case, the cost model by Turchi uses the DELSOL3

formula described in [135] for the tower cost estimation. Basically, the approach for the calculation is very similar, but uses different coefficients given in equation 6.10. The required investments for solar tower and piping are summarized in table 6.5.

$$C_{to} = 15,300,000 \cdot e^{h_t \cdot 0.0113} \qquad [\text{US } \$] \tag{6.10}$$

Parameter	Turchi 2013		Fichtner 2010		
	Design	Scaled	Design	Scaled	Unit
Gross power output	115	13.2	50	13.2	$\mathrm{MW_{el}}$
Tower height	215	80	255	80	m
Total	**33.2**	**7.2**	**9.2**	**3.5**	$\mathrm{M\$}$

Table 6.5: *Tower costs*

The comparison shows that the Fichtner formula strongly underestimates the tower costs in contrast to the cost projections for the receiver and the heliostat field. The DELSOL3 formula [135] delivers a more reasonable projection. The reasons can be found in differences in the calculation for the distribution of auxiliary equipment between tower and receiver like piping and insulation.

Thermal energy storage

The costs for the thermal energy storage system are calculated by adding the investment costs for the two molten salt storage tanks, the storage media, controls, insulation and piping. The size of the storage depends on the thermal power required by the power block and the respective maximal storage time. It also determines the tank volume. The capacity of the thermal storage Q_{sto} can be calculated by the nominal thermal design capacity Q_{nom} of the power block multiplied by the maximal storage time given in equation 6.11.

$$Q_{sto} = Q_{nom} \cdot t_{sto} \qquad [\mathrm{MWh_{th}}] \tag{6.11}$$

The calculation for required investment costs of the thermal energy storage are given in table 6.6.

It can be stated that the costing methods summarized in table 6.6 for the thermal energy storage show similar results for both models. Nevertheless, the data obtained from Fichtner cost model result in slightly higher costs. The scaled specific costs for

Parameter	Turchi 2013		Fichtner 2010		
	Design	Scaled	Design	Scaled	Unit
Gross power output	115	13.2	50	13.2	$\mathrm{MW_{el}}$
Thermal energy storage, specific	26	31	28	32	$\$/\mathrm{kW_{th}}$
Storage capacity	4185	525	1782	664	$\mathrm{MW_{th}}$
Total	**108.7**	**16.5**	**50.6**	**21**	M$

Table 6.6: *Thermal energy storage costs*

the model plant are higher compared to the reference plant which can be attributed to the smaller plant size and the constant fixed installation costs for the two tank storage system.

Power block and balance of plant

The power block cost category includes the cost for the steam turbines and all auxiliary systems. Furthermore, the costs for the feed water system, cooling system, condensate system, water treatment system, piping and controls are added in this category. The size of the power block is also subject to its efficiency and the rated electricity output of the plant $P_{el,gen}$. The cost category balance of plant includes the steam generation system, respective piping, hot salt pumps, controls and the support structures. The dimensions are subject to the thermal design of the production plants. The required investments for the power block and balance of plant are calculated in table 6.7.

Parameter	Turchi 2013		Fichtner 2010		
	Design	Scaled	Design	Scaled	Unit
Gross power output	115	13.2	50	13.2	$\mathrm{MW_{el}}$
Power block, specific costs	1185	1520	1283	2421	$\$/\mathrm{kW_{el}}$
Balance of plant, specific costs	349	538	586	859	$\$/\mathrm{kW_{el}}$
Total	**176.4**	**27.2**	**93.5**	**43.3**	M$

Table 6.7: *Power block and balance of plant costs*

The comparison of the specific costs per $\mathrm{kW_{el}}$ show that the cost for the power block has significant scaling effects. Generally, power plants are subject to great economies of scale which results in higher specific costs for a smaller power block. The design plant cost factors are quite similar, while these for the model plant show a big deviation. The reason can be found using the linear regression applied in the calculation by Fichtner which is less plausible compared to the detailed estimation by Turchi. The same arguments apply

to cost structure of the balance of plant. However, the balance of plant costs projected by Fichtner are comparatively high in contrast to the estimations by Turchi.

Indirect costs

The indirect cost category represents costs which cannot be directly allocated to the plant components. It is given as a percentage of the engineering, procurement and construction costs (EPC) described above. Furthermore, the cost groups differ depending on the cost model. Turchi includes land cost in the indirect cost, whereas Fichtner the planning costs for the plant. Both projections add the cost of ownership to the indirect costs. Fichtner estimates a fixed percentage of 8 % for EPC planning and 5.5 % for owner costs. Turchi scales the percentage of indirect cost with the size of the plant. The indirect costs of the model plant calculate to 12.7 % for the Turchi cost model and 13.5 % for the Fichtner model, respectively.

Total CAPEX

The total CAPEX is obtained by the addition of the total category costs discussed in the previous sections. Using all design and scaled unit cost in combination with their respective plant design data results in the capital expenditures of each plant per category. The specific CAPEX can be calculated dividing the total CAPEX by the plants gross electricity generation. Table 6.8 summarizes the results for the model plant using Turchi and Fichtner costing methods.

Parameter	Turchi 2013	Fichtner 2010	Unit
Site enhancement	4.75	6.37	M$
Heliostat field	35.33	63.34	M$
Receiver	22.44	53.26	M$
Tower	7.23	3.48	M$
Thermal energy storage	16.48	20.99	M$
Power block	20.06	31.95	M$
Balance of plant	7.10	11.34	M$
Contingencies	7.94	19.07	M$
Owners cost	15.40	12.38	M$
Indirect cost	19.10	27.64	M$
Total CAPEX	**140.43**	**237.45**	M$
Specific CAPEX	**10638**	**17989**	$\$/\mathrm{kW_{el}}$

Table 6.8: *Total and specific CAPEX of the CSP plant*

The information given in table 6.8 can be also visualized as cost breakdowns with given share for each category. Figure 6.4 shows the breakdown for the model plant using the Turchi cost model and figure 6.5 the projection for the model plant using Fichtner data, respectively.

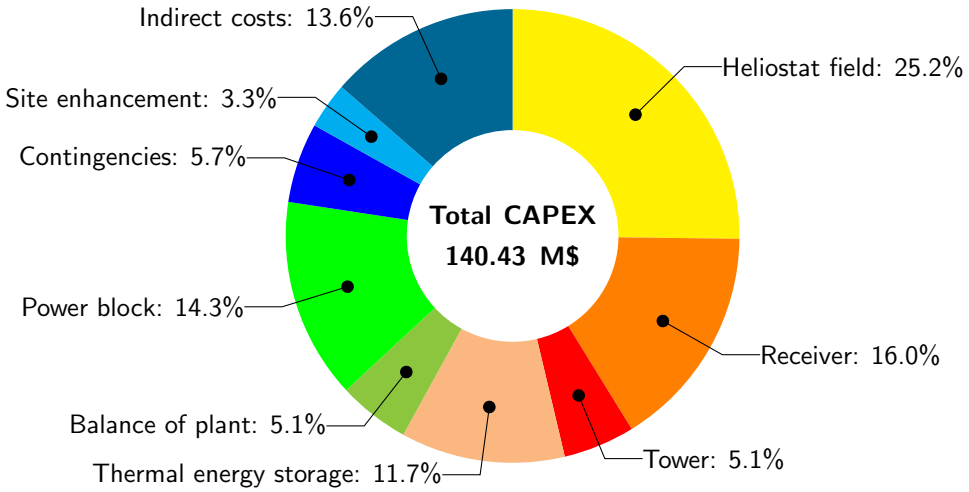

Figure 6.4: *CAPEX breakdown for the model plant, Turchi cost model*

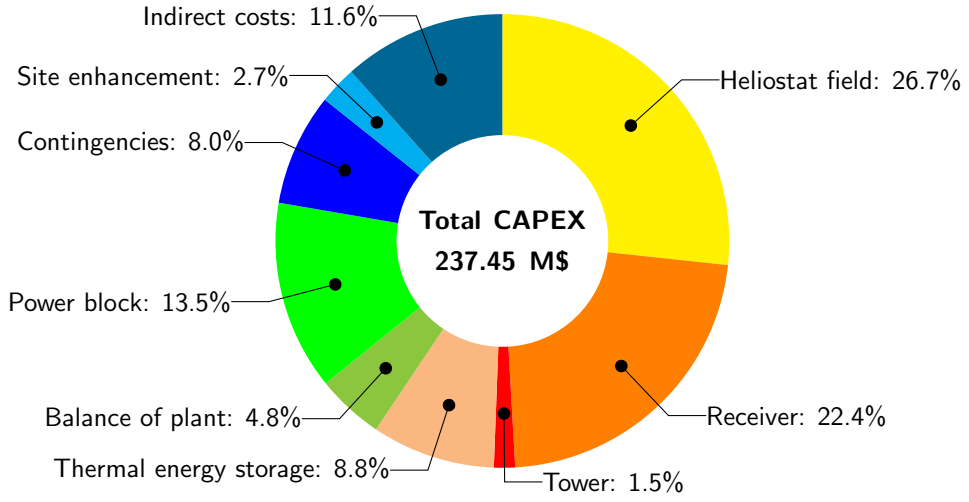

Figure 6.5: *CAPEX breakdown for the model plant, Fichtner cost model*

Analyzing the cost structure of the model plant, the comparison of the projected CAPEX shows different results. It can be stated that the comparison of tower and receiver costs show the highest deviation while the distribution of the cost share is quite similar for the other categories. Furthermore, the impact of the thermal energy storage is much lower in the Fichtner projection compared to Turchi. The cost increase can be also attributed to the dominant share of receiver cost which does not grow proportionally to the heliostat field costs. The reason for that can be found in the reference cost factor which is already

quite high in the Fichtner model. However, the shrinking impact of the heliostat field cost can be seen as main difference between the two costing models. In other words, the heliostat field is easier to scale compared to the other cost categories. The mechanism applies for both models. Furthermore, this observation is plausible: since the heliostat field consists of a large number of single units resulting in variable total costs. At the same time, the other components like receiver and power block include a large share of fixed cost independent of the installed capacity.

Summarizing, the calculations show that the capital expenditures estimated using Fichtner data are significantly higher compared to the results obtained from the Turchi cost model. The reason can be attributed to the general scaling errors. Due to the low availability of information, only linear regression has been applicable, despite it is considered as not sufficient. However, the Turchi cost model is more up-to-date and delivers more reasonable results in terms of scaling. In consequence of that, the obtained data from the Turchi cost model is used for further calculations.

6.4.2 Desalination unit

The cost structure of the capital expenditures for the desalination unit is given by five functional categories, which are typical for thermal desalination units:

- *Heat exchangers*: The category includes the power plant condenser (HEX1), heat recovery (HEX2), distillate cooling (HEX3) and preheating (HEX4). The heat exchangers for salt water are fabricated using titanium due to resistance against corrosion. The cost calculation base on the needed heat transfer area in m^2.

- *Pumps*: Including all required pumps for circulation mass flows (evaporator and condenser reactors) as well as supplemental pumps for brine and distillate streams. The circulation pumps need to be frequency controlled in order to allow for variable volume flows in part-load operation.

- *Piping and vessels*: The reactor vessels are fabricated using fiber reinforced plastic to generally avoid corrosion. The size is being determined by the thermal capacity and the required volume flows (see chapter 4.4 and 4.4.1). The piping includes all necessary connections between the heat exchangers and the reactors.

- *Controls*: The category includes the sensors, controls and wiring needed for the plant operation.

- *Civil engineering works and connections*: Given in percentage for external water connections and ground preparation.

In addition to the mentioned cost categories, there needs to be added another category for indirect costs. They account for expenditures which cannot be assigned to a particular components. Another cost category applicable are the investments for engineering, construction and procurement (EPC). Due to the relatively new release of the low-temperature desalination to the commercial market, there are no economic data in related work until now. The costs of the demonstration plant commissioned in 2009 have been much higher due to sophisticated measuring techniques and sensors. Nevertheless, the lessons learned identified several cost saving potentials which are included in this calculation.

Based on the results from the technical model, the financial data for this study has been acquired by personal communication with the chief technical officer and can be considered as quite accurate [15]. The capital expenditures of the low temperature distillation are listed in table 6.9 representing the categories explained above.

Component	Cost	Unit
Heat exchangers	1,020,250	$
Pumps	145,750	$
Piping and reactors	225,250	$
Controls	119,250	$
Civil works and connections	304,750	$
EPC costs	364,375	$
Indirect costs	430,625	$
Total CAPEX	**2,610,250**	$
Specific CAPEX	**1,305**	$\$/(\mathrm{m}^3/\mathrm{d})$

Table 6.9: *Total and specific CAPEX of the desalination unit*

The results of table 6.9 are visualized in figure 6.6 showing the cost breakdown of the desalination plant. It has been already expected that the major cost factor are the sea water resistant heat exchangers comprising about 40% of the investment. The stability against corrosion requires titanium heat exchangers which are twice as expensive as comparable other models made of stainless steel. The remaining cost categories like pumps, piping, vessels and controls amount to about 30% of capital expenditures, which is considerably less compared to the heat exchangers. The indirect and EPC costs share the last 30% of the investment.

The results of this estimation are relatively accurate, because they are calculated using primary source information and a special scaling calculation is not necessary. Therefore, there is no need for further adjustment and they are applied in the subsequent considerations.

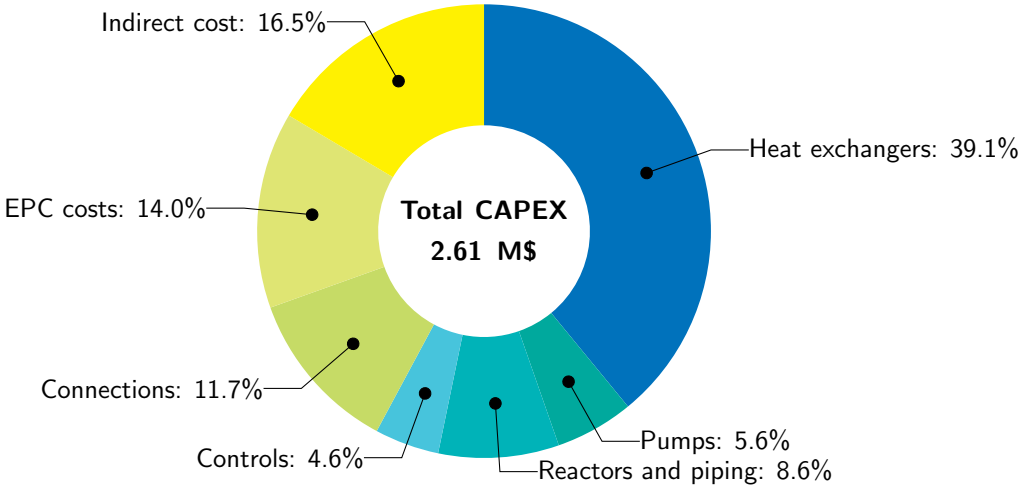

Figure 6.6: *CAPEX breakdown for the low temperature desalination*

6.4.3 Operational expenditures

The cost structure of operational expenditures (OPEX) for the solar tower system is defined as the variable costs of power generation, maintenance cost and personnel expenses. They are usually calculated as a percentage of the CAPEX. The main operational costs of the solar power plant can be expected from the heliostat field maintenance. This includes mainly mirror cleaning and replacement as well as maintenance of the 2-axis tracking system. The influence of dusty ambient conditions (sand storms) and occasionally high wind loads has not been investigated yet. The empirical values from the literature range between 2% for large scale plants and 2.5% for small scale plants [47, 63, 133]. As the examined model plant can be considered as a small scale plant, the operational expenditures of 2.5% of the total investment are considered annually in all calculations for the model plant.

For low temperature distillation, the operational expenditures are comparatively low for a desalination system. They can be considered annually about 1.5% of the CAPEX [12]. Since the low temperature desalination works by the mechanisms of thermal treatment at low temperatures and pressures, the designed heat exchange parameters need to be maintained. Due to the special developed spraying system, the impact on scaling and fouling compared to tube bundle heat exchangers is negligible small (see also chapter 2,

section 2.5.1 and figure 2.20). Furthermore, this spraying system also reduces the need for chemicals and material replacements. For all subsequent calculations 1.5% of the total investment are considered annually as operational expenditures.

Component	Percentage	OPEX per year	Unit
Solar power plant	2.5%	3,510,000	$\$/\mathrm{a}$
Low temperature desalination	1.5%	40,000	$\$/\mathrm{a}$
Total		**3,550,000**	$\$/\mathrm{a}$

Table 6.10: *Total OPEX for the model plant per year, rounded*

Table 6.10 shows the annual operational expenditures for the solar power plant and the desalination system by the CAPEX calculated with Turchi cost model. It can be seen, that the major share can be assigned to the solar power plant. The desalination unit just causes around 1% of the total OPEX for the model plant and can be almost neglected. It is especially important comparing this system with reverse osmosis (RO) desalination units, which need high electricity supply for pumping and regular replacement of the membrane depending on the feed water quality. The OPEX of such systems are significantly higher which is due to frequent service intervals.

6.5 Results

The comparison of combined power and water production plants adds another layer of complexity. In this context, the calculation of the optimal ratio of power and water production is of special interest. The calculation of this optimal ratio requires the determination of the levelized cost of electricity and the levelized water cost according to section 6.2.1 and 6.2.2. The calculations are performed using the results of the previous chapters to determine the CAPEX and OPEX. Due to the timeliness and better scaling properties of the Turchi cost model [4, 63, 115], all results from Fichtner are not considered.

To assure the comparability of those calculations results, it is necessary to make some basic financial assumptions. The calculation is performed by the assumption of weighted average cost of capital of 8%, which is reported by IEA [53] and a total plant lifetime t_c of 20 years.

6.5.1 Levelized costs

After the calculation of CAPEX and OPEX in sections 6.4 and 6.4.3, the levelized product costs can be analyzed. Although the concept of levelized cost has known limitations, the model plant can be described sufficiently using these key indicators. The plant has a very high capacity factor CF of more than 80% and very high capacity credit CC avoiding the general challenges for renewable energy generation.

To calculate the levelized water costs (LWC) it is necessary to define the fuel allocation to the desalination plant which has been discussed in section 6.2.4. Due to the option to compare the results with other research outcomes, the reference cycle method is used in order to allocate the fuel between power and water production. It is robust and delivers valid results. The reference cycle method considers the electricity not generated due to the desalination heat supply.

Furthermore, the calculation allows two possible methods. As the desalination system replaces the conventional power plants cooling system, the investments can be calculated as one complete investment. It results in a lowered total CAPEX and thus in a lowered LWC. Table 6.11 summarizes both calculations for a "single investment" considering two separate investments for power and desalination plant, while "combined investment" describes the approach considering an integrated investment cost for the power plant and the desalination system.

	Single investment	Combined investment	Unit
Levelized cost of electricity (LCOE)	0.18	0.18	$\$/\mathrm{kWh}$
Levelized cost of water (LWC)	2.99	2.49	$\$/\mathrm{m}^3$

Table 6.11: *Levelized product costs for the cogeneration plant per year*

Naturally, the approach with integrated investment for power plant and desalination unit achieves significant lower levelized water cost. It is remarkably that the levelized cost of electricity are only minor influenced. The reason for that can be seen in the minor share of capital expenditures of the desalination unit, compare also to section 6.4.2. However, the levelized water cost in both scenarios are rather high compared to installed desalination plants. The reason is explained by the chosen calculation method (reference cycle). The lost electricity cost causes a high price as it is accounted using the LCOE of the cogeneration plant. Furthermore, the combined approach seems more plausible since the thermal desalination replaces the cooling system of the power plant. The exact cost share by each plant component could be subject to future research and would

identify cost saving potentials. Basing on the results of chapter 5 would also allow for an exergo-economic analysis described in [125, 126].

6.5.2 Cogeneration ratio

The combined power and water production has been analyzed in chapter 4, section 4.4 and is used now for the economic calculations. In combination with the economic data obtained, a function can be fitted to determine the cost-optimal cogeneration ratio between power and water production.

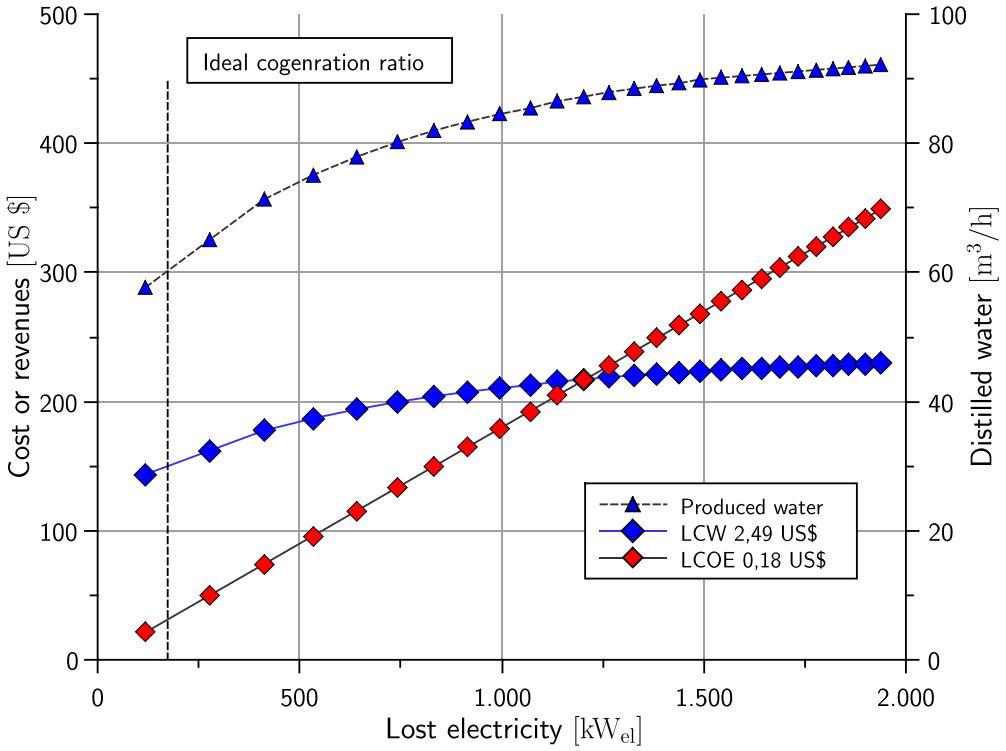

Figure 6.7: *Water production and lost electricity*

Figure 6.7 visualizes the cost and revenues in relation to the electricity losses in power generation. Assuming constant financial boundary conditions, the ideal cogeneration ratio reaches the optimal conditions in the point where the difference between the revenue generated by water production and the respective heat cost for water production is maximized. Figure 6.7 shows the water production as a function of the energy consumption. With other words, it can be also expressed as not-generated electricity in the power plant and the respective evolving costs and revenue functions.

The cost-optimal cogeneration ratio for the discussed case in figure 6.7 calculates to a water production of 63 $\mathrm{m^3/h}$ (around 1500 $\mathrm{m^3/d}$) and lost electricity of 170 $\mathrm{kW_{el}}$. How-

ever, it means that only a maximized power generation could reach economic competitiveness (see also chapter 4, case 2 in section 4.3.2). Due to thermodynamic limitations, this ratio is technically difficult to maintain under the current boundary conditions and assumptions. The best compromise can be seen in the water production of 70 $\mathrm{m^3/h}$ (1680 $\mathrm{m^3/d}$) associated with an energy loss of 950 $\mathrm{kW_{el}}$. This ratio has been also used to calculate the levelized product cost. The operational parameters can be compared to the model parameters calculated in section 4.3.2 for case 2.

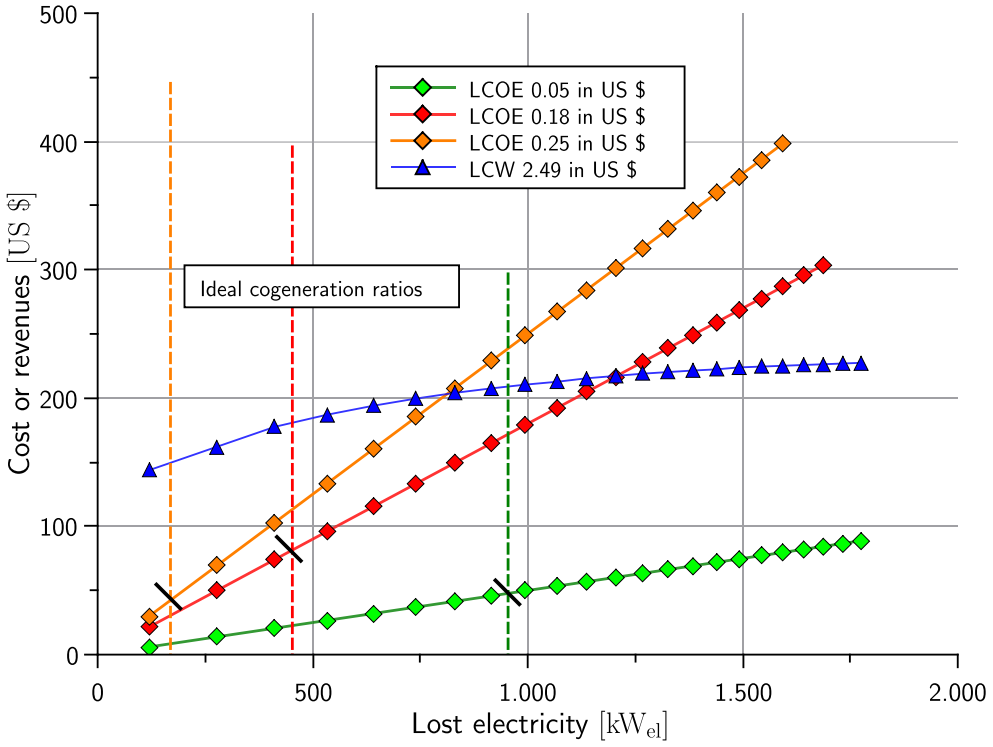

Figure 6.8: *Optimal cogeneration ratios for increasing LCOE*

The final sales price for water and electricity varies because of several reasons and locations. First, the sales price is influenced by the availability of the resource. Secondly, there are a numerous other factors like distribution cost, taxes and subsidies. However, the water price can heavily influence the ideal cogeneration ratio and has to be examined under different assumptions.

Figure 6.8 shows the ideal cogeneration ratios for a fixed water price (LWC) and different cost functions for the lost electricity (LCOE). It illustrates the reference cycle method and respective financial effects. Furthermore, figure 6.8 shows that the optimal cogeneration ratio shifts to a higher water production when the LCOE is assumed to be low.

In general, it can be stated that the application of the reference cycle may underestimate the real water costs, especially when it is applied to an energy intensive desalination

processes. The low-temperature desalination examined in this thesis can operate at low pressures and temperatures compared to other thermal desalination processes. Therefore, it seems more appropriate to apply an exergy costing method to obtain more accurate results. It could lead to different optimal cogeneration rations favoring an increased water production and can be subject to further research using the results of chapter 5 and section 5.6.

To identify the best cogeneration ratio for a specific site, an analysis of the financial boundaries of the local market and the demand scenarios can be executed. In regions where potable water is scarce and thus water tariffs are high, the maximized production of water can be favorable even at a comparatively high loss in electricity production efficiency.

Chapter 7

Case study

The case study focuses on the integration of the introduced model plant into a real demand scenario of a city in Egypt and the assessment, to which extent the energy and water demand can be covered by this technology. Due to the availability of meteorological as well as power and water demand data, the city of El Gouna is chosen. In addition, El Gouna is heading to be the first "carbon neutral" city of Africa [136]. Therefore, the overall goal should be a 100% supply with renewable energies. The financial boundary conditions need to be carefully considered in order to understand the local electricity and water market for the development of respective demand scenarios. In regions with scarce potable water resources and in consequence high water prices, the maximized desalination of water can be favorable even at comparatively high losses in electricity generation. As previously discussed in chapter 6, the cogeneration ratio is of special interest and requires an analysis for a specific site.

Furthermore, the power generation using the described CSP plant is not designed to provide the complete electricity demand. In order to complement the renewable power generation, an additional PV and wind power plant are modeled in order to cover the residual demand [30]. The character of power generation is different compared to the CSP plant with thermal storage, delivering only fluctuating power depending on environmental conditions. Nevertheless, the installation cost for PV and wind power are significantly lower. The integrated energy system can contribute with their benefits to secure a reliable energy supply. In order to compare the power generation of each technology, the PV and wind power plants are modeled in the same dimension of 2 $\mathrm{MW_{el}}$.

7.1 Site specific considerations

Due to the availability of sufficient meteorological data [31] as well as electricity [30] and water demand data [32,33], the selected site for the model plant has been chosen on the shore of the Red Sea in El Gouna, Egypt. In general, the analysis of the meteorological data shows a high direct irradiation for the complete year favoring the power conversion in a CSP plant (see also chapter 4, section 4.1 and appendix A). The yearly precipitation has not been measured by the meteorological station, but the literature shows negligible small amounts [95, 96].

The city of El Gouna has been originally planned as a tourism resort but has developed to a real town with around 16,000 inhabitants over the last two decades. The actual power and water demand depends strongly on the actual occupancy of the 16 hotels. Currently, there are also about 700 private owned mansions, 1500 apartments, about 120 restaurants, a hospital, an international school and an university campus. The 18-hole golf course of the Steigenberger Hotel has a special influence on the irrigation water demand. The total area is covered with a vegetation amount up to 945,000 m^2 [32, 33]. Because El Gouna is located in Egypt, there are some special constraints compared to other cities in the country. One of the major differences is that the city allows only limited access to Egyptian citizens and can be considered as gated community with its own security service. Table 7.1 summarizes the power and water demand for 2013.

Month 2013	Electricity $\mathrm{MWh_{el}}$	Water m^3
January	6472	161879
February	6003	144031
March	7111	150667
April	7739	202654
May	9911	212178
June	10274	239528
July	10748	243079
August	10645	264184
September	9051	258147
October	8763	233159
November	6908	205754
December	6961	174223
Total	**100586**	**2489483**

Source: El Gouna Electrics

Table 7.1: *Power and water demand in 2013, El Gouna, Red sea [30, 32]*

7.1.1 Electricity demand

The power demand has been supplied by several diesel generators with heavily subsidized fuel prices and thus at very low costs [32]. Due to the strong increase of the diesel prices, a high-voltage power line attached to the national grid of Egypt has been build which is in operation since 2012. The price for electricity is about 0.12 to 0.20 US $/kWh for the end consumers [32]. Egypts first CSP plant, integrated combined cycle concentrated solar power plant, located south of Cairo [133] has been commissioned in 2011. Although a feed-in tariff for electricity for CSP plants has not been introduced yet, there have been some tax exemptions for the plant in Kuraymat.

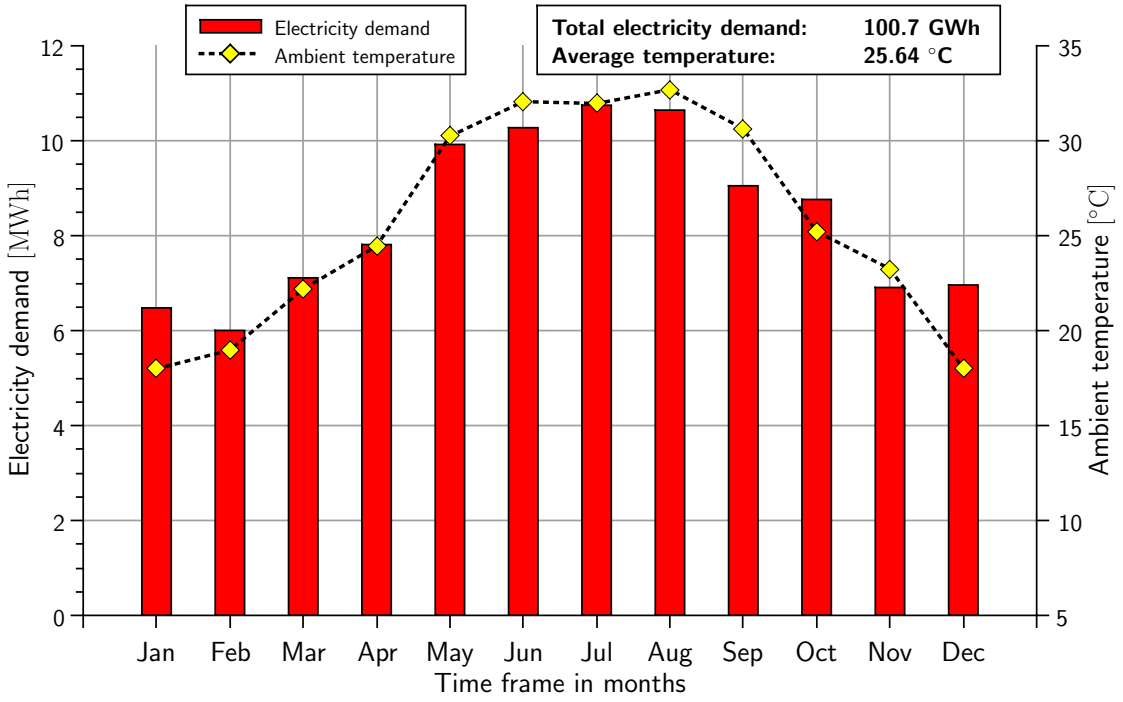

Figure 7.1: *Monthly electricity demand and ambient temperature in El Gouna [30, 31]*

Figure 7.1 visualizes the electricity demand for each month in 2013[1]. The total power consumption of El Gouna sums up to 100.7 $\mathrm{GWh_{el}}$ in 2013. It can be stated that the lowest electricity demand occurs in the winter monthes (November to March) and the highest electricity demand accrues during the summer season (May to August). The values range from 6 to 10.7 $\mathrm{MWh_{el}}$. The reason for these deviations can be mainly seen in the power demand of the air-conditioning systems of the hotels and private apartments. The assumption is proven by the strong correlation between the ambient temperature for the time period which is also visualized in figure 7.1.

[1] Due to data completeness reasons, the data include March to December 2013 and January to February 2014. In the following analysis, the data is treated as from 2013

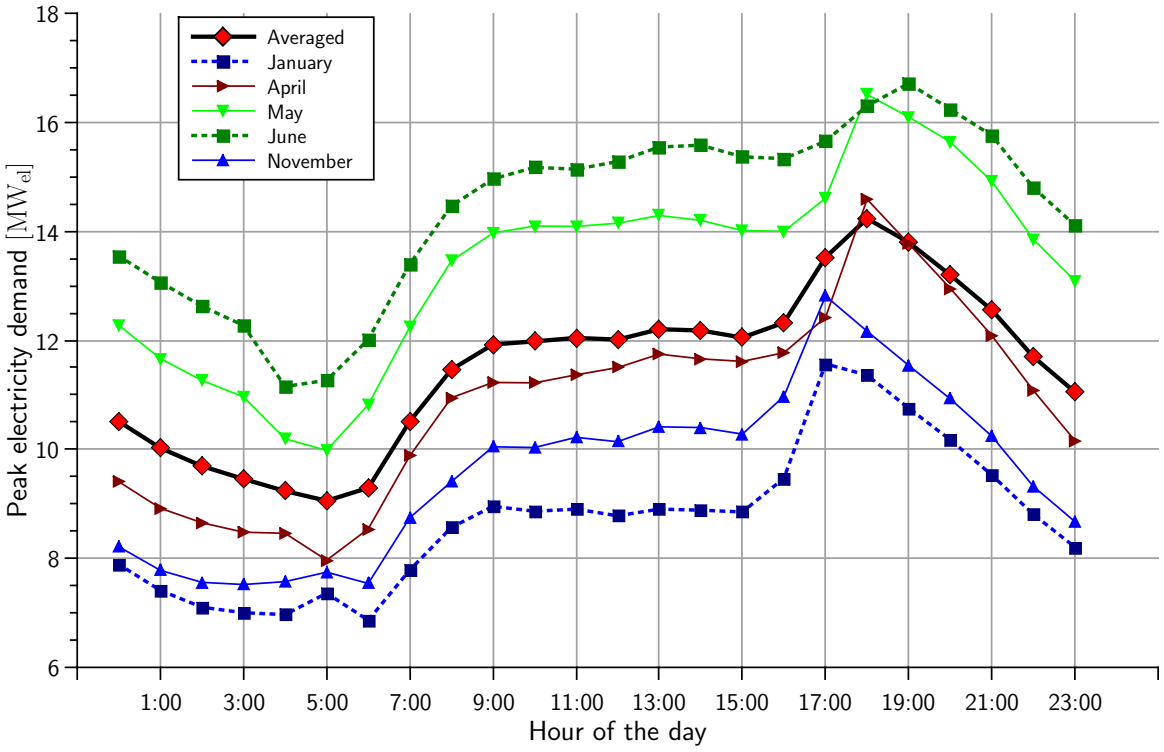

Figure 7.2: *Hourly peak electricity demand curve per day [30]*

In order to model the supply scenario with renewable energies, the daily load is of high interest and needs to be carefully analyzed. The analysis of the available data is shown in figure 7.2 for each hour of the day for selected months of the year 2013. The peak loads vary strongly depending on the hour of the day. The months with the lowest consumption (January) and the highest consumption (June) are specially visualized in figure 7.2. Generally, the lowest consumptions occurs during the morning hours from 4:00 am to 6:00 am while the peak demand occurs in the evening hours from 5:00 pm to 7:00 pm, shown by the average power demand line. The morning low and evening peak shift depending on duration of the day. The power demand varies strongly from the European countries, which typically show two peaks in the morning and afternoon hours. Looking at the power demand curve of whole Egypt, there are no major deviations in comparison to the city of El Gouna [137].

7.1.2 Water demand

All available water sources in El Gouna need to be desalinated or need to be brought via pipelines from the Nile Delta in Lower Egypt. The latter is often disrupted and not very reliable in many districts. In consequence of that, a huge desalination capacity is required.

In El Gouna, there is an installed desalination capacity of 9,500 $\mathrm{m^3/d}$ for drinking water and 1,500 $\mathrm{m^3/d}$ for irrigation water. A pipeline from Hurghada with Nile water has supplied around 500 $\mathrm{m^3/d}$ [32] but is not being used any more. All desalination plants are working with reverse osmosis (RO) technology. The intake is realized by several wells delivering brackish water from the nearby mountains with a salinity of around 7 $\mathrm{g/L\ TDS}$. Some RO plants also use beach wells with a seawater salinity of 31 to 41 $\mathrm{g/L\ TDS}$. Those plants are mostly small plants with a capacity of 500 to 1000 $\mathrm{m^3/d}$ which are not permanently operated. They are only used if the supply from the brackish water wells is not sufficient. In total, there are 8 desalination plants for saline water and 7 plants for brackish water with a capacity of 5,500 $\mathrm{m^3/d}$ and 4,000 $\mathrm{m^3/d}$, respectively.

Parameter	Value	Unit
pH	8.43	–
Conductivity	58.3	$\mathrm{mS/cm}$
Oxygen content, O_2	60.7	$\%$
Total solids, TS	45.2	$\mathrm{g/L}$
Total suspended solids, TSS	0.08	$\mathrm{g/L}$
Total dissolved solids, TDS	43.7	$\mathrm{g/L}$
Total organic carbon, TOC	3.64	$\mathrm{mg/L}$
Anion: $\mathrm{Cl^-}$	17189	$\mathrm{mg/L}$
Anion: $\mathrm{Br^-}$	6.89	$\mathrm{mg/L}$
Anion: $\mathrm{SO_4^{2-}}$	2897	$\mathrm{mg/L}$
Cation: $\mathrm{Ca^{2+}}$	449	$\mathrm{mg/L}$
Cation: $\mathrm{K^+}$	506	$\mathrm{mg/L}$
Cation: $\mathrm{Mg^{2+}}$	1168	$\mathrm{mg/L}$
Cation: $\mathrm{Na^+}$	1150	$\mathrm{mg/L}$

Sample date: 15.02.2015

Table 7.2: *Seawater analysis El Gouna, Red sea, analysis from [33]*

The model plant uses a direct seawater pipeline for cooling and desalination purpose. It requires the exact analysis of the available sea water which is summarized in table 7.2. The seawater analysis shows a salinity above the average seawater with total dissolved solids of 43.7 $\mathrm{g/L\ TDS}$ (compare also to table 2.6 in section 2.4). Furthermore, minor traces of bromine have been detected.

Figure 7.3 shows the monthly water demand for the year 2013 in $\mathrm{m^3}$. The correlation with the ambient temperature is not that strong compared to the electricity demand in section 7.1.1 and figure 7.1. High ambient temperatures are therefore not necessarily correlated with high water consumption. The lowest demand accrues in February and the

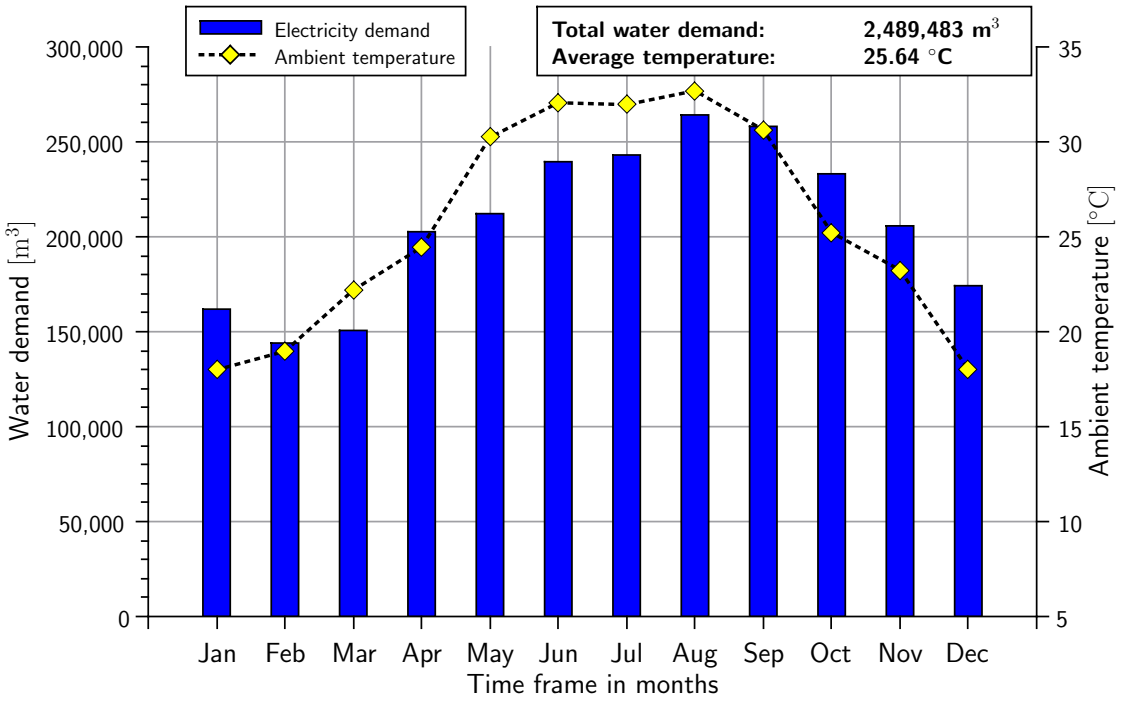

Figure 7.3: *Water demand and ambient temperature in El Gouna [31–33]*

highest in August 2013, which is one month offset compared to the electricity demand. Furthermore, more than 30% of the irrigation water demand is used for the Steigenberger golf course. A more detailed analysis could be performed by the integration of hotel occupancy figures. Naturally, a high occupancy leads to higher water consumption by hotel guests.

Concerning the prices, one cubic meter of fresh water is sold to the hotels at about 2.55 US \$/m^3 (Source: El Gouna Water and Wastewater management)[2]. The tariff can be considered as extremely high compared to other regions in Egypt, where the water price starts at 0.04 US \$/m^3 for costumers consuming less than 10 cubic meter per month and tops at 0.11, 0.12 and 0.48 US \$/m^3 respectively for domestic, tourist and special industrial use.

Although the weather conditions and the demand situation in El Gouna is ideal for combined concentrated solar power and water generation, the model plant can barely compete with current market prices. The economies of scale for concentrated solar power plants are too influential. If the size of the plant is scaled up by a factor of four, it would likely reach economic competitiveness, but would also occupy significantly more land area.

[2] 15 EGP for drinking water, 5 EGP for treated waste-water for irrigation, prices from 2013

7.2 Modeling of demand and supply

The following section shortly outlines a demand and supply scenario based on the actual data sets and simulation results of chapter 4. The CSP plant with integrated thermal desalination is one major part of the electricity and water supply, delivering power on demand using the thermal storage system. In order to increase the demand coverage using renewable energies, additional fluctuating energy supply systems are modeled. In consequence of that, it can be expected that surplus energy could be generated over the day. A new solution is proposed for using the surplus energy to extend the operation time of the CSP and thus, increase the electricity generation, the CSP capacity factor as well as the amount of desalinated water.

7.2.1 Electricity demand forecast

The available data analyzed in section 7.1.1 is based on live measured energy demand data in 2013 [30]. Due to the political circumstances, the analyzed year cannot be representative for the future development of the city. Already one year later, it is reported that the hotel occupancy is increased and thus also the energy and water demand. To respect the average growth of the demand, the yearly demand is scaled up according to the latest available report of the Egyptian Electricity Holding Company (EEHC) [137] using the following equation:

$$D_{f,a} = D_{act} \cdot (1 + r)^a \tag{7.1}$$

The future electricity demand $D_{f,a}$ in the year a is scaled up by the actual electricity demand D_{act} of today, represented by the provided data in [30]. The average growth rate r is estimated with 5% per year a according to [137]. The provided analysis is based on the years 2010 to 2013. In order to estimate the future energy demand, a is set to ten years. The chosen time frame allows for the planning and erection of the designed model plant and is also capable to meet future electricity demand scenarios.

Figure 7.4 maps the demand in ten years for three days of June. The plotted ambient temperature again shows the strong correlation between the electricity demand and the actual temperature of the particular hour of the day.

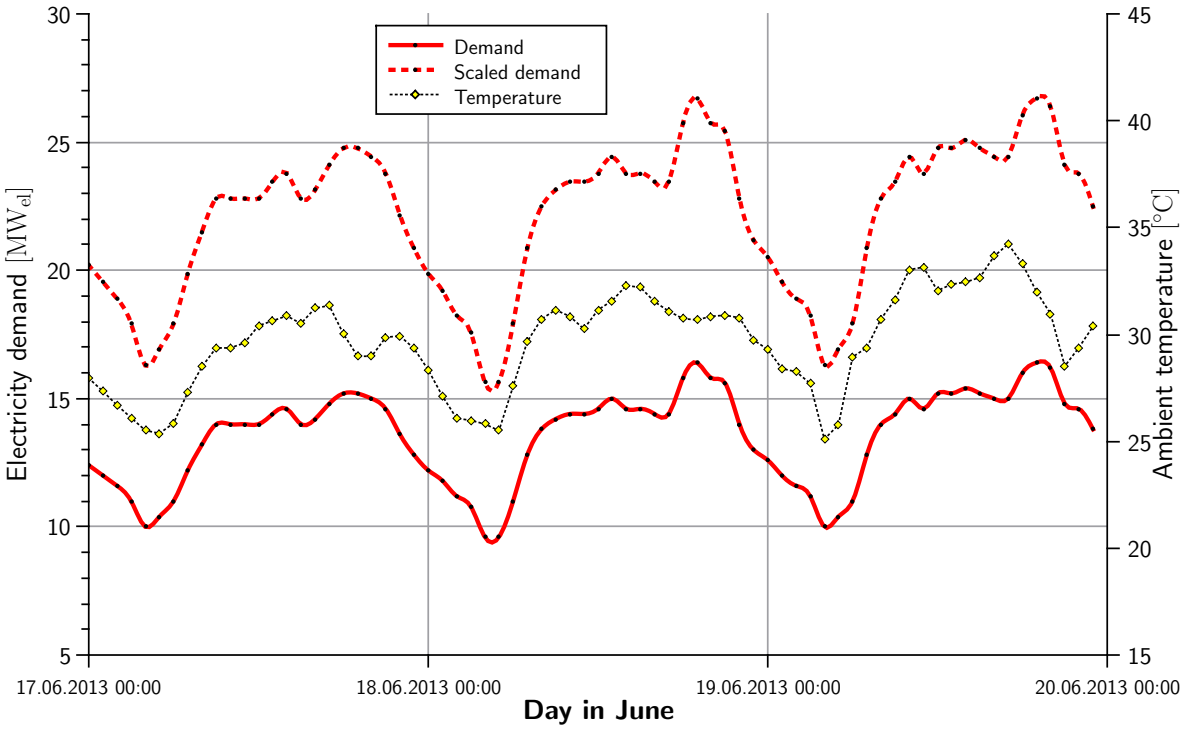

Figure 7.4: *Scaled electricity demand and ambient temperature for three days in June 2013 [30, 31]*

7.2.2 Photovoltaic model plant

Photovoltaic (PV) energy can be considered as a strong emerging renewable energy technology due to several reasons. During the last decades, the technology has been drastically improved by advanced research in material science, mainly basing on silicon and semiconductor processing industries. Improved manufacturing quality and mass production have let to cost reductions through economies of scale. Currently, many manufacturers of solar photovoltaic panels compete on the global market and it can be expected, that the technology still has margins for further cost reduction and efficiency gains.

Nevertheless, PV energy supply systems are not able to generate electricity on demand and are considered as fluctuating energy resources as their power output directly depends on the available solar irradiation. Small scale systems for domestic use can be fitted with battery storage systems in order to supply energy during night times, but such systems are inadequate and too expensive for power plant scale. However, due to the cheap prices and strong commercialization, PV can significantly reduce the consumption of fossil energy carriers. The advantages lay in the combination with other renewable energy supply systems, wherefore a PV system is suitable to support the demand coverage of the modeled supply scenario.

In order to calculate the net power generation of a PV system, the solar resource and the incident angle on the PV panel are the main impact factors [138]. Normally, PV panels are mounted at a fix tilted angle depending on the chosen location. Due to the modeling of a heliostat field for the CSP plant, it is intended to integrate the PV panels on additional heliostats in the field (see also figure 3.3 and table 3.3). It can be expected that the chosen arrangement increases the PV power output during the day. The usage of a certain number of additional two-axis tracked heliostats fitted with PV panels instead of reflective mirrors optimizes the incident angle to the sun position. Furthermore, one portion of the generated electricity can be directly used to cover solar field parasitic power consumption, mainly caused by the molten salt pumps. Their power demand directly corresponds to the generated electricity by the PV panels.

The meteorological ambient conditions have been discussed in section 3.2 to calculate the direct normal irradiation (DNI). Because a PV system also converts diffuse irradiation measured by the meteostation (see also table 3.2), the calculated DNI values in section 4.1.2 cannot be used directly. They need to be converted into the global tilted irradiation value (GTI) depending on the solar angles at the particular time of the day (compare also to figure 3.2). Due to the arrangement of the PV panels on heliostats, the tilt angle of the PV panel and the horizontal plane is denoted as β_c corresponds to the solar elevation angle γ discussed in section 3.2. In order to simplify the calculation, the diffuse horizontal radiation D is normalized depending on the solar elevation angle to the diffuse normal irradiation DN and added to the DNI. The calculation results in the global tilted irradiation denoted as GTI which is calculated under the assumption that the PV panels are arranged on two-axis tracked heliostats:

$$\begin{aligned} DNI &= \frac{G - D}{\sin\gamma} \\ DN &= \frac{D}{\sin\gamma} \\ GTI &= DNI + DN = \frac{G - D}{\sin\gamma} + \frac{D}{\sin\gamma} \end{aligned} \tag{7.2}$$

In order to respect the maximal tilt angle of the heliostats during sun rise and sun set, all sun elevation angles γ below 10° are set to zero. The resulting GTI values are higher compared to the DNI values, which is caused by the addition of the diffuse normal irradiation. At noon, the GTI irradiation reaches up to 1100 $\mathrm{W/m^2}$.

PV performance model

After the discussion of the irradiation on the PV panels and the incident angles, the net power output of the complete plant can be calculated. The calculation procedure is adapted from [138]. In the first step, the calculation of the maximum power point voltage, denoted as U_{mpp}, at given irradiation GTI is described with the following equation. All values with the index 0 describe the reference conditions given by the manufacturer:

$$U_{mpp} = U_{mpp,0} \cdot \frac{\ln GTI}{\ln GTI_0} \tag{7.3}$$

The same applies for the maximum power point current I_{mpp} at irradiation level GTI:

$$I_{mpp} = I_{mpp,0} \cdot \frac{GTI}{GTI_0} \tag{7.4}$$

The PV panel heats up during operation which has a diminishing effect to the power output. Usually, the effect is expressed by the heat-up coefficient τ_{PV} which is given in Kelvin per solar irradiance using the unit $\frac{\mathrm{K}}{\mathrm{W/m^2}}$. The temperature of the PV panel T_{PV} consequently calculates to:

$$T_{PV} = T_{amb} + GTI \cdot \tau_{PV} \tag{7.5}$$

In order to calculate the maximum power point output P_{mpp} of the complete array, the number of PV panels switched in series n_s and in parallel n_p need to be multiplied by the temperature correction term. The manufacturer gives a coefficient for the thermal properties of the PV panel, which is expressed with α_{mpp} and usually given in $\%/\mathrm{K}$:

$$P_{mpp} = n_s \cdot n_p \cdot U_{mpp} \cdot I_{mpp}(1 + \alpha_{mpp} \cdot (T_{PV} - T_{amb})) \tag{7.6}$$

The power output of the complete PV system is additionally influenced by three main losses which are given by efficiencies factors η. The panel soiling is expressed by η_{soil} respecting the power reduction due to dirt. Possible AC-DC inverter losses are respected by η_{inv} and the total field efficiency is respected by η_{fld}. In summary of the equations 7.3 to 7.6, the total power output of the PV system calculates like the following:

$$P_{PV,net} = P_{mpp} \cdot \eta_{soil} \cdot \eta_{inv} \cdot \eta_{fld} \tag{7.7}$$

Specification of the PV module

In the next step, an appropriate PV panel needs to be specified. Due to the abundant presence of possible manufacturers, a standard module from the renown company BOSCH GmbH [44] has been chosen. It is a crystalline silica based solar module which has a high processing quality and long-term stable power output. One module consists of 60 mono-crystalline solar cells mounted to a black anodized aluminum frame. Each PV module has a dimension of 1660 x 990 mm for one PV module. The operating temperature is given by the manufacturer with -40 to $+85$ °C. The soiling factor η_{soil} assumes a clean condition and an inverter efficiency has been chosen allowing for 96% efficiency. Table 7.3 summarizes all parameters at reference conditions of $GTI_0 = 1000\ \mathrm{W/m^2}$ and $T_{amb,0} = 25°C$.

Parameter	Symbol	Value	Unit
Type and model number	BOSCH c-Si M60S	M245	-
Maximum power point output	P_{mpp}	245	W
Maximum power point voltage	U_{mpp}	30.11	V
Maximum power point current	I_{mpp}	8.14	A
Temperature coefficient	α_{mpp}	-0.44	$\%/\mathrm{K}$
Module area	$A_{pv,m}$	1.64	$\mathrm{m^2}$
Heat-up gradient	τ_{pv}	0.04	$\mathrm{K/W/m^2}$
Soil factor	η_{soil}	96	%
Inverter efficiency	η_{inv}	96	%
Field efficiency	η_{fld}	98	%

Table 7.3: *PV module properties and efficiencies [44]*

Dimensioning of the PV model plant

Knowing the properties of one single PV module and its power output allows for the calculation of the total power output of the model plant. In order to integrate the system in the heliostat filed, the capacity is limited to 2 $\mathrm{MW_{el}}$ at nominal conditions. The capacity requires the deployment of 8800 PV modules using the properties of table 7.3. One CSP heliostat fitted with mirrors has a reflective surface of 100 $\mathrm{m^2}$. Theoretically, the replacement of the mirrors with PV modules would allow for 60 PV modules on one heliostat. To respect the possible additional weight of the PV modules, it is calculated with 55 PV modules per heliostat, denoted with n_s. The modules on the heliostat are switched in series. All PV heliostats together n_p are switched in parallel and sum up to

a total nominal power generation of 2.16 $\mathrm{MW_{el}}$ at peak. The calculation results of the complete PV model plant are summarized in table 7.4.

Parameter	Symbol	Value	Unit
Heliostats with PV modules, in parallel	n_p	160	-
PV modules per heliostat, in series	n_s	55	-
MPP voltage, system	$U_{mpp,0,sys}$	1656	V
MPP current, system	$I_{mpp,0,sys}$	1302	A
MPP power, system	$P_{mpp,0,sys}$	2157	kW
PV system, total aperture area	$A_{pv,sys}$	14462	$\mathrm{m^2}$
Total number of heliostats (CSP and PV)	n_{tot}	1943	-

Table 7.4: *PV model plant, system parameters*

7.2.3 Wind model plant

In addition to the PV model plant, the analysis of the ambient conditions in section 4.1 also showed high average wind speeds per month at the given location. High wind speeds favor the deployment of a wind turbine to generate additional electricity to cover the demand of the city. The wind power technology can be considered as fully commercialized and the Red Sea coast of Egypt is one of the windiest regions of the country. Several projects have been realized during the last years, while the most prominent is the wind park at Zafarana with an installed capacity of 500 $\mathrm{MW_{el}}$. However, wind power supply is also considered as a fluctuating energy resource which strongly depends on the available wind speed at the given location. The same implications like for PV plants apply here as well. In this case study, just one exemplary wind turbine with an installed capacity of 2 $\mathrm{MW_{el}}$ is modeled in order to support the renewable electricity generation.

The mechanical power P_w from a wind turbine depends on four main factors, which are the prevailing wind speed v_w, the rotor area A_{ro}, the power coefficient c_b and the density of the air ρ_{air}. The following equation 7.8 bases on the theory of wind conversion and summarizes the calculation.

$$P_w = \frac{1}{2}\rho_{air} \cdot c_b \cdot A_{ro} \cdot v_w^3 \tag{7.8}$$

While the density of the air ρ_{air} and the wind speed v_w depend on the ambient conditions, the other factors are influenced by the dimensioing and the design of the wind turbine. Especially at low wind speeds, the power coefficient c_b strongly influences the power

output and can theoretically not exceed more than 59.3%. The factor is also called Betz-coefficient[3] and can be derived from the fluid mechanics and the conservation of momentum. Due to the strong influence of the prevailing wind speed v_w in the cube (see also equation 7.8), the careful analysis of the location is most crucial in order to achieve a high power output.

Wind performance model

The wind performance model is adapted from [139]. In order to calculate the net power output from a given wind turbine, the available wind speed needs to analyzed and calculated according to the rotor height. The hourly wind data from [31] is used (see also table 3.2) which is measured at a given height $h_1 = 10\ \mathrm{m}$. The measured wind speed is denoted as $v(h_1)$ in $\mathrm{m/s}$. Furthermore, the available wind speed at rotor height $v(h_2)$ depends on the surrounding area which is expressed by a ground roughness factor z_0. Obstacles like bushes, trees and buildings are causing turbulences which diminish the power output of the wind turbine. The following equation is used to calculate the wind speed at the rotor height $v(h_2)$:

$$v(h_2) = v(h_1) \cdot \frac{\ln\left(\frac{h_2 - d}{z_0}\right)}{\ln\left(\frac{h_1 - d}{z_0}\right)} \tag{7.9}$$

The height of possible obstacles d near the measurement can be used for the calculation given in equation 7.9. Because of the selected location, it can be stated that there are no obstacles neither near the meteorological station nor at the foreseen location of the wind turbine. Therefore, d is set to zero.

In a next step, the density of the air ρ_{air} needs to be corrected. It has a linear effect to the power output of the wind turbine. The density is mainly affected by the atmospheric pressure, the elevation and the ambient temperature. In this model, the effect is respected by a factor η_{den} which is calculated as follows:

$$\eta_{den} = \frac{\rho_{air}}{\rho_0} = \frac{p_{amb} \cdot (t_0 + 273.15)}{p_0 \cdot (t_{amb} + 273.15)} \tag{7.10}$$

[3] named after Albert Betz, 1885-1968, who did theoretical work about the maximum possible mechanical power of the wind

The values with the index 0 in equation 7.10 represent the reference conditions. The reference conditions are assumed with the temperature $t_0 = 20°\mathrm{C}$, the pressure $p_0 = 1013\ \mathrm{mbar}$ and the density $\rho_0 = 1.255\ \mathrm{kg/m^3}$.

Specification of the wind turbine

In order to calculate the additional power generation of a wind turbine, one turbine from one of the available wind turbine manufacturers needs to be selected. The company ENERCON GmbH provides a detailed documentation about their product portfolio [34]. Having more than 25 years of experience in wind turbine manufacturing with a high production depth, it can be assumed that the quality standards and the reliability are suitable for the operation in challenging environments. The turbine E-82 [34] has a power output of 2050 $\mathrm{kW_{el}}$ which seems to be suitable for the integration in the energy supply model. Due to the special construction of all ENERCON generators, the turbine does not need a gearbox and can operate with variable turn-rates. An annular ring-generator with a frequency converter allows for turn rates from 6 to 18 rpm. The individual blade adjustment ensures high c_b factors especially at low wind speeds.

Parameter	Symbol	Value	Unit
Type and model number	ENERCON	E-82	-
Nominal power capacity	P_{nom}	2050	kW
Start up wind speed	v_{in}	3.5	$\mathrm{m/s}$
Nominal wind speed	v_{nom}	13	$\mathrm{m/s}$
Shut-down wind speed	v_{out}	25	$\mathrm{m/s}$
Rotor height	h_2	78	m
Roughness index	z_0	0.03	m
Grid connection efficiency	η_{con}	96	%

Table 7.5: *Wind turbine properties and site characteristics [34]*

For the calculation of the power output depending on the prevailing wind speed, the characteristic power curve needs to be numerically modeled. Generally, all wind power curves have the same shape depending on the wind speed in the rotor area. The first design depending on the key figure is the start-up wind speed denoted as v_{in}, which can be considered as the minimal wind speed for power generation. The wind speed range to the nominal power generation requires constant blade adjustment by the pitch-regulation to ensure the highest possible c_b for optimized energy conversion (up to 50%). Reaching the nominal wind speed, denoted as v_{nom}, gives a power output according to the design capacity. In order to avoid mechanical damage, the wind turbine is shut down at the

maximum possible wind speed v_{out} and it is turned out of the wind. All parameters and site specific characteristics are summarized in table 7.5.

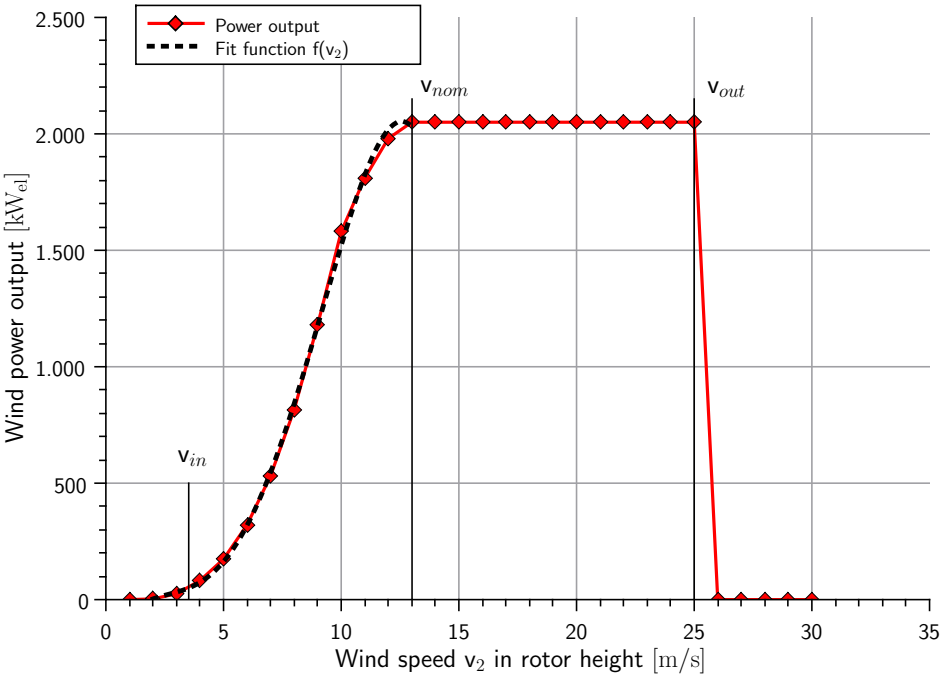

Figure 7.5: *Wind turbine power curve with approximated fit function, data from [34]*

Figure 7.5 shows the development of the power curve with the mentioned design-depending wind speeds. The manufacturer provides a detailed power curve for each wind speed according to the selected turbine E-82 [34]. The exact values for the sectors can be found in table 7.5.

The modeling of the power output depending on the prevailing wind speed in the rotor height v_2 requires the adaption of a fit function. However, a polynomial function of the fourth order denoted as $f(v_2)$ can be used to fit the course of the power function between v_{in} and v_{nom} given by the manufacturer [34]. The fit function is visualized in figure 7.5 by a dotted black line. The following equation 7.11 has been developed to ensure a correlation coefficient of $R^2 = 0,9991$ to the manufacturer data:

$$f(v_2) = -0.579\ v_2^4 + 13.736\ v_2^3 - 85.231\ v_2^2 + 231.86\ v_2 - 220.47 \tag{7.11}$$

The complete wind power curve in figure 7.5 is modeled according to the following equation 7.12. The units are given in $\mathrm{kW_{el}}$ for P_{E82} and in $\mathrm{m/s}$ for v_2, respectively:

$$P_{E82}(v_2) = \begin{cases} 0 & \text{if} \quad v_2 < v_{in} \\ f(v_2) & \text{if} \quad v_{in} < v_2 < v_{nom} \\ 2050 & \text{if} \quad v_{nom} < v_2 < v_{out} \\ 0 & \text{if} \quad v_2 > v_{out} \end{cases} \tag{7.12}$$

Summarizing, the wind power output P_w is lowered by the correction factor for the air density η_{den} according to ambient pressure and temperature (see equation 7.10) as well as the efficiency of the power connection to the grid η_{con}. Equation 7.13 visualizes the complete calculation:

$$P_w = P_{E82}(v_2) \cdot \eta_{den} \cdot \eta_{con} \tag{7.13}$$

7.3 Storage of surplus power by heat

It can be expected that the modeling of a supply scenario with a CSP plant as well as fluctuating resources like PV and wind power generates surplus power exceeding the given electricity demand. The total installed renewable power sums up to 18 $\mathrm{MW_{el}}$ while 14 $\mathrm{MW_{el}}$ are covered by the CSP plant and 2 $\mathrm{MW_{el}}$ by PV and wind power, respectively. Like discussed before, only the CSP with the thermal storage can supply power on demand depending on the actual storage level. The PV and wind power plant are completely depending on the environmental resources.

Figure 7.6 visualizes the problem for three exemplary days in February, 1-3, by the hourly analysis. Especially during the day, the modeled system generates surplus power which exceeds the scaled electricity demand. Generally, there are several options for the handling of forcasted surplus power which are explained as follows:

- *Avoiding surplus power:* In the best case, the generation of surplus could be avoided through optimal design according to the demand. The design of the CSP with the thermal desalination unit allows flexible condensation pressures which shifts the power generation to more water production (see also section 4.4 and 4.4.1). Due to the fact, that water can be easily stored, the surplus electricity generation could be avoided to a certain extent. In the examined case, the condensation pressure and thus, the energy and water cogeneration ratio is kept fixed for the whole year according to the results of chapter 6. The reduction of the power of solar field has economic disadvantages and is not considered in this case. Another option could be

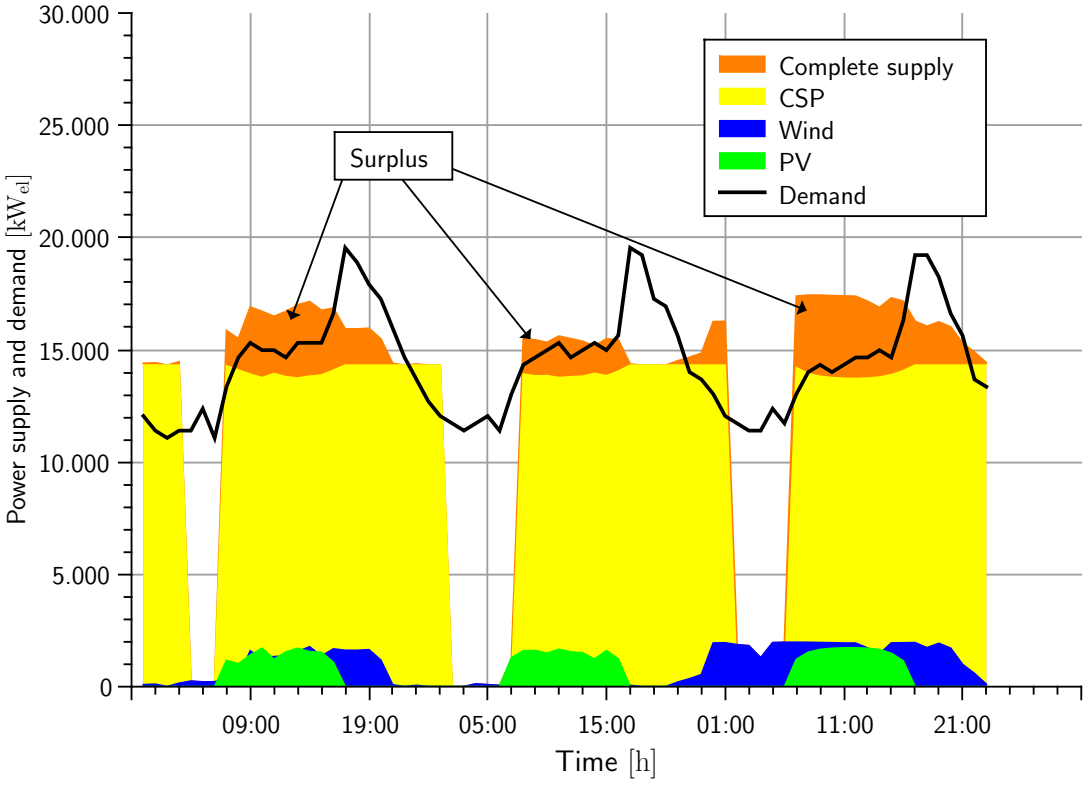

Figure 7.6: *Supply and demand scenario with surplus power*

the supply of the reverse osmosis desalination plants (RO) with the surplus power, but the operation of RO plants with variable loads requires a special design.

- *Grid feed:* Because of the existing high-voltage line to the national grid of Egypt, the generated surplus electricity could be fed into the national network, which can be seen as common solution. Having an increasing amount of fluctuating renewable energy sources attached to the national grid, creates a problem for existing power plants powered by fossil fuels, with have significant time delays to react on variable loads. Furthermore, the operation in part-load causes generally lowered efficiencies in energy conversion and thus increasing fuel consumption. The problem intensifies with an increasing amount of fluctuating renewable energy sources in the national grid.

- *Storage of surplus power:* Another possible solution could be the conversion of the surplus power into usable heat. In most cases, the conversion of electricity into heat in common power systems does not make sense. The reason for this can be found in the fact, that common steam-cycle power plants only generate up to 40% electricity by the heat supplied in the steam generator. The remaining 60% are considered as waste heat rejected in the cooling system to the environment. The conversion of the generated electricity back to heat causes significant exergetic

losses, which cannot be justified in power systems mainly fueled by fossil energy carriers (explanation see above point).

However, assuming an increasing amount of fluctuating renewable energy sources like PV and wind power in electricity grids, the latter mentioned approach needs to be discussed again. The existence of a large thermal storage in combination with a conventional power block gives the option to load the storage using surplus energy. Technically, it can be expressed by heating up the molten salt using a simple electric device (e.g. electric heater) powered by the generated surplus power to load the thermal storage during hours when the supplied power exceeds the demand. The method generates an additional heat source to load the thermal storage besides the concentrated solar incident power on the receiver. Variable loads of the electrical heating device and short operation times are technically possible and always allow a high conversion efficiency. The modeled fluctuating resources in this case study are rather small dimensioned and designed to generally minimize surplus power, but the theoretical approach is outlined shortly.

7.3.1 Theoretical model of power to heat conversion

The relation between the available heat Q is depending on the temperature difference ΔT, the specific heat capacity of the fluid expressed by c_p and the mass flow m of the fluid (also compare to section 2.5):

$$Q = m \cdot c_p \cdot (T_2 - T_1) \tag{7.14}$$

The considered fluid is defined as the molten salt of the thermal storage system. The conversion of the surplus power to the heat Q_{sp} is assumed to be ideal with an efficiency of 1 (through mechanism of electrical resistance). So the available heat is equivalent to the generated surplus power, denoted with Q_{sp}. The temperature difference ΔT can be understood as the temperature difference of the two molten salt storage tanks, thus defining the temperatures to $T_{sto,h}$ for the hot tank and $T_{sto,c}$ for the cold tank (see also section 3.3.2) which gives a fixed $\Delta T = 280\ \mathrm{K}$. The specific heat capacity $c_{p,ms}$ of the molten salt can be found in available literature and is assumed with $c_{p,ms} = 1,5381\ \mathrm{J/gK}$ [37,62]. Rearranging equation 7.14 to the mass flow of the molten salt, results in equation 7.15 to calculate the additional mass flow $\dot{m}_{a,ms}$ in the hot tank depending on the surplus power Q_{sp}:

$$\dot{m}_{a,ms} = \frac{\dot{Q}_{sp}}{c_{p,ms} \cdot (T_{sto,h} - T_{sto,c})} \tag{7.15}$$

The calculation neglects possible heat transfer and pressure losses as well as needed pumping power to supply the molten salt from the cold tank to the hot tank. While the heat transfer losses strongly depend on the technical construction of the device (available heat exchange area), the pumping power can be compared to the hot molten salt pump supplying the steam generator of the power plant (see also section 3.3.2).

7.4 Results of renewable energy integration

The following section summarizes the results of the CSP as well as the PV and wind power plant according to the given scaled demand based on [30] and section 7.2.1. Special attention is given to the extended operation times of the CSP plant using the generated surplus power to load the thermal storage like described in sections 7.3 and 7.3.1.

7.4.1 Power and water supply by CSP plant

The modeled CSP plant is able to supply in average around 61% of the scaled electricity demand in the following ten years (section 7.2.2 and figure 7.4). The monthly coverage ranges from 53% in July and August during high-season time and thus high electricity demand. Furthermore, the ambient temperatures are maximized during those months. During low-season in January to March, the monthly coverage is increased and can reach up to 85%.

Figure 7.7 presents the power and water production for the complete year which has been calculated using the data from the meteorological station [31]. The total power generation ranges between 6700 up to 9500 $\mathrm{MWh_{el}}$ per month using the cogeneration ratio calculated in chapter 6, section 6.5.2. The achievable capacity factors of the CSP plant range between 78% in December and up to 93% in June which is due to the high solar irradiation and the increased day length. It is important to mention that the operation time of the CSP always covers the peak demands in the evening hours from 5:00 pm to 7:00 pm, which has been analyzed in section 7.1.1 and figure 7.2. The shut-down time of the CSP plant is realized during low-loads from 4:00 am to 6:00 am, depending on the level of the thermal storage system.

For the months November to February, the plant is operated in part-load with 83.3% of its capacity in order to extend the operation time during the hours without solar irradiation. October 2013 has been a more sunny month compared to September of the

same year, which results in a higher power generation as well as capacity factor (compare also to figure 4.2). Furthermore, the lowest month for power generation is November, which is due to short day length and thus reduced irradiation. The occurrence of cloudy days is also raised limiting the available direct normal irradiation.

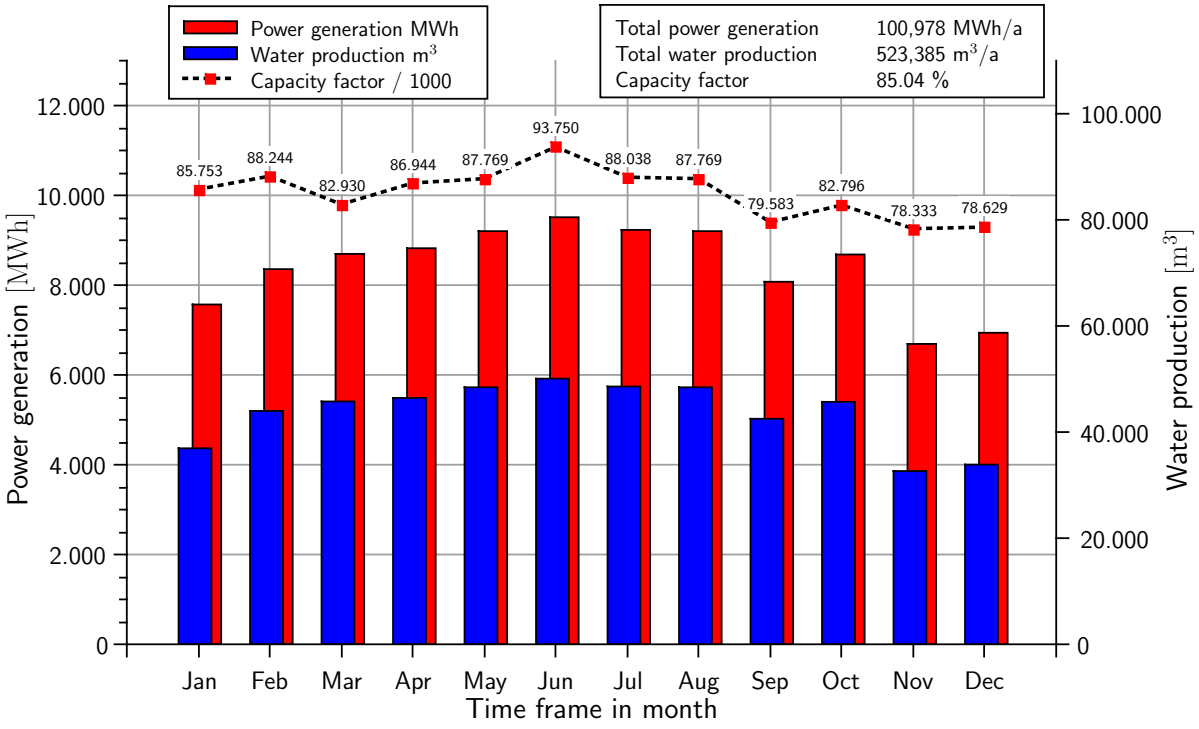

Figure 7.7: *CSP and desalination, monthly power and water production*

Throughout the year, the water production is limited and covers only around 21% of the given fresh water demand [140]. Due to the fixed operating point and optimized cogeneration ratio, the water production always shares a constant portion of the electricity generation. The monthly coverage ranges between 16% in November up to 31% in February. The water production and the total share can be easily increased by changing the condensation pressure examined in section 4.4.1. In this case study, the condensation pressure is kept constant at 0.14 bar.

7.4.2 Power supply by PV and wind power plant

The deployment of additional 2 $\mathrm{MW_{el}}$ capacity by a PV and 2 $\mathrm{MW_{el}}$ by a wind power plant extends the supply and thus the scaled demand coverage. Due to the relative small size of the systems, they can be completely integrated on the land area of the CSP plant. In addition, the comparison of two different technologies in total power generation in the selected location is easily possible. It can be expected that the generated surplus energy

is also increased. Figure 7.8 visualizes the total power generation which depends on the actual solar irradiation on a tilted surface (namely the GTI, see section 7.2.2) and the prevailing wind speed measured by the meteorological station [31].

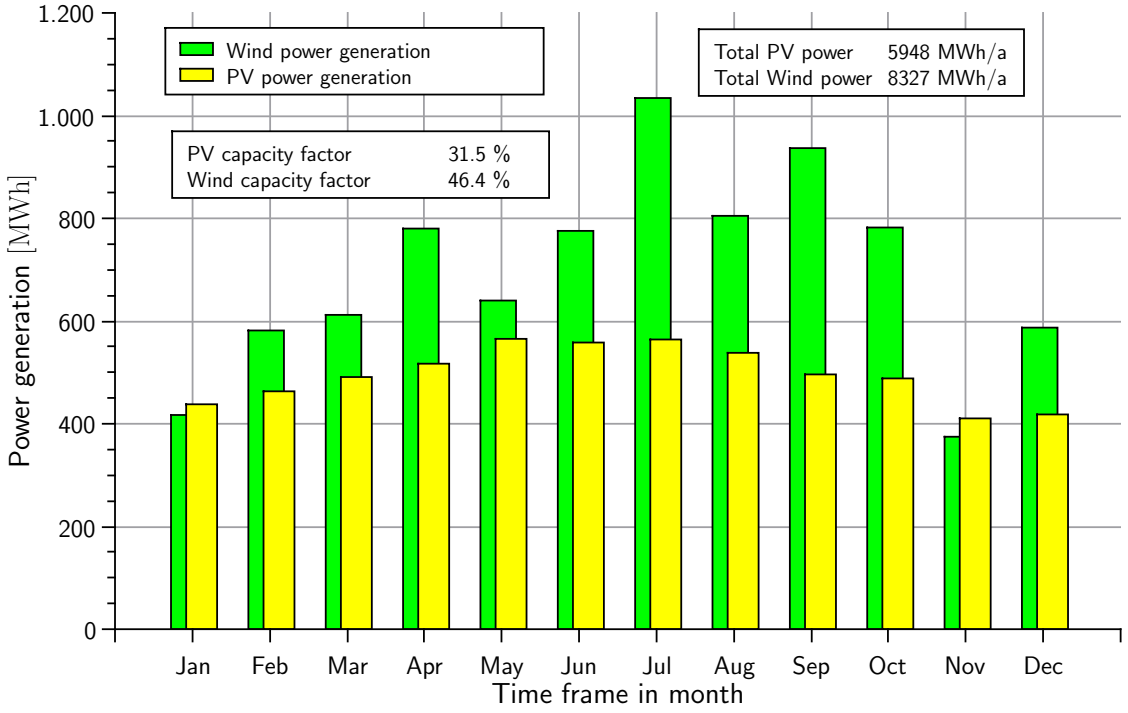

Figure 7.8: *PV and wind power plant, monthly power generation*

Furthermore, the results in figure 7.8 also show, that the installed wind power plant (see section 7.2.3) provides a significantly higher capacity factor compared to the PV model plant. While the PV plant achieves a total capacity factor of 31.5%, the wind power plant reaches up to 46.4%. It can be concluded that the selected location is more suitable for wind power generation, because the power generation clearly exceeds the solar power which is converted by the PV plant. The months with the lowest power generation for both plants are November and January, reaching a combined power generation from 810 up to 870 $\mathrm{MWh_{el}}$. However, the most yielding months are July to October, achieving a monthly power generation from 1310 up to 1640 $\mathrm{MWh_{el}}$.

The economic analysis needs a more differentiated examination due to the different characters of PV and wind power generation. Both calculations are performed using the software SAM (System Advisory Model) [114] using the same financial assumptions like calculated in chapter 6. In order to derive a brief estimation of financial parameters, the PV and wind design data (see sections 7.2.2 and 7.2.3) are transferred to SAM. More information for SAM are given in section 6.3.2 and about the methodology in section 6.2. All meteorological data from El Gouna [31] are used to perform the simulation.

Costs of PV model plant

Generally, the costs of the PV modules are subject to cost reductions during the future [67, 141]. In 2008, the average system costs sum up to 4050 $\mathrm{US}\ \$/\mathrm{kW}$ for c-Si modules [141] according to table 7.3. Due to strong effects of economies of scale, efficiency gains in manufacturing, development of new PV technologies and the global competition, the prices for PV modules are declining and have dropped to 1050 $\mathrm{US}\ \$/\mathrm{kW}$ in 2012. In order to estimate the complete PV plant, there needs to be respected additional costs categories similar to the cost breakdowns discussed in section 6.4.1. The installed system price for commercial c-Si PV systems sums up to 4,590 $\mathrm{US}\ \$/\mathrm{kW}$ including additional heliostats (2-axes trackers), power inverters, installation overheads and site preparation [141]. Assuming an installed PV capacity of 2.16 $\mathrm{MW_{el}}$, the total costs for this PV plant can be estimated to 9.914 $\mathrm{M\$}$.

The calculation results using SAM provides a more detailed analysis and are presented in table 7.6. It shows the LCOE and gives an overview about the expected costs for a period of 20 years without including feed-in tariffs or other governmental incentives. All financial boundary conditions from section 6.4.1 are used. The results represent the full costs of the PV system also containing expenses for O&M which have been estimated to 30 $\$/\mathrm{kW_{el}}$ [142]. The total investment including labor and site preparation sum up to 8.392 $\mathrm{M\$}$. Overall, the resulting $LCOE_{PV}$ ranges between 17-21 $¢/\mathrm{kWh}$ while the nominal $LCOE_{PV,n}$ also respects a discount rate for inflation.

Parameter	Symbol	Value	Unit
Annual energy	$P_{PV,tot}$	6,335	$\mathrm{MWh_{el}}$
Capacity factor	CF_{PV}	0.33	$[-]$
First year kWhAC/kWDC	PV_{gen}	2,967	$\mathrm{kWh/kW}$
Levelized cost (nominal)	$LCOE_{PV,n}$	21	$¢/\mathrm{kWh}$
Levelized cost (real)	$LCOE_{PV,r}$	17	$¢/\mathrm{kWh}$
Electricity cost savings	S_{PV}	477	US $
Net present value	B_{PV}	-12,498,515	US $
Total initial cost	C_{PV}	8,391,787	US $

Table 7.6: *PV model plant, financial results*

Costs of wind model plant

Concerning the costs of installed wind plants, the market prices strongly differ in terms of onshore and offshore applications. Generally, the energy generation using wind power

plants can be considered as technically matured and highly commercialized [143]. As a result, the effects to the financial parameters depends mainly on the given location and the prevailing wind speed. The literature provides data for installed wind power capacity around 1000-2000 $\$/\mathrm{kW}$ for onshore applications and around 4000 $\$/\mathrm{kW}$ for offshore applications [142, 144, 145]. Due to the installation of one single turbine without the effects of economies of scale, the costs are estimated with 2000 $\$/\mathrm{kW}$ for this calculation. However, the total investment costs would sum up to 4,1 $\mathrm{M}\ \$$.

Table 7.7 provides an overview about the SAM results for the selected wind power plant. All parameters including the meteorological data have been included to ensure an optimal comparability of the results. The investment costs of the wind turbine have been estimated basing on literature and project reports [143, 146]. It can be clearly seen, that the high wind speeds drastically lower the costs through the increase of the capacity factor. Despite there have been chosen high O&M costs of 40 $\$/\mathrm{kW_{el}}$ [142,144], the results show a very low $LCOE_W$. Concluding, the total investment for the wind power plant including tower foundations, labor and site preparation sum up to 5,336 $\mathrm{M\$}$. Under the assumption of 20 year life time, the values for $LCOE_W$ ranges about 0.98 to 1.21 $¢/\mathrm{kWh}$. Due to the integration of the wind power plant in an existing power supply infrastructure, the balance of plant costs can be estimated lower compared to literature values [142–146].

Parameter	Symbol	Value	Unit
Annual energy	$P_{W,tot}$	8,539	$\mathrm{MWh_{el}}$
Capacity factor	CF_W	0.47	$[-]$
Levelized cost (nominal)	$LCOE_{W,n}$	1.21	$¢/\mathrm{kWh}$
Levelized cost (real)	$LCOE_{W,r}$	0.98	$¢/\mathrm{kWh}$
Net present value	B_W	-1,003,950,656	US $
Initial cost	C_W	5,335,642	US $

Table 7.7: *Wind model plant, financial results*

7.4.3 Total demand coverage

The percentages of demand coverage are presented in figure 7.9 based on the scaled demand calculated according to section 7.2.1. While the total demand coverage of the single CSP system ranges from 53% up to 85%, the integrated system with additional PV and wind power can increase the coverage up to 98%. The yearly coverage sums up to 61% using only the CSP plant while the integrated system covers up to 71%.

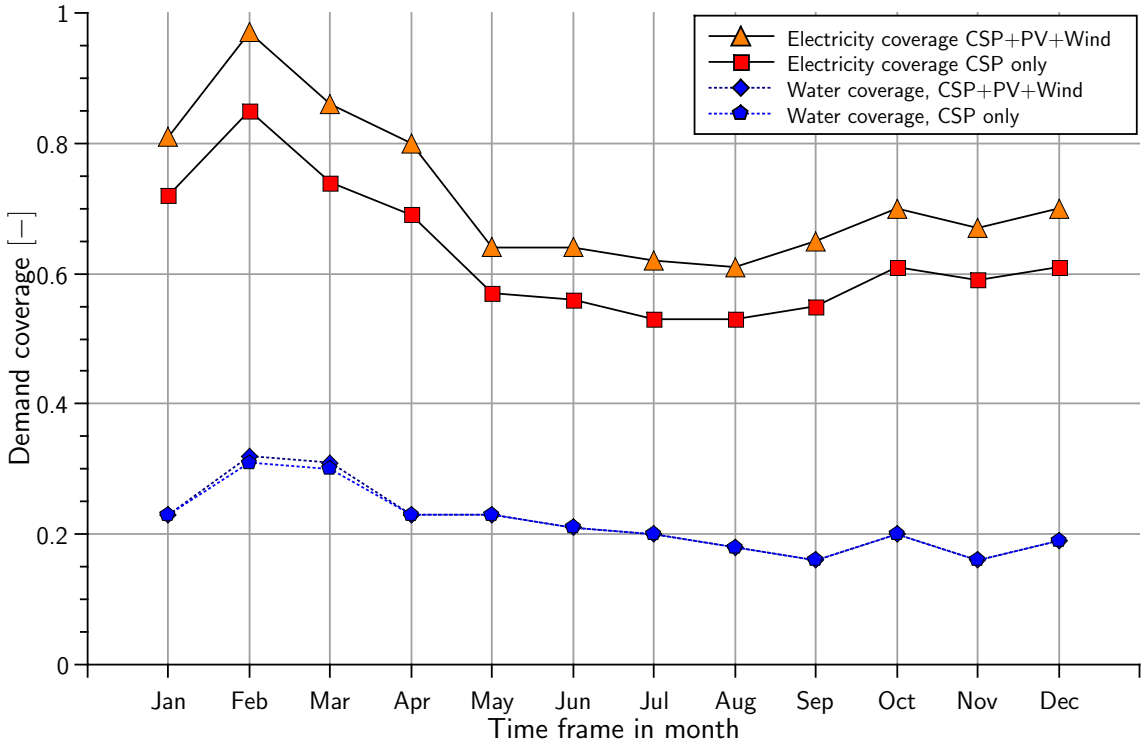

Figure 7.9: *Power and water demand coverage of the integrated system*

The effect of the integrated system to the water demand coverage is limited, because there is no additional water desalinated using PV and wind power. The only extension can be seen during the winter months by the extension of the CSP operation time using the generated surplus power. The effect lays in the area of 1% and does not change the total water demand coverage over the complete year.

The following figures 7.10 and 7.11 compare three typical days during the summer and winter term and present the renewable energy mix by the integrated system. Furthermore, the analysis of the winter days in figure 7.10 visualize the evolution of surplus power, which is discussed in the following section.

However, figures 7.10 and 7.11 also allow a direct comparison in terms of residual power demand which needs to be supplied from the national grid. The winter days in figure 7.10 show an interrupted operation of the CSP plant during hours with low loads creating gaps of two or three hours down-time. During those hours, the wind power plant decreases the residual power demand depending on the actual wind condition. The strong ascending power demand during the morning hours is supported by the solar energy plants (both PV as well as the CSP). February, 15th, shows a lowered irradiation in the afternoon hours which lowers the PV plant power generation as well as the operation time of the CSP in the following night.

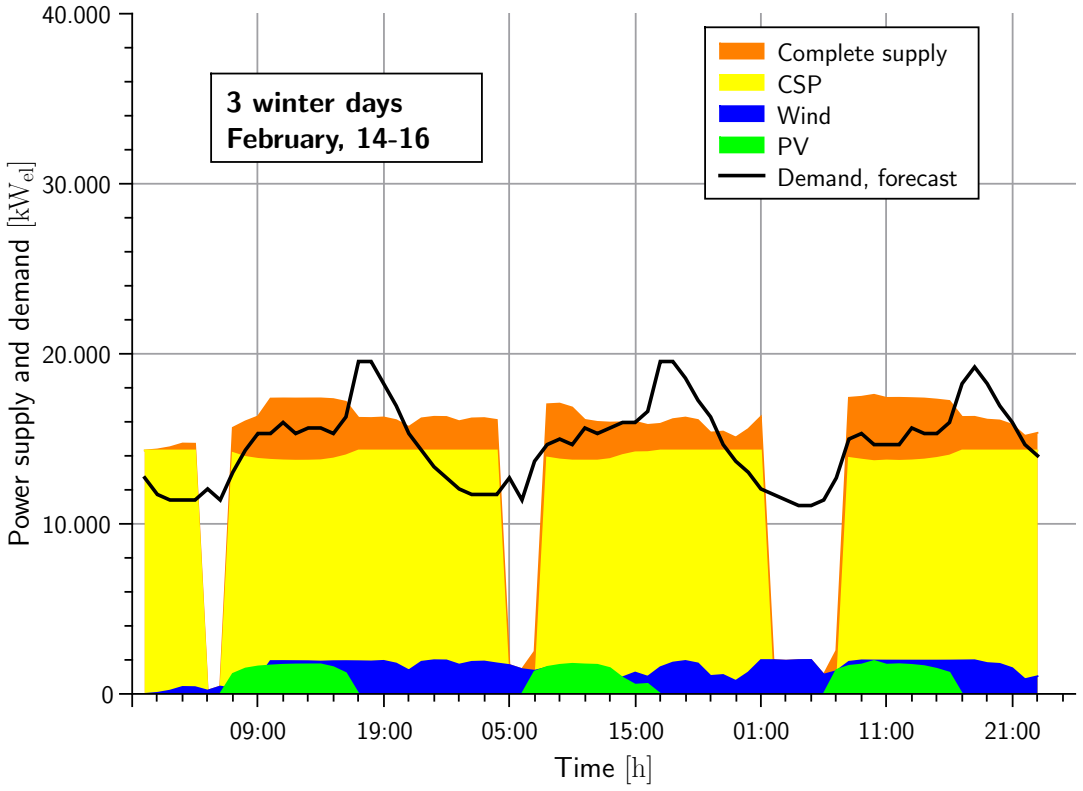

Figure 7.10: *Exemplary supply and demand during winter season*

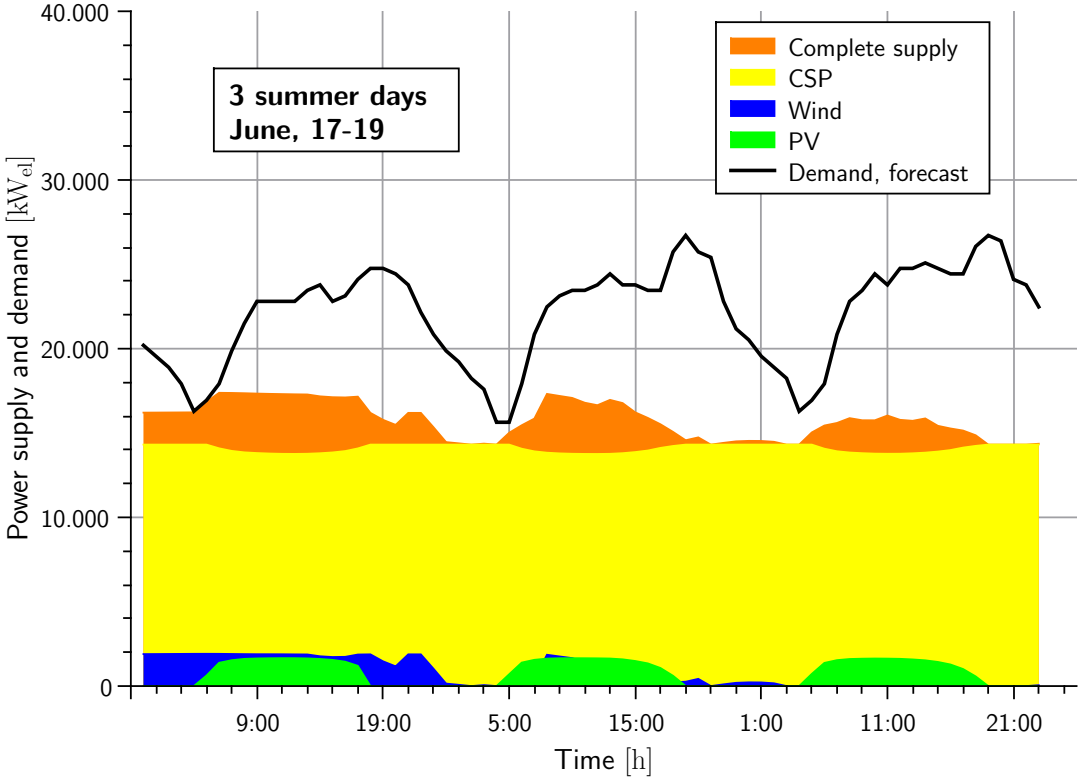

Figure 7.11: *Exemplary supply and demand during summer season*

During the summer days in figure 7.11, the CSP plant can operate around the clock and provides firm capacity to the demand. The power generated by the fluctuation resources fit to a certain extend to the needed electricity, but do not cover the peak loads around 7:00 pm evening. Furthermore, the electricity demand of the molten salt pumps cause a slight decline of the CSP power output of around 600 $\mathrm{kW_{el}}$ during the day. The parasitic energy consumption of the heliostat field and molten salt pumps fit exactly to the generated power of the PV plant. Therefore, the whole integrated system is not influenced by this power decline during day operation. The combination of CSP and PV seems to be beneficial in order to minimize the parasitic losses of the power plant.

7.4.4 Generation of surplus power

The occurrence of surplus power results when the supply exceeds the actual power demand. Especially when using fluctuating energy sources like PV and wind power it is favored to use the surplus generation, which can be either stored or fed into the grid (see also the graphical evolution of surplus power in figure 7.10).

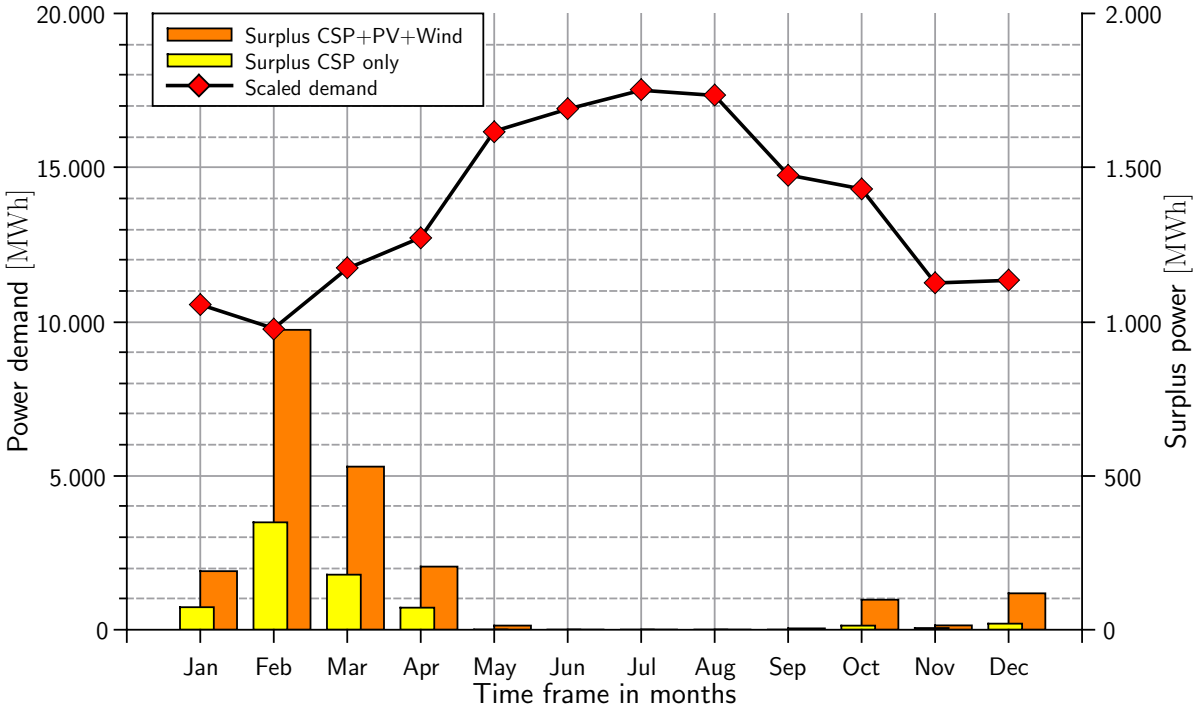

Figure 7.12: *Monthly scaled electricity demand and surplus power*

In this case study, only the CSP plant allows to deliver power on demand depending on the actual level of the thermal storage system. If the irradiation during the day cannot charge the storage sufficiently, the power generation is interrupted because of the

empty hot storage tank. The maximized operation of the CSP plant only creates a total cumulative surplus of 711 $\mathrm{MWh_{el}}$ during the year.

Adding the PV and wind power plant with a design capacity of 4 $\mathrm{MWh_{el}}$ increases the generated surplus power by 1434 $\mathrm{MWh_{el}}$ during the year, generating a total surplus of 2145 $\mathrm{MWh_{el}}$. Figure 7.12 presents the exact surplus power by monthly values on the right axis with respect to the scaled power demand. The highest surplus is generated during the months January to April. The peak surplus sums up to 5605 $\mathrm{kW_{el}}$ in February. During the summer term with generally high electricity demand, the generated surplus drops almost to zero. In other words, all generated power by the renewable energy system is consumed by the city.

7.4.5 Storage of surplus power

Using the described system in section 7.3 and the results of figure 7.6, the whole generated surplus is converted into usable heat for the thermal storage system. In consequence of that, the process allows the direct utilization of generated power to increase the operation time of the CSP plant. Under the stated assumptions in section 7.3, a peak power of 5000 $\mathrm{kW_{el}}$ generates additional 41,8 $\mathrm{t/h}$ molten salt in the hot storage tank. Comparing the amount to 300 $\mathrm{t/h}$ mass flow used for steam generation, in the examined case the extension of the additional run-time of the CSP plant is only marginal. In this analysis, possible hybridization and co-firing of the CSP plant is not considered.

Figure 7.13 visualizes the increased operation time of the CSP by generated surplus power from the PV and wind power plant. It can be stated that only during the winter season occurs a noticeable extension of the CSP operation time. The CSP power generation is increased by up to 4.5% in February, the other months show a negligible extension of the operation time ranging around 1.5%. The calculation of the complete year results in a generated power extension of 0.8%.

Table 7.8 presents the exact amounts of the total power generation per month, the generated surplus power and the resulting additional CSP operation time. Generally, the highest amounts of surplus power evolves during the winter months (compare also to figure 7.12). The resulting extension of the CSP operation ranges up to 27 hours in February and zero during the summer months. In total, the yearly extension reaches almost up to 62 hours for the complete year.

The reason for the limited effect in this scenario has several causes. In the first place, the dimension of the PV and wind power plant is rather small compared to the CSP plant.

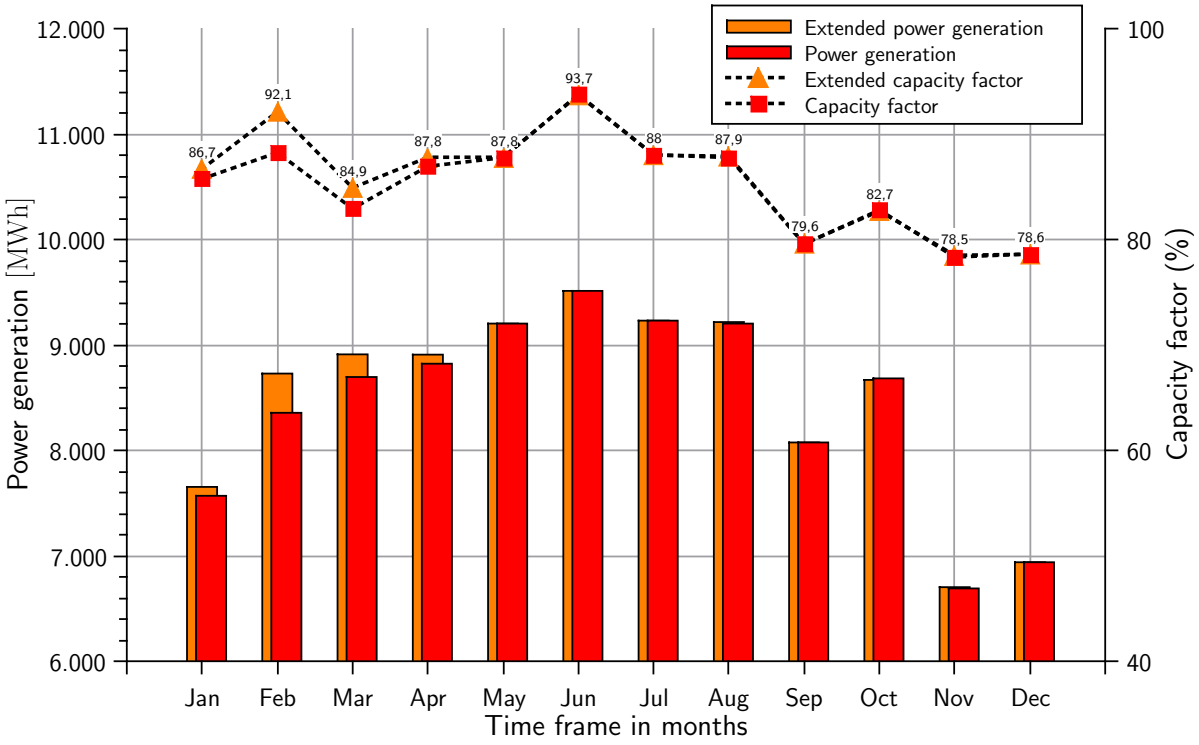

Figure 7.13: *Extended CSP operation time using surplus power from PV and wind*

Month	Total power generation $\mathrm{MWh_{el}}$	Surplus generated $\mathrm{MWh_{el}}$	Additional CSP operation time h
January	8519	190	6.36
February	9787	978	27.26
March	10037	529	14.75
April	10206	205	5.71
May	10431	13	0.38
June	10866	0	0
July	10866	0	0
August	10568	0	0
September	9544	4	0.12
October	9981	97	2.71
November	7516	14	0.47
December	7956	118	3.95
Total	**116277**	**2150**	**61.70**

Table 7.8: *Total power generation, available surplus and additional CSP operation time*

The design capacity of 4 $\mathrm{MW_{el}}$ for both technologies hold only a minor share compared to the 14 $\mathrm{MW_{el}}$ CSP design capacity. Increasing the amount of PV and wind power installed, would generate higher amounts of surplus energy which can be stored using the thermal storage system of the CSP plant. Secondly, the whole integrated system has

been dimensioned in order to generally minimize the generation of surplus power. The goal of this case study has been the dimension of a system to cover the demand of the city, not to feed-in power to the national grid. The available land area in coastal regions with seawater access is limited and can be considered as more expensive compared to desert sites with no water access. It is more likely to use the available land for tourism purpose as for power plants.

7.4.6 Estimation of investment cost

In order to estimate the complete financial investment for the whole integrated energy supply system, the results from section 6.4.1 of the CSP and desalination unit as well as the results from section 7.4.2 are used. All calculations base on SAM [114] like discussed in the previous sections. The total investment costs (total CAPEX) for the integrated system sum up to 154.2 $\mathrm{M\$}$. The total power generation can be calculated to 115.3 $\mathrm{GWh_{el}}$. Figure 7.14 presents the relative share of each technology to the power generation. The needed land area is fixed due to the integration of the PV and wind power plant in the occupied area of the CSP and desalination plant.

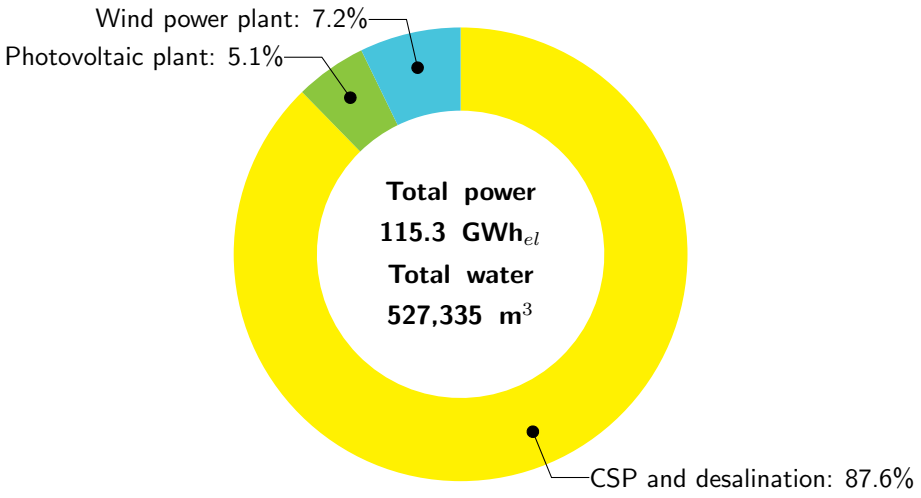

Figure 7.14: *Total power generation by each technology*

Basing on the monthly power generation of each technology and the weighed averaged mean share of the electricity supply, the derivation of a common $LCOE_{tot}$ value of the integrated system becomes possible. Table 7.9 summarizes the calculation for the discussed system configuration. Due to the technology characteristics and the complexity of the integrated system, a more detailed investigations could be subject to further research.

Technology	Total power generation $\mathrm{MWh_{el}}$	Levelized cost ¢/kWh	Averaged LCOE ¢/kWh
CSP	100,978	18	15.7
PV	5,948	21	10.8
Wind	8,327	1	0.01

Table 7.9: *Integrated system, total levelized cost of electricity*

In general, the lower investment cost and financial performance of wind model plant decrease the $LCOE_{CSP}$ by 2.3 ¢/kWh and the $LCOE_{PV}$ by 10 ¢/kWh. The effect is caused by the highly efficient wind power plant which generates a financial benefit due to the excellent wind conditions at the selected site. Summarizing, the total levelized costs of electricity $LCOE_{tot}$ calculate to 17 ¢/kWh without any governmental incentives or subsidies. Furthermore, it needs to be noted that the deployment of wind power plants appears to be financially more profitable compared to solar energy systems.

7.4.7 Integration and occupied land area

The design and the model of the CSP plant have been sufficiently discussed in chapter 3.3 and section 3.3.1. Due to the arrangement of the heliostats around the the tower like shown in figure 3.3, the occupied land area principally has a round shape. Based on the assumptions of section 7.2.2, the integrated power supply system is integrated in the given layout of the field. The assembly of PV modules on given heliostats replacing the mirrors lead to cost advantages through economies of scale. In addition to that, the PV modules generate more electricity by orientating them continually in an optimal angle to the solar irradiation.

The wind turbine described in section 7.2.3 can be placed optionally on the edges of the field. It is favorably to orientate the turbine according to the prevailing wind speed. The analysis of the meteorological data has shown that the most frequent wind direction is North-West. As a result, one possible option to integrate the PV and wind model plant is given in figure 7.15 (compare also to figure 3.3). The total occupied land area calculates to 1266 x 1126 m, which sums up to an total area of 1.426 $\mathrm{km^2}$.

The required land is marked in figure 7.16 according to Google Maps. The locations is chosen close to the road Hurghada - Cairo in order to allow a possible expansion of the city on undeveloped land. The presence of an own substation connected to the national grid as well as a waste-water treatment plant simplifies the media connection for electricity and water.

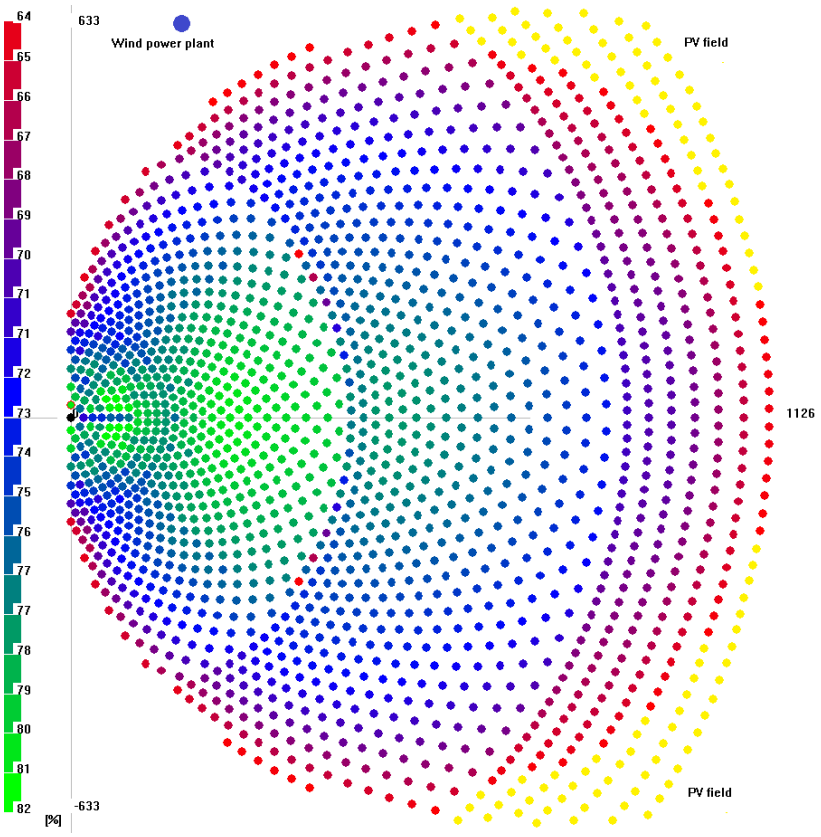

Figure 7.15: *Heliostat field layout with integrated PV and wind power plant, modified from [18–20]*

The exact position of each heliostat is subject to further optimizations in order to optimize the field efficiency (compare also to section 3.3.1). It is required to respect possible elevations and ground conditions as well as the distance to the seawater source. As a consequence, figure 7.16 presents just one possible solution according to the performed simulation of the solar power plant in chapter 4.

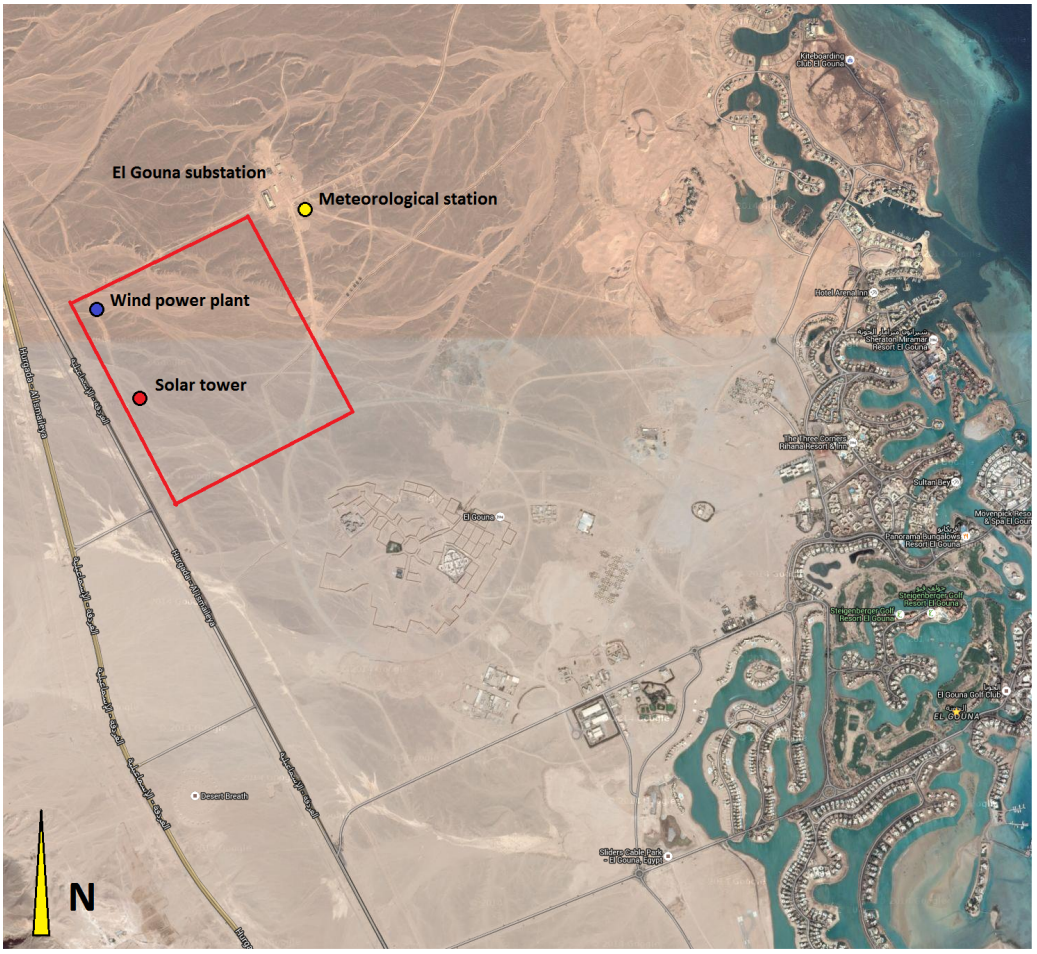

Figure 7.16: *Used land area in El Gouna, modified from Google Maps*

Chapter 8

Conclusion

The previous chapters have presented a conceptual design of one possible solution for the renewable generation of electricity and integrated thermal desalination of seawater. In the case study, the modeled system has been integrated into a real scenario using an energy mix with PV and wind power plants. The technological approach to combine these processes presents several advantages: lower dependencies on fossil fuels, a consequent reduction of climate gas emissions, and the protection of finite water reserves. However, the approach is significantly more costly compared to conventional power solutions.

In chapters 2 and 3, the available state-of-the-art technologies in concentrating solar power generation and thermal desalination have been assessed. Special attention has been given to the heat transfer mechanisms in thermal desalination processes. The development of a simulation model integrating the different technologies allowed a analysis with respect to energy, exergy and economic aspects. The simulation results are used in chapters 4 and 5 to assess the cogeneration of power and water using the newly developed low-temperature desalination [12, 15, 75].

A first economic evaluation has been performed in chapter 6 with special respect to CAPEX costs as well as the cogeneration ratios between power and water production. All results have been calculated using real environmental data obtained by a meteorological station [31] described in sections 3.2 and 4.1. The case study in chapter 7 integrates the modeled system in a real demand scenario of the city El Gouna in Egypt. The renewable energy mix comprises of an additional small PV and wind power plant which is analyzed with special respect to the demand coverage and surplus power handling. The whole system is integrated on the land area for the CSP plant.

The technology development status and some general remarks for future research potentials can be derived from the exergetic analysis which has been calculated in chapter 5.

Component	$\dot{E}_F$ kW	$\dot{E}_P$ kW	$\dot{E}_D$ kW	ϵ_k %	$y*_{D,k}$ %	$y_{D,k}$ %
Solar field	158,514	66,431	92,083	41.9	91.9	42.6
Power block	43,847	39,329	4524	89.7	4.6	2.1
Desalination	13,913	10,346	3572	74.4	3.5	1.7

Table 8.1: *Exergy analysis of the complete system*

Table 8.1 presents the summary for the solar field, the power block and the thermal desalination unit. The exergetic efficiencies ϵ_k show the thermodynamic efficiency of each process (see also sections 5.1.3). In addition, these efficiencies also allow for conclusions concerning the relative development of the technology. The power block can be seen as fully developed working with high exergetic efficiencies above 85%. In opposite, the CSP technology still needs research, mostly to reduce the construction costs and use the economies of scale effect. Table 8.1 also shows that the solar field accounts for 92% to the overall system exergy destruction which is mainly due to unavoidable heat and radiation losses. The combination with thermal desalination plants creates an additional product with high market value. The analysis has shown the relative high thermodynamic efficiency and the cogeneration effects to the power generation in the CSP plant.

As the analyzed system in the selected configuration has not been discussed in literature before, there is much room for process optimization and further research with respect to the technology integration. The high efficiency of the low-temperature desalination unit can be considered as result of the new developed spraying system which allows a direct contact condensation on sprayed droplets (compare also to the sections 2.4.3 and 2.5.1). However, the development of the LTD system has not yet reached its full potential and proceeds continually while the newest scientific articles mentions the possibility of new applications that use this technology [83]. The key findings of this thesis can serve as a foundation for further research in the following fields:

- *Economics:* The performed exergy analysis in chapter 5 could be used as the basis for an exergo-economic analysis as described in [125] and compared to the results of chapter 6 using a different calculation method. An exergo-economic analysis requires an assessment of the real plant components and its individual pricing. The exergetic efficiencies of the components are used as criteria for the best cost-saving potentials. The derivation of optimal cogeneration ratios could be the result and used as input data for the integration in a real scenario. In addition to that, the results would allow a comparison with similar cogeneration

plants described in literature. The results can underline the high efficient operation of the low-temperature desalination. The effect of the produced water on basis of environmental and social aspects should not however be neglected but need to assessed in different ways. Furthermore, the integrated scenario using a renewable energy mix in chapter 7 requires a more detailed assessment of the financial effects to the cogeneration system.

- *Integration of CSP co-generation:* Due to the special construction and operation of the CSP plant, there are also other options for the integration of the co-generation products technically feasible which have not been discussed. The avoidance of surplus power generation could be performed basing on flexible condensation pressures in order to increase to the water production when the electricity demand is low. It requires a detailed optimization of the CSP power generation with respect to the fluctuating resources like the modeled PV and wind power plant. The water production can be maximized when the power demand is minimized in order to cover the demand more precisely. The influence of changed boundary conditions and financial assumptions can have a significant effect to the results.

- *Integration of thermal storage:* Chapter 7 showed one option to integrate the cogeneration system with large thermal storage into a real power and water demand scenario. The short-term storage of surplus energy by thermal processes need a special investigation on the level of technical solutions and respective plant components (see also section 7.3). The economic benefits may increase with the amount of variable renewable power supply systems, demanding for simple storage solutions with insensitive part-load behavior and short ramp-up times. Other approaches like smart-grids and energy price changes may result in different conclusions who can make the proposed system financially more advantageous than previously described.

- *Seawater access:* The supply with a reliable cooling sink has been modeled by a direct seawater pipeline. The combination with a desalination system always requires a good access to seawater, which is also used as cooling medium. The cooling temperature has an influence on the produced distillate, but in the examined configuration not on the power plant efficiency. Future research should focus on an optimized design of the cooling cycle in order to minimize the exergy destruction in HEX3 and seawater intake system to prevent negative effects to the coastal maritime life. In this analysis, the cooling mass flow has been set to high

values to ensure a sufficient cooling of the whole system without an appropriate optimization and design research for appropriate seawater intake systems.

- *Zero-liquid discharge:* The analysis completely neglects any possible treatment of the desalination waste water, the brine (concentrated saltwater). As the thermal desalination technology can allow for high salt concentrations, the saturation above the precipitation and a following drying process could generate industrial salt as a third product. The current available technologies for such ZLD systems are very limited and the deployment is in an early stage. Due to the increasing problem of contamination of coastal areas seriously affecting the maritime life, there needs to be a technical answer to meet such risks.

As a conclusion, such systems are nowadays too expensive for the deployment in regions with suitable solar irradiation and politically not stable enough for financial investments of this magnitude. The subsidization of more cheaper fluctuating power resources like PV and wind power plants seem more advantageous due to lower technology costs. Nevertheless, the experience in Europe, especially in Germany, show the emergence of new challenges in a reliable supply using renewable energies. Here, all energy storage solutions can help to lower the problem while the development of CSP with large thermal storage systems ensure an optimal integration for a clean and reliable energy supply for power and water production.

Appendix A

Environmental data analysis

The meteorological ground measurement data [31] have been evaluated with the kind support of the German Areospace Center (DLR), Dipl.-Geogr. Steffen Stoekler and Dr. Franz Trieb.

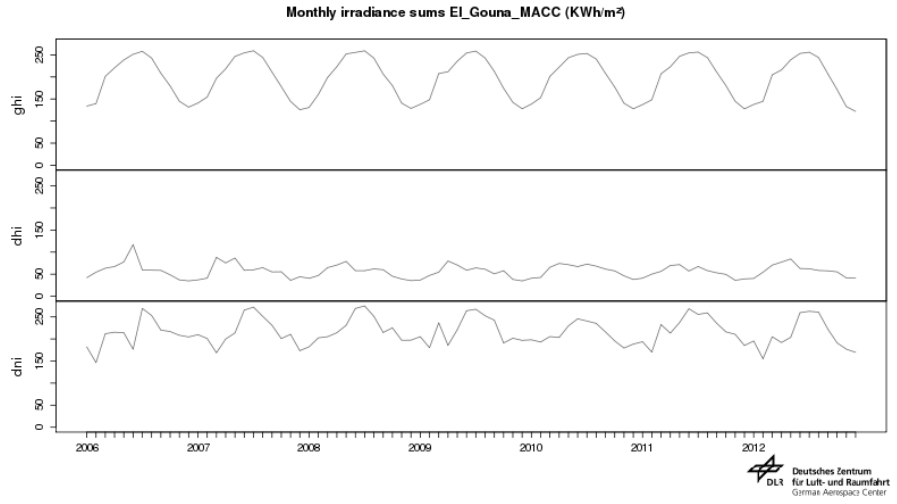

Figure A.1: *Satellite data, monthly irradiance sums for El Gouna, 2006-2012*

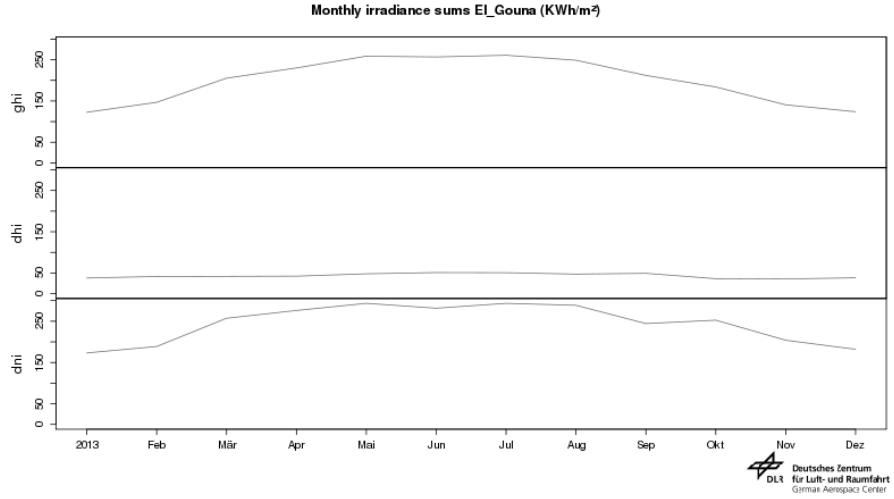

Figure A.2: *Ground measurement, monthly irradiance sums for El Gouna, 2013*

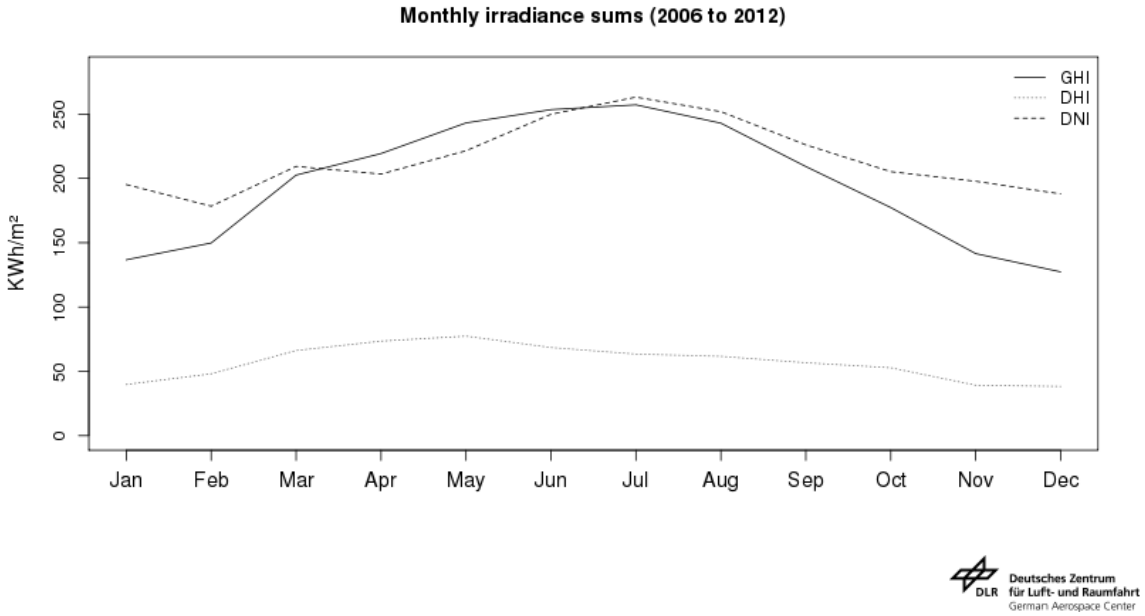

Figure A.3: *Satellite data, yearly irradiance sums for El Gouna, 2006-2012*

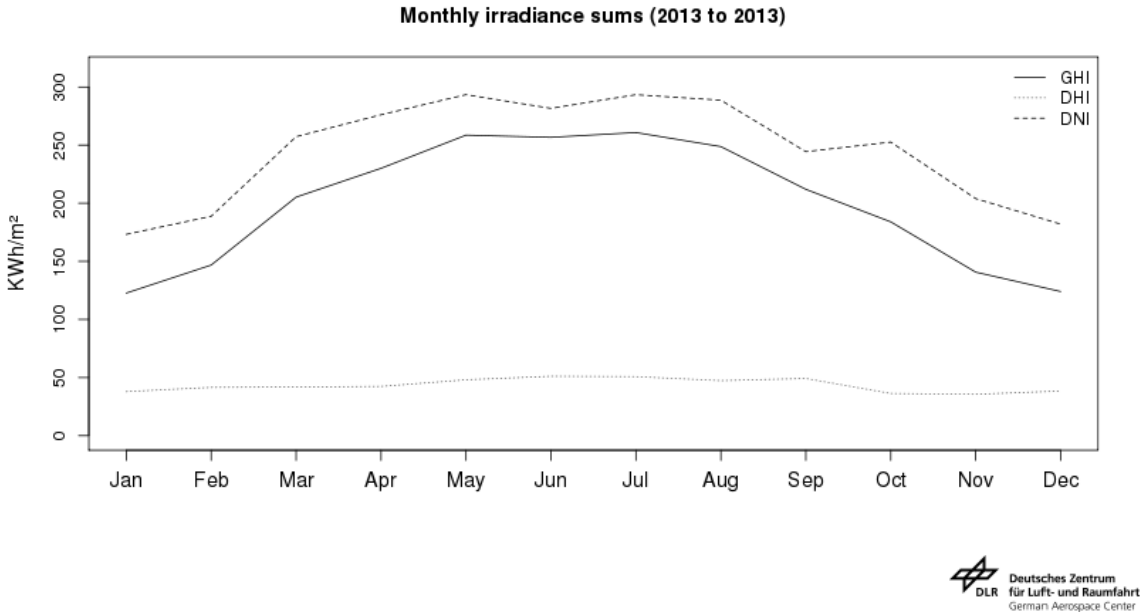

Figure A.4: *Ground measurement, yearly irradiance sums for El Gouna, 2013*

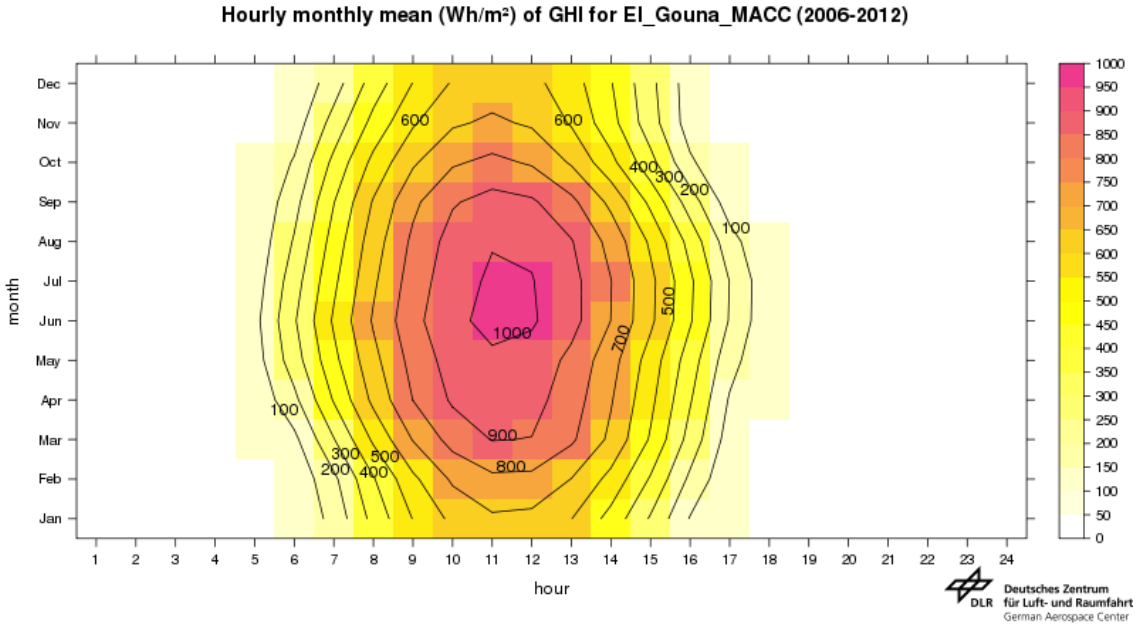

Figure A.5: *Satellite data, GHI hourly monthly mean in* $\mathrm{W/m^2}$ *for El Gouna, 2006-2012*

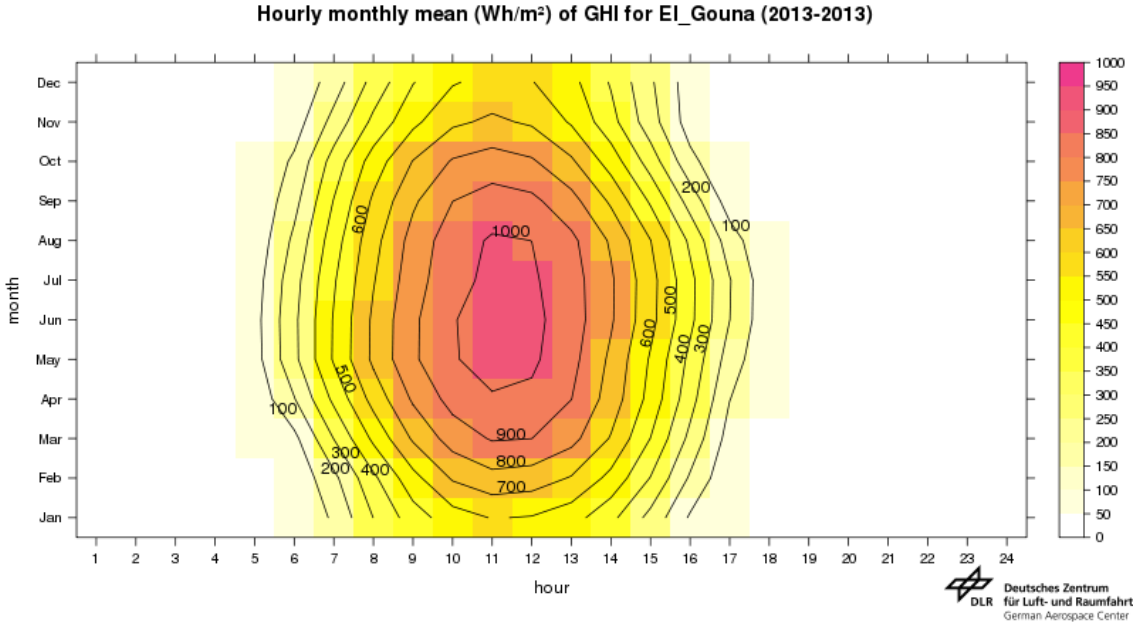

Figure A.6: *Ground measurement, GHI hourly monthly mean in* $\mathrm{W/m^2}$ *for El Gouna, 2013*

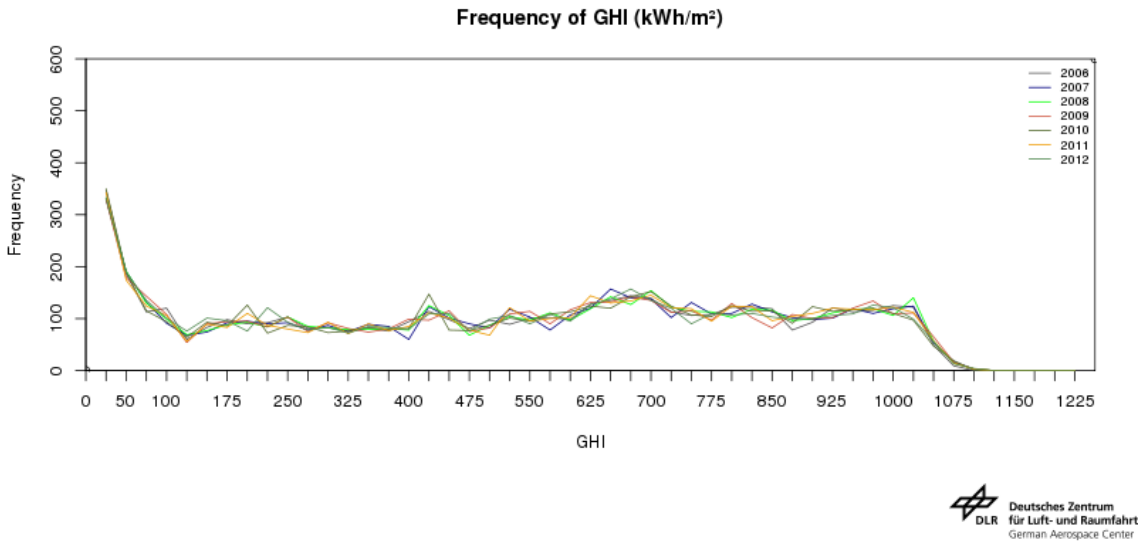

Figure A.7: *Satellite data, GHI frequencies for El Gouna, 2006-2012*

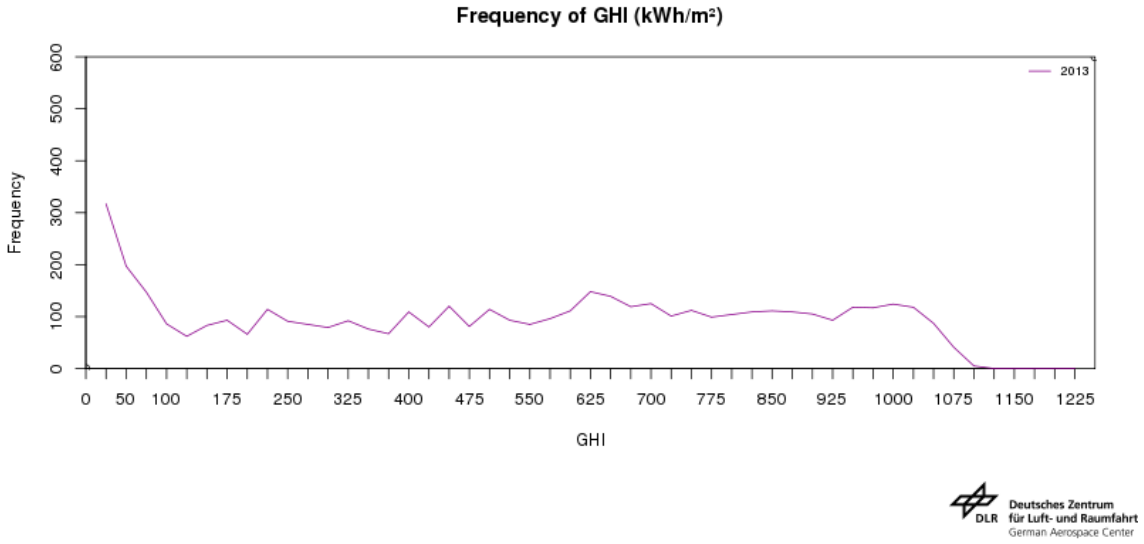

Figure A.8: *Ground measurement, GHI frequency for El Gouna, 2013*

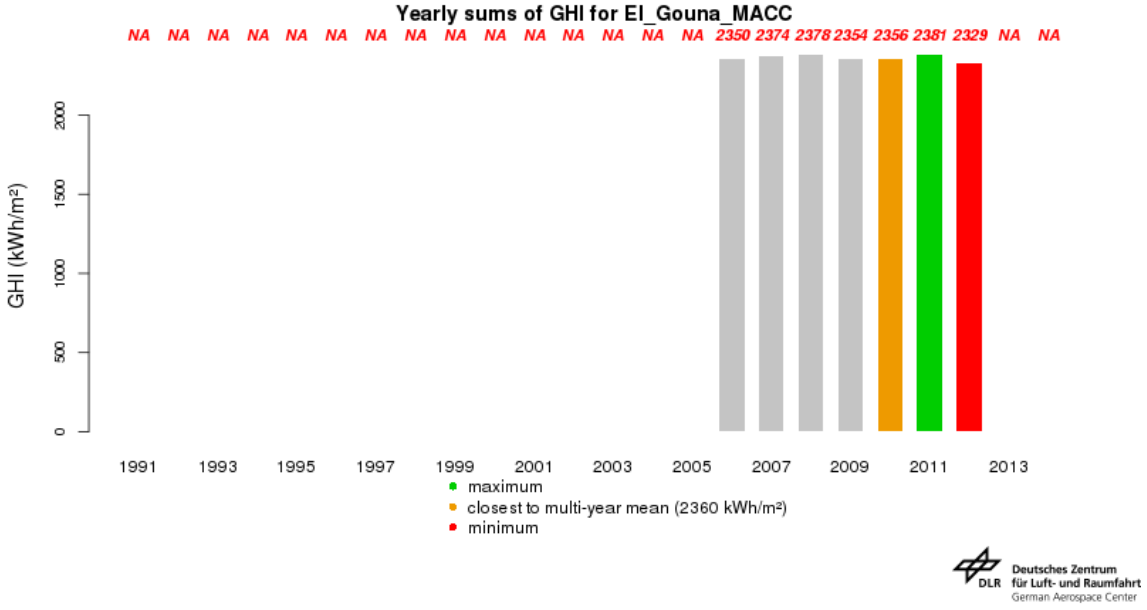

Figure A.9: *Satellite data, GHI yearly sums for El Gouna, 2006-2012*

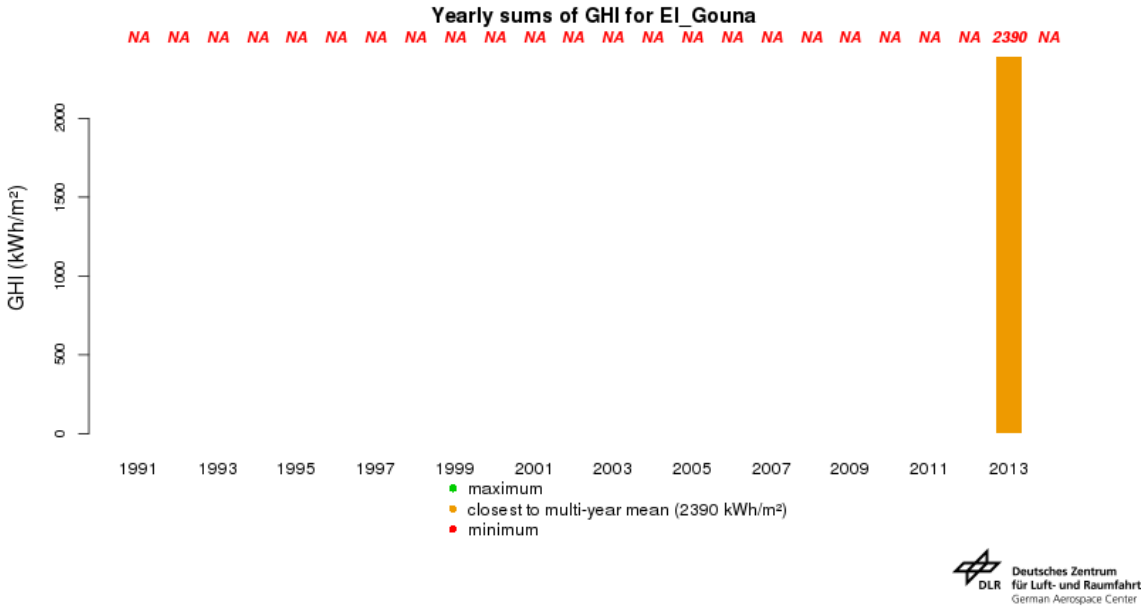

Figure A.10: *Ground measurement, GHI yearly sums for El Gouna, 2013*

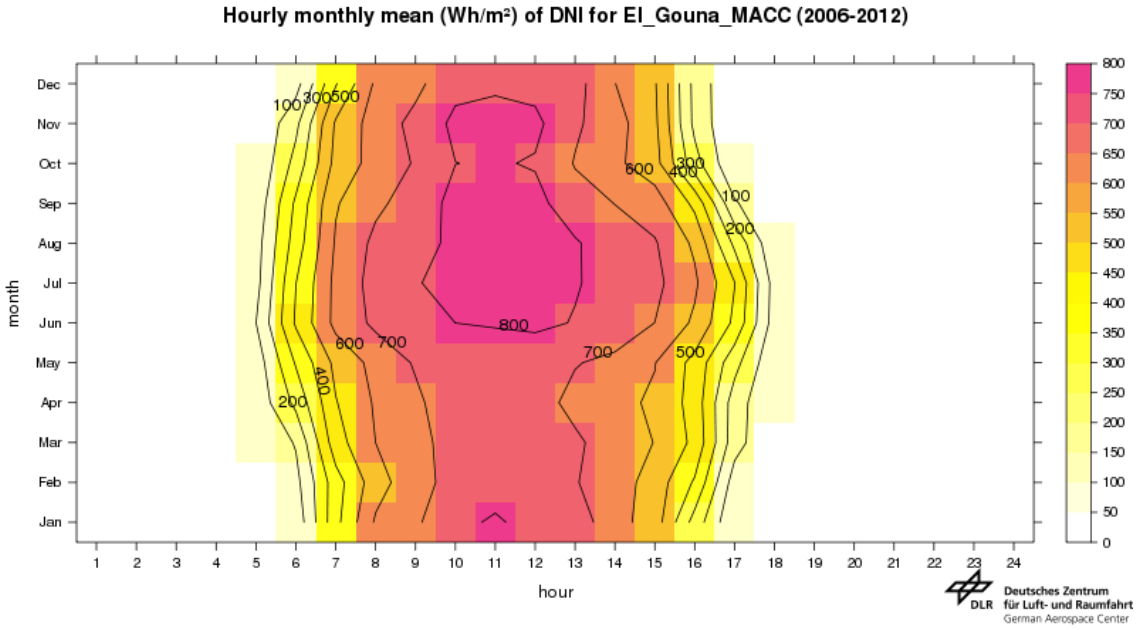

Figure A.11: *Satellite data, DNI hourly monthly mean in* $\mathrm{W/m^2}$ *for El Gouna, 2006-2012*

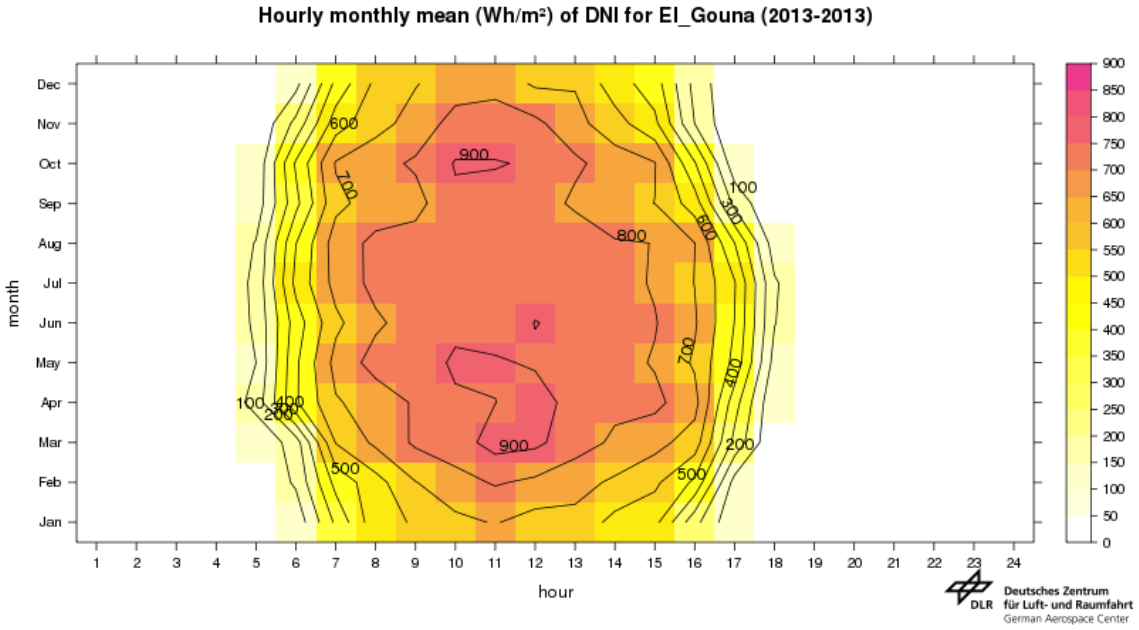

Figure A.12: *Ground measurement, DNI hourly monthly mean in* $\mathrm{W/m^2}$ *for El Gouna, 2013*

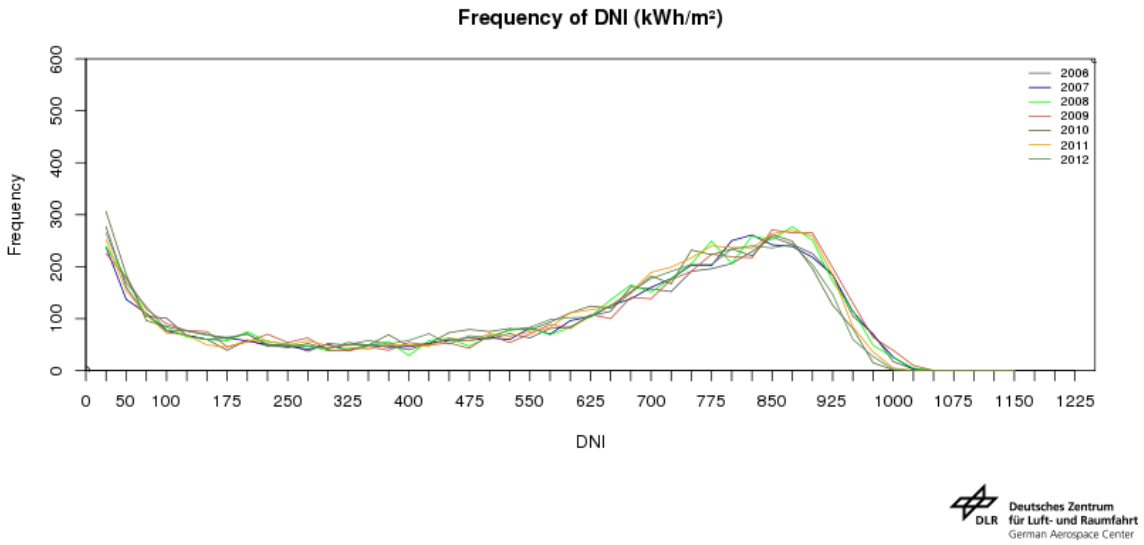

Figure A.13: *Satellite data, DNI frequencies for El Gouna, 2006-2012*

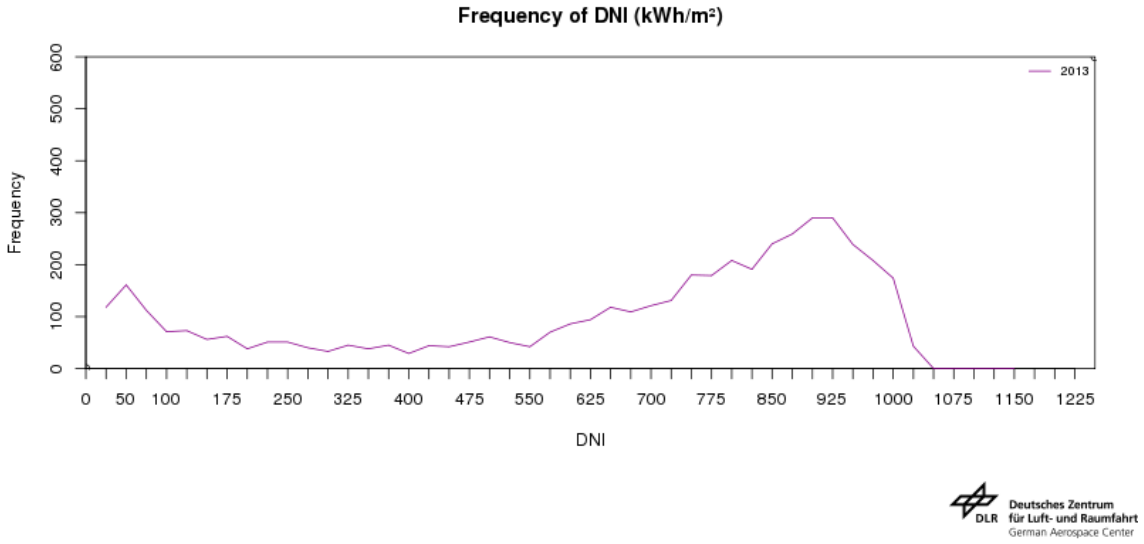

Figure A.14: *Ground measurement, DNI frequency for El Gouna, 2013*

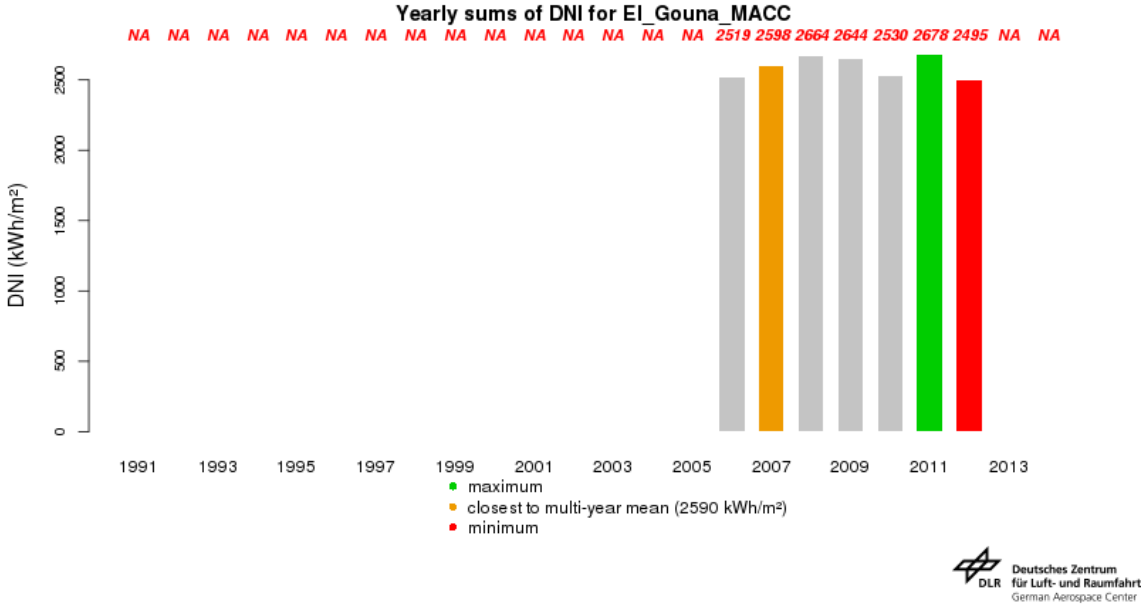

Figure A.15: *Satellite data, DNI yearly sums for El Gouna, 2006-2012*

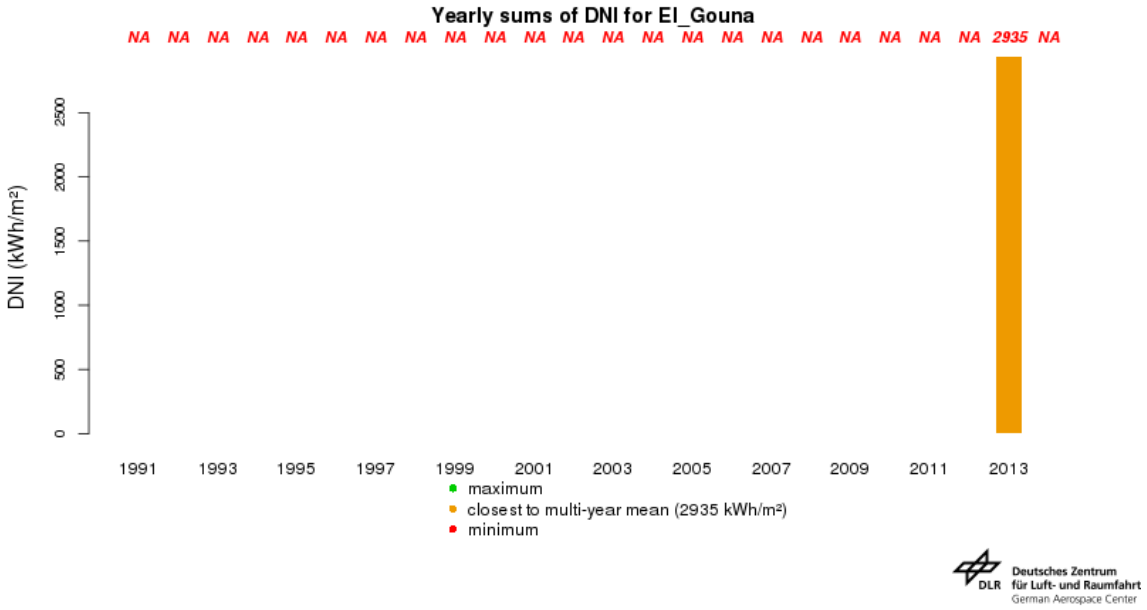

Figure A.16: *Ground measurement, DNI yearly sums for El Gouna, 2013*

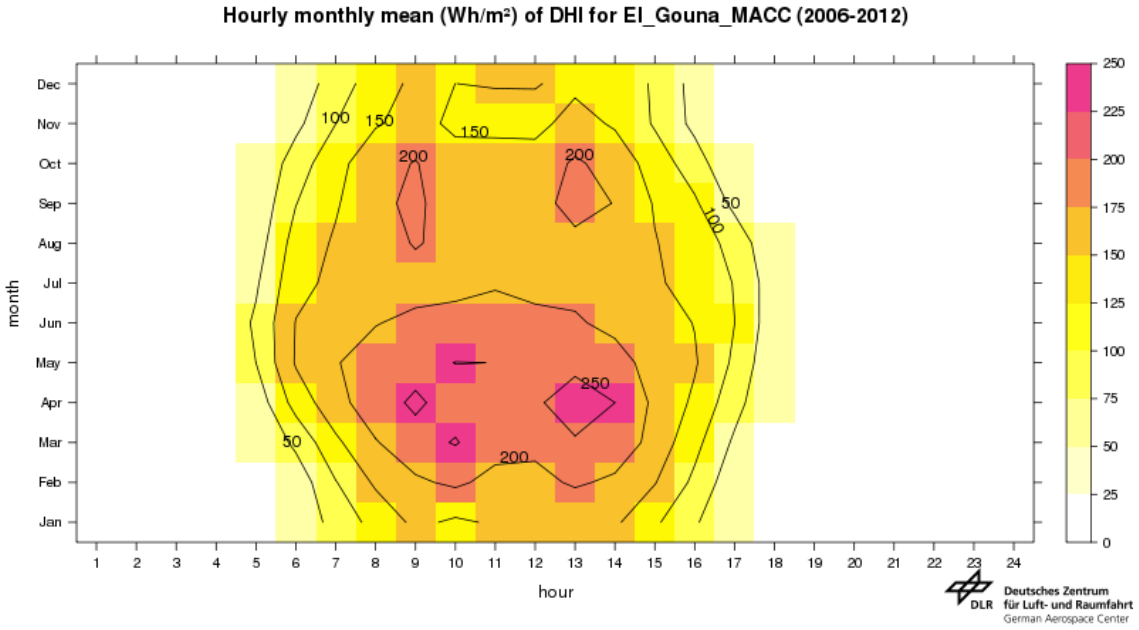

Figure A.17: *Satellite data, DHI hourly monthly mean in* $\mathrm{W/m^2}$ *for El Gouna, 2006-2012*

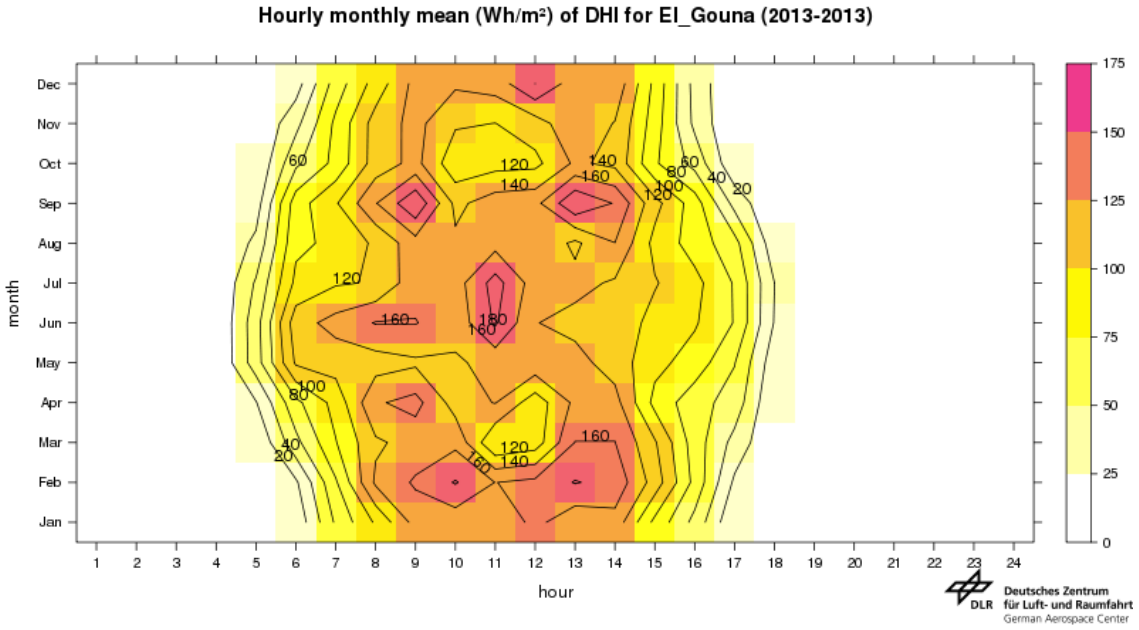

Figure A.18: *Ground measurement, DHI hourly monthly mean in* $\mathrm{W/m^2}$ *for El Gouna, 2013*

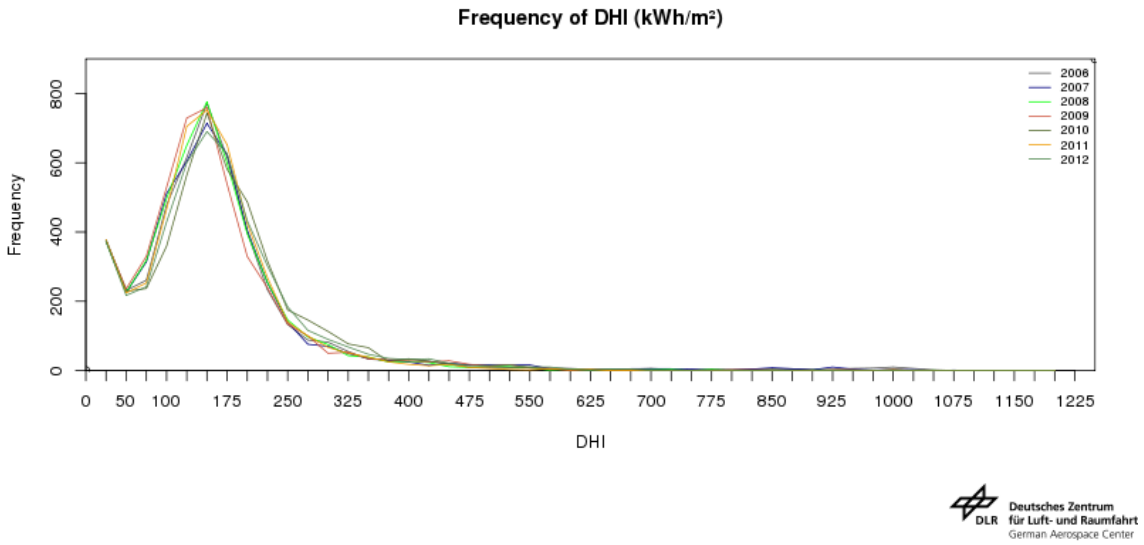

Figure A.19: *Satellite data, DHI frequencies for El Gouna, 2006-2012*

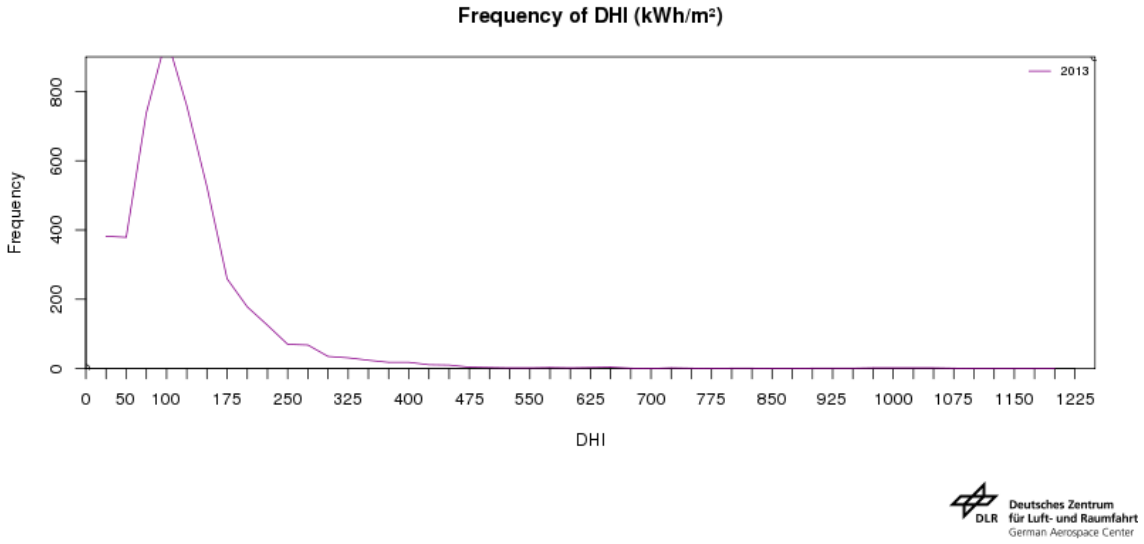

Figure A.20: *Ground measurement, DHI frequency for El Gouna, 2013*

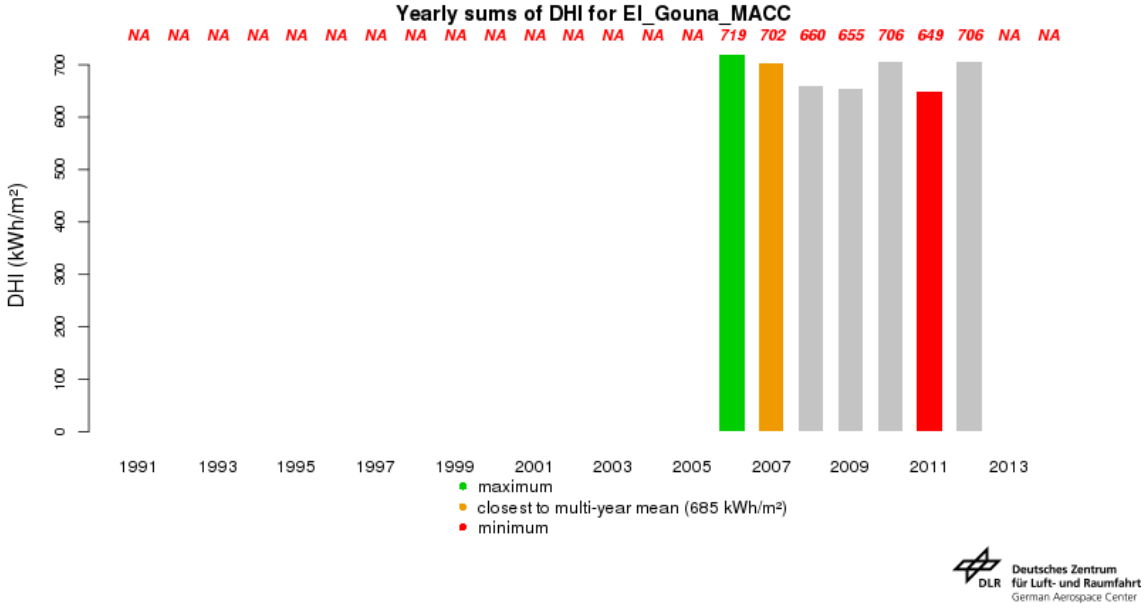

Figure A.21: *Satellite data, DHI yearly sums for El Gouna, 2006-2012*

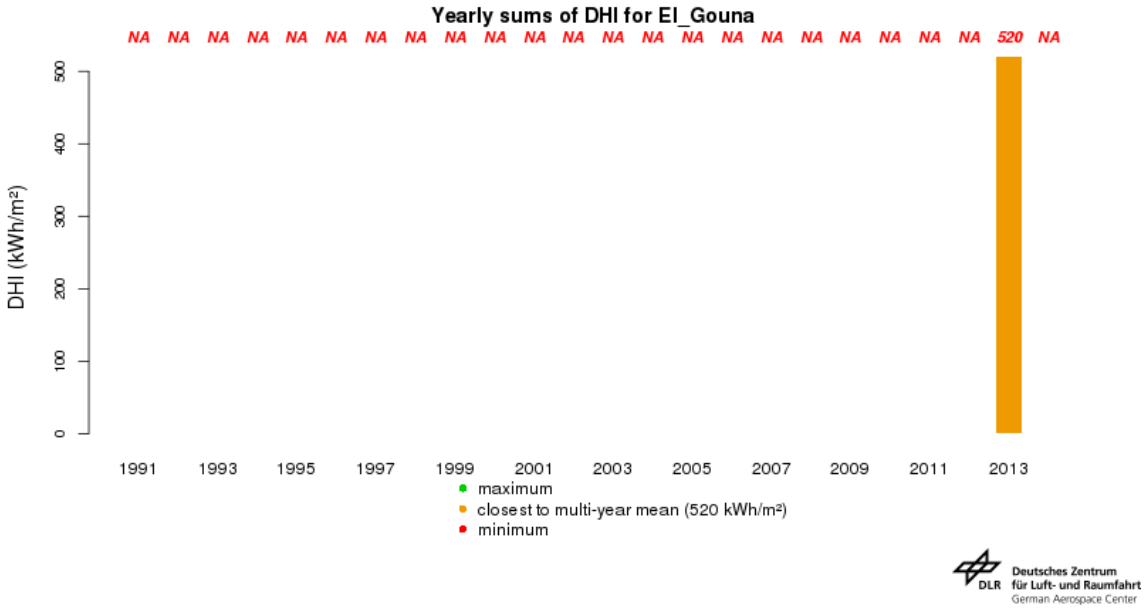

Figure A.22: *Ground measurement, DHI yearly sum for El Gouna, 2013*

Appendix B

Ebsilon simulation

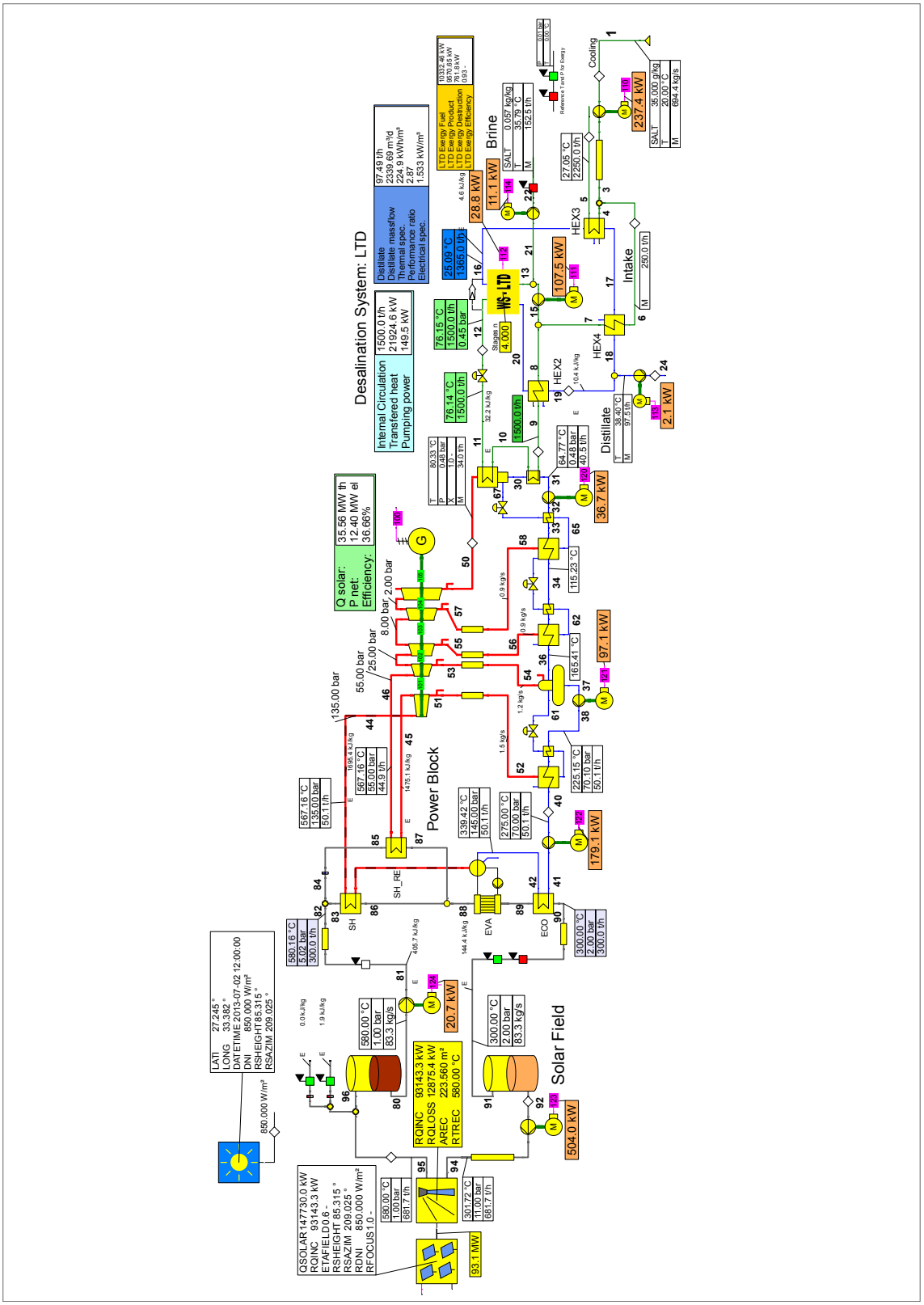

Figure B.1: *Ebsilon simulation, total view*

Bibliography

[1] F. Birol, L. Cozzi, T. Gould, A. Bromhead, T. Gül, and M. Frank. World Energy Outlook. Technical report, International Energy Agency (IEA), Paris, 2012.

[2] SolarGIS. Direct normal Irradiation, Africa and Middle East. GeoModel Solar and Solar GIS, 2011.

[3] IEA. Technology Roadmap, Concentrating Solar Power. *International Energy Agency (IEA)*, 2010.

[4] C. Turchi. Concentrating Solar Power (CSP) Overview. Technical report, National Renewable Energy Laboratory (NREL), 2013.

[5] S. Schoenung. Energy Storage Systems Cost Update - A Study for the DOE Energy Storage Systems Program. *SANDIA Report*, SAND2011-2730, April 2011.

[6] Sulzer. SJT-VCN Molten Salt Circulation Pumps for Concentrated Solar Power. Technical report, Sulzer Pumps, 2013.

[7] Siemens. Steam turbines for CSP plants. Technical report, Siemens AG, Energy Sector, Erlangen, 2010.

[8] H. T. El-Dessouky and H. M. Ettouney. *Fundamentals of Salt Water Desalination*. Number ISBN 0-444-50810-4. Elsevier, 2002.

[9] L. Awerbuch. Introduction to Desalination and its Technologies. Technical report, International Desalination Association (IDA), Desalination Academy, Santa Margherita, 2013.

[10] C. Sommariva. Thermal Desalination processes and economics. Technical report, European Desalination Society (EDS), Italy, 2007.

[11] C. Sommariva. Optimization of thermal Desalination design. Technical report, International Desalination Association (IDA), Desalination Academy, 2013.

[12] M. Lehmann, G. Exer, and C. Merkli. Low Temperature Distillation system by Watersolutions (WS-LTD), General plant and process description. Watersolutions AG, 2012.

[13] W.M. Rohsenow, J.R. Hartnett, and Y.I. Cho. *Handbook of Heat Transfer*. McGraw-Hill Handbooks, third edition, 1998.

[14] P.J. Marto. *Condensation*. McGraw-Hill Handbooks, third edition, 1998.

[15] E. Mansfeldt, M. Lehmann, G. Exer, and C. Merkli. Process comparison MED / WS-LTD. unpublished, Watersolutions AG, January 2013.

[16] P. Schausberger, J. Nowak, and O. Medek. Heat Transfer in Horizontal Falling Film Evaporators. Technical Report IDAWC/DB09-327, IDA World Congress, WABAG, Dubai, UAE, November 2009.

[17] Umweltmeteorologie, Wechselwirkungen zwischen Atmosphäre und Oberfläche, Berechnung der kurz- und langwelligen Strahlung. Technical Report VDI 3789 Blatt 2, Verein Deutscher Ingenieure, VDI Richtlinie, Duesseldorf, 1994.

[18] P. Schwarzbözl, R. Pitz-Paal, B. Belhomme, and M. Schmitz. Visual-HFLCAL - Eine Software zur Auslegung und Optimierung von Solarturmsystemen. *Deutsches Zentrum für Luft- und Raumfahrt (DLR), Institut für Technische Thermodynamik*, 2011.

[19] P. Schwarzbözl, B. Belhomme, R. Buck, R. Uhlig, L. Amsbeck, and M. Schmitz. Simulation solar Turmsysteme. *Deutsches Zentrum für Luft- und Raumfahrt (DLR)*, Köln, 2012. Deutsches Zentrum für Luft- und Raumfahrt (DLR), Institut für Technische Thermodynamik, Solarforschung.

[20] STEAG Energy Services GmbH, 64673 Zwingenberg, Germany. *EBSILON Professional Online Help*, 2012.

[21] J. Wellmann, K. Neuhäuser, F. Behrendt, and M. Lehmann. Modeling an innovative low-temperature desalination system with integrated cogeneration in a concentrating solar power plant. *Desalination and Water Treatment*, pages 1–9, 2014.

[22] J. Wellmann, K. Neuhäuser, F. Behrendt, and M. Lehmann. Modeling the cogeneration of power and water with CSP and low temperature desalination. *Dii Conference, Best Paper Award*, 2012. Berlin.

[23] K. Neuhäuser. Modellierung einer Niedertemperatur Entsalzungsanlage mit Integration in ein solarthermisches Kraftwerk. Master's thesis, TU Berlin, Institut für Energietechnik, May 2013.

[24] G. Tsatsaronis and T. Morozyuk. Script for the lecture Energy Engineering 1. *Technische Universität Berlin, Campus El Gouna*, (3. Chapter Exergy), 2014.

[25] F. Bosnjakovic. *Technische Thermodynamik*. Number ISBN 3-7985-1114-4. Dr. Dietrich Steinkopf Verlag, Darmstadt, 1998.

[26] U. Helman. The Economic and Reliability Benefits of CSP with thermal energy storage: recent studies and research needs. Technical report, Concentrating Solar Power Alliance, December 2012.

[27] S.H. Madaeni, R. Sioshansi, and P. Denholm. Capacity Value of Concentrating Solar Power Plants. Technical Report NREL/TP-6A20-51253, National Renewable Energy Laboratory (NREL), 2011.

[28] S. Giuliano, R. Buck, and S. Eguiguren. Analysis of Solar Thermal Power Plants with thermal Energy Storage and solar-hybrid operation strategy. *Solarpaces*, 162, 2012.

[29] F. Trieb, C. Schillings, P. Viebahn, C. Paul, H. Altowaie, T. Sufian, W. Alnaser, M. Kabariti, W. Shahin, A. Bennouna, et al. AQUA-CSP: Concentrating Solar Power for Seawater Desalination. *German Aerospace Center (DLR), Study for the German Ministry of Environment, Nature Conservation and Nuclear Safety, Stuttgart*, 2007.

[30] T. Azzer, E. Rizkalla, and H. Naseem. Electricity demand of El Gouna 2013. Hourly time series of electricity demand (unpublished), December 2014.

[31] J. Wellmann and I. Langer. Weather Station El Gouna West, Measurement data of 2013. Position Lat. 27.412906 Long. E 33.638252, TU Berlin, Campus El Gouna and FU Berlin, Institut für Meteorologie, 2013.

[32] S. Estafanous. El Gouna, an egyptian dream with no end. Orascom Hotels and Development, 2015.

[33] N. Tzoupanos. Water and wastewater management in El Gouna, Red Sea, Egypt. TU Berlin Campus El Gouna, Department Water Engineering, February 2015.

[34] ENERCON. Enercon Produktübersicht. Technical report, ENERCON GmbH, Aurich, Germany, März 2014.

[35] D.Y. Goswami and F. Kreith. *Handbook of Energy Efficiency and Renewable Energy*. Mechanical and Aerospace Engineering Series. Taylor & Francis, 2007.

[36] M. Seitz. Thermodynamische Simulation und Optimierung von Betriebszyklen bei solarthermischen Kraftwerken mit Flüssigsalzen als Wärmeträgermedien. Master's thesis, Hochschule Augsburg, DLR Stuttgart, September 2012.

[37] T. Bauer, N. Pfleger, N. Breidenbach, M. Eck, D. Laing, and S. Kaesche. Material aspects of Solar Salt for sensible heat storage. *Applied Energy*, (111):1114 – 1119, 2013.

[38] T. Bauer, N. Breidenbach, N. Pfleger, D. Laing, and M. Eck. Overview of molten salt storage systems and material development for solar thermal power plants. Technical report, German Aerospace Center (DLR), Institute of Technical Thermodynamics, 2012.

[39] C. Measures. Chemical composition of seawater; Salinity and the major constituents. Technical Report OCN 623 - Chemical Oceanography, Department of Oceanography, University of Hawaii, Manoa, Hawaii, 2010.

[40] W. Roetzel and B. Spang. *VDI Wärmeatlas, Typische Werte für Wärmedurchgangskoeffizienten*, volume C3. Springer Verlag, Berlin and Heidelberg, 2013.

[41] *VDI Wärmeatlas*. Springer, Berlin, Heidelberg, 2006. VDI Gesellschaft Verfahrenstechnik und Chemieingenieurwesen.

[42] H. Gelbe and I. Mörl. *Dubbel: Komponenten des thermischen Apparatebaus, Bauarten von Wärmeübertragern*, volume K4. K. H. Grothe and J. Feldhusen, 21 edition, 2005.

[43] J.H. Kopp. *Über den Wärme- und Stoffaustausch bei Mischkondensatoren*. PhD thesis, ETH Zürich, 1965.

[44] Bosch Solar Module c-Si M 60 SFmerkli. M245, 245 wp, BOSCH Solar Energy GmbH, January 2013.

[45] F. Birol, L. Cozzi, T. Gül, D. Dorner, M. Baroni, C. Besson, C. Hood, B. Wanner, and D. Wilkinson. World Energy Outlook: Redrawing the energy-climate map. Technical report, International Energy Agency (IEA), Paris, 2013.

[46] W. Immerzeel, P. Droogers, W. Terink, J. Hoogeveen, P. Hellegers, and M. Bierkens. Middle-East and Northern Africa Water Outlook. Technical report, FutureWater, commissioned by the World Bank, Wageningen, The Netherlands, January 2011.

[47] B.D. Negewo. *Renewable energy desalination: an emerging solution to close the water gap in the Middle East and North Africa*. The World Bank, 2012.

[48] F. Trieb. Trans-Mediterranean Interconnection for Concentrating Solar Power (TRANS-CSP). Final report, German Aerospace Center (DLR), Institute of Technical Thermodynamics, Section Systems Analysis and Technology Assessment, Stuttgart, 2006.

[49] Fichtner. MENA Regional Water Outlook, Part II, Desalination Using Renewable Energy, Task 1 Desalination Potential. Technical report, Stuttgart, 2011.

[50] F. Trieb and W. Dürrschmidt. Concentrating Solar Power now, Clean Energy for Sustainable Development. Technical report, The Federal Ministry for the Environment, Nature Conservation and Nuclear Safety (BMU), Berlin, Germany, June 2002.

[51] F. Trieb, S. Kronshage, V. Quaschning, J. Dersch, H. Lerchenmüller, G. Morin, and A. Häberle. SOKRATES-Projekt Solarthermische Kraftwerkstechnologie für den Schutz des Erdklimas. Ap 2, technologiedatenbank und -modelle, modellbildung

und -implementierung, Deutsches Zentrum für Luft- und Raumfahrt, Stuttgart, Fraunhofer Institut für Solare Energiesysteme, Freiburg, PSE, Freiburg, 2004.

[52] P. Viebahn, S. Kronshage, F. Trieb, and Y. Lechon. NEEDS, New Energy Externalities Developments for Sustainability, Final report on technical data, costs, and life cycle inventories of solar thermal power plants. Final report Project no: 502687, 12.2 - RS Ia, Deutsches Zentrum für Luft- und Raumfahrt, Stuttgart (DLR), CIEMAT, 2008. Technical data, costs, and life cycle inventories of solar thermal power plants.

[53] IEA. Technology roadmap: Solar Thermal Electricity. *International Energy Agency*, 2014.

[54] A. Cuellar, F. Bussieres, and C. Marquez. CSP Parabolic Trough Report: Costs and Performance. Technical report, CSP Today, FC Business Intelligence, 2011.

[55] J. Hinkley, B. Curtin, J. Hayward, A. Wonhas, R. Boyd, C. Grima, A. Tadros, R. Hall, K. Naicker, and A. Mikhail. Concentrating solar power–drivers and opportunities for cost-competitive electricity. *Clayton South: CSIRO*, 2011.

[56] DLR. German Aerospace Center – Analysis & Technology Assessment publications. http://www.dlr.de/tt/en/desktopdefault.aspx/tabid-2908/.

[57] IEA. International Energy Agency – selected publications available online. http://www.iea.org/publications/.

[58] SENER. Case Study: GEMASOLAR Central Tower Plant. Csp today, SENER Engineering and Systems Inc, San Francisco, 2010.

[59] T. Keck and W. Schiel. Envirodish and Eurodish - System and Status. Technical report, Schlaich Bergermann und Partner (SBP GmbH), 2003.

[60] BrightSource. Ivenpah Solar Electric Generating System. Technical report, BrightSource, 2014.

[61] 2014: The Year of Concentrating Solar Power. Technical Report DOE/EE-1101, US Department of Energy (DOE), May 2014.

[62] R.G. Reddy. Novel Molten Salts Thermal Energy Storage for Concentrating Solar Power Generation. Presentation, Solar Energy Technologies Program Peer Review, US Department of Energy, 2010.

[63] C. Turchi and G. Heath. Molten Salt Power Tower Cost Model for the System Advisor Model. *National Renewable Energy Laboratory, Golden, CO, Technical Report No. NREL/TP-5500-57625*, 2013.

[64] A. P. Fraas. A new approach to the design of steam generators for molten salt reactor power plants. *Oak Ridge National Laboratory, Union Carbide Corporation*, ORNL-TM-2953, 1971.

[65] G. J. Kolb. An Evaluation of Possible Next-Generation High-Temperature Molten-Salt Power Towers. *SANDIA Report*, (SAND2011-9320), 2012.

[66] C. Bahl, D. Laing, M. Hempel, and A. Stückle. Concrete thermal energy storage for solar thermal power plants and industrial processes. In *Proceedings of Solar Paces Conference*, 2009.

[67] C. Kost, J. N. Mayer, J. Thomsen, N. Harmann, C. Senkpiel, S. Philipps, S. Nold, S. Lude, and T. Schlegl. Stromgestehungskosten Erneuerbare Energien. Technical report, Fraunhofer-Institut für Solare Energiesysteme (ISE), Freiburg, 2013.

[68] J. Goyal. Delivering utility-scale CSP projects and improving competitiveness through storage. In *World Future Energy Summit*. AREVA Solar, 2014.

[69] F. Krakau. Simulation and experimental analysis of a thermochemical reactor for high temperature heat storage. Master's thesis, TU Berlin, Institut für Energietechnik and Deutsches Zentrum für Luft und Raumfahrt (DLR), Berlin und Stuttgart, 2014.

[70] D. Laing, D. Lehmann, and C. Bahl. Concrete storage for solar thermal power plants and industrial process heat. In *IRES III 2008, 3rd International Renewable Energy Storage Conference*, Berlin, 2008.

[71] A. Cipollina, G. Micale, and L. Rizzuti. *Seawater Desalination*. Number ISBN 978-3-642-01149-8. Springer Verlag, 2009.

[72] C. Sommariva. *Desalination and Advanced Water Treatment: Economics and Financing*. Balaban Desalination Publications, 2010.

[73] J. Blanco, P. Palenzuela, D. Alarcon-Padilla, G. Zaragoza, and M. Ibarra. Preliminary thermoeconomic analysis of combined parabolic trough solar power and desalination plant in port Safaga (Egypt). *Desalination and Water Treatment*, 51:1887–1899, 2013.

[74] P. Palenzuela, D. Alarcón, J. Blanco, E. Guillén, M. Ibarra, and G. Zaragoza. Modeling of the heat transfer of a solar multi-effect distillation plant at the Plataforma Solar de Almería. *Desalination and Water Treatment*, 31:257 – 268, July 2011.

[75] M. Lehmann. Grundlagen zur Simulation des WS-LTD Niedertemperatur Entsalzungsmodul für variable Temperaturspektren und variable Stufigkeit. unpublished internal paper, Watersolutions AG, March 2012.

[76] S. Al-Hengari, M. El-Bousiffi, and W. El-Mudir. Performance analysis of a MSF desalination unit. *Desalination*, (182):73 – 85, March 2005.

[77] P. Fiorini and E. Sciubba. Thermoeconomic analysis of a MSF desalination plant. *Desalination*, (182):39 – 51, March 2005.

[78] L. Awerbuch. Future Directions in Integration of Desalination, Energy and the Environment. Technical report, International Desalination Association (IDA), Boston, 2009.

[79] M.A.K. Al-Sofi and M.M. Srouji. Fuel allocation in dual-purpose plants. *Desalination*, 100(1-3):65–70, 1995.

[80] A.M. El-Nashar. Optimal design of a cogeneration plant for power and desalination taking equipment reliability into consideration. *Desalination*, 229(1-3):21 – 32, 2008.

[81] Y. Wang and N. Lior. Fuel allocation in a combined steam-injected gas turbine and thermal seawater desalination system. *Desalination*, 214(13):306 – 326, 2007.

[82] S. Meier and D. Altdorfer. Niedertemperaturdestillation im fremdgasbefreiten Raum. Diplomathesis, University of Applied Sciences, Northwestern Switzerland, 2000.

[83] T. Loveday. Is low temperature the next hot prospect? *Desalination and Water Treatment*, 24(4):23–25, March 2015.

[84] S. Martin and L. Treier. Messungen und Simulationen zur Niedertemperaturdestillation und Aerosoltransport. Diplomathesis, University of Applied Sciences, Northwestern Switzerland, 2002.

[85] G. Kotrle. Niedertemperaturdestillation - Messungen und Simulationen. Diplomathesis, University of Applied Sciences, Northwestern Switzerland, 2003.

[86] F. Hug. Niederdruckdestillation - Untersuchung der Einflussfaktoren. Diplomathesis, University of Applied Sciences, Northwestern Switzerland, 2005.

[87] S. Wiedemeier. Simulation und experimentelle Untersuchung der Vakuumdestillation zur Wasserentsalzung. Diplomathesis, University of Applied Sciences, Northwestern Switzerland, 2004.

[88] F. Krakau. Simulation of a low grade heat driven multi effect distillation (MED) process. Master's thesis, Technische Universität Berlin, Institut für Energietechnik, 2013.

[89] T. Brendel. *Solare Meerwasserentsalzungsanlagen mit mehrstufiger Verdunstung*. PhD thesis, Fakultät für Maschinenbau, Ruhr-Universitaet Bochum, Bochum, 2003.

[90] R. Semiat and Y. Galperin. Effect of non-condensable gases on heat transfer in the tower MED seawater desalination plant. *Desalination*, (140):27–46, 2001.

[91] Isidor Ernst Giglmayr. *Modellierung von Kraft- und Heizkraftwerken, Vergleich von Software zur thermodynamischen Prozessrechnung*. PhD thesis, Technische Universität Graz, Fakultät für Maschinenbau, 2001.

[92] Commission for Instruments and Methods of Observations (CIMO), Geneva, Switzerland. *Guide to meteorological instruments and methods of observation*, 2012.

[93] Meteorological Measuring System. Manual and technical descriptions, Theodor Friedrichs, Meteorologische Geräte und Systeme GmbH, Schenefeld, January 2013. Serial number 2012-20610.

[94] DLR. Solar MED Atlas. Technical report, Institute of Technical Thermodynamics, Department of Systems-Analysis and Technology Assessment, Stuttgart, Germany, 2014. Version 1.0.341-12912, languages available English, French, Arabic.

[95] J. Remund, S. Müller, S. Kunz, B. Huguenin-Landl, C. Studer, D. Klauser, and C. Schilter. *Meteonorm, Global Meteorological Database; Handbook Part I, Software*. Meteotest, 3012 Bern, Switzerland, version 7.1 edition, September 2014.

[96] J. Remund, S. Müller, S. Kunz, B. Huguenin-Landl, C. Studer, D. Klauser, and C. Schilter. *Meteonorm, Global Meteorological Database; Handbook Part II, Theory*. Meteotest, 3012 Bern, Switzerland, version 7.0.0 edition, May 2012.

[97] Kipp&Zonen. CMP3 Pyranometer Instruction sheet. Technical report, Kipp&Zonen B.V., Delft, Netherlands, 2010.

[98] Normenausschuss Lichttechnik (FNL), editor. *DIN 5035: Tageslicht in Innenräumen*. Deutsches Institut für Normung e.V. (DIN), Germany, teil 2 edition, Februar 1985.

[99] K. Menny. *Strömungsmaschinen, Hydraulische und thermische Kraft- und Arbeitsmaschinen*. Teubner, Wiesbaden, 5th edition edition, 2006.

[100] A. Rothert. Auswertung der Meteorologischen Daten der Power Station El Gouna, Egypt, mit Bezug auf Standortfaktoren fuer Solaranlagen. Bachelor thesis, FU Berlin, Institut für Meteorologie, September 2014.

[101] J. C. W. Balyos. Exergetische Analyse eines Simulationsmodells eines solarthermischen Kraftwerks mit integrierter Niedertemperatur-Entsalzungsanlage. Bachelorthesis, TU Berlin, Institut für Energietechnik, June 2014.

[102] G. Tsatsaronis. Definitions and nomenclature in exergy analysis and exergoeconomics. *Energy*, 32(4):249 – 253, 2007.

[103] A. Bejan, G. Tsatsaronis, and M. Moran. *Thermal Design and Optimzation*. Wiley-Interscience, 1996.

[104] F. Candau. On the exergy of radiation. *Solar Energy*, (75):241–247, 2003.

[105] W. G. LeRoux, T. Bello-Ochende, and J. P. Meyer. A review on the thermodynamic optimisation and modelling of the solar thermal Brayton cycle. *Renewable and Sustainable Energy Reviews*, 28(677-690), 2013.

[106] J. Ahrendts. Solarkraftwerke. *Forschung im Ingenieurwesen*, 54(4):130–136, 1988.

[107] N. Schweimanns. An economic analysis of the cogeneration of power and water. Master's thesis, TU Berlin, Institut für Energietechnik, Fachgebiet EVUR, April 2015.

[108] M. Moser, F. Trieb, and J. Kern. Combined water and electricity production on industrial scale in the MENA countries with concentrating solar power. In *6th EuroMed Conference*, pages 3–6, 2010.

[109] M. Moser, F. Trieb, J. Kern, H. Allal, N. Cottret, J. Scharfe, M.-L. Tomasek, and E. Savoldi. The MED-CSD project: potential for concentrating solar power desalination development in Mediterranean countries. *Journal of Solar Energy Engineering*, 133(3), 2011.

[110] F. Trieb, H. Müller-Steinhagen, J. Kern, J. Scharfe, M. Kabariti, and A. Al Taher. Technologies for large scale seawater desalination using concentrated solar radiation. *Desalination*, 235(13):33 – 43, 2009.

[111] F. Verdier, W. Immerzeel, F. Trieb, R. Baten, M. Moser, T. Fichter, P. Droogers, W. Terink, and J. Hoogeveen. MENA Regional Water Outlook, Phase 1, Final Report. Technical report, Fichtner, FutureWater and DLR, 2011.

[112] T. Laukemann, F. Trieb, M. Moser, and T. Fichter. MENA Regional Water Outlook, Phase 2, Final Report. Technical report, Fichtner and DLR, 2012.

[113] F. Trieb and H. El-Nokraschy. Concentrating Solar Power for Seawater Desalination in MENA Region. In *12th International Water Technology Conference*, 2008.

[114] N. Blair, A. P. Dobos, J. Freeman, T. Neises, M. Wagner, T. Ferguson, P. Gilman, and S. Janzou. System Advisor Model (SAM) General Description. Technical Report NREL/TP-6A20-61019, National Renewable Energy Laboratory, CO 80401, February 2014.

[115] S. Casimiro, J. Cardoso, D.-C. Alarcón-Padilla, C. Turchi, C. Loakimidis, and J.F. Mendes. Modeling Multi Effect Distillation Powered by CSP in TRNSYS. *Proceedings of the SolarPACES International Conference*, (49):2241 – 2250, 2014.

[116] I. Mauleón. The Cost of Renewable Power: A Survey of Recent Estimates. In A. Ansuategi, J. Delgado, and I. Galarraga, editors, *Green Energy and Efficiency*, Green Energy and Technology, pages 235–268. Springer International Publishing, 2015.

[117] P.A. Narbel, J.P. Hansen, and J.R. Lien. Basic Physical Processes and Economics. In *Energy Technologies and Economics*, pages 1–50. Springer International Publishing, 2014.

[118] P. Denholm, Y.-H. Wan, M. Hummon, and M. Mehos. An Analysis of Concentrating Solar Power with Thermal Energy Storage in a California 33% Renewable Scenario. Technical Report NREL/TP-6A20-58186, National Renewable Energy Office (NREL), 2013.

[119] Solar Thermal Electricity 2025 – Clean Electricity on Demand: Attractive STE Cost Stabilize Energy Production. Technical report, European Solar Thermal Electricity Association, 2010. AT Kearney GmbH.

[120] M. Moser, F. Trieb, T. Fichter, J. Kern, and D. Hess. A flexible techno-economic model for the assessment of desalination plants driven by renewable energies. *Desalination and Water Treatment*, 2014.

[121] I.F. Roth and L.L. Ambs. Incorporating externalities into a full cost approach to electric power generation life-cycle costing. *Energy*, 29(1215):2125 – 2144, 2004.

[122] C. Namovicz. Assessing the Economic Value of New Utility - Scale Electricity Generation Projects. In *EIA LCOE/LACE Workshop*, 2013.

[123] O. A. Hamed, H. A. Al-Washmi, and H. A. Al-Otaibi. Thermoeconomic analysis of a power/water cogeneration plant. *Energy*, 31(14):2699 – 2709, 2006.

[124] M. A. Lozano and A. Valero. Theory of the exergetic cost. *Energy*, 18(9):939 – 960, 1993.

[125] G. Tsatsaronis and J. Pisa. Exergoeconomic evaluation and optimization of energy systems – application to the CGAM problem. *Energy*, 19(3):287 – 321, 1994.

[126] B. Erlach, G. Tsatsaronis, and F. Cziesla. A new approach for assigning costs and fuels to cogeneration products. *International journal of applied thermodynamics*, 4(3):145, 2001.

[127] A. A. Valero, L. L. Serra, and J. J. Uche. Fundamentals of Exergy Cost Accounting and Thermoeconomics. Part I: Theory. *Journal of Energy Resources Technology*, 128(1):1–8, 2005.

[128] K.W. Li. *Applied Thermodynamics: Availability Method And Energy Conversion*. Taylor & Francis, 1995.

[129] N. M. Wade. Energy and cost allocation in dual-purpose power and desalination plants. *Desalination*, 123(23):115 – 125, 1999. Selected papers presented at The {WSTA} Fourth Gulf Water Conference.

[130] F. Trieb. Global potential of concentrating solar power. In *SolarPACES*, 2009.

[131] M. Kaltschmitt, W. Streicher, and A. Wiese. Solar Thermal Power Plants. In Martin Kaltschmitt, Wolfgang Streicher, and Andreas Wiese, editors, *Renewable Energy*, pages 171–228. Springer Berlin Heidelberg, 2007.

[132] IEA. Modelling the capacity credit of renewable energy sources. *International Energy Agency*, 2011.

[133] N. Kulichenko and J. Wirth. *Concentrating solar power in developing countries: Regulatory and financial incentives for scaling up*. The World Bank, 2012.

[134] W. Zhang. Concentrating Solar Power–State of the Art, Cost Analysis and Pre-Feasibility Study for the Implementation in China. Master's thesis, University of Stuttgart, Germany, 2009.

[135] B. L. Kistler. A user's manual for DELSOL3: a computer code for calculating the optical performance and optimal system design for solar thermal central receiver plants. Technical report, Sandia National Labs., Livermore, CA (USA), 1986.

[136] G. Cole. El Gouna goes Carbon Neutral. *Sawiris Foundation for Environmental Development*, January 2014. Press release.

[137] EEHC. Annual Report 2012/13. Technical report, Egyptian Electriciy Holding Company, 2013. Arab Republic of Egypt, Ministry of Electricity and Energy.

[138] F. Trieb. PV Performance Model. *Script for the lecture Integration of Renewable Energies*, Section 11, October 2012.

[139] F. Trieb. Wind Performance Model. *Script for the lecture Integration of Renewable Energies*, Section 12, October 2012.

[140] N. Tzoupanos and S. Estafanous. Drinking water consumption of El Gouna, Red Sea, Egypt. TU Berlin Campus El Gouna, Department Water Engineering and El Gouna Water, 2014.

[141] IRENA. Renewable Energy Technologies, Cost Analysis series: Solar Photovoltaics. Volume 1: Power Sector Issue 4/5, International Renewable Energy Agency (IRENA), Bonn, Germany, 2012.

[142] EIA. Updated Capital Cost Estimates for Utility Scale Electricity Generating Plants. *US Energy Information Administration (EIA)*, April 2013.

[143] Strom aus Wind - eine Investition in unsere Zukunft. Technical report, Beermann Windkraft GmbH, Maierfeld KG, Januar 2011. Windpark Maierfeld in den Marktgemeinden Kindingen und Titting.

[144] IRENA. Renewable Power Generation Costs in 2012: An Overview. Technical report, International Renewable Energy Agency (IRENA), Bonn, Germany, June 2013.

[145] Sören Krohn, Poul-Erik Morthorst, and Shimon Awerbuch. The Economics of Wind Energy. Report, European Wind Energy Association, March 2009.

[146] Wirtschaftlichkeit der WKA in Gailingen. Technical report, Bürgerinitiative für einen verantwortungsvollen Umgang mit Windenergie, April 2012.

[147] A. Almulla, A. Hamad, and M. Gadalla. Integrating hybrid systems with existing thermal desalination plants. *Desalination*, 174:171–192, 2005.

[148] N. H. Aly and A. K. El-Fiqi. Thermal performance of seawater desalination systems. *Desalination*, (158):127 – 142, January 2003.

[149] R. Borsani and S. Rebagliati. Fundamentals and costing of MSF desalination plants and comparison with other technologies. *Desalination*, (182):29–37, March 2005.

[150] H.-J. Bungartz, S. Zimmer, M. Buchholz, and D. Pflüger. *Modellbildung und Simulation, eine anwendungsorientierte Einführung*. Springer, Heidelberg, 2009.

[151] A. Desportes. Integration einer Meerwasserentsalzungsanlage in ein Solarkraftwerk. Master's thesis, Hochschule München, Fachbereich 06, Feinwerk- und Mikrotechnik / Physikalische Technik, 2010.

[152] P. Droogers, W. Immerzeel, W. Terink, J. Hoogeveen, M. F. P. Bierkens, L. P. H. van Beek, and B. Debele. Water resources trends in Middle East and North Africa towards 2050. *Hydrology and Earth System Sciences*, (16):3101 – 3114, April 2012.

[153] Y.M. El-Sayed and R.A. Gaggioli. A Critical Review of Second Law Costing Methods – I: Background and Algebraic Procedures. *Journal of Energy Resources Technology*, 111(1):1–7, 1989.

[154] M. Falchetta. Thematic research summary, Concentrating solar power. Technical report, National Agency for New Technologies Energy and Sustainable Economic Development (ENEA) and Energy Research Knowledge Centre (ERKC), European Commission, November 2013.

[155] C.B. Field, V.R. Barros, D.J. Dokken, K.J. Mach, M.D. Mastrandrea, T.E. Bilir, M. Chatterjee, K.L. Ebi, Y.O. Estrada, R.C. Genova, B. Girma, E.S. Kissel, A.N. Levy, S. MacCracken, P.R. Mastrandrea, and L.L. White. Summary for policymakers. In: Climate Change 2014: Impacts, Adaptation, and Vulnerability. Part A: Global and Sectoral Aspects. Contribution of Working Group II to the Fifth Assessment Report of the Intergovernmental Panel on Climate Change. Cambridge university press, Intergovernmental Panel on Climate Change, Cambridge, United Kingdom and New York, 2014.

[156] G. Ford. CSP: bright future for linear fresnel technology? *Renewable Energy Focus*, 2008.

[157] trAIDe GmbH in Zusammenarbeit mit Chemonics Egypt Consultants. Eine Markt- und Branchenanalyse für die Teilnehmer des MEP Wasserwirtschaft Ägypten 2012. *MEP Ägypten*, 2012.

[158] D. Horst. Performance Simulation For Parabolic Trough Concentrating Solar Power Plants And Export Scenario Analysis For North Africa. Master's thesis, Faculty of Engineering at Cairo University, Giza, Egypt, 2012.

[159] A. Ibrahim. Renewable energy sources in the Egyptian electricity market: A review. *Renewable and Sustainable Energy Reviews*, (doi:10.1016/j.rser.2011.07.149), 2011.

[160] IEA. *World Energy Outlook 2014*. IEA, Paris, 2014.

[161] IEA. Technology roadmap: Energy Storage. *International Energy Agency*, 2014.

[162] IRENA. International Renewable Energy Agency – publications available online. http://www.irena.org/Publications/.

[163] IRENA. Renewable Energy Technologies, Cost Analysis series: Concentrating Solar Power. Volume 1: Power Sector Issue 2/5, International Renewable Energy Agency (IRENA), Bonn, Germany, June 2012.

[164] M. Isaka, G. Simbolotti, G. Tosato, and D. Gielen. Water Desalination Using Renewable Energy: technology brief. *IRENA and IEA–ETSAP*, 2012.

[165] R. Kempener, G. Simbolotti, and G. Tosato. Thermal storage: technology brief. *IRENA and IEA–ETSAP*, 2013.

[166] J. Kern. Concentrating Solar Power for seawater desalination, Solutions to feed the world. In *Saudi International Water Technology Conference Riyadh*, Riyadh, Kingdom of Saudi-Arabia, November 21-22, 2011 2011.

[167] C. Kost, J. N. Mayer, J. Thomsen, N. Hartmann, C. Senkpiel, S. Philipps, S. Nold, S. Lude, N. Saad, and T. Schlegl. Levelized Cost of Electricity - Renewable Energy Technologies. *Fraunhofer Institut For Solar Energy systems (ISE)*, 2013.

[168] P. De Laquil, B.D. Kelley, and R.L. Lessley. Solar Central Receiver Technology Advancement for Electric Utility Applications, Phase 1 Topical Report. Technical Report Report No. 007.2-88.2, Pacific Gas & Electric Company, September 1988. Pacific Gas and Electric Co., San Ramon, CA (United States); Bechtel National, Inc., San Francisco, CA (United States).

[169] K. Madaly and J. Hoffmann. Identifying the optimum storage capacity for a 100 MW CSP plant in South Africa. Master's thesis, Stellenbosch University, 2014.

[170] D.M. Marsh. The Water-Energy Nexus: A Comprehensive Analysis in the Context of New South Wales. Dissertation, Faculty of Engineering and Information Technology, University of Technology, Sydney, 2008.

[171] S. Martinez Romero and W. Hughes. Bringing Variable Renewable Energy Up to Scale: Options for Grid Integration Using Natural Gas and Energy Storage. Technical report, 2015.

[172] C.R. Mertes. CSP EMEA 2012. *CSP Emea*, 2012.

[173] A. Mills and R. Wiser. Changes in the Economic Value of Variable Generation at High Penetration Levels: A Pilot Case Study of California. Technical Report LBNL-5445E, Ernest Orlando Lawrence Berkeley National Laboratory, Berkeley, CA, June 2012.

[174] K.H. Mistry, R.K. McGovern, G.P. Thiel, E.K. Summers, S.M. Zubair, and J.H. Lienhard. Entropy Generation Analysis of Desalination Technologies. *Entropy 2011*, (13):1829 – 1864, 2011.

[175] M. Moser. Concentrated Solar Power combined with MED-Plants. *DME Seminar*, 2013.

[176] M. Moser, F. Trieb, and T. Fichter. Potential of Concentrating Solar Power Plants for the Combined Production of Water and Electricity in MENA Countries. *Journal of Sustainable Development of Energy, Water and Environment Systems* , 1(2):122–140, 2013.

[177] NREL. National Renewable Energy Laboratory – Energy Analysis publications. http://www.nrel.gov/analysis/publications/.

[178] P. Palenzuela, G. Zaragoza, and D.-C. Alarcón-Padilla. Characterisation of the coupling of multi-effect distillation plants to concentrating solar power plants. *Energy*, 82(0):986 – 995, 2015.

[179] M. Papapetrou, M. Wieghaus, and C. Biercamp. *Roadmap for the development of desalination powered by Renewable Energy*. Promotion of renewable energy for water production through desalination (PRODES), Munich, Germany, 2010.

[180] G. Plessmann, M. Erdmann, M. Hlusiak, and Ch. Breyer. Global Energy Storage Demand for a 100% Renewable Electricity Supply. *Reiner Lemoine Institut gGmbH*, 2013.

[181] C. Sommariva. Management and Economics. Technical report, International Desalination Association (IDA), Desalination Academy, 2013.

[182] Stocker, D. Qin, G.-K. Plattner, M. Tignor, S.K. Allen, J. Boschung, A. Nauels, Y. Xia, V. Bex, and P.M. Midgley. Climate Change 2013: The Physical Science Basis. Contribution of Working Group I to the Fifth Assessment Report of the Intergovernmental Panel on Climate Change. Cambridge University Press ISBN 978-1-107-05799-1, Intergovernmental Panel on Climate Change, United Kingdom and New York, 2013.

[183] A.H. Tarrad and L.M. Majeed. The Application of a Step by Step Technique for the Performance Prediction Of Thermal Power Plant Surface Condensers. *Journal of Engineering*, (16):4748 – 4770, 2010.

[184] R. Yousef and M. Sakr. Desalination Technology Roadmap 2030. *The Cabinet Information and Decision Support Center Egypt*, 2007.

[185] G.M. Zak. Thermal Desalination: Structural Optimization and integration in Clean Power and Water. Master's thesis, Massachusetts Institute of Technology, Department of Mechanical Engineering, June 2012.

ISBN 978-3-945682-21-0